UNIVERSITY OF CALIFORNIA

Santa Barbara

Ocean Sediment Core Age Models, Stacks, and Benthic Foraminiferal $\delta^{18}O$ Lags

A dissertation submitted in partial satisfaction of the

requirements for the degree Doctor of Philosophy

in Earth Science

by

Devin Scott Rand

Committee in charge:

Professor Lorraine Lisiecki, Chair

Professor Syee Weldeab

Professor David Lea

December 2023

The dissertation of Devin Scott Rand is approved.

_____
Syee Weldeab

_____
David Lea

_____
Lorraine Lisiecki, Committee Chair

December 2023

Ocean Sediment Core Age Models, Stacks, and Benthic Foraminiferal $\delta^{18}O$ Lags

by

Devin Scott Rand

ACKNOWLEDGEMENTS

There are many people to whom I will be forever grateful and who are in part responsible for the completion of this thesis.

To begin, this work is a direct result of the collaboration between myself, Lorraine Lisiecki, Taehee Lee, Chip Lawrence, and Jake Gebbie. Weekly meetings with this interdisciplinary team not only served to lift my spirits but resulted in a truly meaningful contribution to the field of paleoclimate and paleoceanography.

My committee, Syee Weldeab and David Lea provided constructive criticism and insightful conversation. They never failed to reveal gaps in my knowledge and ultimately strengthened my research.

My fellow graduate students and friends provided inspiration in both my professional endeavors as well as my outdoor hobbies. Climbing trips and surfing excursions with these great people have kept me happy and grounded over the past six years. They will surely be impossible to replace and I hope to stay in touch.

My family for their unconditional love and support. My twin brother Cory and my older sister Lauren constantly push me to strive for more, and my mother Sheryl and father David have and will always support my professional and personal decisions.

Finally, I owe everything I have learned and every skill I have developed in the past six years to my advisor Lorraine. Through guidance and mentorship, she has taught me to be a statistician, a writer, and a scientist.

VITA OF DEVIN SCOTT RAND
September 2023

EDUCATION

Bachelor of Science in Math and Physics, University of Oregon, June 2014
Master of Science in Earth Science, UCSB, September 2019
Doctor of Philosophy in Earth Science, UCSB, September 2023

RESEARCH EXPERIENCE

2017-2023: Graduate Student Researcher, Department of Earth Science, UCSB
2017-2017: Research Assistant, Department of Geology, Portland State University
Summer, 2012: Research Assistant, Department of Mechanical Engineering, CSU
2011-2014: Research Assistant, Department of Physics, UO

TEACHING AND MENTORING

2017-2023: Teaching Assistant, Department of Earth Science, UCSB
2021-2023: Mentor, Department of Earth Science, UCSB
2021-2023: GEMSS Leadership, Department of Earth Science, UCSB
2013-2014: Teaching Assistant, Department of Physics, UO

SELECTED AWARDS

2023: G.K. Gilbert Award
2023: George Tunnel Memorial Fellowship
2022: Research Excellence
2018: AGU Outstanding Student Presentation Award

PUBLICATIONS

Bowman, Christen L., Devin S. Rand, Lorraine E. Lisiecki, and Samantha C. Bova. "An 800-kyr planktonic $\delta^{18}O$ stack for the West Pacific Warm Pool." Earth System Science Data Discussions 2023 (2023): 1-19.

Hobart, Bethany, Lorraine E. Lisiecki, Devin Rand, Taehee Lee, and Charles E. Lawrence. "Late Pleistocene 100-kyr glacial cycles paced by precession forcing of summer insolation." Nature Geoscience (2023): 1-6.

Lee, Taehee, Devin Rand, Lorraine E. Lisiecki, Geoffrey Gebbie, and Charles E. Lawrence. "Bayesian age models and stacks: Combining age inferences from radiocarbon and benthic $\delta^{18}O$ stratigraphic alignment." EGUsphere 2022 (2022): 1-29.

Lisiecki, Lorraine E., Alan M. Jones, Devin Rand, Taehee Lee, and Charles E. Lawrence. "Comparing age model techniques for the last glacial cycle: A case study of ten Iberian Margin sediment cores." Quaternary Science Reviews 287 (2022): 107559.
Harvard

Repschläger, Janne, Ning Zhao, Devin Rand, Lorraine Lisiecki, Juan Muglia, Stefan Mulitza, Andreas Schmittner et al. "Active North Atlantic deepwater formation during Heinrich Stadial 1." Quaternary Science Reviews 270 (2021): 107145.

ABSTRACT

Ocean Sediment Core Age Models, Stacks, and Benthic Foraminiferal $\delta^{18}O$ Lags

by

Devin Scott Rand

Accurate and precise age models are essential to interpret the climate signals preserved in ocean sediment cores, yet age models are often constructed with only a single dating technique. Radiocarbon dating directly dates discrete sediment layers but suffers from low resolution and is restricted to the last 55 ka BP, while benthic $\delta^{18}O$ stratigraphic alignment is vulnerable to temporal offsets between $\delta^{18}O$ signals, or lags.

Here I present a new Bayesian software package to construct ocean sediment core age models by statistically combining direct age information, such as radiocarbon data, with probabilistic benthic $\delta^{18}O$ stratigraphic alignment. The software package also offers a novel stack construction algorithm capable of building regional and continuous benthic $\delta^{18}O$ stacks.

I also develop a novel method to calculate time-dependent benthic $\delta^{18}O$ lags complete with statistical uncertainty estimates. Specifically, lags are calculated by subtracting radiocarbon age models from benthic $\delta^{18}O$ age models and are relative to the

target stack. The uncertainty from each age model is incorporated into the lag calculation via the subtraction of Markov Chain Monte Carlo Samples.

I apply this method to calculate lags for 33 Atlantic sediment cores, the results of which indicate three distinct regions based on the timing of benthic $\delta^{18}O$ change. I find statistically significant leads in the intermediate West Atlantic, statistically significant lags in the deep South West and Abyssal North West Atlantic, and I find that cores in the East Atlantic share the timing of $\delta^{18}O$ change with the target stack. In addition, I calculate the regional lag between the Iberian Margin and Eastern Equatorial Pacific and I find that it is 1.5 kyr smaller than the original 3.9 kyr estimate.

While lags will help future investigators during age model construction, I also interpret them to reflect asynchronous surface signals, transit times from the surface to the deep ocean, and water mass geometry changes during Termination

TABLE OF CONTENTS

I. Introduction

Ocean sediment cores are invaluable repositories containing indicators of past climates, yet their analysis necessitates robust age models. Common age model construction techniques include radiocarbon dating, in which discrete sediment layers are directly dated, and benthic $\delta^{18}O$ stratigraphic alignment, in which an age model is constructed by aligning $\delta^{18}O$ signals. Yet each technique has its limitations. Radiocarbon is constrained to 55 ka BP and is often lower resolution than other climate proxies while stratigraphic alignment is susceptible to asynchronous benthic $\delta^{18}O$ signals (benthic $\delta^{18}O$ lags) which potentially introduces errors in the final age model. Yet these lags can also yield crucial insights into their underlying causes.

My thesis advances the intersection between ocean sediment core age models and benthic $\delta^{18}O$ lags. I introduce a new Bayesian software package that combines age information from radiocarbon data and probabilistic stratigraphic alignment. This package can also generate improved benthic $\delta^{18}O$ stacks, which serve as enhanced alignment targets. Furthermore, I develop a new method for calculating benthic $\delta^{18}O$ lags and I produce lag estimates within the Atlantic Ocean and between the Iberian Margin and the Eastern Equatorial Pacific. These lag calculations will help future researchers select appropriate alignment target. In addition, lags can also shed light on the following factors that cause them: asynchronous hemispheric surface signals, surface signal transit times to the deep ocean, and water mass geometries.

A summary of each chapter is provided below.

Chapter II: I introduce a new Bayesian software package for constructing ocean sediment core age models and benthic $\delta^{18}O$ stacks. The package combines the direct age information from radiocarbon data with information from the stratigraphic alignment of benthic $\delta^{18}O$ signals. Furthermore, the software package can calculate benthic $\delta^{18}O$ stacks from a smaller dataset, allowing for the construction of stacks that are representative of a single region defined by a homogeneous $\delta^{18}O$ signal.

Chapter III: I present a statistical method to calculate time-dependent benthic $\delta^{18}O$ lags that include statistical uncertainty estimates. Lags are determined by subtracting radiocarbon-only age models from benthic $\delta^{18}O$-only models which are constructed using the software package presented in Chapter II. I validate this method by replicating the $\delta^{18}O$ offsets previously observed in a depth transect of 12 ocean sediment cores sampled from the Brazil Margin.

Chapter IV: I apply the lag-calculation method from Chapter III to 33 Atlantic sediment cores and I find three distinct regions defined by the timing of $\delta^{18}O$ change during Termination 1. The intermediate North West Atlantic exhibits statistically significant leads, the deep South West and abyssal North West Atlantic feature statistically significant lags, and the East Atlantic shares the timing of $\delta^{18}O$ change with the target stack. I also note that leads peak in the first half of Termination 1, while lags are more prominent in the second half. I hypothesize that leads result from sub-surface warming caused by a weakened circulation state, while lags arise from a glacial circulation regime leading to a mid-depth age maximum. Furthermore, I find a statistically significant correlation between leads/lags and the percent change in southern component water. Finally, I propose an empirically

derived lag equation dependent on transit times, water mass geometries, and a southern hemisphere surface lag.

Chapter V: I compare the method introduced in Chapter 2 with two alternative approaches to calculate the regional lag between the Iberian Margin and the Eastern Equatorial Pacific. This comparative analysis results in a 1.5 kyr reduction in the estimated lag between these two regions.

This thesis serves to enhance ocean sediment core age models by combining age information from radiocarbon and benthic $\delta^{18}O$. Additionally, the ability to construct regional stacks based on the maps of benthic $\delta^{18}O$ lags will guide future researchers in selecting or constructing alignment targets. Furthermore, the lags themselves offer valuable insights into the climate system's evolution during Termination 1.

II. Bayesian Age Models and Stacks: Combining Age Inferences From Radiocarbon and Benthic $\delta^{18}O$ Stratigraphic Alignment

Abstract

Previously developed software packages that generate probabilistic age models for ocean sediment cores are designed to either interpolate between different age proxies at discrete depths (e.g., radiocarbon, tephra layers, or tie points) or perform a probabilistic stratigraphic alignment to a dated target (e.g., of benthic $\delta^{18}O$) and cannot combine age inferences from both techniques. Furthermore, many radiocarbon dating packages are not specifically designed for marine sediment cores and default settings may not accurately reflect the probability of sedimentation rate variability in the deep ocean, requiring subjective tuning of parameter settings. Here we present a new technique for generating Bayesian age models and stacks using ocean sediment core radiocarbon and probabilistic alignment of benthic $\delta^{18}O$ data, implemented in a software package named BIGMACS (Bayesian Inference Gaussian Process regression and Multiproxy Alignment of Continuous Signals). BIGMACS constructs multiproxy age models by combining age inferences from both radiocarbon ages and probabilistic benthic $\delta^{18}O$ stratigraphic alignment and constrains sedimentation rates using an empirically derived prior model based on 37 ^{14}C-dated ocean sediment cores (Lin et al., 2014). BIGMACS also constructs continuous benthic $\delta^{18}O$ stacks via a Gaussian process regression, which requires a smaller number of cores than previous stacking methods. This feature allows users to construct stacks for a region that shares a homogeneous deep water $\delta^{18}O$ signal, while leveraging radiocarbon dates across multiple cores. Thus, BIGMACS efficiently generates local or regional stacks with smaller

uncertainties in both age and $\delta^{18}O$ than previously available techniques. We present two example regional benthic $\delta^{18}O$ stacks and demonstrate that the multiproxy age models produced by BIGMACS are more precise than their single proxy counterparts.

1 Introduction

The accuracy with which ocean sediment core data can reconstruct the timing of past climate events depends on the quality of the core's age model (i.e., estimates of age as a function of core depth). However, age models are often constrained by only a single dating proxy type. A common technique is radiocarbon dating, which directly dates individual sediment layers. However, this method is restricted to the last 55 ka BP, suffers from variable surface reservoir ages (Waelbroeck et al., 2001; Sikes et al., 2016; Stern & Lisiecki, 2013; Skinner et al., 2019), and radiocarbon data are often lower resolution than benthic $\delta^{18}O$ data. Radiocarbon age models are sometimes supplemented with stratigraphic tie points to a dated target, however this method requires the subjective identification of shared features that are often recorded in different archives. An alternative technique is the stratigraphic alignment of benthic $\delta^{18}O$ to a target stack (e.g., Imbrie et al., 1984; Lisiecki & Raymo, 2005), which represents the mean benthic $\delta^{18}O$ signal across multiple cores. Benthic $\delta^{18}O$ is often measured at higher resolution than radiocarbon data, but this dating technique provides only relative age information between cores by assuming that the input and target have synchronous benthic $\delta^{18}O$ signals. Temporal offsets between the aligned records can cause age errors in the aligned age model (Skinner & Shackleton, 2005; Labeyrie et al., 2005; Waelbroeck et al., 2011; Stern & Lisiecki, 2014; Lund et al., 2015).

Software packages exist to produce age models by interpolating between age proxies (such as radiocarbon ages, tephra layers, or/and tie points; Blaauw & Christen 2011;

Lougheed & Obrochta, 2019), or by performing a probabilistic benthic $\delta^{18}O$ alignment (in which residuals between input and target records are minimized; Lin et al., 2014; Ahn et al., 2017), but none of these packages can probabilistically combine age inferences from both dating techniques. While one study presented a Bayesian multiproxy age model for a single core from the Arctic Ocean, the methodology is specific to the high latitude region in which radiocarbon data is unreliable and aligned porosity rather than benthic $\delta^{18}O$ (Muschitiello et al., 2020). Furthermore, many age modelling software packages were not specifically designed for marine sediment cores (Ramsey, 1995; Haslett & Parnell, 2008; Blaauw, 2010; Blaauw & Christen 2011) and default settings may not accurately reflect the probability of sediment accumulation rate variability in marine settings. Users must often subjectively choose parameter settings which may ultimately affect the interpretation of paleoclimate records.

Here we present a new technique for generating Bayesian age models and stacks of ocean sediment core data, implemented in a software package named BIGMACS (Bayesian Inference Gaussian Process regression and Multiproxy Alignment of Continuous Signals). BIGMACS constructs radiocarbon age models, benthic $\delta^{18}O$ age models, and multiproxy age models which combine age inferences from both radiocarbon ages and $\delta^{18}O$ stratigraphic alignment. Radiocarbon ages directly date sediment layers while benthic $\delta^{18}O$ provides relative age constraints between radiocarbon ages and beyond 55 ka BP. We use the term "multiproxy" to indicate the combined inference from two types of "age proxies": absolute age information provided by radiocarbon and relative age information from the stratigraphic alignment of benthic $\delta^{18}O$. Note that this method is distinct from an alignment of multiple climate proxies (e.g., benthic and planktonic $\delta^{18}O$). BIGMACS can also

probabilistically incorporate other types of age information at specified depths, such as inferences from tephra layers, magnetic reversals, or user-identified tie points. Sedimentation rates are realistically constrained with an empirically derived prior model from Lin et al. (2014) rather than subjective parameter settings. Median age models and their uncertainties are defined by the distribution of Markov Chain Monte Carlo (MCMC) samples. The distribution of MCMC samples at a given depth of a radiocarbon age model reflects the absolute age uncertainty of the sediment. However, $\delta^{18}O$ age model uncertainty reflects only the relative age uncertainty and excludes the absolute age uncertainty of the alignment target. BIGMACS does not use any orbital tuning unless users choose to align to a target stack that has been orbitally tuned.

Another functionality of BIGMACS is the automated construction of multiproxy benthic $\delta^{18}O$ stacks using an iterative process that simultaneously considers the probabilistic fit to both absolute age information (e.g., from radiocarbon dates) and relative age information from alignment of all cores' benthic $\delta^{18}O$ signals. Age models for each core are constructed by aligning benthic $\delta^{18}O$ to the stack from the previous iteration, and then a new stack is calculated from the aligned $\delta^{18}O$ from every core. Radiocarbon ages (if included) help constrain the age models for their respective cores during each iteration of stack construction. Similar to "errors-in-variables" regression, which is used to construct the Intcal20 curve due to uncertainty in both the radiocarbon measurements and their calendar ages (Reimer et al., 2020; Heaton et al., 2020), BIGMACS calculates a time series of mean and variance for benthic $\delta^{18}O$ by performing Gaussian process regressions (Rasmussen and Williams, 2006) across MCMC age model samples. The resulting stack variance is a combination of both age model uncertainty from individual cores and the spread of benthic

$\delta^{18}O$ from every core. This method requires fewer cores than previous stacking methods (e.g., Ahn et al., 2017; Lisiecki & Stern, 2016) and, thus, allows users to construct target stacks from a small number of neighbouring cores that share homogeneous $\delta^{18}O$ signals.

Section 2 provides a summary of some common techniques used for radiocarbon dating, $\delta^{18}O$ alignment and $\delta^{18}O$ stack construction. Section 3 describes the statistical methods used in BIGMACS, including an overview of the Bayesian framework, the prior model that constrains sedimentation rates, and the likelihood models for different proxy types. We also describe the methods used to draw MCMC age model samples and the regression technique employed to construct continuous stacks from a small number of cores. In section 4, we present two example regional Atlantic stacks: a Deep Northeast Atlantic (DNEA) stack, and an Intermediate Tropical West Atlantic (ITWA) stack. The two stacks are composed of 6 and 4 cores respectively, that are chosen based on an evaluation of their water mass histories. In section 5, we compare a multiproxy age model, a $\delta^{18}O$-only age model, and a radiocarbon-only age model for one additional core. We demonstrate that age model precision is increased when using both radiocarbon ages and $\delta^{18}O$ alignment. Finally, we discuss potential future applications of BIGMACS and the factors affecting its runtime.

2 Background

2.1 Radiocarbon Age Models

Radiocarbon ages must be calibrated from ^{14}C years to calendar years with a calibration curve that accounts for the changing magnetic fields of the Sun and Earth, solar storms, and variations in the terrestrial carbon cycle (Reimer et al., 2020; Heaton et al., 2020; Heaton et al., 2021). The uncertainty of the calibrated age is a combination of the calibration curve uncertainty, the radiocarbon measurement uncertainty, the time-dependent

local reservoir age offset from the calibration curve (ΔR) and the associated reservoir age uncertainty. Techniques to calibrate radiocarbon ages have evolved from interpolation techniques such as Calib (Stuiver & Reimer, 1993) to Bayesian calibration methods (e.g., Oxcal by Ramsey, 1995; Bcal by Buck and Christen, 1999; Matcal by Lougheed & Obrochta, 2016) which typically generate asymmetric, nonparametric calendar age distributions due to slope changes in the calibration curve.

Planktonic foraminiferal radiocarbon dates must be corrected for the reservoir age of the surface ocean relative to the atmosphere or calibrated with a curve that accounts for the reservoir age of the surface ocean (e.g., the Marine20 curve; Heaton et al., 2020). Previous studies have used different methods to estimate past reservoir ages, including using modern measurements from the Global Ocean Data Analysis Project (GLODAP, Key et al., 2004, Waelbroeck et al., 2019) and the Calib database (Reimer & Reimer, 2001), comparing stratigraphically aligned age models with radiocarbon age models (Stern & Lisiecki, 2013; Skinner et al., 2021), and modelled reservoir ages from a Large Scale Geostrophic Ocean General Circulation Model (LSG-OGCM, Butzin et al., 2020; Butzin et al., 2017, Langner & Mulitza 2019; Heaton et al., 2020).

Constructing a sediment core age model, which estimates sediment ages for all core depths, from a sequence of radiocarbon ages requires assumptions or models of the core's evolving sedimentation rate between dated intervals. The median age model and age model uncertainty depend on the radiocarbon calibration method, the applied sedimentation rate constraints, and the outlier identification procedure (Christen, 1994; Ramsey, 2009b, Christen & Peréz, 2009). Multiple software packages have been published to construct probabilistic radiocarbon age models that apply a variety of statistical techniques (e.g.,

Ramsey, 1995, 2001, 2008, 2013; Blaauw & Christen, 2005; Haslett & Parnell 2008; Blaauw, 2010; Blaauw & Christen, 2011; Lougheed & Obrochta, 2019).

Oxcal (Ramsey, 1995) provides modelling routines for multiple depositional environments; the routine known as the P_Sequence is commonly used for modelling marine and lacustrine cores. P_Sequence uses a Poisson process in which the number of depositional events per unit depth is determined by a tuneable, user-specified parameter which affects the uncertainty of the age model. Oxcal also includes multiple options to identify outliers, including an agreement index which measures the overlap between the posterior distribution of the age model and the radiocarbon likelihood at depths where radiocarbon ages exist.

Bchron (Haslett & Parnell, 2008) constructs age-depth models using a monotone Markov process and piecewise linear interpolation paths with random durations. Bchron requires few user-specified parameter settings and posits less prior knowledge on sedimentation rate constraints; thus, age models constructed with Bchron often have larger age uncertainties than other software packages, particularly for radiocarbon records of low resolution (Blaauw & Christen, 2011). Bchron identifies two types of outliers based on the shift required to satisfy the monotonicity constraint. Standard outliers have a prior probability of 5% and require a shift defined *a priori* by a normal distribution with variance equal to double the radiocarbon analytical measurement error. Larger outliers have a prior probability of 0.1% and are excluded from the age model construction process.

Bacon (Blaauw & Christen, 2011) separates cores into fixed segments and uses an auto-regressive gamma process to simulate sedimentation rates. The user specifies tuneable priors for a beta distribution that controls age model autocorrelation and a gamma

distribution that governs sedimentation rate variability. Radiocarbon ages are modelled with a generalized student's t-distribution (Christen & Peréz, 2009) that scales the error associated with radiocarbon measurements. The amount of scaling depends on two parameters which are set by default to assign a 70% chance that the reported error was underestimated by a factor between 1 and 2. Christen & Peréz (2009) explain that the choice of these parameter values is a "practical guideline" which they estimated to reflect the state of radiocarbon data at the time.

Undatable (Lougheed & Obrochta, 2019) uses a Monte Carlo sampling algorithm designed to emulate statistical models of sedimentation rate variability with the goal of producing quick runtimes. Users set two parameters: a scaling parameter that scales age uncertainties at the midpoints between radiocarbon ages and a bootstrapping percent that provides a framework to address outlier radiocarbon ages. These parameters have large effects on the resulting age model, requiring the user to select appropriate values, e.g., according to recommendations in Lougheed & Obrochta, (2019), rather than relying on a prior model of sedimentation rate variability.

2.2 Benthic $\delta^{18}O$ Age Models

In the calcite shells of foraminifera, the ratio of ^{18}O to ^{16}O measured relative to a standard, denoted $\delta^{18}O$, is a proxy for global ice volume, local water temperature and the local $\delta^{18}O$ of seawater, which often correlates with salinity. Due to the relatively homogeneous temperature and salinity changes of the deep ocean, previous studies have assumed benthic $\delta^{18}O$ changes synchronously (Shackleton, 1967) and have used the proxy as a global stratigraphic signal to construct ocean sediment core age models (e.g., Pisias et al., 1984; Lisiecki and Raymo, 2005). The most conservative technique for aligning records

to a target is to assume that large, easily identifiable features in the signals, such as glacial terminations, occurred simultaneously, create tie points between these features, and linearly interpolate between the tie points (e.g., Huybers & Wunsch, 2004). However, this linear interpolation method may misalign smaller scale features due to changes in sedimentation rates between tie points.

Software packages have been published that automate the alignment process and optimize the fit of the entire signal. Lisiecki & Lisiecki (2002) developed the deterministic software package Match, which utilizes dynamic programming to minimize a cost function based on sedimentation rate changes and the sum-of-square error misfit between signals. Match was used to align 57 benthic $\delta^{18}O$ records and construct the global "LR04" Plio-Pleistocene stack (Lisiecki & Raymo, 2005) and a 1.5-Myr multiproxy geomagnetic paleointensity and $\delta^{18}O$ stack (Channell et al., 2009).

The Bayesian package HMM-Match (Lin et al., 2014) performs a point-based alignment using a hidden Markov model and returns estimates of alignment uncertainty based on the distribution of MCMC age model samples. HMM-Match considers the probability of every possible alignment given the fit to the alignment target and the modelled sedimentation accumulation rate changes. The probability of a given benthic $\delta^{18}O$ residual to the target is modelled with a fixed Gaussian distribution based on the record's $\delta^{18}O$ residuals and a mean shift from the target. Sedimentation rates are realistically constrained using a log-normal mixture distribution fit to normalized sedimentation rate estimates derived by linearly interpolating between calibrated radiocarbon ages in 37 cores.

Heaton et al., (2013) presents an age model construction method which uses a Gaussian process regression to interpolate between benthic $\delta^{18}O$ tie points. The method

incorporates uncertainty from the target age model, tie point identification, and interpolation between tie points and was used to construct chronologies for records incorporated into the IntCal13 and Intcal20 curve (Reimer et al., 2013; Reimer et al., 2020). Heaton et al., (2013) argue against using a deterministic automated alignment process (e.g., Lisiecki and Lisiecki, 2002) due to a lack of uncertainty estimates and concerns about aligning across different proxy types which may differ in sensitivity to climate responses. We assert that using BIGMACS to align across a set of sediment cores with homogeneous signals of the same proxy (such as benthic $\delta^{18}O$ in neighbouring cores), addresses these concerns. BIGMACS formally incorporates multiple sources of age uncertainty to create probabilistic alignments that are both more informative and less subjective than tie point identification.

Diachronous benthic $\delta^{18}O$ signals are an additional source of uncertainty in benthic $\delta^{18}O$ aligned age models. Previous studies have identified temporal offsets up to 4 kyr between $\delta^{18}O$ records during terminations (Skinner & Shackleton, 2005; Lisiecki & Raymo, 2009; Stern & Lisiecki, 2014). Because stratigraphic alignment relies on the assumption that benthic $\delta^{18}O$ between the input and the target core varies synchronously, these offsets can cause age errors in $\delta^{18}O$-aligned age models. Thus, without a direct dating proxy (e.g., radiocarbon, tephra, etc.), $\delta^{18}O$ stratigraphic alignment is an inadequate tool to study the sequence of climate responses at different locations during glacial terminations (e.g., Khider et al., 2017) or millennial-scale events. Causes of offsets in the timing of benthic $\delta^{18}O$ change include asynchronous surface signals, changes in deep ocean water mass geometry, or/and different deep water transit times (Gebbie, 2012). To mitigate the impacts of diachronous $\delta^{18}O$ change, benthic $\delta^{18}O$ alignment should ideally be restricted to cores which

have experienced a similar history of deep water mass change. We present one method to identify cores with synchronous benthic $\delta^{18}O$ signals in section 4.1.

2.3 Benthic $\delta^{18}O$ Stacks

Benthic $\delta^{18}O$ stacks are used as a common framework by which new paleoceanographic measurements are compared and are often used as targets during stratigraphic alignment (e.g., Imbrie et al., 1984; Lisiecki & Raymo, 2005; Channell et al., 2009). Stacks require that the individual $\delta^{18}O$ records are first aligned to have comparable relative or absolute ages so that each point in the stack represents a snapshot of $\delta^{18}O$ values from multiple locations at the same time. Inaccuracy in relative age estimates between cores will typically decrease the signal-to-noise ratio of the stacked signal, but over-alignment of noise in the signals could artificially enhance variability that was not globally synchronous. The risk of over-alignment can be reduced by placing constraints on sedimentation rate variability (e.g., Lisiecki & Lisiecki, 2002; Lin et al., 2014).

To create a stack using software that performs pairwise alignments of cores, all $\delta^{18}O$ records to be included in the stack are aligned to a single target core, which is typically a $\delta^{18}O$ record that spans the entire length of the stack with high resolution, low noise, and no apparent hiatuses. Any problems in the signal of the target core could propagate to create errors in core alignments and the average $\delta^{18}O$ value of the stack. In the LR04 global stack, the authors checked for such errors by performing pairwise alignments to multiple target cores and comparing the stacks (Lisiecki and Raymo, 2005); however, this is a laborious process and requires subjective evaluation. Because $\delta^{18}O$ variability is not globally synchronous (Skinner & Shackleton, 2005; Labeyrie et al., 2005; Waelbroeck et al., 2011;

Stern & Lisiecki, 2014; Lund et al., 2015), Lisiecki and Stern (2016) created regional stacks and used a different alignment target for Atlantic versus Pacific cores.

The sensitivity of stacks to the choice of a single alignment target can be mitigated by aligning to a target that incorporates information from all cores in the stack. HMM-Stack (Ahn et al., 2017), which models the stack using a profile Hidden Markov model (HMM), begins with an initial alignment to a user specified target and then aligns all cores to an iteratively updated stack, which is optimized to fit all cores in the stack. Here we present a new stack construction algorithm which offers several improvements to HMM-Stack, including the opportunity to simultaneously incorporate age constraints from all cores during the stacking process.

3. Background

3.1 Bayesian Framework

BIGMACS probabilistically constructs realistic age models and stacks by combining information from age proxies and stratigraphic alignment with the prior model of sedimentation rate variability from Lin et al., (2014). In Bayesian statistics, the age information from proxy data are termed likelihoods. Specifically, likelihoods return the probability of observing the age proxies given the proposed age model and the set of model parameters. Here we refer to likelihoods as the emission model. Simply stated, the emission model returns the probabilities of residuals (or misfit) between observed data and estimated values from a particular age model. The emission model for each proxy (radiocarbon, $\delta^{18}O$,

and additional age information) is discussed in section 3.3 and detailed formulations are given in the supplement (S2 and S4.1).

The prior model represents our *a priori* understanding of sedimentation rate variability and is termed the transition model. The transition model calculates the probability of a simulated sequence of sedimentation rates, independent of the proxy data, as described in section 3.2 and the supplement (S1 and S4.1). The transition model probabilities for a particular depth in the core are calculated as a function of both sedimentation rate change and normalized sedimentation rate (i.e., sedimentation rate expressed as a ratio the core's estimated mean sedimentation rate), given model parameters which are derived from the same sedimentation rate data as Lin et al., (2014).

The posterior distribution is calculated using Bayes' rule and is proportional to the product of transition and emission models. The posterior distribution of a multiproxy age model includes likelihoods returned by the radiocarbon emission model, the benthic $\delta^{18}O$ emission model, and the additional age emission model. Because there is no closed form for this posterior distribution (i.e., it is not known), we employ a sampling approximation. To improve computational efficiency, we sample the posterior using a combination of the particle smoothing (Doucet et al. 2001; Klaas et al. 2006) and Metropolis Hastings algorithms (Metropolis et al. (1953); Hastings (1970); Martino et al. (2015); section 3.4).

In Bayesian statistics, the parameter of interest (in this case the age of sediment at a given depth) is represented by the posterior distribution, rather than a single value. Therefore, a Bayesian 95% credible interval spans 95% of the central portion of the posterior distribution. This is compared to a frequentist 95% confidence interval, which posits that there is a 95% chance that the limits are correct and encapsulate the true value.

Here the 95% credible intervals and the median age model are defined by the distribution of Monte Carlo samples drawn from the posterior distribution.

The stacking algorithm is completed in two steps: an age model construction step in which a set of $\delta^{18}O$ records are aligned in parallel to a target stack (as described above), and a stack construction step in which a nonparametric regression is performed across the $\delta^{18}O$ data on the set of aligned cores. These two steps are performed iteratively until convergence. The alignment target during age model construction is the stack from the previous iteration; for the first iteration, an initial target stack is provided by the user. The stack construction process is described in more detail in section 3.5 and S5.

3.2 Transition Model

For a given age, the transition model calculates the probability of the normalized sedimentation rate and the change in sedimentation rate from the previous depth (for a mathematical description, see S1 and S4.1). In its default mode, BIGMACS uses the transmission model developed for the HMM-Match software by Lin et al. (2014); this study calculated the probabilities of normalized sedimentation rates with an empirically derived prior distribution fit to the observed sedimentation rates in 37 radiocarbon dated cores. Here we summarize the methods of Lin et al., (2014) to construct the prior; however, for more information see the original publication.

Radiocarbon ages were calibrated with the Marine09 calibration curve (Reimer et al., 2009) and sedimentation rates were assumed to be constant between radiocarbon ages. To identify outliers and age reversals in a statistically robust manner, a Bchron age model (Haslett & Parnell, 2008) was constructed for each core. Sedimentation rates were calculated by interpolating between the modes of the Bchron ages at the depths of the radiocarbon

measurements. The resulting sedimentation rates were only included in the final compilation if the following criteria was met: (1) the core was south of 40 degrees N if in the Atlantic (due to high latitude North Atlantic reservoir ages, Lisiecki & Stern 2013), (2) the core had an average sedimentation rate of at least 8 cm/kyr, and (3) adjacent pairs of radiocarbon dates were between 0.5 kyr and 4 kyr apart. After the criteria was met, the compilation totalled 544 kyr of sediment from 37 ocean sediment cores (Figure 1, Table S1). The original study interpolated sedimentation rates every 1 kyr; however, we interpolate by 1 cm depth increments and fit a new log-normal mixture distribution (Figure 2). Interpolating sedimentation rates by depth correctly represents the frequency at which higher sedimentation rates are observed in the sediment archive, whereas interpolating by time over represents frequency of lower sedimentation rates (which deposit less sediment per unit time).

Changes in sedimentation rates depend on both the current and previous sedimentation rate, and thus the previous two depths. However, because storing all sampled combinations of three consecutive depths is intractable for computation ($O(N^3)$, where N is the number of age model samples), normalized sedimentation rates are classified into three states: expansion, contraction, and steady. Expansion specifies a below average sedimentation rate which effectively stretches the local portion of the record. Contraction specifies a higher sedimentation rate than the average, which requires "squeezing" the record during alignment to the target. If the local sedimentation rate is within 8% of the core's average, the state is classified as steady. In BIGMACS the probabilities of transitioning from one state to the other states are optimized via the Baum-Welch Expectation Maximization algorithm (Rabiner, 1989; Dubrin et al., 1998). However users

can also choose to keep these probabilities fixed using the sedimentation rate data from Lin et al., (2014).

BIGMACS allows a sedimentation rate change at every depth where there is proxy data ($\delta^{18}O$, ^{14}C, or additional age information). However, in the case of low-resolution records, BIGMACS imposes a minimum age model resolution, which forces a sedimentation rate calculation every 15 cm. This depth interval was selected based on the depth spacing between the radiocarbon data used for the prior (Lin et al., 2014). Furthermore, BIGMACS normalizes sedimentation rates relative to a time-dependent average sedimentation rate calculated using the Nadaraya-Watson Kernel (Langrene and Warin, 2019). This accounts for longer scale changes in the depositional environment, which can be associated with transitions between glacial and interglacial oceanographic conditions.

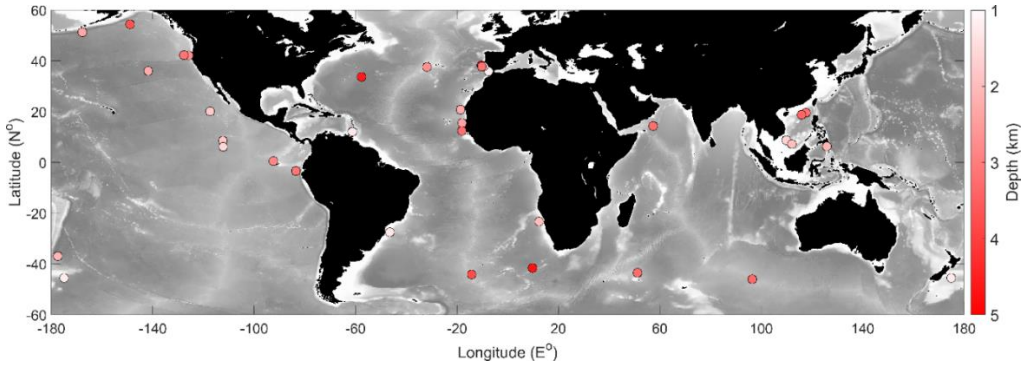

Figure 1: Locations of cores from Lin et al., (2014) used to construct the mixed log-normal distribution.

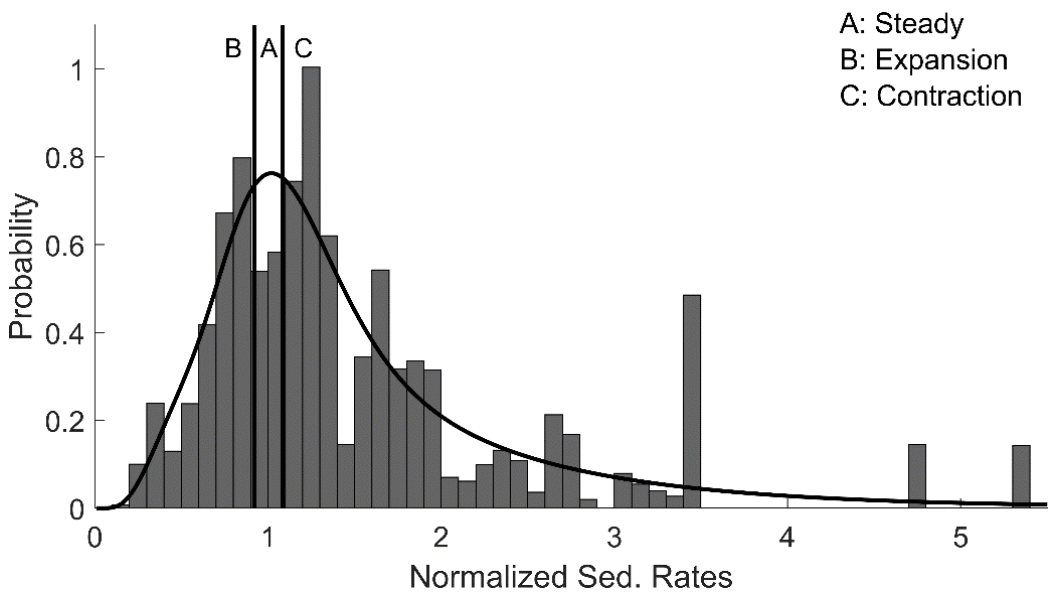

Figure 2: The log-normal mixture fit to observed sedimentation rates from 37 cores compiled in Lin et al., (2014). Sedimentation rates are interpolated to 1 cm increments.

3.3 Emission Model

BIGMACS uses different emission models for radiocarbon, $\delta^{18}O$ and additional age information (see S2 and S4.1 for more information). For radiocarbon and $\delta^{18}O$ data, the emission model is specified via generalized student's t-distributions (Christen & Peréz, 2009).

For radiocarbon data, the emission model returns the likelihood of observing age offsets from measured radiocarbon ages and depends on the radiocarbon measurement, calibration curve, and the reservoir age. The emission model also depends on two fixed parameters that control the scaling of the standard deviation. While Christen & Peréz (2009) and Blaauw & Christen (2011) set the fixed parameters of α and β to three and four, we choose values of ten and eleven which produces a distribution that is more peaked and more similar to a Gaussian distribution. In other words, our student's t-distribution has smaller tails than the distribution from Christen & Perez, (2009) causing age model samples to pass

closer to the mean radiocarbon age. This effectively improves agreement between the age model and the radiocarbon observations.

The $\delta^{18}O$ emission model returns the likelihood of observing different magnitudes of $\delta^{18}O$ offsets from the alignment target and depends on the target stack's time-dependent mean and variance. During alignment, Gaussian stacks are translated into a generalized student's-t distribution with the fixed parameters of α and β set to three and four, respectively, based on observed $\delta^{18}O$ residuals for the ITWA and DNEA stacks (Figure S1), to address potential $\delta^{18}O$ outliers. The $\delta^{18}O$ emission model also includes core-specific scale and shift parameters which are learned across alignment iterations with the Baum-Welch Expectation Maximization algorithm (Rabiner, 1989; Durbin et al., 1998). These parameters account for vital effects among different benthic foraminifera species (e.g., Marchitto et al., 2014) and different local water mass properties at different locations (e.g., temperature and $\delta^{18}O$ of seawater). The final mean and amplitude of the stack will reflect a resolution-weighted average of the stack's component cores; thus, the average shift and scale parameters of the stacked cores will be close to zero and one (when weighted by the resolution of $\delta^{18}O$ data in each core). Optionally, the user can choose not to shift or scale individual cores during stack construction; with this setting, the variance in the stack would reflect the total $\delta^{18}O$ variance across cores.

The emission model for the additional age information (e.g., stratigraphic tie points or dated tephra layers) can either be specified as a uniform or Gaussian distribution with a mean and uncertainty specified by the user. Specifying the model as a uniform distribution will assign an equal probability for the age model to pass anywhere through the given uncertainty range. A Gaussian distribution will assign higher probabilities to age model

samples that pass close to the mean of the additional age but allows for potentially larger residuals due to the tails of the distribution assigning non-zero probabilities.

3.4 Record Alignment

This section describes the sampling strategy employed during age model construction. Formulations for the sampling algorithm are provided in the supplement (S4.2).

Because the posterior is not given as a distribution in a closed form, age model samples are drawn using a Markov-Chain Monte Carlo (MCMC) algorithm (Peters, 2008; Martino et al., 2015). To increase computational efficiency, BIGMACS first initializes each sample using particle smoothing (Doucet et al. 2001; Klaas et al. 2006) and then refines the initialized samples with the MCMC algorithm. Particle smoothing can be understood as a continuous version of a Hidden Markov model (HMM, Durbin et al. (1998)). Whereas the HMM considers all possible hidden states because they are finite, the particle smoothing considers only a finite number of proposals because there are infinitely many possible states. In BIGMACS, the hidden states, or "particles", represent possible ages for each depth in the core. Particle smoothing consists of a forward algorithm and a backward algorithm. The forward algorithm iteratively samples and reweights particles, while the backward algorithm samples from the particles one-by-one in reverse based on their assigned weights. BIGMACS first runs particle smoothing with the state-space model defined by the transition and emission models.

BIGMACS then runs the Metropolis-Hastings algorithm (Metropolis et al. (1953); Hastings (1970); Martino et al. (2015)) to sample the proposed ages with starting points provided by the particle smoothing algorithm. The Metropolis-Hastings algorithm updates

the samples block-wise, meaning that hidden states in the same sedimentation state category (expansion, contraction, and steady) are simultaneously treated in each iteration. Initialized age samples from particle smoothing allows the use of shorter chains to reach the burn-in phase.

Once the set of sampled ages are obtained, BIGMACS updates parameters of the transition and emission models via the Expectation Maximization (EM) algorithm (Dempster et al., 1977) and then iterates the process with the updated transition and emission models until convergence. If a stack is to be constructed, the final age samples are inputs to the stack construction algorithm.

3.5 Stack Construction Algorithm

Here we describe the Gaussian Process regression used to construct a stack construction. A formal mathematical description is presented in the supplement (section S5). During stack construction BIGMACS first aligns records to an initial $\delta^{18}O$ stack by drawing age model samples from the posterior, and then updates the stack based on the new alignments. The updated stack serves as the target for the next alignment iteration and the whole process is repeated until convergence.

A benthic $\delta^{18}O$ stack serves as a target for aligning multiple records simultaneously. Because age models are continuous, we design the stack construction algorithm to also be continuous, such that a mean and standard deviation can be defined explicitly for any age. Previous stack construction methods (Lisiecki & Stern 2016; Ahn et al., 2017) involved binning $\delta^{18}O$ data and were thus limited by the amount of data in each bin. In contrast, the continuous approach of BIGMACS allows the creation of a stack using a smaller number of records and/or with uneven data resolution over time.

BIGMACS constructs a stack using Gaussian process regression (Rasmussen and Williams, 2006), which is a continuous and nonparametric kernel-based method. In contrast to the well-known polynomial regression, a distinctive feature of Gaussian process regression is that its variance function is permitted to change along the inputs (i.e. the x-axis). BIGMACS uses the Ornstein-Uhlenbeck (OU, Rasmussen and Williams, 2006) kernel, which we find allows enough variance to resolve millennial scale events (e.g., see sections 4.3 and 6.1.2). BIGMACS trains the OU kernel's hyperparameters, which adjust its amplitude and width, across iterations based on the data used to make the stack.

To allow the stack to reflect changes in the variance of $\delta^{18}O$ as a function of time, BIGMACS follows a heteroscedastic Gaussian process regression (Lee & Lawrence 2019) instead of a homoscedastic one. A homoscedastic Gaussian process assumes that the residuals of the data from the regression is constant but nevertheless adjusts its variance function to the proximity of data points. Thus, its variance function is narrow when data points are dense and wide where the data are less dense. A heteroscedastic Gaussian process model (used by BIGMACS) has a variance function that changes in response to the spread of the data points along inputs which allows the variance of the regression to be sensitive to the spread of responses in addition to changes in variance associated with data density from the homoscedastic Gaussian process model.

Gaussian process regressions have two major drawbacks: time complexity and outlier sensitivity. A matrix inversion, which has a time complexity equal to size of the data set cubed, is required to estimate hyperparameters for the kernel and to compute the posterior predictions. Thus, the model becomes intractable as the size of dataset increases. To address this, BIGMACS adopts the variational free energy approximation (Titsias, 2009)

to make the time complexity linear to the size of dataset. Outliers are identified by the Gaussian modelling of residuals. During stack construction BIGMACS disregards outliers before performing the regression. The following two steps are iterated: 1) kernel hyperparameters are estimated after disregarding outliers, 2) outliers are classified based on the stack constructed from the estimated kernel hyperparameters.

After BIGMACS obtains a Gaussian process regression using the $\delta^{18}O$ data from every core on each sample age model, the software averages the set of regressions using moment-matching (Murphy, 2012) to produce a single Gaussian model stack in a closed form. Detailed formulations for the stack construction algorithm can be found in the supplementary note (section S5).

4 Results

To demonstrate the performance of BIGMACS with differing amounts and quality of data, we present two example stacks: a Deep Northeast Atlantic (DNEA) stack and an Intermediate Tropical West Atlantic (ITWA) stack. The DNEA stack is constructed using high-resolution data with relatively little noise; it consists of 2,112 $\delta^{18}O$ data points and 150 radiocarbon ages from six cores that range in depth between 2273 and 3166 m (two from the western Iberian Margin and three off the west coast of Africa). The ITWA stack is constructed from 1,066 $\delta^{18}O$ data points and 51 radiocarbon ages across four cores from the Caribbean to the northern coast of Brazil that range in depth from 1100 and 1299 m; these cores contain a relatively large number of $\delta^{18}O$ outliers. Core locations for both stacks are plotted in Figure 3. The DNEA stack spans a full glacial cycle while the ITWA stack extends to ~55 ka. We used the Deep North Atlantic (DNA) and Intermediate North Atlantic (INA) stacks from Lisiecki & Stern (2016) as initial targets for the DNEA and ITWA stacks,

respectively. Default settings were used to construct both stacks. Additionally, we construct radiocarbon-only and $\delta^{18}O$-only age models for each input core to compare with the stack's multiproxy age models.

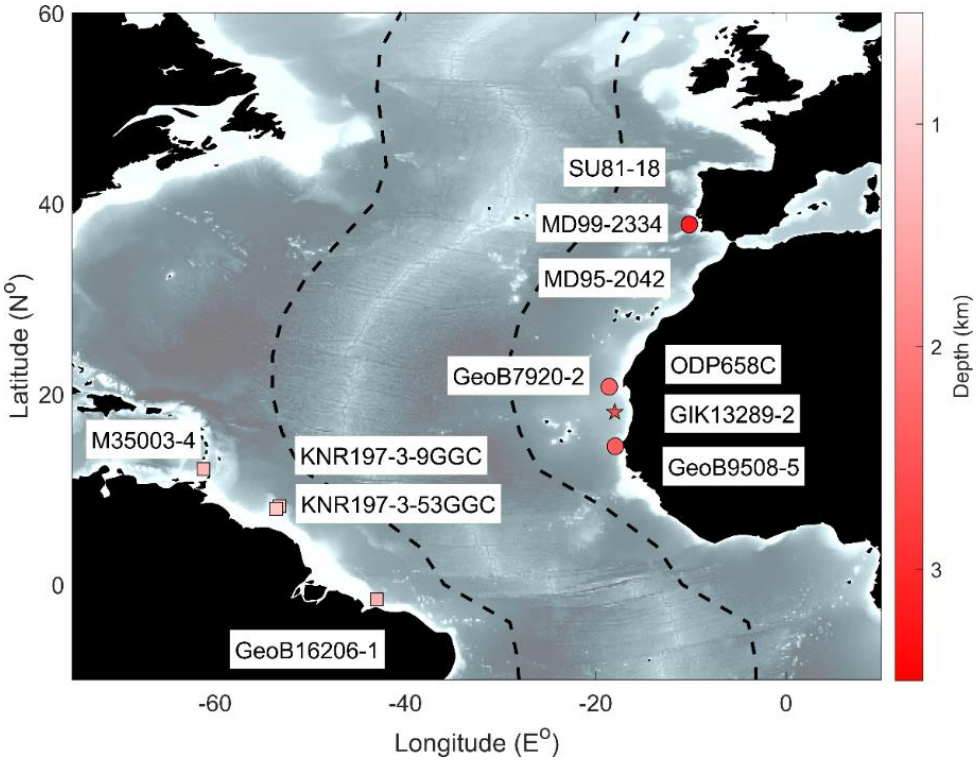

Figure 3: Cores used to construct the DNEA stack (circles) and the ITWA stack (squares). A star indicates the core for which we use the DNEA stack as the alignment target. Dotted lines indicate east and west transects plotted in Figure 4.

Core	Lat °N	Lon °E	Depth m	^{14}C Citation	δ^{18}O Citation
DNEA					
MD95-2042	37.80	349.83	3146	Shackleton et al., 2004; Bard et al., 2017	Shackleton et al., 2000
MD99-2334	37.80	339.83	3166	Skinner et al., 2003; Skinner & Shackleton., 2004; Skinner et al., 2014; Skinner et al., 2021	Skinner & Shackleton, 2005
SU81-18	37.77	349.82	3135	Vogelsang et al., 2001;	Waelbroeck et al., 2001
GeoB7920-2	20.75	341.42	2278	Collins et al., 2011	Tjallingii et al., 2008
ODP658C	20.75	341.42	2273	deMenocal et al., 2000	Knaack & Sarnthein, 2005
GeoB9508-5	14.5	342.05	2384	Mulitza et al., 2008	Mulitza et al., 2008
ITWA					
M35003-4	12.09	298.76	1299	Hülls & Zahn, 2010	Hülls & Zahn, 2000
KNR197-3-53GGC	8.23	306.77	1272	Oppo et al., 2018	Oppo et al., 2018
KNR197-3-9GGC	7.93	306.42	1100	Oppo et al., 2018	Oppo et al., 2018
GeoB16206-1	-1.58	316.98	1367	Porthilo-Ramos et al., 2017	Voigt et al., 2017
Example					
GIK13289-2	18.07	341.99	2485	Sarnthein et al., 1994	Sarnthein et al., 1994

Table 1: Core locations and data citations.

4.1 Core Selection and Assessing Homogeneity

When choosing alignment targets or a population of cores to construct a stack, we suggest that researchers evaluate core locations with respect to water mass reconstructions and directly compare the features of the δ^{18}O time series to evaluate whether the algorithm's

assumption of homogeneous $\delta^{18}O$ variability is reasonable. Before constructing a regional stack, the user should select cores evaluated to have homogeneous $\delta^{18}O$ signals or similar water mass histories. Figure 4 shows model estimates of the fraction of Southern Component Water (SCW) in two Atlantic transects, during the present day (coloured contours, Gebbie & Huybers, 2010) and at the LGM (solid black line, Oppo et al., 2018). Here SCW refers to water that formed in the Antarctic and sub-Antarctic regions defined by Gebbie & Huybers (2010).

Core sites in the DNEA stack are just below the core of modern Northern Component Water (NCW, Figure 4) and are bathed today by 23-26% SCW and 74-77% NCW (Table S1). Glacial water mass reconstructions suggest that water mass composition at these sites was very similar during the LGM (Gebbie & Huybers, 2010; Oppo et al., 2018). A relatively constant water mass composition during the deglaciation at these sites is also suggested by neodymium isotope compilations (Howe et al., 2016; Pöppelmeier et al., 2020). Collectively, these studies support our assumption that the benthic $\delta^{18}O$ signals of these cores changed homogeneously (i.e., nearly synchronously) during Termination 1.

The cores compiled for the ITWA stack are located near the boundary between AAIW and NADW, yielding more variability in their modelled water mass percentages. SCW percentages for cores in the ITWA stack range from 31-48% for the modern and 20-28% for the LGM. During the deglaciation, AAIW experienced expansion in this region as demonstrated by a decrease in nutrients in the phosphate maximum zone (Oppo et al., 2018). Thus, the cores in the ITWA stack may have experienced moderately heterogeneous water mass changes during Termination 1. Despite moderate differences between these sites,

BIGMACS is able to align these records and generate a stack that is representative of their $\delta^{18}O$ variability.

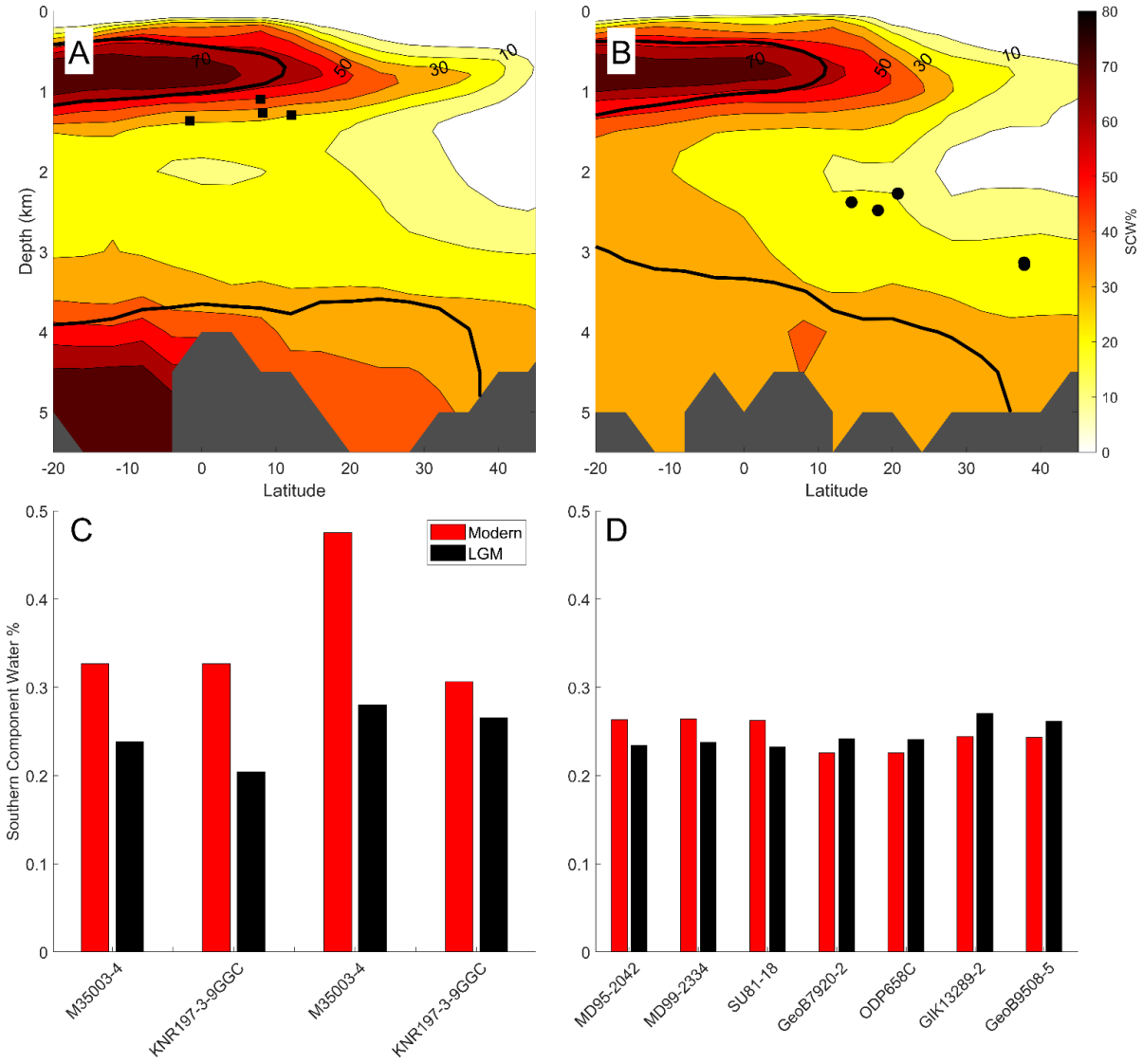

Figure 4: (A) Western and (B) Eastern Atlantic transects of water mass composition. Transect paths are shown as dotted lines in Figure 3. Colored contours show modern Southern Component Water percentages (Gebbie & Huybers 2010) along each transect and solid black line shows the 50% contour during the LGM (Oppo et al., 2018). Solid circles represent cores in the DNEA stack, squares are cores in the ITWA stack. Histograms of modern (red) and LGM (black) southern component water percentages for cores in the (C) ITWA and (D) DNEA stacks.

4.2 Age Proxies

To calibrate radiocarbon ages to calendar years, we use the Marine20 calibration curve (Heaton et al., 2020), a constant reservoir age offset (ΔR) equal to zero, and a reservoir age standard deviation of 200 years (although it should be noted that future users can find potential reservoir age offsets using the Calib database; Reimer & Reimer, 2001). We make no corrections for the different planktonic species used to measure radiocarbon in each core (see Table 1 for data citations).

For the longest core in each stack, we provide additional age information (crosses in Figures 5A and 6A) beyond the last radiocarbon date. MD95-2042 in the DNEA stack is constrained with ages from Lisiecki & Stern (2016) identified based on an alignment of the alkenone-based SST record (Pailler & Bard, 2002) to a synthetic Greenland $\delta^{18}O$ record on a speleothem age model (Barker et al., 2011; Barker & Diz., 2014). M35003-4 in the ITWA stack is constrained by an age estimate of 55.4 ka BP at 9.5 m depth based on the alignment by Hülls & Zahn, (2000) of variations in N. *dutertrei* and $CaCO_3$ to Dansgaard/Oeschger events in the GISP2 $\delta^{18}O$ record (Grootes & Stuiver, 1997). This additional age information is modelled using Gaussian distributions with the standard deviations reported in Lisiecki & Stern (2016) for MD95-2042 and a standard deviation of 1 kyr for M35003-4.

4.3 Stack Results

Figure 7 compares the DNEA and ITWA stacks. The ITWA stack is, on average, 0.56 ‰ lighter than the DNEA stack due to the differences in deep water properties at the core sites. The ITWA core sites which span 1100-1299 m are bathed by warmer and less saline waters than the DNEA cores from 2273-3166 m. The time-dependent standard deviation in each stack (defined by the distribution of Gaussian Process regressions) reflects

the variance in the aligned $\delta^{18}O$ records. Between 0 and 60 ka BP, the average standard deviation is 0.13 ‰ in the DNEA stack and 0.2 ‰ in the ITWA stack. In particular, the ITWA stack has larger standard deviation during the termination, which reflects anomalously high $\delta^{18}O$ values during the deglaciation in some of the ITWA cores. For example, many of the records in the ITWA stack include several anomalously high $\delta^{18}O$ values during the deglaciation; Oppo et al., (2018) attributes these outliers to slope instabilities at the Demerara Rise. Because BIGMACS models a Gaussian distribution for $\delta^{18}O$ residuals, the outliers produce large, symmetric confidence intervals about the mean.

The standard deviations of the two BIGMACS stacks are both smaller than the DNA and INA regional stacks from Lisiecki & Stern (2016), which average 0.24 ‰ and 0.36 ‰, respectively. This likely stems from greater benthic $\delta^{18}O$ spatial variability within the larger regions defined in Lisiecki & Stern (2016) and the application of (small) record-specific shift and scale adjustments to the DNEA and ITWA cores during stacking with BIGMACS.

The Gaussian process regression also creates smoother stacks than previous binning methods. Figure S3 compares the new DNEA and ITWA stacks with the Deep North Atlantic (DNA) and Intermediate North Atlantic (INA) regional stacks from Lisiecki & Stern (2016). The Gaussian process regression creates estimates of $\delta^{18}O$ for each point in time by incorporating information from neighbouring data points, which increases the stack's autocorrelation compared to the binning procedure used in Lisiecki & Stern (2016). Given the large volume of the deep ocean, we expect changes in benthic $\delta^{18}O$ to respond gradually; hence smoothing may actually increase the signal-to-noise ratio of "local" stacks with less densely sampled $\delta^{18}O$ measurements and relatively few cores. Although there is a risk that the Gaussian process regression may over-smooth the data, our DNEA stack still

resolves millennial scale events. For example, Figure 5(a) shows peaks at 24, 29 and 38 kyr corresponding to approximate ages of Heinrich Events H2 to H4 (Hemming, 2004), similar to the DNA stack (Figure S3).

To evaluate the multiproxy age models of the ITWA and DNEA stacks, we compare them with radiocarbon-only and $\delta^{18}O$-only age models for each core (with inclusion of the same additional ages in cores MD95-2042 and M35003-4). We find good agreement between median radiocarbon-only and multiproxy age models for each core (panels B and C in Figures 5 and 6), indicating that the $\delta^{18}O$ alignments did not cause the multiproxy age models to stray significantly from the radiocarbon age constraints. Furthermore, the multiproxy age models have 95% credible interval widths that are on average 262 years smaller than the radiocarbon age models and 1.92 kyr smaller than $\delta^{18}O$-only age models (Figure S2).

The good agreement between the radiocarbon and multiproxy median age models also supports our assertion that the input cores for each stack share homogeneous $\delta^{18}O$ signals. If the $\delta^{18}O$ records changed asynchronously, the alignments (which rely on the assumption of synchronous $\delta^{18}O$ change) would likely cause differences between the median age estimates of the radiocarbon-only and multiproxy age models. This assertion of synchronous $\delta^{18}O$ change is also supported by the relatively small shift and scale parameters learned for each core during the stacking procedure, indicating similar $\delta^{18}O$ values across all core sites (Table S1).

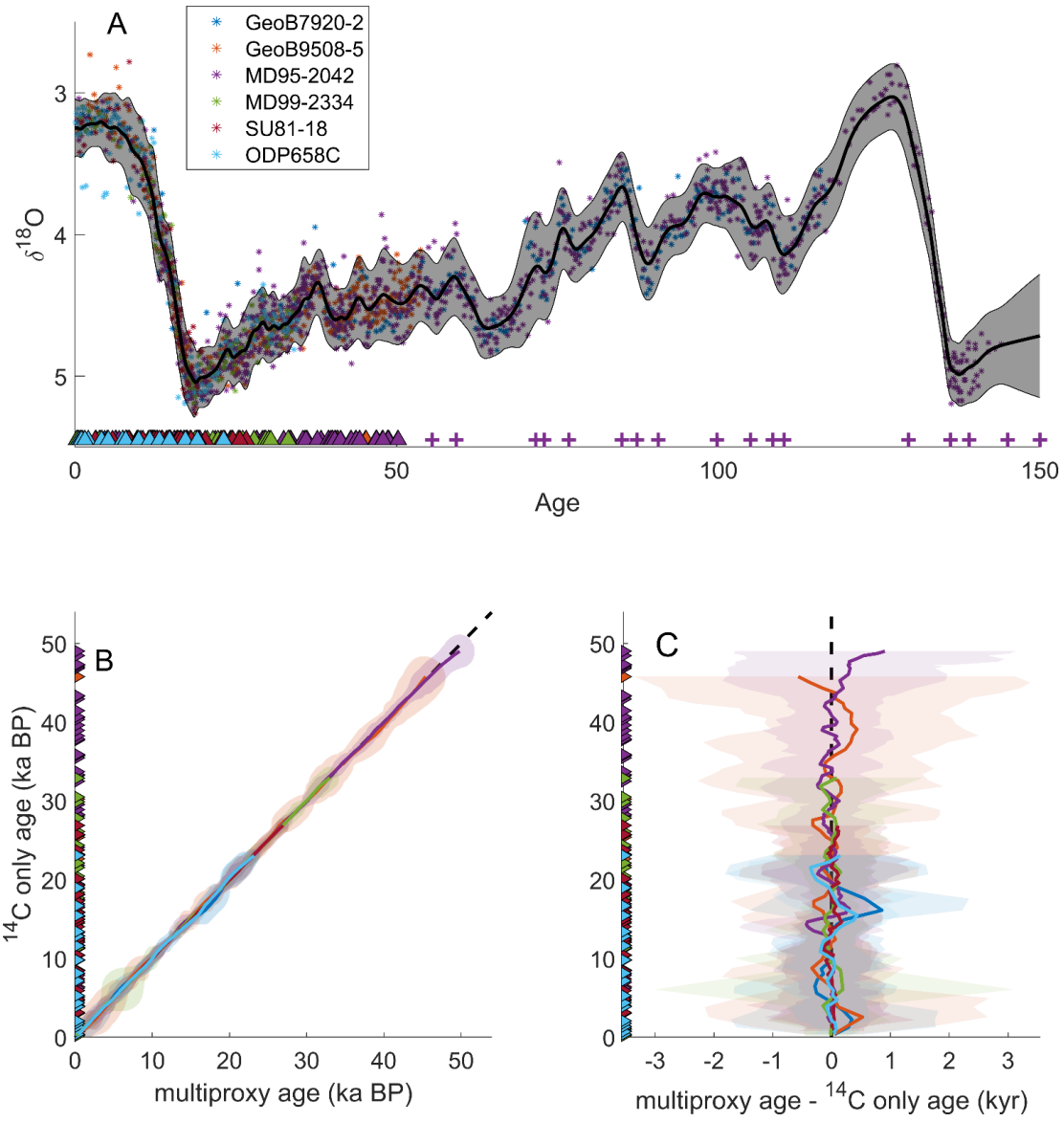

Figure 5: The Deep Northeast Atlantic (DNEA) stack. (A) The solid black line and shaded region represents the median stack value and 2-sigma upper and lower bounds. Filled circles are the shifted and scaled $\delta^{18}O$ data points from each core on the multiproxy age models. Filled triangles mark the radiocarbon ages from the respective cores. Purple crosses are the tie points for MD95-2042 taken from Lisiecki & Stern (2016). (B) ^{14}C-only age models vs. the multiproxy age models for each core in the DNEA stack. Each core plots along the black dashed 1:1 line. (C) The difference between the multiproxy age models and the ^{14}C age models for each core in the DNEA stack. Coloured shading shows the joint uncertainty distribution for ^{14}C and multiproxy age estimates for each core.

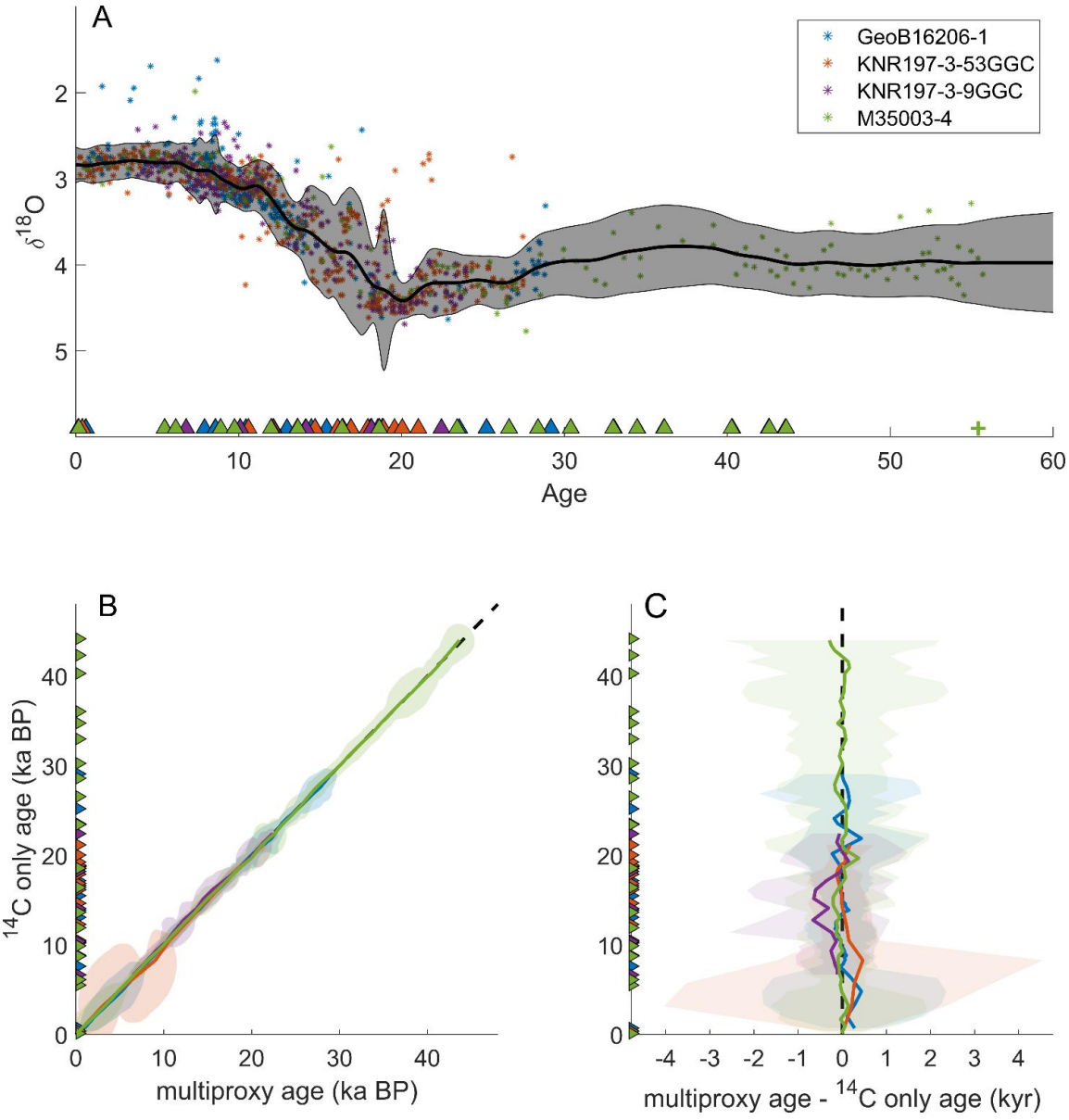

Figure 6: The Intermediate Tropical West Atlantic (ITWA) stack. (A) The solid black line and shaded region represents the median stack value and 2-sigma upper and lower bounds. Filled circles are the shifted and scaled $\delta^{18}O$ data points from each core on the multiproxy age models. Filled triangles mark radiocarbon ages from the respective cores. The green cross is the tie point for M35003-4 from Hulz et al., (2000). (B) ^{14}C-only age models vs. the multiproxy age models for each core in the ITWA stack. Each core plots along the black dashed 1:1 line. (C) The difference between the multiproxy age models and the ^{14}C age models for each core. Coloured shading shows the joint uncertainty distribution for ^{14}C and multiproxy age estimates for each core.

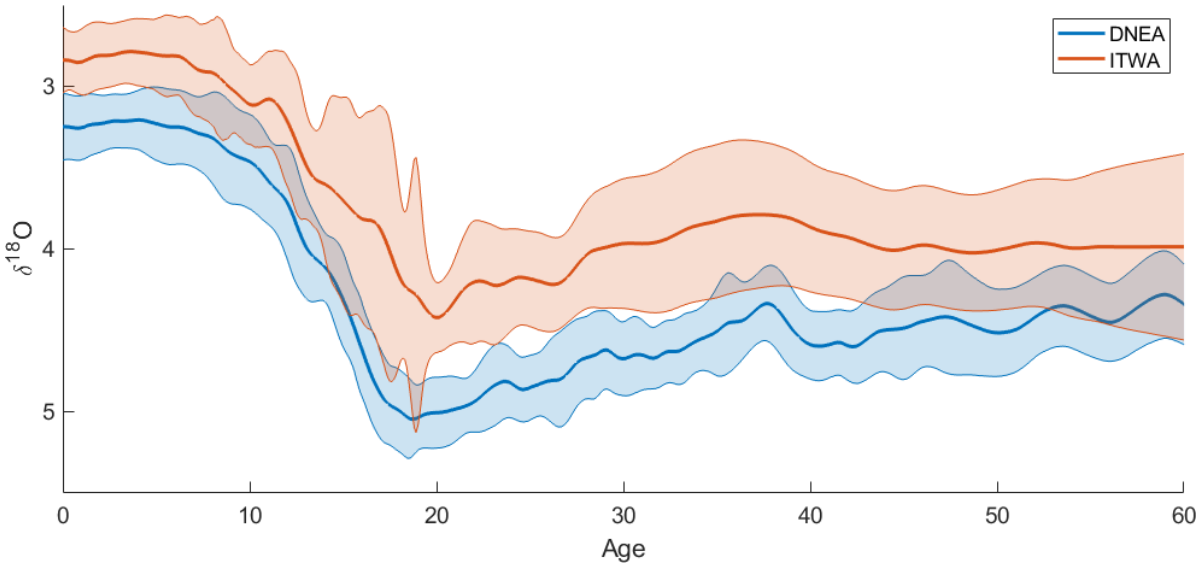

Figure 7: Comparison of the DNEA and ITWA stacks. Median values are displayed as the thick solid line, and shading marks plus and minus two standard deviations.

5 GIK13289-2 Age Model Comparison

To further evaluate the differences between single proxy and multiproxy age models, we compare three age models for GIK13289-2 constructed by BIGMACS: a radiocarbon-only age model, a $\delta^{18}O$-only age model, and a multiproxy age model constrained by both $\delta^{18}O$ and radiocarbon data (Figure 8). The alignment target for the multiproxy and $\delta^{18}O$-only age models is the DNEA stack. While the radiocarbon and multiproxy age models have direct age constraints via radiocarbon ages, the $\delta^{18}O$-only age model provides only relative age constraints. Furthermore, the uncertainty for the $\delta^{18}O$-only age model reflects only the *alignment* uncertainty. The absolute age uncertainty would be a combination of the alignment uncertainty and the absolute age uncertainty from the DNEA stack.

The multiproxy and radiocarbon-only age models show similar median ages. However, the radiocarbon age model has larger confidence intervals between core depths of 1.7 and 2.2 m where there is a ~10-kyr gap between radiocarbon measurements. The

multiproxy age model is constrained by five $\delta^{18}O$ data points between these depths which serve to decrease age uncertainty. At a depth of 2 m, the 95% credible interval width for the multiproxy age model (5.0 kyr) is 3.8 kyr smaller than the 95% credible interval width for the radiocarbon age model (8.8 kyr).

The $\delta^{18}O$-only age model for GIK13289-2 is based only on $\delta^{18}O$ alignment and has considerably larger uncertainty than the multiproxy age model, with a 95% credible interval width as much as 6.6 kyr larger. Furthermore, there is disagreement between the median age models during the Holocene, with a maximum age difference of 2.2 kyr. The apparent error in median age estimates from $\delta^{18}O$-only alignments likely results from near-constant $\delta^{18}O$ values during the Holocene, which allows for more possible alignments that fit the target and a less precise age model. The 95% credible interval for the $\delta^{18}O$ age model spans both the multiproxy and radiocarbon median ages, suggesting realistic uncertainty estimates for the alignment.

In Figure 9, the purple shading of the $\delta^{18}O$-based age model represents age model sample density. The non-Gaussian nature of the $\delta^{18}O$-based age estimates is evident at the end of the age model, where the median age and darker shading are located near the upper end of the 95% credible interval. The multiproxy age model samples at this depth (which are constrained by the final radiocarbon age) agree with the dense cluster of $\delta^{18}O$-only age model samples. Frameworks have been developed to use the distribution of age model samples, such as those provided by BIGMACS, to estimate the probability of timing differences between climate responses recorded in multiple cores (Parnell et al., 2008; Khider et al., 2017).

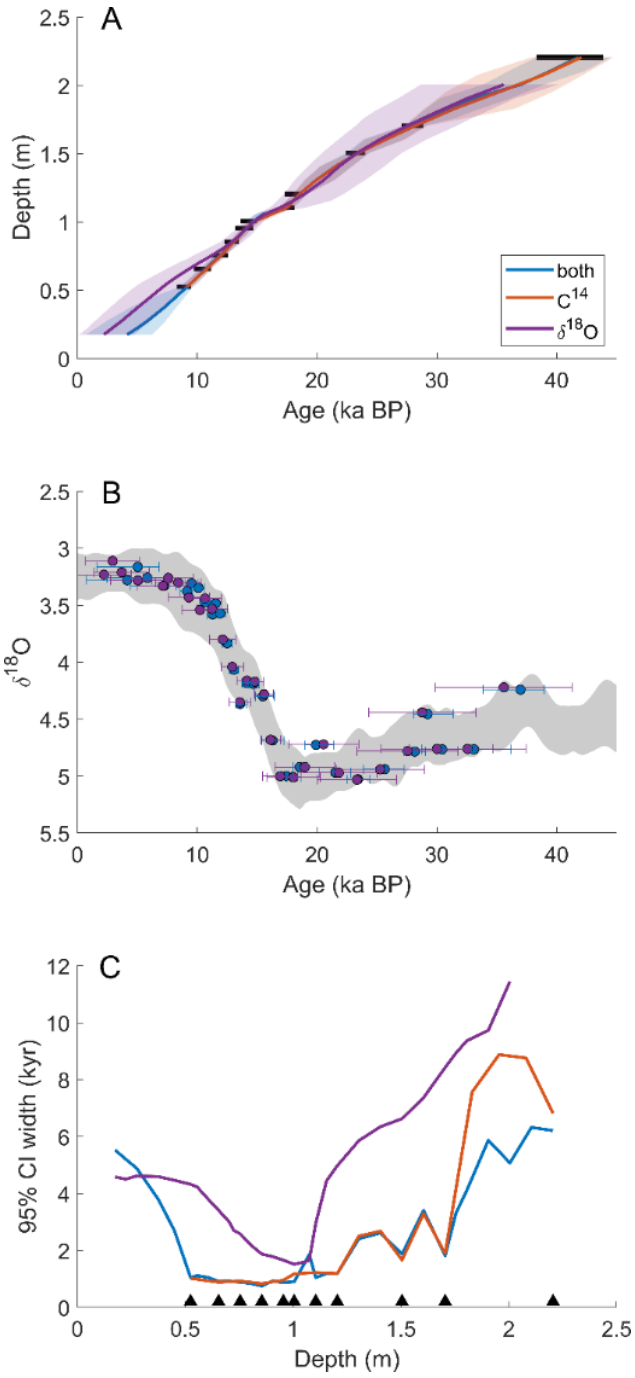

Figure 8: Comparison of a $\delta^{18}O$-only age model, radiocarbon-only age model, and multiproxy age model for GIK13289-2. (A) Age vs. depth plot, solid black lines represent calibrated radiocarbon ages. (B) The shifted and scaled $\delta^{18}O$ for the $\delta^{18}O$-only age model and multiproxy age model aligned to the DNEA stack. (C) 95% credible interval widths for each age model. Black triangles indicate the depths of the radiocarbon ages. Note that the radiocarbon-only age model does not extend beyond the top ^{14}C date of ~10 ka BP, and we do not display the ^{14}C age model in panel (B).

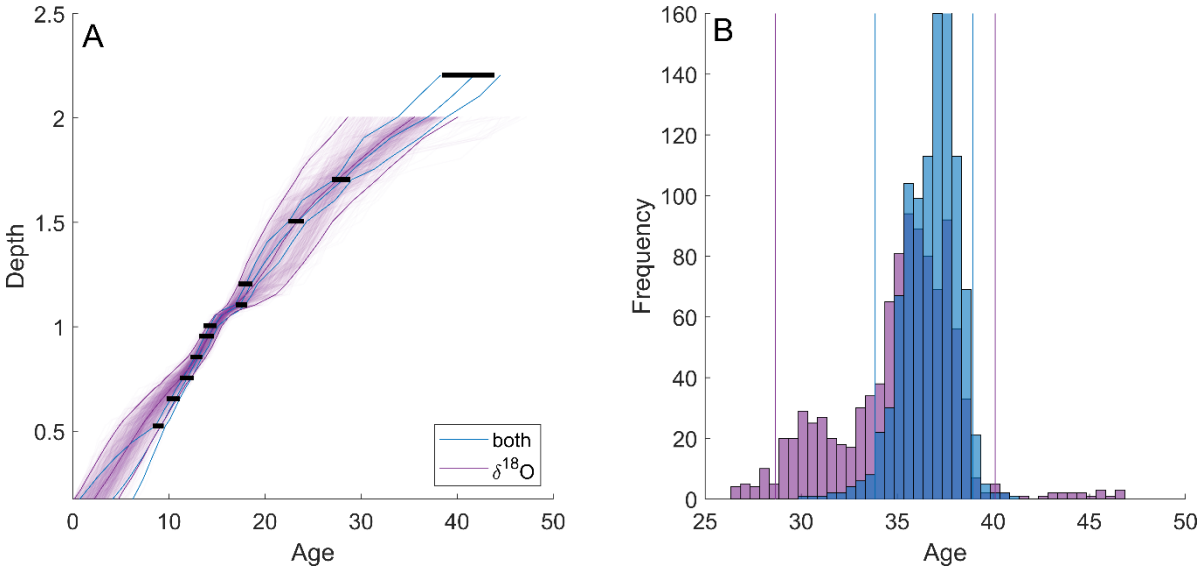

Figure 9: (A) Sample density of the $\delta^{18}O$-only age model for GIK13289-2. The median age model and 95% credible bands are plotted as solid purple lines. The multiproxy median age model and 95% confidence bands are also plotted (solid blue lines) along with the calibrated radiocarbon ages (horizontal black lines). (B) Histogram of $\delta^{18}O$-only age samples (purple) and multiproxy age model samples (blue) for the last depth in the $\delta^{18}O$-only age model (approximately 2 m). Vertical lines mark the 95% credible intervals at the same depth for both age models.

6 Discussion

6.1 Applications

In this section we discuss the advantages and limitations of the BIGMACS software compared to other available age modelling and stacking techniques and provide practical advice on the types of applications most suitable for BIGMACS.

6.1.1 Applicability of the Transition Model

Most software packages which generate probabilistic age models (e.g., Bacon, Oxcal, Undatable) use models of sedimentation rate variability with tuneable parameters, which affect the amount of age uncertainty between age proxies measured at discrete depths (e.g., radiocarbon, tephra layers, tie points, etc.). During benthic $\delta^{18}O$ alignment,

sedimentation rate constraints also limit the degree to which the input record is stretched or squeezed to match the target record. In most cases, users have no specific information on which values for sedimentation rate parameters are most appropriate for the specific core analysed. Thus, parameter tuning usually increases the subjectivity and labour involved to create an age model. Therefore, BIGMACS is designed to be used without parameter tuning. Because BIGMACS uses a prior that is constructed from a global compilation of marine sediment cores representing different environments (Lin et al., 2014; see Figure 1 and table S1), the age uncertainty returned by BIGMACS is physically realistic for most marine cores and less subjective than using tuned parameters in other software packages.

The current version of BIGMACS uses the same prior that was used in HMM-Match (Lin et al., 2014) based on a global compilation of cores. BIGMACS can also adjust its state change probabilities based on information learned from the particular cores being aligned (see S4.3). However, BIGMACS has the flexibility to use other priors that may focus on a particular oceanographic setting or based on larger compilations of sedimentation rate variability that may be created. For example, Mulitza et al., (2021) presents a compilation of 6153 radiocarbon ages from 598 ocean sediment cores. This is potentially enough data to construct regionally specific priors if trends in the behaviours of sedimentation rates are observed in different environments.

In addition to larger and/or more regionally focused compilations, future work includes plans to address several limitations of the method used for the Lin et al. (2014) compilation. Lin et al. (2014) used Bchron age models to identify outliers and reversals, and calculated sedimentation rates by interpolating between the mode of the Bchron age model for each calibrated ^{14}C date rather than the full probability distribution (see S1 for a more

thorough description). Additionally, Lin et al. (2014) used radiocarbon ages were calibrated with the Marine09 curve (Reimer et al., 2009) with $\Delta R=0$ for reservoir ages. Although we expect this to introduce relatively little bias to the sedimentation rate priors, future priors should use the updated Marine20 curve and estimates of marine reservoir ages (Heaton et al., 2020).

If users find that the default transition model does not allow enough sedimentation rate variability to fit the age proxies for a particular set of cores, it is also possible to use your own prior distribution (see the User's Manual). However, we have not encountered such problems in testing the software, and we encourage users to exercise caution when changing this distribution.

6.1.2 Multiproxy Age Models

Multiproxy age models generated by BIGMACS provide additional advantages compared to traditional probabilistic ^{14}C age models. In ^{14}C-only age models, each core's age model is constrained only by the ^{14}C dates from an individual core; however, multiproxy age models can use age constraints from multiple nearby cores, which are often available for locations of particular paleoceanographic interest (e.g., cores SU81-18, MD95-2042, and MD99-2334 on the Iberian Margin). For cores sharing a similar water mass history (which is likely for neighbouring cores from similar water depths), multiproxy age models use both benthic $\delta^{18}O$ alignment and ^{14}C dates to generate age models for each core that are constrained by all ^{14}C dates in the group of cores. This is particularly useful for cores with lower resolution ^{14}C dating or with ambiguous ^{14}C outliers. Our example of GIK13289-2 (Figure 8) demonstrates that multiproxy alignment is helpful for extending age estimates beyond the range of ^{14}C dates (e.g., the Holocene portion of GIK13289-2) and decreasing

age uncertainty between widely spaced ^{14}C dates, even in cases where benthic $\delta^{18}O$ data are also relatively low resolution. In most cases, these age model benefits are enhanced when BIGMACS is used to generate a multiproxy stack (e.g., Figures 5 and 6) instead of alignment to a fixed target.

Users should be aware that the age uncertainties returned by BIGMACS for age models generated by multiproxy alignment or stacking do not include the age uncertainty of the alignment target. Thus, age uncertainties (other than those from ^{14}C-only mode) should interpreted as relative age uncertainties that reflect alignment uncertainty, rather than absolute age uncertainty. For multiproxy stacks constrained by densely sampled ^{14}C dates with small calibration uncertainty, such as the DNEA stack from 0-25 ka (Figure 5), the absolute age uncertainty of the stack will be small. However, where the absolute age uncertainty of the alignment target or stack is larger, an assessment of a core's absolute age uncertainty should incorporate both the absolute age uncertainty of the target/stack and alignment uncertainty. For example, absolute age uncertainty for the DNEA stack beyond 45 ka can be estimated by constructing an age model for MD95-2042 using only the ^{14}C dates and additional age information (i.e., tie points marked as crosses in Figure 5A). Because GeoB7920-2 contains no direct age proxies beyond 45 ka, it's absolute age uncertainty could be estimated as the sum of variance in the alignment uncertainty (the age model uncertainty resulting from alignment to the DNEA stack) and the variance of the age model constructed for MD95-2042 using only radiocarbon data and the additional tie points.

6.1.3 Stacking

Creating a multiproxy stack in BIGMACS offers several advantages compared to traditional stacking techniques. First, BIGMACS can create multiproxy stacks with as few

as two cores. All cores in the multiproxy stack must have benthic $\delta^{18}O$ for alignment, but the stack can include cores that lack ^{14}C or other age constraints. Second, whereas most previous stacks have been constructed by pairwise alignments of each core to a single target (e.g., Lisiecki and Stern, 2016), BIGMACS aligns all cores simultaneously while updating the alignment target until convergence is achieved. This process reduces the time required to create a stack as well as sensitivity to the choice of the initial alignment target. Third, the multiproxy stack's age model and alignments evolve simultaneously based on the direct age proxies in all the aligned cores, whereas most previously constructed stacks aligned all cores before estimating the stack's age model (e.g., Huybers and Wunsch, 2004; Lisiecki & Raymo, 2005; Lisiecki & Stern, 2016). Although BIGMACS and HMM-Stack both iteratively update the alignment target using the aligned $\delta^{18}O$ signals, stacks produced by HMM-Stack implicitly inherit the age model of the original alignment target because HMM-Stack contains no procedure to input absolute age information or adjust the alignment target's age model.

Another innovation in BIGMACS is the use of the Gaussian process regression to create time-continuous estimates of the $\delta^{18}O$ stack's mean and variance. Most previous stacks relied on either interpolation of each core's $\delta^{18}O$ measurements to an even time spacing (e.g., Huybers & Wunsch, 2004) or binning and averaging all cores' $\delta^{18}O$ measurements within a certain time window (e.g., Lisiecki and Raymo, 2005). The Gaussian process regression requires fewer cores, samples at any resolution without interpolation, smooths the stack to increase its signal-to-noise ratio, and realistically increases stack variance across $\delta^{18}O$ gaps. Learned hyperparameters of the OU kernel determine the overall smoothness of each stack and, hence, the timescale of features that are well described by the

stack. For the stacks presented here, smoothing from the Gaussian process regression inhibits precise estimates of the amplitude and rate of change of events occurring on timescales of ~2 kyr or less. For example, the DNA stack of Lisiecki and Stern (2016), which averaged $\delta^{18}O$ values using 0.5 kyr bins, decreased by 0.47 ‰ in 1.5 kyr (from 87 to 85.5 ka) during Heinrich event 8; however, in the DNEA stack produced by BIGMACS, the $\delta^{18}O$ change is spread over an interval at least twice as long (89 to 85 ka BP, Figure S3). Additionally, although a $\delta^{18}O$ response during Greenland interstadial 19 is recorded in both the DNA and DNEA stack at 72 ka, smoothing by the Gaussian process regression and alignment uncertainty appears to have reduced its amplitude in the BIGMACS DNEA stack.

An important caveat that applies to all $\delta^{18}O$ alignments, including BIGMACS multiproxy alignments and stacks, is that the $\delta^{18}O$ records aligned should all be homogeneous, meaning that they share the same underlying $\delta^{18}O$ signal. Because previous studies have observed temporal offsets between benthic $\delta^{18}O$ signals from core sites bathed by different water masses (Skinner & Shackleton, 2005; Labeyrie et al., 2005; Waelbroeck et al., 2011; Stern & Lisiecki, 2014), users should only align or stack cores which share the same deep water mass history over the length of the records analysed. Whether $\delta^{18}O$ is homogeneous across core sites can, in part, be evaluated by comparing the amplitude of change and mean offset (after species-corrections) between cores. For example, BIGMACS estimates only small shift and scale differences between the cores included in the DNEA and ITWA stacks (Table S1), although large shifts are observed between the stacks. Another test is to compare the core sites' present-day deep water mass composition and reconstructions or models of deep water mass extents at the LGM. Although glacial water mass estimates are inherently uncertain due to differences between various models and reconstructions,

BIGMACS offers the flexibility to easily build different stacks to evaluate the sensitivity of results to different models of benthic $\delta^{18}O$ homogeneity.

BIGMACS may be able to align and stack proxies other than benthic $\delta^{18}O$; however, the software can currently only align and stack one proxy at a time. For BIGMACS to accurately construct a probabilistic stack of an alternate proxy, the proxy must be homogeneous across the records in the stack with residuals that can reasonably be described with the generalized student's t-distribution that BIGMACS uses for the $\delta^{18}O$ emission model. Because the emission model is based on the variance that best describes the observations, it does not require a specific assumption about the level of noise in the measurements. However, low ratios of signal-to-noise in the proxy aligned could yield unreliable results. Preliminary analysis of planktonic $\delta^{18}O$ alignments and stacks have yielded encouraging results, but the more heterogeneous nature of surface variability requires caution in the selection of cores which can reasonably be considered homogeneous.

The computational complexity of BIGMACS also places constraints on its applications. For the records in this study, multiproxy alignment of a single core to a target takes only 1-2 minutes while the multiproxy stacks take 1-2 hours to build on a typical desktop machine. In testing, we have successfully created $\delta^{18}O$-only and multiproxy stacks of Late Pleistocene $\delta^{18}O$ spanning the past 800 kyr, which take approximately 12 hours to run. However, we have not yet evaluated the performance of BIGMACS for records longer than 800 kyr. For a more detailed discussion of the time complexity for BIGMACS, see supplemental text S6.

7 Conclusion

The new software package, BIGMACS, constructs multiproxy sediment core age models and benthic $\delta^{18}O$ stacks constrained by radiocarbon ages, $\delta^{18}O$ alignment, and additional age constraints. BIGMACS requires no parameter tuning and uses an empirically derived prior model of sedimentation rate variability specific to the marine depositional environment. Radiocarbon ages are modelled using a student's t-distribution, following the methods of Christen and Peréz (2009). BIGMACS also constructs time-continuous stacks using Gaussian process regression and requires fewer cores than traditional binning methods. This facilitates building stacks for more localized regions using as few as two cores from within a homogeneous water mass as assessed by deep water mass reconstructions and/or evaluation of the estimated shift and scale parameters for the aligned cores. Example regional stacks are presented for the Deep Northeast Atlantic (DNEA) and Intermediate Tropical West Atlantic (ITWA). The stacks' median $\delta^{18}O$ values provide well-dated regional climate signals, while the stacks' standard deviations include the effects of spatial variability, multiproxy age uncertainty, measurement noise, and, in the ITWA stack, the effects of $\delta^{18}O$ outliers likely caused by sediment disturbances. Finally, a comparison of radiocarbon-only, $\delta^{18}O$-only, and multiproxy age models for one core demonstrates that the multiproxy age model yields smaller age uncertainties, particularly between radiocarbon measurements and during the Holocene $\delta^{18}O$ plateau.

Supplement

S1 Transition Model

At a given core depth n, the transition model returns the probability of an age sample A_n and the sedimentation rate state W_n, given the normalized sedimentation rate and the previous sedimentation rate state W_{n+1}:

$$\pi(A_n, W_n | A_{n+1}, W_{n+1}, \phi, d_n, d_{n+1}, r) = \pi_1(W_n | W_{n+1}, \phi)\pi_2(A_n | A_{n+1}, W_n; d_n, d_{n+1}, r).$$

Here $\pi_1(W_n | W_{n+1}, \phi)$ returns the probability of transitioning from W_{n+1} to W_n. The 3x3 matrix parameter ϕ contains the probabilities of transitioning from each state to all other states. The three sedimentation rate states are expansion, steady, and contraction and have respective normalized sedimentation rate ranges of $(0, 0.9220)$, $[0.9220, 1.0850)$, and $[1.0850, \infty)$. ϕ can either remain fixed or can be optimized during age model construction.

The second term $\pi_2(A_n | A_{n+1}, W_n; d_n, d_{n+1}, r)$ returns the probability of the required sedimentation rate and is calculated using the mixed log-normal distribution fit to the normalized sedimentation rates from Lin et al., (2014):

$$\pi_2(A_n | A_{n+1}, W_n; d_n, d_{n+1}, r) \propto \left(\sum_{k=1}^{2} \omega_k \cdot Lognormal\left(\frac{A_{n+1} - A_n}{r \cdot (d_{n+1} - d_n)} \middle| \mu_k, \sigma_k \right) \right) \cdot 1_{\left\{ \frac{A_{n+1} - A_n}{r \cdot (d_{n+1} - d_n)} \in \mathbb{I}_{W_n} \right\}}(A_n).$$

Here d_n is the current depth, d_{n+1} is the pervious depth, and A_{n+1} is the previous age. Sedimentation rates are normalized by the depth-dependent average sedimentation rate, or r, which is calculated using the Nadaraya-Watson Kernel (Langrene and Warin, 2019). The variables, ω_k, μ_k, and σ_k are fixed weights, means and standard deviations that describe the log-normal mixture. The last term on the right is equal to 1 when the sedimentation rate is in the range of W_n and 0 otherwise. This effectively truncates the log-normal mixture and only allows sedimentation rates within the range of the given state.

Core	Latitude	Longitude	Depth (m)	Resolution (yrs)
DSDP594	-45.52	-174.95	1204	570
GeoB1711	-23.32	12.38	1967	550
GeoB7920-2	20.75	-18.58	2278	400
GeoB9508-5	15.5	-17.95	2384	170
GeoB9526-5	12.43	-18.05	3233	370
GIK17940-2	20.12	-117.38	1727	270
GIK17961-2	8.51	-112.33	1795	1020
GIK17964-2	6.16	-112.21	1556	760
H214	-36.92	-177.43	2045	340
KF13	37.58	-31.84	2690	1450
KNR159-5-36GGC	-27.51	-46.47	1268	370
KNR31-GPC5	33.69	-57.63	4583	150
M35003-4	12.09	-61.2433	1299	380
MD01-2416	51.27	-167.73	2317	80
MD01-2421	36.02	-141.78	2224	200
MD02-2489	54.39	-148.92	3640	120
MD03-2698	38.24	-10.39	4602	1350
MD07-3076Q	-44.15	-14.22	3770	280
MD84-527	-43.49	51.19	3262	690
MD88-770	-46.02	96.46	3290	590
MD95-2042	37.8	-10.17	3146	100
MD97-2120	-45.53	174.93	1210	120
MD97-2151	8.73	109.87	1598	210
MD98-2181	6.3	125.82	2114	130
MD99-2334K	37.8	-10.17	3146	300
MD99-2339	35.89	-7.53	1177	90
ODP1145	19.58	117.63	3175	1870
PO200-10-6-2	37.82	-9.5	1086	400
RC11-83	-41.6	9.8	4718	340
SO42-74KL	14.32	57.35	3212	360
SO50-31KL	18.76	115.87	3360	300
SU81-18	37.77	-10.18	3135	340
TR163-22	0.52	-92.4	2830	240
V19-30	-3.38	-83.52	3091	360
V35-5	7.2	112.08	1953	640
W8709A-13	42.12	-125.75	2712	970
W8709A-8	42.26	-127.68	3111	1200

Table S1: The 37 cores used to construct the transition model from Lin et al., (2014). The final column "resolution" lists the average number of years between calibrated radiocarbon ages.

S2 Emission Model

The radiocarbon emission model returns the likelihood of an observed radiocarbon measurement $y_{n,1}$ given a proposed calendar age A_n. The likelihood is calculated with a generalized student's t-distribution which depends on the calibration curve $\mu_C(A_n)$, the calibration curve uncertainty $\sigma_C^2(A_n)$, reservoir age ϱ_n, the combination of analytical measurement uncertainty and reservoir age uncertainty ς_n, and the fixed parameters a_1 =10 and b_1=11:

$$g_1(y_{n,1}|A_n) = T\left(y_{n,1}\middle|\mu_C(A_n) + \varrho_n, \sqrt{\frac{b_1}{a_1}(\sigma_C^2(A_n) + \varsigma_n)}; 2a_1\right).$$

The $\delta^{18}O$ emission model returns the likelihood of an observed $\delta^{18}O$ data point $y_{n,2}$ given a proposed age A_n and is also modeled with a generalized student's t-distribution. The $\delta^{18}O$ emission model depends on the target stack's time-dependent mean $\overline{\mu}(A_n)$ and variance $\overline{v}(A_n)$, the core specific shift h and scale σ parameters, and the fixed parameters a_2=3 and b_2=4:

$$g_2(y_{n,2}|A_n) = T\left(y_{n,2}\middle|\sigma \cdot \overline{\mu}(A_n) + h, \sqrt{\frac{b_2}{a_2}(\sigma)^2 \cdot \overline{v}(A_n)}; 2a_2\right).$$

Here we set a_2 and b_2 based on the observed residuals in the DNEA and ITWA stacks (Figure S1). The thicker tails generated by a_2=3 and b_2=4 (compared to the values of 10 and 11 used for ^{14}C) better fit the larger residuals. The degrees of freedom for each generalized

student's t-distribution is equal to $2a_i$, thus the radiocarbon distribution has 22 degrees of freedom and the $\delta^{18}O$ emission model has six degrees of freedom.

The emission model for the additional age information can be specified as either a uniform distribution or Gaussian distribution with mean $y_{n,3}$ and uncertainty $\underline{\sigma_n}$ specified by the user:

$$g_3(y_{n,3}|A_n) = N(y_{n,3}|A_n, \underline{\sigma_n}^2) \vee U(y_{n,3}|A_n - \underline{\sigma_n}, A_n + \underline{\sigma_n}).$$

If a Gaussian distribution is specified, $\underline{\sigma_n}$ is the standard deviation; if a uniform distribution is specified, $\underline{\sigma_n}$ is the 50% confidence interval width.

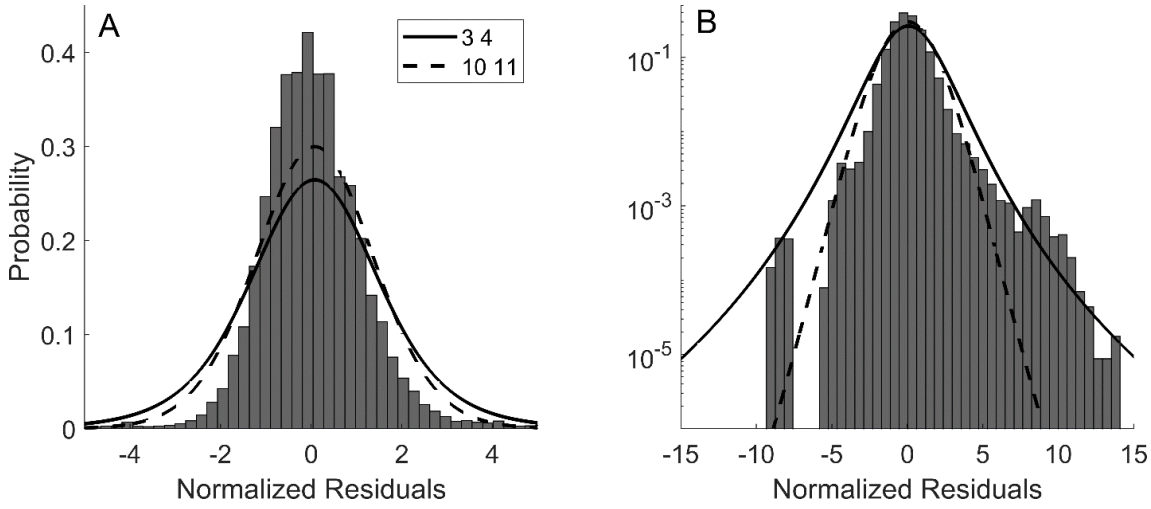

Figure S1: Normalized $\delta^{18}O$ residuals combined from the ITWA and DNEA stacks on a linear y-axis (A) and a log scale (B). Note the expanded x-axis in panel (B). Residuals are normalized by the standard deviation of the stack. The students t-distribution with a_2=3 and b_2=4 better fits the larger residuals.

S3 Additional Figures and Tables

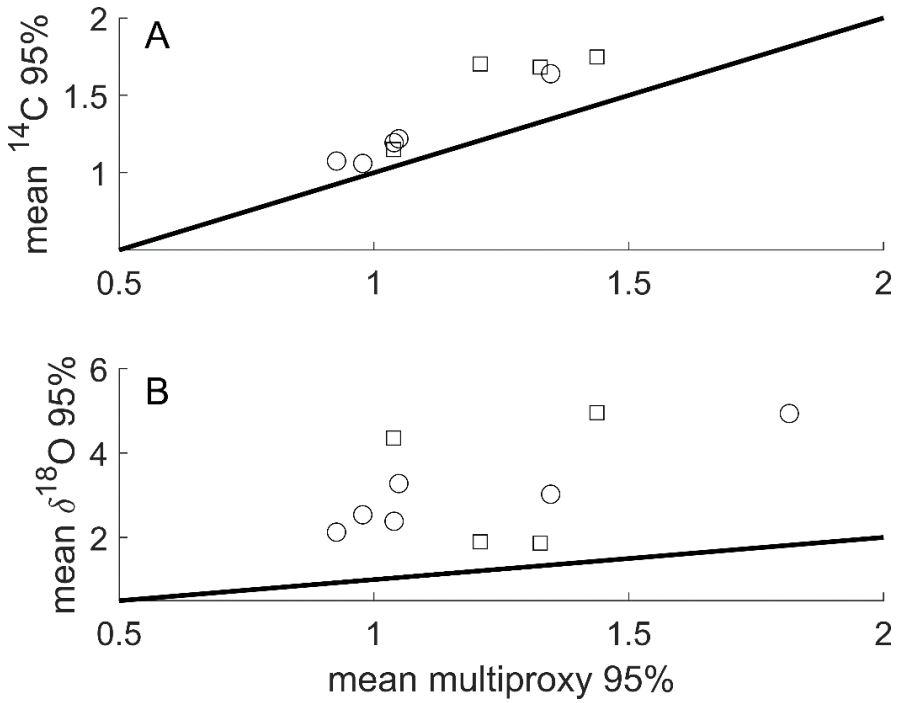

Figure S2: Comparison of the mean 95% confidence interval widths for BIGMACS age models using radiocarbon-only (A) and δ^{18}O-only (B) mode compared to multiproxy age models for cores in the DNEA (squares) and ITWA (circles) stacks. The solid black line marks a 1:1 ratio. The 95% confidence interval widths for radiocarbon-only and δ^{18}O-only age models, respectively, are on average 262 years and 1.92 kyr larger than the 95% confidence interval widths for multiproxy age models.

Core	Modern %	LGM %	Shift (‰)	Scale
DNEA				
MD95-2042	26	23	0.25	0.98
MD99-2334	26	24	-0.07	1.04
SU81-18	26	23	0.08	1
GeoB7920-2	23	24	-0.01	0.98
ODP658C	23	24	0.16	0.92
GeoB9508-5	24	26	0.11	0.99
ITWA				
M35003-4	33	24	-0.25	0.99
KNR197-3-53GGC	33	20	0.09	1
KNR197-3-9GGC	48	28	0.3	0.91
GeoB16206-1	31	27	0.06	0.99

Table S1: SCW percentages at core sites based on modern (Gebbie & Huybers, 2012) and LGM (Oppo et al., 2018) water mass reconstructions. Also, the shift and scale parameters applied to each core during alignment and stacking as estimated by BIGMACS.

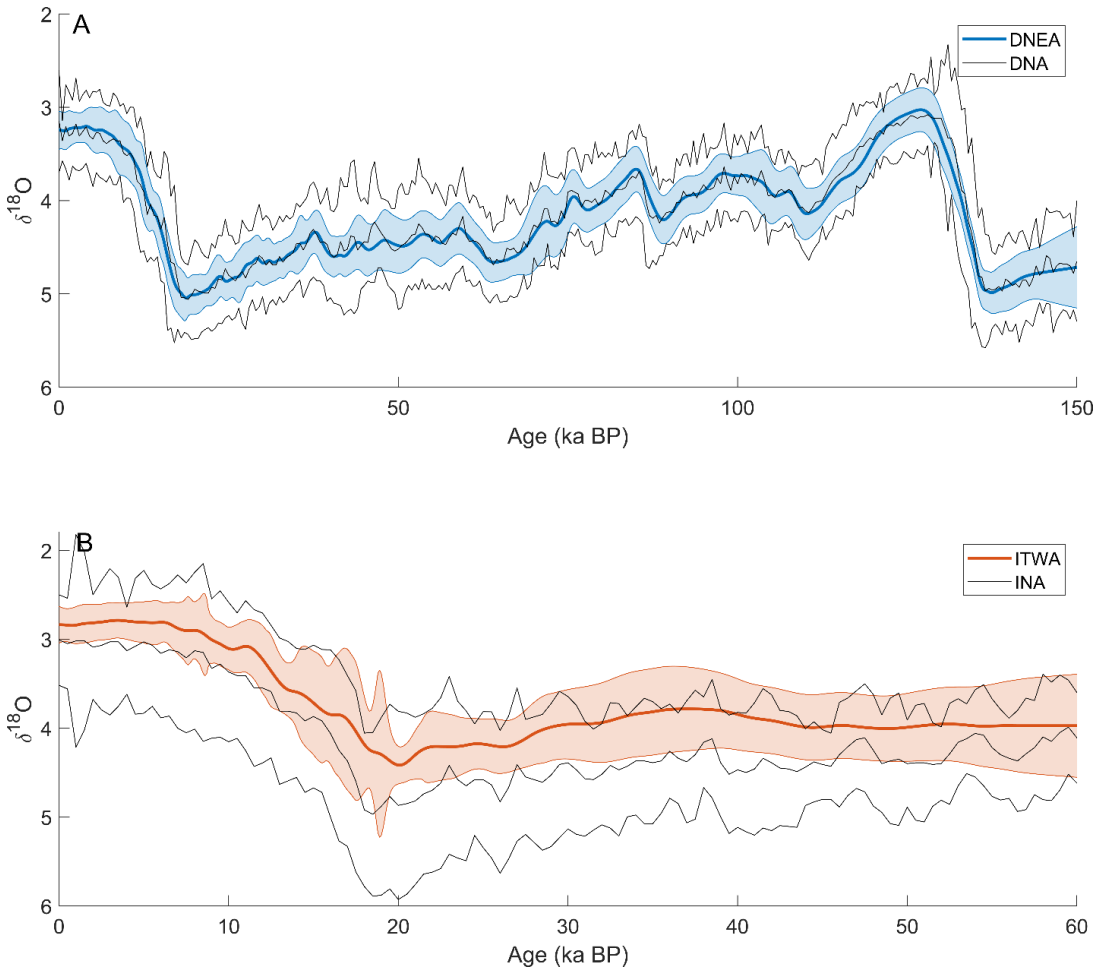

Figure S3: (A) The DNEA stack compared to the DNA stack (Lisiecki & Stern, 2016) used as the initial alignment target. (B) The ITWA stack compared to the INA stack (Lisiecki & Stern, 2016) used as the initial alignment target. Lines mark the mean and 95% confidence interval for each stack. The DNA and INA stacks were constructed using more cores spanning a larger oceanographic region.

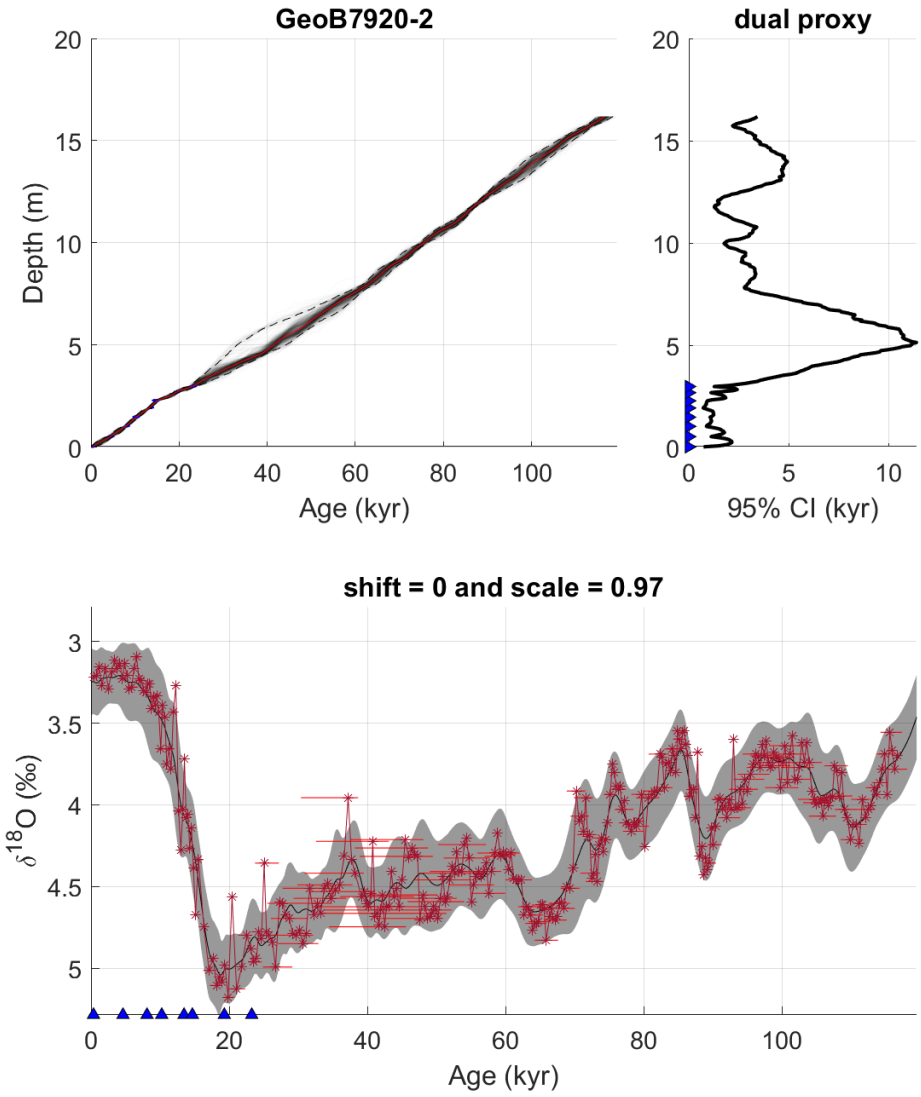

Figure S4: Age model summary for GeoB7920-2. (Top Left) Age vs. Depth plot with the median age model displayed in red and the 95% credible interval displayed as dotted black lines. Shading reveals samples density and radiocarbon ages are shown in blue. (Top Right) Width of the 95% credible interval with the depths of radiocarbon ages displayed as blue triangles on the y-axis. (Bottom) The alignment to the final stack benthic d18O displayed in red, age uncertainty represented by red horizontal lines (95% credible interval), and radiocarbon ages shown as blue triangles.

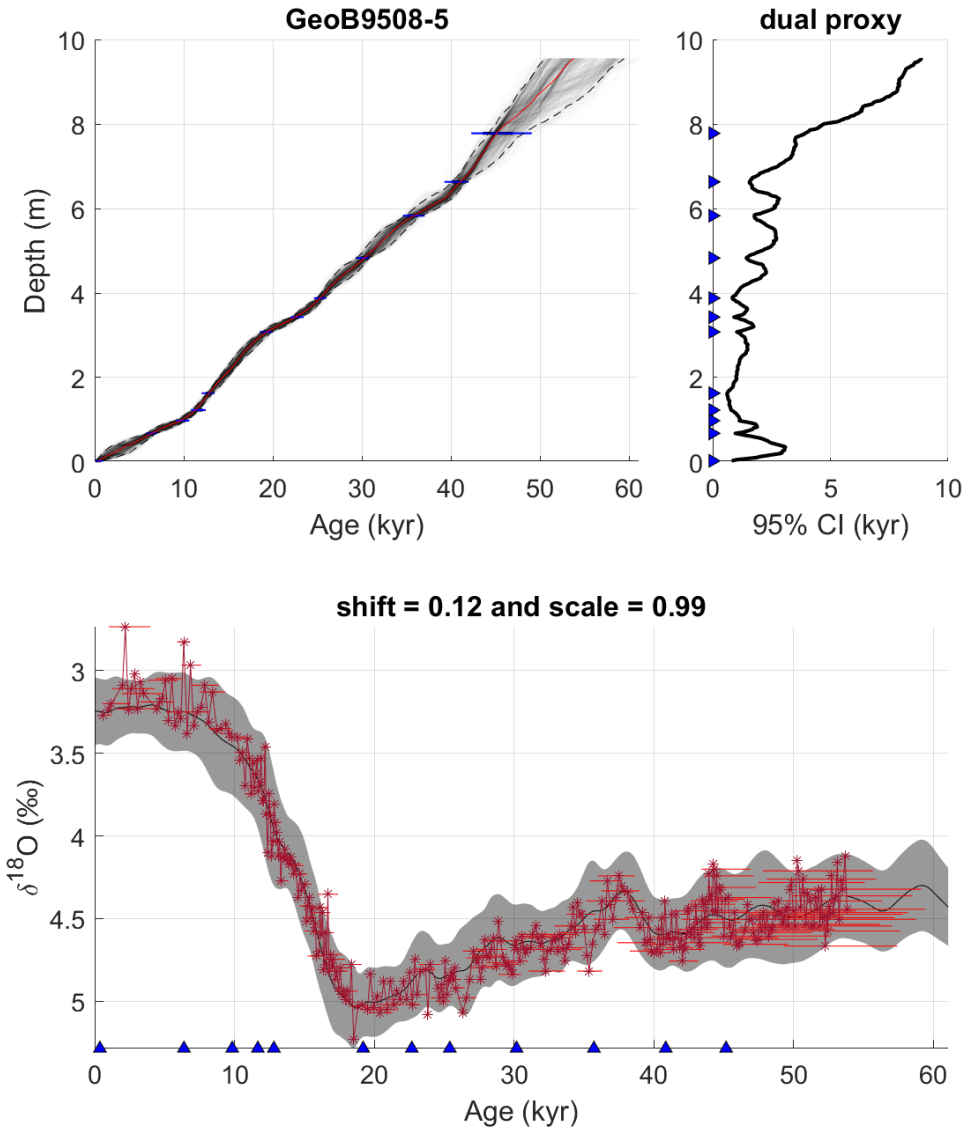

Figure S5: Age model summary for GeoB9508-5

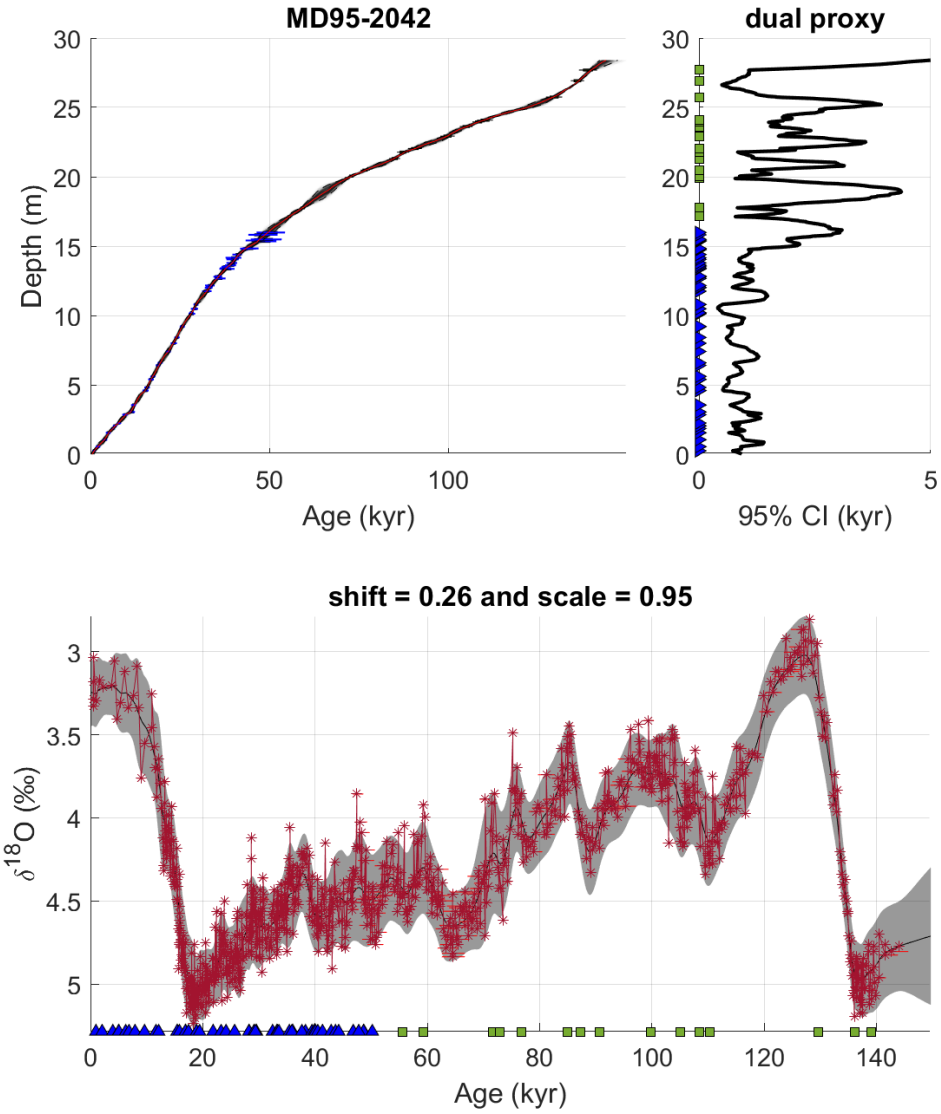

Figure S6: Age model summary for MD95-2042. Additional ages are displayed as green squares.

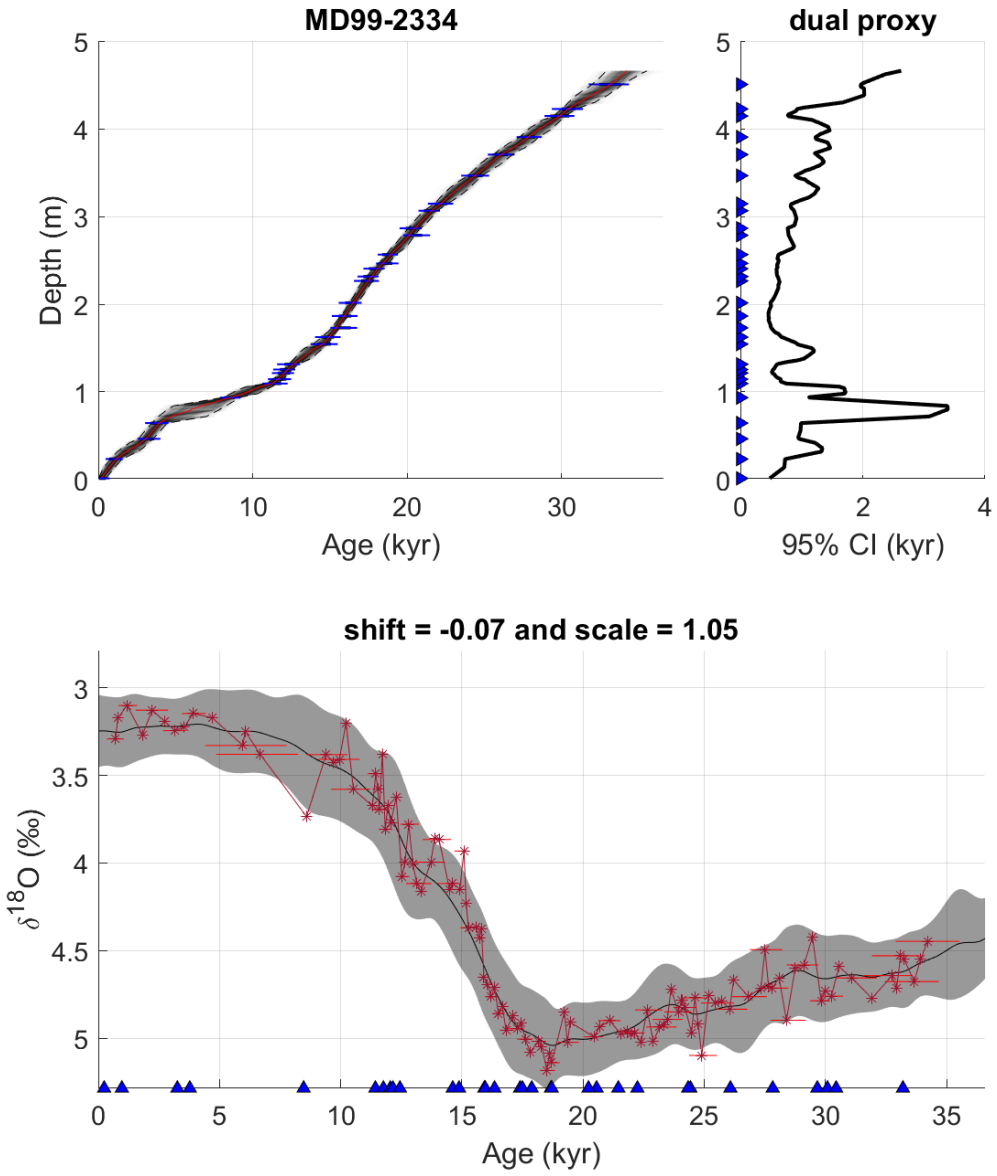

Figure S7: Age model summary for MD99-2334

Figure S7: Age model summary for MD99-23

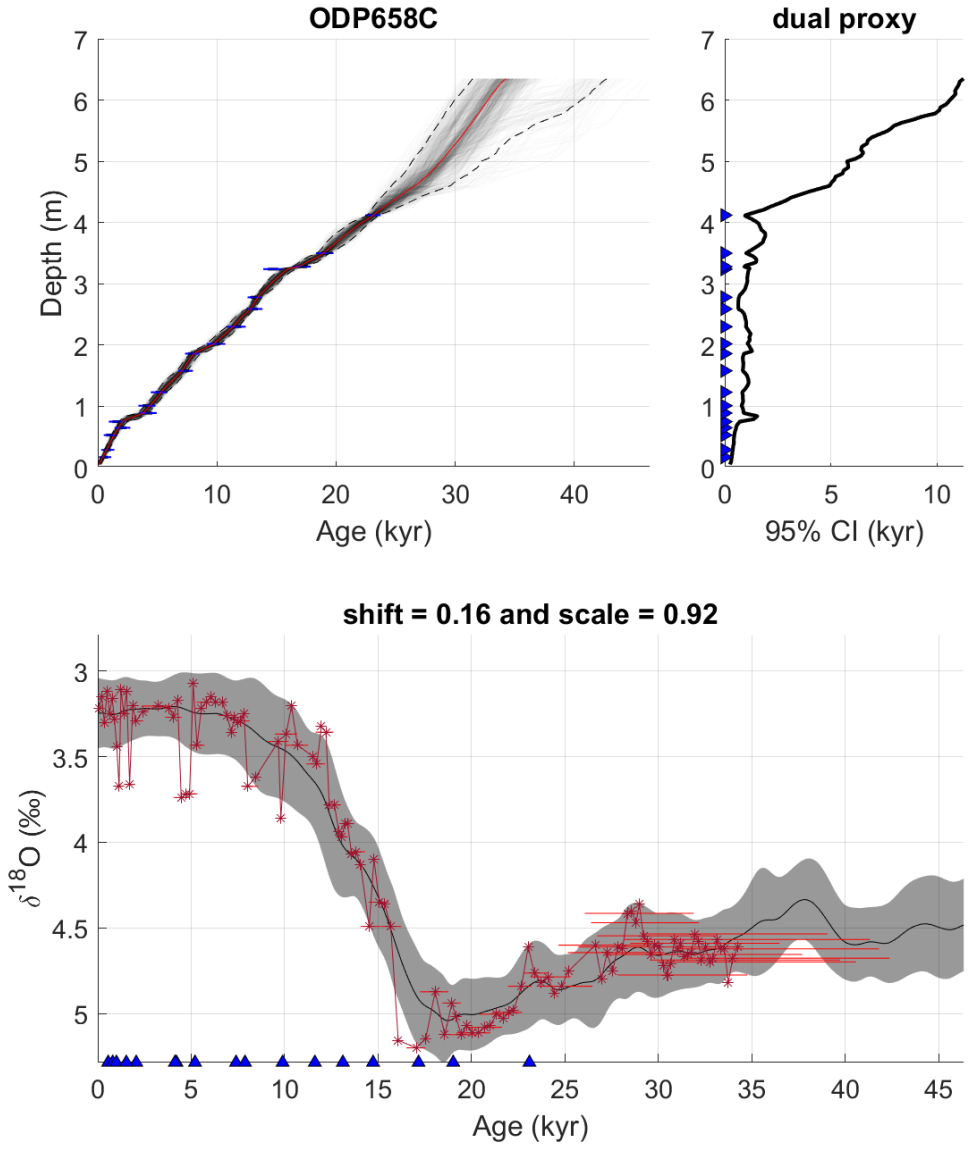

Figure S8: Age model summary for ODP658C.

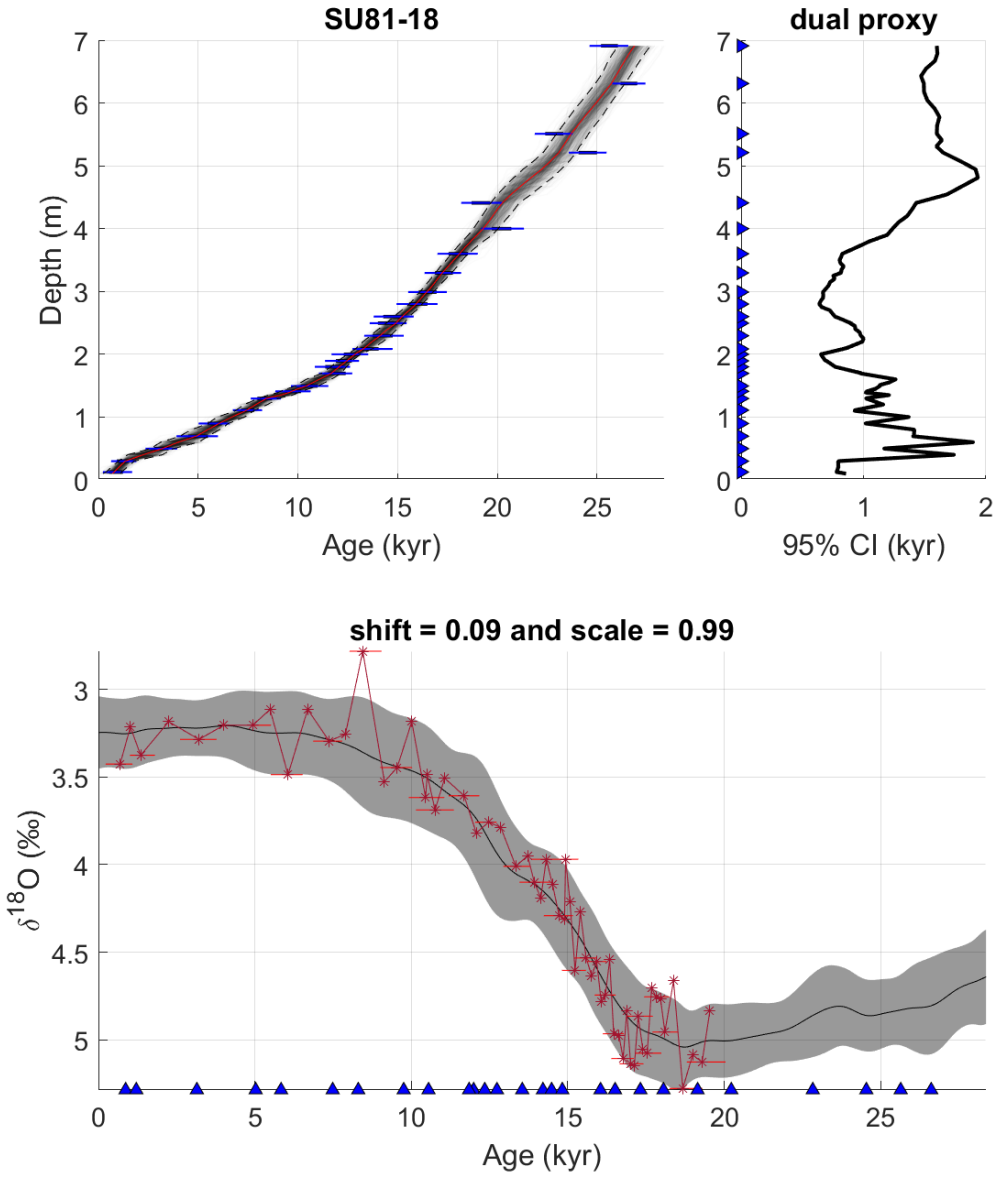

Figure S9: Age model summary for SU81-18.

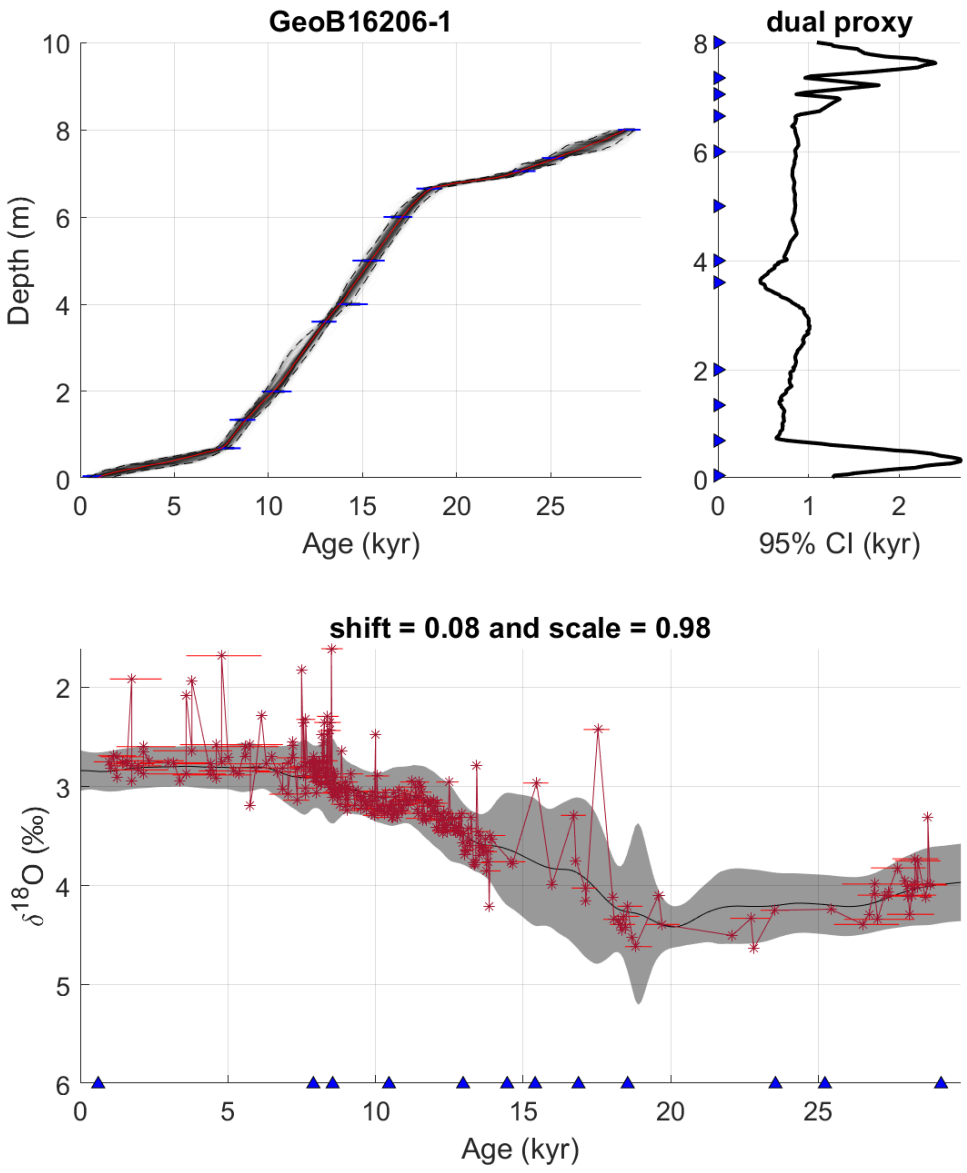

Figure S10: Age model summary for GeoB16206-1

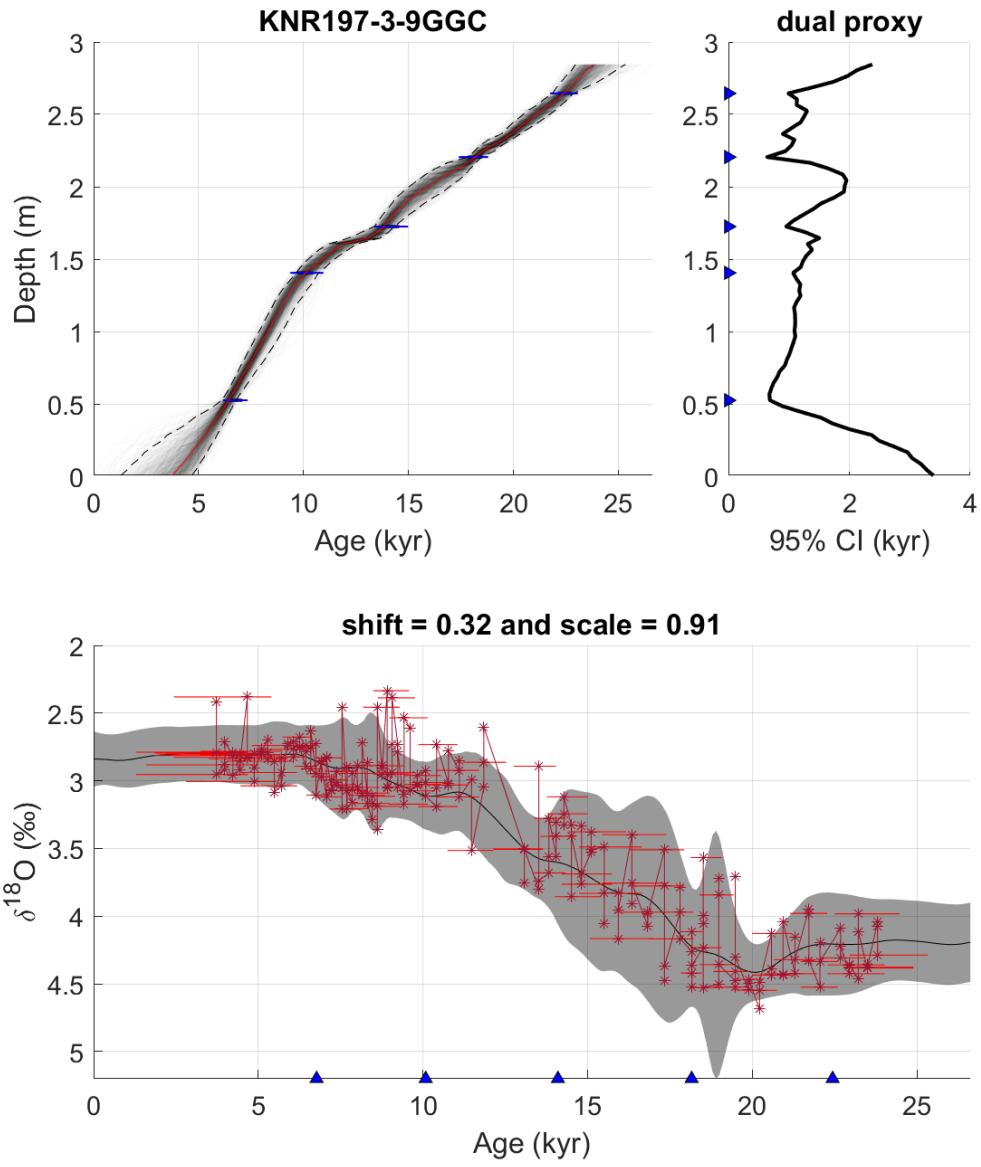

Figure S11: Age model summary for KNR197-3-9GGC.

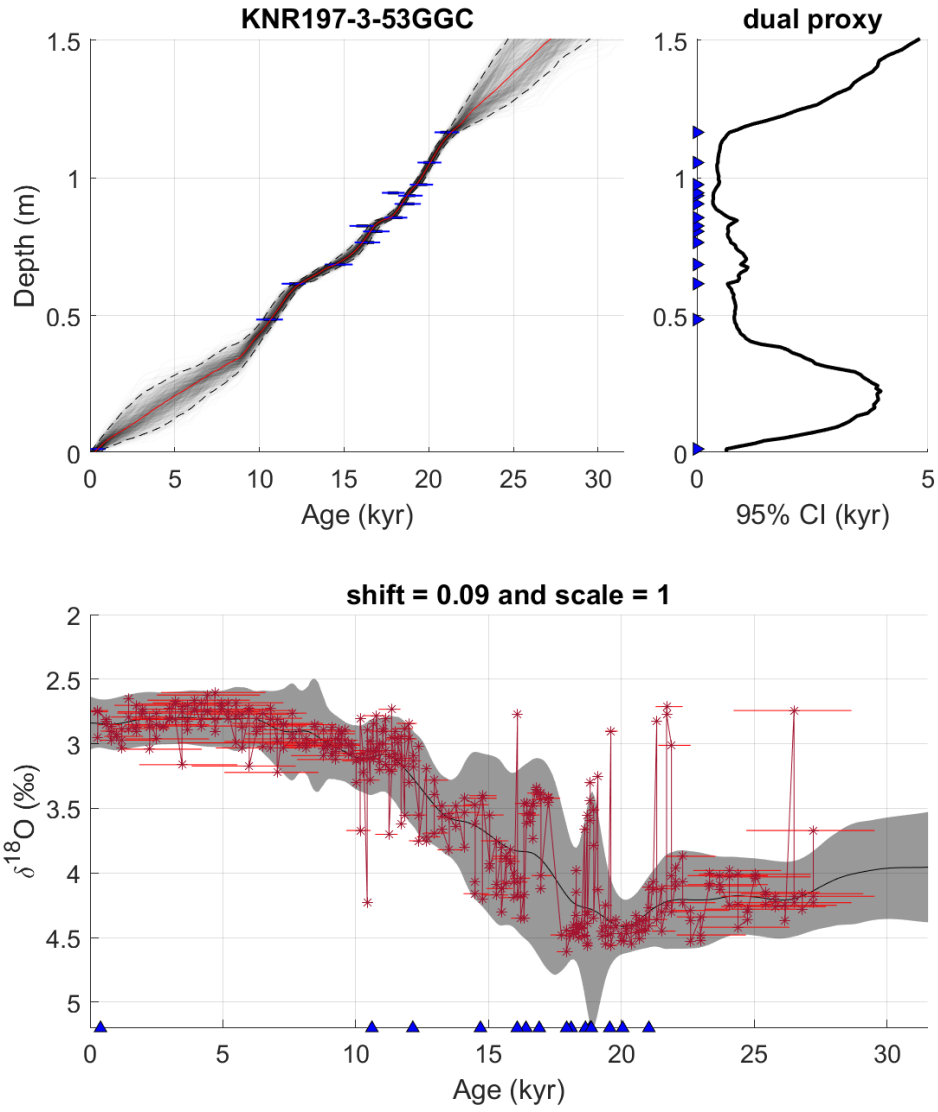

Figure S12: Age model summary for KNR197-3-53GGC.

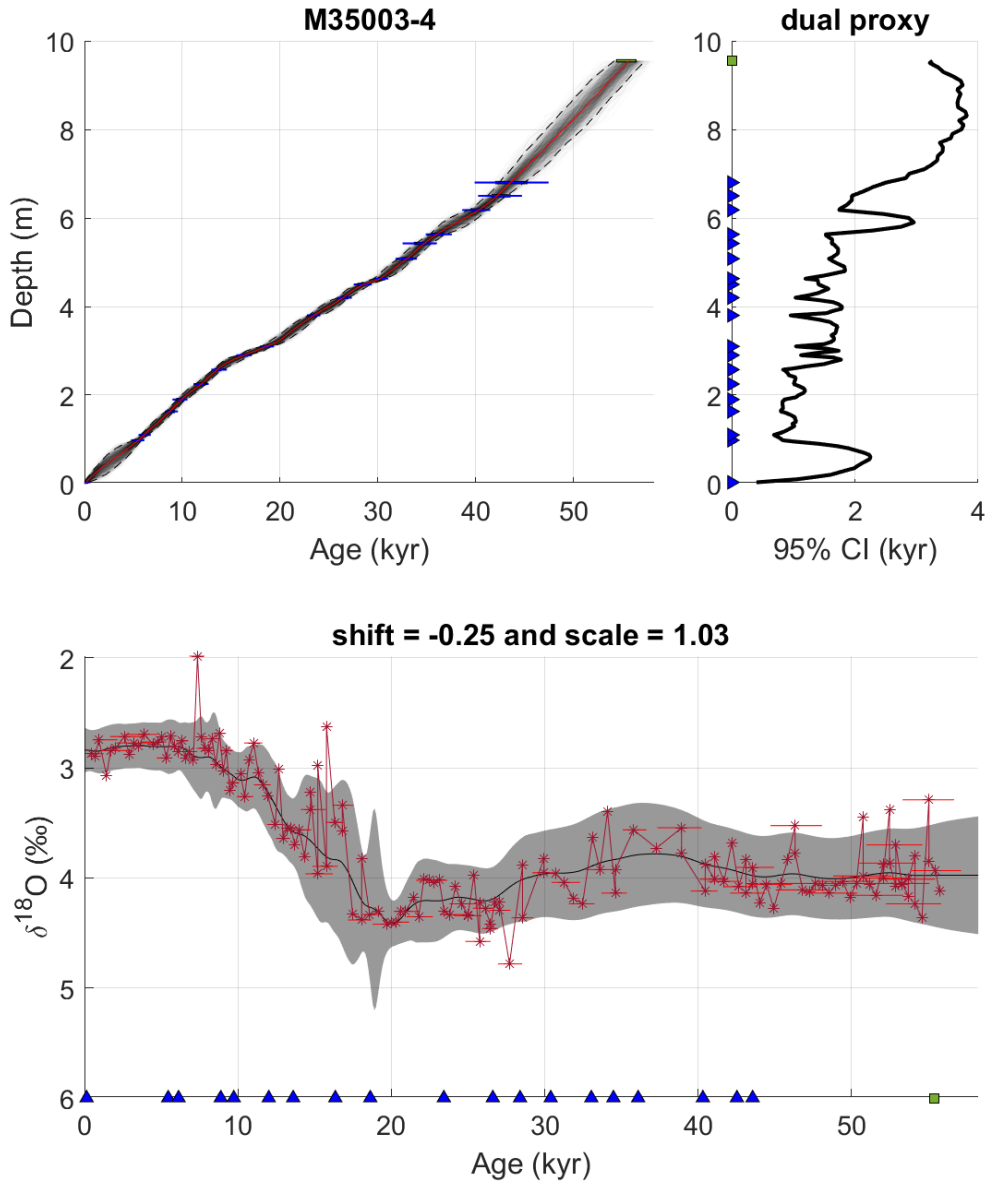

Figure S13: Age model summary for M35003-4.

S4 Alignment Algorithm

The alignment algorithm of BIGMACS consists of two parts: one is to sample age paths from the posterior distribution by the hybrid of particle smoothing [Doucet et al. (2001)] and Markov-chain Monte Carlo (MCMC) algorithm [Martino et al. (2015)], and the

other is to estimate the alignment parameters given the sampled age paths. Supplemental sections S1 and S2 introduced quantitative descriptions of the transition and emission models used by BIGMACS. Here, we present detailed formulations of all parts of the algorithm. The following definitions are assumed throughout the supplementary materials. Suppose that there are M sediment cores.

- $\mathrm{D} = \left\{\mathrm{D}^{(m)}\right\}_{m=1}^{\mathrm{M}}$: a set of core depths, where $\mathrm{D}^{(m)} = \left\{d_n^{(m)}\right\}_{n=1}^{\mathrm{L}_m}$ is those of sediment core m.
- $\mathrm{Y} = \left\{\mathrm{Y}^{(m)}\right\}_{m=1}^{\mathrm{M}}$: a set of proxy observations, where $\mathrm{Y}^{(m)} = \left\{y_n^{(m)}\right\}_{n=1}^{\mathrm{L}_m}$ is those of sediment core m.
    - $y_n^{(m)} = \left(y_{n,1}^{(m)}, y_{n,2}^{(m)}, y_{n,3}^{(m)}\right)$: a pair of radiocarbon, $\delta^{18}\mathrm{O}$ observations and other proxies that give age information at depth $d_n^{(m)}$, respectively.
- $\Theta = \left\{\phi^{(m)}, r^{(m)}, \sigma^{(m)}, h^{(m)}\right\}_{m=1}^{\mathrm{M}}$: a set of core-specific parameters that are used in the alignment algorithm.
    - $\phi^{(m)}$ is a transition matrix that maps $\{\mathbb{C}, \mathbb{A}, \mathbb{E}\}$ to itself.
    - $r^{(m)}$ is a depth-scale parameter that rescales $\mathrm{D}^{(m)}$ to adjust the differences in average accumulation rates.
    - $\sigma^{(m)}$ is a core-specific scale parameter for $\delta^{18}\mathrm{O}$.
    - $h^{(m)}$ is a core-specific shift parameter for $\delta^{18}\mathrm{O}$. These scale and shift parameters standardize $\delta^{18}\mathrm{O}$ observations core-specifically to align them to the stack. Details (in formulation) can be found in the definition of likelihood (emission model) in Section S4.1.

- $\mathrm{A} = \left\{\mathrm{A}^{(m)}\right\}_{m=1}^{\mathrm{M}}$: a set of hidden age paths to sample, where $\mathrm{A}^{(m)} = \left\{\mathrm{A}_n^{(m)}\right\}_{n=1}^{\mathrm{L}_m}$ is those of sediment core m.
- $\mathrm{W} = \left\{\mathrm{W}^{(m)}\right\}_{m=1}^{\mathrm{M}}$: a set of medium latent variables, where $\mathrm{W}^{(m)} = \left\{\mathrm{W}_n^{(m)}\right\}_{n=1}^{\mathrm{L}_m}$ is those of sediment core m.
    - $\mathrm{W}_n^{(m)} \in \{\mathbb{C}, \mathbb{A}, \mathbb{E}\}$ stands for contraction, average and expansion, respectively.

S4.1. State-space Modelling

The goal is to sample $\widetilde{\mathrm{A}}^{(m,k)} \sim p\left(\mathrm{A}^{(m)} \middle| \mathrm{D}, \mathrm{Y}, \Theta\right)$ for each sediment core m, and each age sample k, where $p\left(\mathrm{A}^{(m)} \middle| \mathrm{D}, \mathrm{Y}, \Theta\right)$ is the posterior of the hidden age path $\mathrm{A}^{(m)}$ given depths, proxy observations and alignment parameters. To define the posterior, we have the following prior and likelihood, or the transition and emission models in the terminology of the state-space model [Hangos et al. (2001)]:

- Prior (Transition Model)

$$\pi\left(\mathrm{A}^{(m)}, \mathrm{W}^{(m)} \middle| \mathrm{D}^{(m)}, \Theta\right)$$

$$= \pi\left(\mathrm{A}_{\mathrm{L}_m}^{(m)}, \mathrm{W}_{\mathrm{L}_m}^{(m)}\right) \prod_{n=1}^{\mathrm{L}_m - 1} \pi\left(\mathrm{A}_n^{(m)}, \mathrm{W}_n^{(m)} \middle| \mathrm{A}_{n+1}^{(m)}, \mathrm{W}_{n+1}^{(m)}; d_n^{(m)}, d_{n+1}^{(m)}, \phi^{(m)}, r^{(m)}\right)$$

$$\pi\left(\mathrm{A}_n^{(m)}, \mathrm{W}_n^{(m)} \middle| \mathrm{A}_{n+1}^{(m)}, \mathrm{W}_{n+1}^{(m)}; d_n^{(m)}, d_{n+1}^{(m)}, \phi^{(m)}, r^{(m)}\right)$$

$$\propto \pi_1\left(\mathrm{W}_n^{(m)} \middle| \mathrm{W}_{n+1}^{(m)}, \phi^{(m)}\right) \pi_2\left(\mathrm{A}_n^{(m)} \middle| \mathrm{A}_{n+1}^{(m)}, \mathrm{W}_n^{(m)}; d_n^{(m)}, d_{n+1}^{(m)}, r^{(m)}\right)$$

, where π_1 and π_2 are defined as follows:

$$\pi_1\left(\mathrm{W}_n^{(m)} \middle| \mathrm{W}_{n+1}^{(m)}, \phi^{(m)}\right) = \phi^{(m)}_{\mathrm{W}_{n+1}^{(m)}, \mathrm{W}_n^{(m)}}$$

$$\pi_2\left(\mathrm{A}_n^{(m)}\middle|\mathrm{A}_{n+1}^{(m)},\mathrm{W}_n^{(m)};d_n^{(m)},d_{n+1}^{(m)},r^{(m)}\right)$$

$$\propto\left(\sum_{k=1}^{2}w_k\cdot LogNormal\left(\frac{\mathrm{A}_{n+1}^{(m)}-\mathrm{A}_n^{(m)}}{r^{(m)}\cdot\left(d_{n+1}^{(m)}-d_n^{(m)}\right)}\middle|\underline{\mu}_k,\underline{\sigma}_k\right)\right)$$

$$\cdot 1_{\left\{\frac{\mathrm{A}_{n+1}^{(m)}-\mathrm{A}_n^{(m)}}{r^{(m)}\cdot\left(d_{n+1}^{(m)}-d_n^{(m)}\right)}\in\mathbb{I}_{\mathrm{W}_n^{(m)}}\right\}}\left(\mathrm{A}_n^{(m)}\right)$$

, where $\mathbb{I}_{\mathbb{C}}=(0,0.9220)$, $\mathbb{I}_{\mathbb{A}}=[0.9220,1.0850)$, $\mathbb{I}_{\mathbb{E}}=[1.0850,\infty)$ are the intervals that partition $\mathbb{R}_{>0}$ and $\left\{w_k,\underline{\mu}_k,\underline{\sigma}_k\right\}_{k=1}^{2}$ are the fixed weight, mean and standard deviation parameters of the mixture of log-normal distributions, which are trained from [Lin et al., 2014]. To be specific, $\left(w_1,\underline{\mu}_1,\underline{\sigma}_1\right)=\left(0.642432,0.0198,\sqrt{0.0216}\right)$ and $\left(w_2,\underline{\mu}_2,\underline{\sigma}_2\right)=\left(0.357568,0.0297,\sqrt{0.0929}\right)$. In words, each latent variable $\mathrm{W}_n^{(m)}$ confines the transition from an age $\mathrm{A}_{n+1}^{(m)}$ to another $\mathrm{A}_n^{(m)}$ in one of the three regions $\{\mathbb{C},\mathbb{A},\mathbb{E}\}$ that correspond to $\mathbb{I}_{\mathbb{C}}$, $\mathbb{I}_{\mathbb{A}}$ and $\mathbb{I}_{\mathbb{E}}$. In the transition model, the transition matrix $\phi^{(m)}$ and depth-scale parameter $r^{(m)}$ are the parameters to estimate in the training phase, given the sampled age path $\mathrm{A}^{(m)}$, for each core m.

- Likelihood (Emission Model)

$$p\left(\mathrm{Y}^{(m)}\middle|\mathrm{A}^{(m)};\Theta\right)=\prod_{n=1}^{\mathrm{L}_m}p\left(y_{n,1}^{(m)},y_{n,2}^{(m)},y_{n,3}^{(m)}\middle|\mathrm{A}_n^{(m)}\right)$$

$$=\prod_{n=1}^{\mathrm{L}_m}g_1\left(y_{n,1}^{(m)}\middle|\mathrm{A}_n^{(m)}\right)g_2\left(y_{n,2}^{(m)}\middle|\mathrm{A}_n^{(m)}\right)g_3\left(y_{n,3}^{(m)}\middle|\mathrm{A}_n^{(m)}\right)$$

, where g_1, g_2 and g_3 are defined as follows:

$$g_1\left(y_{n,1}^{(m)}\middle|\mathrm{A}_n^{(m)}\right) = \mathcal{T}_{2a_1}\left(y_{n,1}^{(m)}\middle|\mu_{\mathrm{C}}\left(\mathrm{A}_n^{(m)}\right) + \varrho_n^{(m)}, \sqrt{\frac{b_1}{a_1}\left(\sigma_{\mathrm{C}}^2\left(\mathrm{A}_n^{(m)}\right) + \varsigma_n^{(m)}\right)}\right)$$

$$g_2\left(y_{n,2}^{(m)}\middle|\mathrm{A}_n^{(m)}\right) = \mathcal{T}_{2a_2}\left(y_{n,2}^{(m)}\middle|\sigma^{(m)} \cdot \overline{\mu}\left(\mathrm{A}_n^{(m)}\right) + h^{(m)}, \sqrt{\frac{b_2}{a_2}(\sigma^{(m)})^2 \cdot \overline{\nu}\left(\mathrm{A}_n^{(m)}\right)}\right)$$

$$g_3\left(y_{n,3}^{(m)}\middle|\mathrm{A}_n^{(m)}\right) = \mathcal{N}\left(y_{n,3}^{(m)}\middle|\mathrm{A}_n^{(m)}, \underline{\nu}_n^{(m)}\right) \text{ or } \mathcal{U}\left(y_{n,3}^{(m)}\middle|\mathrm{A}_n^{(m)} - \sqrt{\underline{\nu}_n^{(m)}}, \mathrm{A}_n^{(m)} + \sqrt{\underline{\nu}_n^{(m)}}\right)$$

, where $\varrho_n^{(m)}$ and $\varsigma_n^{(m)}$ are given together with the radiocarbon determination (a measurement of the amount of radiocarbon in a sample) $y_{n,1}^{(m)}$ a priori, μ_{C} and σ_{C}^2 are the mean and variance functions of the radiocarbon calibration curve [Reimer et al. (2020); Hogg et al. (2020); Heaton et al. (2020)], and $\overline{\mu}$ and $\overline{\nu}$ are the mean and variance functions from the target δ^{18}O stack. (a_1, b_1) and (a_2, b_2) are the pairs of fixed hyperparameters for the generalized Student's t-distribution [Christen and Sergio (2009)] to balance observations that follow the given calibration curve (or stack) and potential outliers. For g_3 that reflects our prior knowledge regarding the ages, BIGMACS allows to pick among the Gaussian-based model and the uniform-based model. For the Gaussian-based model, an uncertainty input $\underline{\nu}_n^{(m)}$ works as the variance while $\underline{\nu}_n^{(m)}$ defines the 50% confidence interval for the uniform-based model. In the emission model, the core-specific scale and shift parameters $\sigma^{(m)}$ and $h^{(m)}$ are estimated in the training phase, given the sampled age path $\mathrm{A}^{(m)}$ and the target δ^{18}O stack, for each core m.

The above prior and likelihood, or transition and emission models, define the following joint distribution:

$$p(\mathrm{Y}, \mathrm{A}, \mathrm{W}|\mathrm{D}, \Theta) = \prod_{m=1}^{\mathrm{M}} \pi\left(\mathrm{A}^{(m)}, \mathrm{W}^{(m)}\middle|\mathrm{D}^{(m)}; \Theta\right) p\left(\mathrm{Y}^{(m)}\middle|\mathrm{A}^{(m)}; \Theta\right)$$

Thus, $p\left(\mathrm{A}^{(m)}, \mathrm{W}^{(m)} \middle| \mathrm{D}, \mathrm{Y}, \Theta\right) = p\left(\mathrm{A}^{(m)}, \mathrm{W}^{(m)} \middle| \mathrm{D}^{(m)}, \mathrm{Y}^{(m)}, \Theta\right) \propto$ $\pi\left(\mathrm{A}^{(m)}, \mathrm{W}^{(m)} \middle| \mathrm{D}^{(m)}, \Theta\right) p\left(\mathrm{Y}^{(m)} \middle| \mathrm{A}^{(m)}; \Theta\right)$ for each m, which allows to run the sampling algorithm parallelly over sediment cores. Note that $\mathrm{W}^{(m)}$ is deterministic given $\mathrm{A}^{(m)}$ and the problem is now defined as a state-space model.

S4.2. Sampling

As mentioned earlier, BIGMACS samples the age paths $\mathrm{A}^{(m)}$ (and $\mathrm{W}^{(m)}$) from the posterior by the hybrid of particle smoothing and MCMC algorithms, given all the parameters to be either fixed or estimated. Though the particle smoothing is an efficient method of sampling continuous hidden states from a state-space model, only a small portion of proposed samples, "particles", contribute to the set of sampled paths in practice. Though MCMC can sample the hidden variables in principle, it might require a very long chain before the burn-in phase, especially if a good initialization is not given. Here, we run the particle smoothing for initializing the sampled age paths and then run the Metropolis-Hastings algorithm [Metropolis et al. (1953); Hastings (1970)] to "refine" the previously initialized paths.

The particle smoothing consists of two parts. The forward algorithm samples a set of candidates, or "particles", from a proposal distribution $q_n^{(m)}$ for each step n, and computes weights on those particles to approximate the forward posterior with an empirical distribution. In formulation, it is expressed as follows:

$$p\left(\mathrm{A}_n^{(m)}, \mathrm{W}_n^{(m)} \middle| \mathrm{D}_{1:n}^{(m)}, \mathrm{Y}_{1:n}^{(m)}, \Theta\right) \approx \sum_{k=1}^{\mathrm{K}} \omega_{n,k}^{(m)} \cdot 1_{\left\{\mathrm{A}_n^{(m)} = a_{n,k}^{(m)}, \mathrm{W}_n^{(m)} = w_{n,k}^{(m)}\right\}}\left(\mathrm{A}_n^{(m)}, \mathrm{W}_n^{(m)}\right)$$

, where $\left\{a_{n,k}^{(m)}, w_{n,k}^{(m)}\right\}_{k=1}^{\mathrm{K}}$ are the sampled particles from $q_n^{(m)}$ at step n and $\left\{\omega_{n,k}^{(m)}\right\}_{k=1}^{\mathrm{K}}$ are the associated weights that are sum to 1. Then, the forward posterior of the next step is updated iteratively as follows:

$$p\left(\mathrm{A}_{n-1}^{(m)}, \mathrm{W}_{n-1}^{(m)} \middle| \mathrm{D}_{1:n-1}^{(m)}, \mathrm{Y}_{1:n-1}^{(m)}, \Theta\right) \approx \sum_{k=1}^{\mathrm{K}} \omega_{n-1,k}^{(m)} \cdot 1_{\left\{\mathrm{A}_{n-1}^{(m)}=a_{n-1,k}^{(m)}, \mathrm{W}_{n-1}^{(m)}=w_{n-1,k}^{(m)}\right\}}\left(\mathrm{A}_{n-1}^{(m)}, \mathrm{W}_{n-1}^{(m)}\right)$$

, where $\left\{a_{n-1,k}^{(m)}, w_{n-1,k}^{(m)}\right\}_{k=1}^{\mathrm{K}} \sim_{i.i.d.} q_{n-1}^{(m)}$ and for $\sum_{k=1}^{\mathrm{K}} \omega_{n-1,k}^{(m)} = 1$,

$\omega_{n-1,k}^{(m)}$

$$\propto \frac{p\left(y_{n-1,1}^{(m)}, y_{n-1,2}^{(m)} \middle| a_{n-1,k}^{(m)}; \Theta\right)}{q_{n-1}^{(m)}\left(a_{n-1,k}^{(m)}, w_{n-1,k}^{(m)}\right)} \sum_{s=1}^{\mathrm{K}} \omega_{n,s}^{(m)} \pi\left(a_{n-1,k}^{(m)}, w_{n-1,k}^{(m)} \middle| a_{n,s}^{(m)}, w_{n,s}^{(m)}; d_{n-1}^{(m)}, d_n^{(m)}, \phi^{(m)}, r^{(m)}\right)$$

The backward algorithm samples each hidden alignment given the depth above it (from the top of the core down) as well as all inputs and outputs iteratively until a complete path is sampled. In formulation, it is expressed as follows:

$$p\left(\mathrm{A}_n^{(m)} = a_{n,k}^{(m)}, \mathrm{W}_n^{(m)} = w_{n,k}^{(m)} \middle| \mathrm{A}_{n-1}^{(m)} = \tilde{a}_{n-1}^{(m)}, \mathrm{W}_{n-1}^{(m)} = \tilde{w}_{n-1}^{(m)}\right)$$

$$\propto \omega_{n,k}^{(m)} \cdot \pi\left(\tilde{a}_{n-1}^{(m)}, \tilde{w}_{n-1}^{(m)} \middle| a_{n,k}^{(m)}, w_{n,k}^{(m)}; d_{n-1}^{(m)}, d_n^{(m)}, \phi^{(m)}, r^{(m)}\right)$$

Note that the particle smoothing is reduced to a hidden Markov model (HMM) [Durbin et al. (1998)] if the proposal distribution is set to have the same finite support and all elements in the support are sampled once as particles. Also, because the particle smoothing does not compute the exact forward posterior, this method has limitations that HMMs do not. First, performance is dependent on the user-specific proposal distributions. Second, a small number of output outliers might ruin the inference, especially if the transition model is too rigid. Third, the weights assigned to the particles are often too small

to affect the backward sampling algorithm, which might cause a trouble in learning emission and transition models by the Baum-Welch EM algorithm [Dempster et al. (1977); Durbin et al. (1998)]. To resolve the first limitation, here, we iterate the sampling part consisting of the particle smoothing and Metropolis-Hastings and the parameter estimation part for Θ until convergence. Suppose that we obtained T sampled age paths $\left\{\widetilde{\mathrm{A}}^{(m,t)}\right\}_{t=1}^{\mathrm{T}}$ in the last round, where each $\widetilde{\mathrm{A}}^{(m,t)} = \left\{\tilde{a}_n^{(m,t)}\right\}_{n=1}^{\mathrm{L}_m}$. Then, each proposal $q_n^{(m)}$ at the current round is designed as follows:

$$q_n^{(m)} = \frac{1}{\mathrm{T}}\sum_{t=1}^{\mathrm{T}} 1_{\left(\tilde{a}_n^{(m,t)}-d,\tilde{a}_n^{(m,t)}+d\right)}$$

, where $d > 0$ is a bandwidth hyperparameter and $\left(\tilde{a}_n^{(m,t)} - d, \tilde{a}_n^{(m,t)} + d\right)$ is an interval. In other words, candidates at step n of the current round are randomly sampled from a randomly chosen interval $\left(\tilde{a}_n^{(m,t)} - d, \tilde{a}_n^{(m,t)} + d\right)$ among $t = 1,2,\cdots,\mathrm{T}$. These reasons prevent us from relying only on the particle smoothing in sampling; we therefore use particles only to initialize the samples.

One advantage of the particle smoothing is that we can quickly sample hidden alignments by the backward algorithm once particles and weights are obtained in the forward algorithm. To guarantee the independence of samples, we first initialize the age paths one-by-one by the particle smoothing and then run the Metropolis-Hastings algorithm on each of them.

The basic framework of the Metropolis-Hastings algorithm starts with computing the following acceptance ratio γ:

$$\gamma = \min\left\{1, \frac{\pi\left(\dot{\mathrm{A}}^{(m)}, \dot{\mathrm{W}}^{(m)} \middle| \mathrm{D}^{(m)}; \Theta\right) p\left(\mathrm{Y}^{(m)} \middle| \dot{\mathrm{A}}^{(m)}; \Theta\right)}{\pi\left(\mathrm{A}^{(m)}, \mathrm{W}^{(m)} \middle| \mathrm{D}^{(m)}; \Theta\right) p\left(\mathrm{Y}^{(m)} \middle| \mathrm{A}^{(m)}; \Theta\right)} \cdot \frac{q\left(\mathrm{A}^{(m)}, \mathrm{W}^{(m)} \middle| \dot{\mathrm{A}}^{(m)}, \dot{\mathrm{W}}^{(m)}\right)}{q\left(\dot{\mathrm{A}}^{(m)}, \dot{\mathrm{W}}^{(m)} \middle| \mathrm{A}^{(m)}, \mathrm{W}^{(m)}\right)}\right\}$$

, where $\left(\mathrm{A}^{(m)}, \mathrm{W}^{(m)}\right)$ is the previously updated age path, $q\left(\cdot \middle| \mathrm{A}^{(m)}, \mathrm{W}^{(m)}\right)$ is the proposal distribution conditioned on $\left(\mathrm{A}^{(m)}, \mathrm{W}^{(m)}\right)$, and $\left(\dot{\mathrm{A}}^{(m)}, \dot{\mathrm{W}}^{(m)}\right)$ is the proposed candidate that is sampled from $q\left(\cdot \middle| \mathrm{A}^{(m)}, \mathrm{W}^{(m)}\right)$. Then, update $\left(\mathrm{A}^{(m)}, \mathrm{W}^{(m)}\right)$ with $\left(\dot{\mathrm{A}}^{(m)}, \dot{\mathrm{W}}^{(m)}\right)$ if γ is bigger than or equal to a uniform random number in $(0,1)$; otherwise, keep $\left(\mathrm{A}^{(m)}, \mathrm{W}^{(m)}\right)$. Once we are in a burn-in phase, stop iteration and return the final $\left(\mathrm{A}^{(m)}, \mathrm{W}^{(m)}\right)$ as the sample.

Note that the Markov structure of the transition model and conditionally independent emission model allow us to efficiently run the algorithm: age samples in a block are simultaneously proposed, evaluated, and potentially updated.

To be more specific, the proposal distribution $q\left(\cdot \middle| \mathrm{A}^{(m)}, \mathrm{W}^{(m)}\right)$ is defined as follows:

$$q\left(\dot{\mathrm{A}}_n^{(m)}, \dot{\mathrm{W}}_n^{(m)} \middle| \mathrm{A}^{(m)}, \mathrm{W}^{(m)}\right)$$

$$= \begin{cases} \mathcal{N}\left(\dot{\mathrm{A}}_n^{(m)} \middle| \mathrm{A}_n^{(m)}, \frac{1}{8}\left(\mathrm{A}_{n+1}^{(m)} - \mathrm{A}_n^{(m)}\right)\right) \cdot 1_{\left\{\frac{\mathrm{A}_{n+1}^{(m)} - \dot{\mathrm{A}}_n^{(m)}}{r^{(m)} \cdot \left(d_{n+1}^{(m)} - d_n^{(m)}\right)} \in \mathbb{I}_{\dot{\mathrm{W}}_n^{(m)}}\right\}}, & n = 1 \\ \mathcal{N}\left(\dot{\mathrm{A}}_n^{(m)} \middle| \mathrm{A}_n^{(m)}, \frac{1}{8}\left(\mathrm{A}_n^{(m)} - \mathrm{A}_{n-1}^{(m)}\right)\right) \cdot 1_{\left\{\frac{\dot{\mathrm{A}}_n^{(m)} - \mathrm{A}_{n-1}^{(m)}}{r^{(m)} \cdot \left(d_n^{(m)} - d_{n-1}^{(m)}\right)} \in \mathbb{I}_{\dot{\mathrm{W}}_{n-1}^{(m)}}\right\}}, & n = \mathrm{L}_m \\ \mathcal{U}\left(\dot{\mathrm{A}}_n^{(m)} \middle| \mathrm{A}_{n-1}^{(m)}, \mathrm{A}_{n+1}^{(m)}\right) \cdot 1_{\left\{\frac{\mathrm{A}_{n+1}^{(m)} - \dot{\mathrm{A}}_n^{(m)}}{r^{(m)} \cdot \left(d_{n+1}^{(m)} - d_n^{(m)}\right)} \in \mathbb{I}_{\dot{\mathrm{W}}_n^{(m)}}\right\}}, & otherwise \end{cases}$$

, where $\mathcal{U}\left(\dot{\mathrm{A}}_n^{(m)} \middle| \mathrm{A}_{n-1}^{(m)}, \mathrm{A}_{n+1}^{(m)}\right)$ means that $\dot{\mathrm{A}}_n^{(m)}$ follows a uniform distribution on the interval $\left(\mathrm{A}_{n-1}^{(m)}, \mathrm{A}_{n+1}^{(m)}\right)$.

S4.3. Parameter Estimation

To estimate $\Theta = \{\Theta^{(m)}\}_{m=1}^{M} = \{\phi^{(m)}, r^{(m)}, \sigma^{(m)}, h^{(m)}\}_{m=1}^{M}$, we apply the Baum-Welch EM algorithm by iterating the following steps, with a prior π_0 on $\Theta^{(m)}$, given the sampled age path $A^{(m)}$, for each m:

- E-step: define the following $Q(\Theta^{(m)}|\Theta^{(m,t)})$:

$$Q(\Theta^{(m)}|\Theta^{(m,t)}) = \mathbb{E}_{A^{(m)},W^{(m)}|D^{(m)},Y^{(m)},\Theta^{(m,t)}}[\log \pi(A^{(m)}, W^{(m)}|D^{(m)}; \Theta^{(m)}) + \log p(Y^{(m)}|A^{(m)}; \Theta^{(m)}) + \log \pi_0(\Theta^{(m)})]$$

- M-step: find $\Theta^{(m)} = \Theta^{(m,t+1)}$ that maximizes $Q(\Theta^{(m)}|\Theta^{(m,t)})$:

$$\Theta^{(m,t+1)} = \underset{\Theta^{(m)}}{\operatorname{argmax}}\, Q(\Theta^{(m)}|\Theta^{(m,t)})$$

To compute the above $Q(\Theta^{(m)}|\Theta^{(m,t)})$, we approximate it from the samples $\{A^{(m,k,t)}, W^{(m,k,t)}\}_{k=1}^{K}$ drawn from the posterior $p(A^{(m)}, W^{(m)}|D^{(m)}, Y^{(m)}, \Theta^{(m,t)})$ by the hybrid of particle smoothing and MCMC independently, as described in subsection S4.2:

$$Q(\Theta^{(m)}|\Theta^{(m,t)}) \approx \frac{1}{K}\sum_{k=1}^{K}\left(\log \pi(A^{(m,k,t)}, W^{(m,k,t)}|D^{(m)}; \Theta^{(m)}) + \log p(Y^{(m)}|A^{(m,k,t)}; \Theta^{(m)})\right) + \log \pi_0(\Theta^{(m)})$$

To optimize $Q(\Theta^{(m)}|\Theta^{(m,t)})$ in the M-step, BIGMACS depends on the gradient ascent algorithm with the above approximation as the objective function to maximize.

Finally, we discuss the depth-scale parameter $r^{(m)}$. Although it may be reasonable to assume $r^{(m)}$is a scalar parameter, BIGMACS considers $r^{(m)}$ to be a continuous function

over ages in order to reflect long-term changes of sedimentation rates, by the following definition, based on the Nadaraya-Watson Kernel regression [Langrene and Warin (2019)]:

$$\log r^{(m)}(a) = \frac{1}{\mathrm{K}}\sum_{k=1}^{\mathrm{K}}\left(\sum_{n=1}^{\mathrm{L}_m-1}\mathcal{K}_h\left(a-\tilde{a}_{n+1,k}^{(m)}\right)\log\frac{\tilde{a}_{n+1,k}^{(m)}-\tilde{a}_{n,k}^{(m)}}{d_{n+1}^{(m)}-d_n^{(m)}}\Big/\sum_{n=1}^{\mathrm{L}_m}\mathcal{K}_h\left(a-\tilde{a}_{n+1,k}^{(m)}\right)\right)$$

, where $h > 0$ is a fixed hyperparameter that controls the smoothness of $r^{(m)}$. BIGMACS chose a large $h = 20$ as the default so that the transition model still depends on the transition matrix.

S5. Stack Construction Algorithm

The stack construction algorithm in BIGMACS is designed to construct a set of sample-specific Gaussian process regression models [Rasmussen and Williams (2006)] and average them into a single Gaussian model at each age. However, first we resolve the following three issues: 1) outlier classification from the given $\delta^{18}O$ observations, 2) kernel hyperparameter estimation for the Gaussian process regression, and 3) construction of heteroscedastic observational variances of $\delta^{18}O$ continuously. In this section, we will discuss these issues together with stack construction. The following definitions are assumed throughout the supplementary materials.

- $\Psi = \{\mathbb{K}, \Lambda\}$: a set of regression hyperparameters.
    - $\mathbb{K}$ is a kernel covariance function controlled by kernel hyperparameters. For example, an Ornstein-Uhlenbeck kernel is defined as follows, for a set of hyperparameters η and η:

$$\mathbb{K}(u, v) = \eta^2 exp(-\xi^2|u - v|)$$

    - Λ is an observational variance function.

- $\vec{\mathrm{Y}}$: a vector that aggregates all δ^{18}O observations of sediment cores, after the standardization.
    - Here, the term 'standardization' means that each observation has been standardized based on the core-specific scale and shift parameters estimated in the alignment part.
- $\widetilde{\mathrm{A}} = \left\{\widetilde{\mathrm{A}}^{(k)}\right\}_{k=1}^{\mathrm{K}}$: a set of vectors that aggregates all sampled age paths of sediment cores.
    - $\widetilde{\mathrm{A}}^{(k)} = \left\{\widetilde{\mathrm{A}}^{(m,k)}\right\}_{m=1}^{\mathrm{M}}$: a vector that concatenates each of the kth path among sediment cores.
- $\underline{\mathrm{A}}$: a set of induced pseudo-inputs. This set is for the variational free energy approximation [Titsias (2009)] and predefined in the same domain of ages.
- $\underline{\mu}$: a constant scalar for the mean value of stack.

The stack construction algorithm first iterates steps in subsections S5.2, S5.3 and S5.4 until convergence and then update the new one by the method in S5.1.

S5.1. Stack Construction

The goal is to construct a generative model of the standardized δ^{18}O at a query age. In formulation, the stack is in the following form:

$$p(y|a;\mathrm{Y},\mathrm{D},\Theta,\Psi) = \int p\left(y\middle|a;\vec{\mathrm{Y}},\mathrm{A},\Psi\right)p(\mathrm{A}|\mathrm{D},\mathrm{Y};\Theta)\,d\mathrm{A}$$

, where $p(\mathrm{A}|\mathrm{D},\mathrm{Y};\Theta)$ is the posterior distribution of the hidden age paths given depths and proxy observations and $p\left(y\middle|a;\vec{\mathrm{Y}},\mathrm{A},\Psi\right)$ is the regression model given the hidden age

paths and a set of regression hyperparameters Ψ. Because it is impossible to represent $p(\mathrm{A}|\mathrm{D},\mathrm{Y};\Theta)$ in a closed distribution, we instead compute the following approximation:

$$p(y|a;\mathrm{Y},\mathrm{D},\Theta,\Psi)=\int p\left(y\middle|a;\vec{\mathrm{Y}},\mathrm{A},\Psi\right)p(\mathrm{A}|\mathrm{D},\mathrm{Y};\Theta)\,d\mathrm{A}\approx\frac{1}{\mathrm{K}}\sum_{k=1}^{\mathrm{K}}p\left(y\middle|a;\vec{\mathrm{Y}},\widetilde{\mathrm{A}}^{(k)},\Psi\right)$$

BIGMACS adopts a Gaussian process regression for modelling each $p\left(y\middle|a;\vec{\mathrm{Y}},\widetilde{\mathrm{A}}^{(k)},\Psi\right)$, after considering outliers and estimating regression parameters Ψ. Suppose that we have already done so, i.e., outliers from $\left(\widetilde{\mathrm{A}}^{(k)},\vec{\mathrm{Y}}\right)$ have been discarded and Ψ is given a priori. Then, we have the following variational free energy approximation [Titsias (2009)] of the Gaussian process regression model for each k:

$$p\left(y\middle|a;\vec{\mathrm{Y}},\widetilde{\mathrm{A}}^{(k)},\Psi\right)=\mathcal{N}\left(y\middle|\overline{\mu}^{(k)}(a),\overline{v}^{(k)}(a)+\Lambda^{(k)}(a)\right)$$

, where:

$$\overline{\mu}^{(k)}(a)=\underline{\mu}+\mathbb{K}_{a\underline{\mathrm{A}}}\left(\mathbb{K}_{\underline{\mathrm{A}}\underline{\mathrm{A}}}+\mathbb{K}_{\underline{\mathrm{A}}\widetilde{\mathrm{A}}^{(k)}}\left(\Lambda_{\widetilde{\mathrm{A}}^{(k)}}^{(k)}\right)^{-1}\mathbb{K}_{\widetilde{\mathrm{A}}^{(k)}\underline{\mathrm{A}}}\right)^{-1}\mathbb{K}_{\underline{\mathrm{A}}\widetilde{\mathrm{A}}^{(k)}}\left(\Lambda_{\widetilde{\mathrm{A}}^{(k)}}^{(k)}\right)^{-1}\left(\vec{\mathrm{Y}}-\underline{\mu}\right)$$

$$\overline{v}^{(k)}(a)=\mathbb{K}_{aa}-\mathbb{K}_{a\underline{\mathrm{A}}}\mathbb{K}_{\underline{\mathrm{A}}\underline{\mathrm{A}}}^{-1}\mathbb{K}_{\underline{\mathrm{A}}a}+\mathbb{K}_{a\underline{\mathrm{A}}}\left(\mathbb{K}_{\underline{\mathrm{A}}\underline{\mathrm{A}}}+\mathbb{K}_{\underline{\mathrm{A}}\widetilde{\mathrm{A}}^{(k)}}\left(\Lambda_{\widetilde{\mathrm{A}}^{(k)}}^{(k)}\right)^{-1}\mathbb{K}_{\widetilde{\mathrm{A}}^{(k)}\underline{\mathrm{A}}}\right)^{-1}\mathbb{K}_{\underline{\mathrm{A}}a}$$

Here, $\mathbb{K}_{\mathrm{AB}}$ is a matrix where each entry is the function value of $\mathbb{K}(a,b)$ for $a\in\mathrm{A}$ and $b\in\mathrm{B}$, and Λ_{A} is a diagonal matrix where each diagonal entry is $\Lambda(a)$ for $a\in\mathrm{A}$, for any sets A and B.

The reason why we consider an approximation instead of the exact Gaussian process regression is to reduce the time complexity stemming from the matrix inversion, especially for the case where the size of $\vec{\mathrm{Y}}$ is large.

To define the stack by a single Gaussian model, BIGMACS again approximates $p(y|a;\mathrm{Y},\mathrm{D},\Theta,\Psi)$ based on the moment-matching [Murphy (2012)], as follows, which results in the stack $\mathcal{N}\left(y\middle|\mu(a),\nu(a)\right)$:

$$p(y|a;\mathrm{Y},\mathrm{D},\Theta,\Psi) \approx \frac{1}{\mathrm{K}}\sum_{k=1}^{\mathrm{K}} p\left(y\middle|a;\vec{\mathrm{Y}},\widetilde{\mathrm{A}}^{(k)},\Psi\right) \approx \mathcal{N}\left(y\middle|\mu(a),\nu(a)\right)$$

, where:

$$\mu(a) = \frac{1}{\mathrm{K}}\sum_{k=1}^{\mathrm{K}} \overline{\mu}^{(k)}(a)\,, \qquad \nu(a) = \frac{1}{\mathrm{K}}\sum_{k=1}^{\mathrm{K}} \left(\overline{v}^{(k)}(a) + \Lambda^{(k)}(a) + \left(\overline{\mu}^{(k)}(a) - \mu(a)\right)^2\right)$$

S5.2. Outlier Classification

Because Gaussian process regression is susceptible to outliers, BIGMACS is designed to classify and discard outliers, according to the idea used in [Lee and Lawrence (2019)]. Let $\mathrm{O}^{(k)} = \left\{\mathrm{O}_n^{(k)}\right\}$ be a set of hidden variables that indicate outliers for $\left(\widetilde{\mathrm{A}}^{(k)},\vec{\mathrm{Y}}\right)$, where $\mathrm{O}_n^{(k)} = 1$ if the associated $\vec{\mathrm{Y}}_n$ at $\widetilde{\mathrm{A}}_n^{(k)}$ is considered to be an outlier in the stack, 0 otherwise.

We rigorously define outliers as data that do not follow the stack $\mathcal{N}\left(y\middle|\mu(a),\nu(a)+\Lambda(a)\right)$; instead, outliers are assumed to follow an alternative model g. We also assume that outliers are independent from the inputs given core depths D, i.e., we have the following prior and likelihood for a small positive hyperparameter $\delta > 0$:

$$\mathrm{O}_n^{(k)} \sim_{i.i.d.} Bernoulli(\delta)$$

$$p\left(\vec{\mathrm{Y}}_n\middle|\widetilde{\mathrm{A}}_n^{(k)},\mathrm{O}_n^{(k)}\right) = \begin{cases} \mathcal{N}\left(\vec{\mathrm{Y}}_n\middle|\mu\left(\widetilde{\mathrm{A}}_n^{(k)}\right),\nu\left(\widetilde{\mathrm{A}}_n^{(k)}\right)\right), & \mathrm{O}_n^{(k)} = 0 \\ g\left(\vec{\mathrm{Y}}_n\middle|\widetilde{\mathrm{A}}_n^{(k)}\right), & \mathrm{O}_n^{(k)} = 1 \end{cases}$$

, where g is defined as follows:

$$g(y|a) = \frac{1}{2}\mathcal{N}\left(\vec{\mathrm{Y}}_n \middle| \mu\left(\widetilde{\mathrm{A}}_n^{(k)}\right) + 3\sqrt{\nu\left(\widetilde{\mathrm{A}}_n^{(k)}\right)}, \nu\left(\widetilde{\mathrm{A}}_n^{(k)}\right)\right) + \frac{1}{2}\mathcal{N}\left(\vec{\mathrm{Y}}_n \middle| \mu\left(\widetilde{\mathrm{A}}_n^{(k)}\right) - 3\sqrt{\nu\left(\widetilde{\mathrm{A}}_n^{(k)}\right)}, \nu\left(\widetilde{\mathrm{A}}_n^{(k)}\right)\right)$$

Then, one can easily get the posterior distribution of $\mathrm{O}_n^{(k)}$ as follows:

$$p\left(\mathrm{O}_n^{(k)} = 1 \middle| \widetilde{\mathrm{A}}_n^{(k)}, \vec{\mathrm{Y}}\right) = \frac{\delta \cdot g\left(\vec{\mathrm{Y}}_n \middle| \widetilde{\mathrm{A}}_n^{(k)}\right)}{\delta \cdot g\left(\vec{\mathrm{Y}}_n \middle| \widetilde{\mathrm{A}}_n^{(k)}\right) + (1-\delta)\mathcal{N}\left(\vec{\mathrm{Y}}_n \middle| \mu\left(\widetilde{\mathrm{A}}_n^{(k)}\right), \nu\left(\widetilde{\mathrm{A}}_n^{(k)}\right)\right)}$$

To reflect the ambiguity of outliers, BIGMACS *samples* outlier indicators from the above posterior for each k, instead of classifying them as outliers if $p\left(\mathrm{O}_n^{(k)} = 1 \middle| \widetilde{\mathrm{A}}_n^{(k)}, \vec{\mathrm{Y}}\right) > 0.5$.

S5.3. Kernel Hyperparameter Estimation

From now on, we assume that each $\left(\widetilde{\mathrm{A}}_n^{(k)}, \vec{\mathrm{Y}}\right)$ excludes sampled outliers. To estimate the kernel covariance function $\mathbb{K}$, we first fix the type of function to the OU kernel and just estimate its hyperparameters. The estimated kernel hyperparameters are supposed to be shared throughout the samples and to maximize the following objective function for the variational free energy approximation:

$$\mathcal{L} = \log \mathcal{N}\left(\vec{\mathrm{Y}} \middle| \underline{\mu}, \Lambda_{\mathrm{A}} + \mathbb{K}_{\mathrm{A}\underline{\mathrm{A}}}\mathbb{K}_{\underline{\mathrm{A}}\underline{\mathrm{A}}}^{-1}\mathbb{K}_{\underline{\mathrm{A}}\mathrm{A}}\right) - \frac{1}{2} \cdot trace\left(\Lambda_{\mathrm{A}}^{-1}\left(\mathbb{K}_{\mathrm{AA}} - \mathbb{K}_{\mathrm{A}\underline{\mathrm{A}}}\mathbb{K}_{\underline{\mathrm{A}}\underline{\mathrm{A}}}^{-1}\mathbb{K}_{\underline{\mathrm{A}}\mathrm{A}}\right)\right)$$

Because A is a hidden variable (age paths) and Λ is defined by k, BIGMACS uses a stochastic gradient ascent algorithm that feeds $\widetilde{\mathrm{A}}^{(k)}$ and $\Lambda^{(k)}$ to A and Λ above, respectively, for a randomly chosen k at each iteration. To deal with the matrix inversion of $\Lambda_{\mathrm{A}} +$

$\mathbb{K}_{\mathrm{A}\underline{\mathrm{A}}}\mathbb{K}_{\underline{\mathrm{A}\mathrm{A}}}^{-1}\mathbb{K}_{\underline{\mathrm{A}}\mathrm{A}}$, we use the following Woodbury matrix identity [Max (1950)] to convert it more practically:

$$\left(\Lambda_{\mathrm{A}} + \mathbb{K}_{\mathrm{A}\underline{\mathrm{A}}}\mathbb{K}_{\underline{\mathrm{A}\mathrm{A}}}^{-1}\mathbb{K}_{\underline{\mathrm{A}}\mathrm{A}}\right)^{-1} = \Lambda_{\mathrm{A}}^{-1} - \Lambda_{\mathrm{A}}^{-1}\mathbb{K}_{\mathrm{A}\underline{\mathrm{A}}}\left(\mathbb{K}_{\underline{\mathrm{A}\mathrm{A}}} + \mathbb{K}_{\underline{\mathrm{A}}\mathrm{A}}\Lambda_{\mathrm{A}}^{-1}\mathbb{K}_{\mathrm{A}\underline{\mathrm{A}}}\right)^{-1}\mathbb{K}_{\underline{\mathrm{A}}\mathrm{A}}\Lambda_{\mathrm{A}}^{-1}$$

S5.4. Heteroscedastic Variance Construction

BIGMACS models observational variance as a continuous function over ages (heterscedastic Gaussian process regression). BIGMACS adopts the following close-form update [Lee and Lawrence (2019)]:

$$\Lambda^{(k)}(a) = \sum\left(\left(\vec{\mathrm{Y}}_n - \overline{\mu}^{(k)}\left(\widetilde{\mathrm{A}}_n^{(k)}\right)\right)^2 + \overline{v}^{(k)}\left(\widetilde{\mathrm{A}}_n^{(k)}\right)\right)\mathcal{K}_h\left(a - \widetilde{\mathrm{A}}_n^{(k)}\right)\Big/\sum\mathcal{K}_h\left(a - \widetilde{\mathrm{A}}_n^{(k)}\right)$$

, where $\mathcal{K}$ and $h > 0$ are a density kernel and a bandwidth hyperparameter that can be tuned as a K-nearest neighborhood bandwidth [Langrene and Warin (2019)], respectively.

S6. Time Complexity

All age models and stacks presented here were constructed on a standard desktop machine. However, longer stacks constructed from a large number of high resolution cores may have run times that require a computing cluster. Here we provide time complexity equations to estimate time complexities of future runs.

Age models are constructed in parallel and the time complexity depends on the number of input cores (L) and the number of available CPU processors (C). During age model construction, parameter values are estimated first and then ages are sampled. Parameter estimation requires the particle smoothing algorithm, the Metropolis Hastings algorithm, and the Baum-Welch Expectation Maximization algorithm. Once parameters are

estimated, ages are sampled with the particle smoothing algorithm and Metropolis-Hastings algorithms. Particle smoothing requires two steps: a forward step and a backward step. During the forward step the time complexity is quadratic to the number of particles (P, default is 100) and linear to the number of proxy observations (N). The backward step is linear to the number of particles, proxy observations, and age model samples (M_0, default is 100). The Metropolis Hastings algorithm has a time complexity linear to the number of proxy observations, steps until the burn-in phase (B, default is 500) and age model samples (M_0). The total time complexity for a single iteration to learn parameter values is equal to $\mathcal{O}\left(\frac{L}{C}(P^2N + PNM_0 + BNM_0)\right)$. Once the parameters are estimated, ages are sampled. If the number of age model samples is set to M (the default is 1000) and the maximum number of iterations in parameter estimation is equal to R (default is 10), the total time complexity for age model construction is equal to $\mathcal{O}\left(\frac{L}{C}R(P^2N + PNM_0 + BNM_0) + \frac{L}{C}(P^2N + PNM + BNM)\right)$. The multiproxy age model for GIK13289-2 (which has 30 $\delta^{18}O$ data points and 12 radiocarbon ages) took approximately 86 seconds to run on a standard desktop machine.

Stack construction iterates between an age model construction step and a stack updating step. The latter consists of kernel parameter estimation, $\delta^{18}O$ outlier classification, heteroscedastic variance estimation and the Gaussian process regression. Kernel parameter estimation requires a fixed number of iterations (S, default is 3000), with each iteration having a time complexity quadratic to the number of induced pseudo-inputs (fixed to N_0, sampled every 0.5 kyr, see S5 for details) and linear to the number of proxy observations. Time complexity for outlier classification is linear to the number of age model samples and proxy observations. Heteroscedastic variance estimation requires computations

proportional to the number of age model samples and quadratic to the number of total proxy observations. Finally, the Gaussian process regression has a time complexity linear to the number of sampled age paths, total proxy observations and the length of the stack (K), and quadratic to the number of induced pseudo-inputs. Therefore, the total time complexity for one stack updating step is $\mathcal{O}\left(\mathrm{T}(\mathrm{SN}_0^2\mathrm{LN} + \mathrm{LNM}_0 + \mathrm{L}^2\mathrm{N}^2\mathrm{M}_0 + \mathrm{N}_0^2\mathrm{LNM}_0\mathrm{K})\right)$.

The stack construction algorithm includes A (default is 5) stack updating steps, and each update includes a new set of age models (i.e., an age model construction step). Thus the total time complexity to construct a stack is equal to $\mathcal{O}\left(\mathrm{A}\left(\frac{\mathrm{L}}{\mathrm{C}}R(\mathrm{P}^2\mathrm{N} + \mathrm{PNM}_0 + \mathrm{BNM}_0) + \mathrm{T}(\mathrm{SN}_0^2\mathrm{LN} + \mathrm{LNM}_0 + \mathrm{L}^2\mathrm{N}^2\mathrm{M}_0 + \mathrm{N}_0^2\mathrm{LNM}_0\mathrm{K})\right)\right)$. The DNEA stack (which contains 6 cores, 2,112 δ^{18}O data points, 150 radiocarbon ages, and extends to 150 kyr) has a total run time of 1.8 hours.

References

1. Ahn, S., Khider, D., Lisiecki, L. E., and Lawrence, C. E.: A probabilistic Pliocene–Pleistocene stack of benthic δ18O using a profile hidden Markov model, Dynamics and Statistics of the Climate System, 2, https://doi.org/10.1093/climsys/dzx002, 2017.
2. Andrés Christen, J. and Pérez E, S.: A New Robust Statistical Model for Radiocarbon Data, Radiocarbon, 51, 1047–1059, https://doi.org/10.1017/S003382220003410X, 2009.
3. Bard, E., Fairbanks, R., Arnold, M., Maurice, P., Duprat, J., Moyes, J., and Duplessy, J.-C.: Sea-level estimates during the last deglaciation based on δ18O and accelerator mass spectrometry 14C ages measured in Globigerina bulloides, Quaternary Research, 31, 381–391, https://doi.org/10.1016/0033-5894(89)90045-8, 1989.
4. Bard, E., Rostek, F., and Ménot-Combes, G.: Radiocarbon calibration beyond 20,000 14C yr B.P. by means of planktonic foraminifera of the Iberian Margin, Quaternary Research, 61, 204–214, https://doi.org/10.1016/j.yqres.2003.11.006, 2004.
5. Bard, E., Ménot, G., Rostek, F., Licari, L., Böning, P., Edwards, R. L., Cheng, H., Wang, Y., and Heaton, T. J.: Radiocarbon Calibration/Comparison Records Based on Marine Sediments from the Pakistan and Iberian Margins, Radiocarbon, 55, 1999–2019, https://doi.org/10.2458/azu_js_rc.55.17114, 2013.
6. Barker, S. and Diz, P.: Timing of the descent into the last Ice Age determined by the bipolar seesaw, Paleoceanography, 29, 489–507, https://doi.org/10.1002/2014PA002623, 2014.
7. Blaauw, M.: Methods and code for 'classical' age-modelling of radiocarbon sequences, Quaternary Geochronology, 5, 512–518, https://doi.org/10.1016/j.quageo.2010.01.002, 2010a.
8. Blaauw, M.: Methods and code for 'classical' age-modelling of radiocarbon sequences, Quaternary Geochronology, 5, 512–518, https://doi.org/10.1016/j.quageo.2010.01.002, 2010b.
9. Blaauw, M. and Christen, J. A.: Radiocarbon peat chronologies and environmental change, Journal of the Royal Statistical Society: Series C (Applied Statistics), 54, 805–816, https://doi.org/10.1111/j.1467-9876.2005.00516.x, 2005.
10. Blaauw, M. and Christen, J. A.: Flexible paleoclimate age-depth models using an autoregressive gamma process, Bayesian Anal., 6, https://doi.org/10.1214/11-BA618, 2011.
11. Brázdil, R., Dobrovolný, P., Trnka, M., Řezníčková, L., Dolák, L., and Kotyza, O.: Extreme droughts and human responses to them: the Czech Lands in the pre-instrumental period, Clim. Past, 15, 1–24, https://doi.org/10.5194/cp-15-1-2019, 2019.
12. Bronk Ramsey, C.: Radiocarbon Calibration and Analysis of Stratigraphy: The OxCal Program, Radiocarbon, 37, 425–430, https://doi.org/10.1017/S0033822200030903, 1995.
13. Bronk Ramsey, C.: Development of the Radiocarbon Calibration Program, Radiocarbon, 43, 355–363, https://doi.org/10.1017/S0033822200038212, 2001.
14. Bronk Ramsey, C.: Dealing with Outliers and Offsets in Radiocarbon Dating, Radiocarbon, 51, 1023–1045, https://doi.org/10.1017/S0033822200034093, 2009.
15. Buck, C. E. and Christen, J. A.: Making Complex Radiocarbon Calibration Software More Accessible: a New Approach?, 3, n.d.
16. Butzin, M., Köhler, P., and Lohmann, G.: Marine radiocarbon reservoir age simulations for the past 50,000 years: Marine Radiocarbon Simulations, Geophys. Res. Lett., 44, 8473–8480, https://doi.org/10.1002/2017GL074688, 2017.
17. Butzin, M., Heaton, T. J., Köhler, P., and Lohmann, G.: A Short Note on Marine Reservoir Age Simulations Used in IntCal20, Radiocarbon, 62, 865–871, https://doi.org/10.1017/RDC.2020.9, 2020.
18. Channell, J. E. T., Xuan, C., and Hodell, D. A.: Stacking paleointensity and oxygen isotope data for the last 1.5 Myr (PISO-1500), Earth and Planetary Science Letters, 283, 14–23, https://doi.org/10.1016/j.epsl.2009.03.012, 2009.
19. Christen, J. A.: Summarizing a Set of Radiocarbon Determinations: A Robust Approach, Journal of the Royal Statistical Society: Series C (Applied Statistics), 43, 489–503, https://doi.org/10.2307/2986273, 1994.
20. Christen, J. A. and E, S. P.: A New Robust Statistical Model for Radiocarbon Data, Radiocarbon, 51, 1047–1059, https://doi.org/10.1017/S003382220003410X, 2009.
21. Collins, J. A., Schefuß, E., Heslop, D., Mulitza, S., Prange, M., Zabel, M., Tjallingii, R., Dokken, T. M., Huang, E., Mackensen, A., Schulz, M., Tian, J., Zarriess, M., and Wefer, G.: Interhemispheric

symmetry of the tropical African rainbelt over the past 23,000 years, Nature Geosci, 4, 42–45, https://doi.org/10.1038/ngeo1039, 2011.
22. deMenocal, P., Ortiz, J., Guilderson, T., Adkins, J., Sarnthein, M., Baker, L., and Yarusinsky, M.: Abrupt onset and termination of the African Humid Period:: rapid climate responses to gradual insolation forcing, Quaternary Science Reviews, 19, 347–361, https://doi.org/10.1016/S0277-3791(99)00081-5, 2000.
23. Dempster, A. P., Laird, N. M., and Rubin, D. B.: Maximum Likelihood from Incomplete Data Via the EM Algorithm, Journal of the Royal Statistical Society: Series B (Methodological), 39, 1–22, https://doi.org/10.1111/j.2517-6161.1977.tb01600.x, 1977a.
24. Dempster, A. P., Laird, N. M., and Rubin, D. B.: Maximum Likelihood from Incomplete Data Via the EM Algorithm, Journal of the Royal Statistical Society: Series B (Methodological), 39, 1–22, https://doi.org/10.1111/j.2517-6161.1977.tb01600.x, 1977b.
25. DeVries, T. and Primeau, F.: Dynamically and Observationally Constrained Estimates of Water-Mass Distributions and Ages in the Global Ocean, Journal of Physical Oceanography, 41, 2381–2401, https://doi.org/10.1175/JPO-D-10-05011.1, 2011.
26. Doucet, A., de Freitas, N., and Gordon, N.: Sequential Monte Carlo Methods in Practice, 12, n.d.
27. Durbin, R., Eddy, S. R., Krogh, A., and Mitchison, G.: Biological Sequence Analysis: Probabilistic Models of Proteins and Nucleic Acids, Cambridge University Press, 332 pp., 1998.
28. Gebbie, G.: Tracer transport timescales and the observed Atlantic-Pacific lag in the timing of the Last Termination, Paleoceanography, 27, https://doi.org/10.1029/2011PA002273, 2012.
29. Gebbie, G. and Huybers, P.: Total Matrix Intercomparison: A Method for Determining the Geometry of Water-Mass Pathways, Journal of Physical Oceanography, 40, 1710–1728, https://doi.org/10.1175/2010JPO4272.1, 2010.
30. Gebbie, G. and Huybers, P.: The Mean Age of Ocean Waters Inferred from Radiocarbon Observations: Sensitivity to Surface Sources and Accounting for Mixing Histories, Journal of Physical Oceanography, 42, 291–305, https://doi.org/10.1175/JPO-D-11-043.1, 2012.
31. Grootes, P. M. and Stuiver, M.: Oxygen 18/16 variability in Greenland snow and ice with 10−3- to 105-year time resolution, Journal of Geophysical Research: Oceans, 102, 26455–26470, https://doi.org/10.1029/97JC00880, 1997.
32. Haslett, J. and Parnell, A.: A simple monotone process with application to radiocarbon-dated depth chronologies, Journal of the Royal Statistical Society: Series C (Applied Statistics), 57, 399–418, https://doi.org/10.1111/j.1467-9876.2008.00623.x, 2008.
33. Hastings, W. K.: Monte Carlo sampling methods using Markov chains and their applications, 13, n.d.
34. Heaton, T. J., Bard, E., and Hughen, K. A.: Elastic Tie-Pointing—Transferring Chronologies between Records via a Gaussian Process, Radiocarbon, 55, 1975–1997, https://doi.org/10.2458/azu_js_rc.55.17777, 2013.
35. Heaton, T. J., Köhler, P., Butzin, M., Bard, E., Reimer, R. W., Austin, W. E. N., Bronk Ramsey, C., Grootes, P. M., Hughen, K. A., Kromer, B., Reimer, P. J., Adkins, J., Burke, A., Cook, M. S., Olsen, J., and Skinner, L. C.: Marine20—The Marine Radiocarbon Age Calibration Curve (0–55,000 cal BP), Radiocarbon, 62, 779–820, https://doi.org/10.1017/RDC.2020.68, 2020a.
36. Heaton, T. J., Blaauw, M., Blackwell, P. G., Ramsey, C. B., Reimer, P. J., and Scott, E. M.: The IntCal20 Approach to Radiocarbon Calibration Curve Construction: A New Methodology Using Bayesian Splines and Errors-in-Variables, Radiocarbon, 62, 821–863, https://doi.org/10.1017/RDC.2020.46, 2020b.
37. Heaton, T. J., Bard, E., Bronk Ramsey, C., Butzin, M., Köhler, P., Muscheler, R., Reimer, P. J., and Wacker, L.: Radiocarbon: A key tracer for studying Earth's dynamo, climate system, carbon cycle, and Sun, Science, 374, eabd7096, https://doi.org/10.1126/science.abd7096, 2021.
38. Hemming, S. R.: Heinrich events: Massive late Pleistocene detritus layers of the North Atlantic and their global climate imprint, Reviews of Geophysics, 42, https://doi.org/10.1029/2003RG000128, 2004.
39. Howe, J. N. W., Piotrowski, A. M., and Rennie, V. C. F.: Abyssal origin for the early Holocene pulse of unradiogenic neodymium isotopes in Atlantic seawater, Geology, 44, 831–834, https://doi.org/10.1130/G38155.1, 2016.
40. Hughen, K., Southon, J., Lehman, S., Bertrand, C., and Turnbull, J.: Marine-derived 14C calibration and activity record for the past 50,000 years updated from the Cariaco Basin, Quaternary Science Reviews, 25, 3216–3227, https://doi.org/10.1016/j.quascirev.2006.03.014, 2006.

41. Hüls, M. and Zahn, R.: Millennial-scale sea surface temperature variability in the western tropical North Atlantic from planktonic foraminiferal census counts, Paleoceanography, 15, 659–678, https://doi.org/10.1029/1999PA000462, 2000.
42. Huybers, P. and Wunsch, C.: A depth-derived Pleistocene age model: Uncertainty estimates, sedimentation variability, and nonlinear climate change, Paleoceanography, 19, https://doi.org/10.1029/2002PA000857, 2004.
43. Key, R. M., Kozyr, A., Sabine, C. L., Lee, K., Wanninkhof, R., Bullister, J. L., Feely, R. A., Millero, F. J., Mordy, C., and Peng, T.-H.: A global ocean carbon climatology: Results from Global Data Analysis Project (GLODAP): GLOBAL OCEAN CARBON CLIMATOLOGY, Global Biogeochem. Cycles, 18, n/a-n/a, https://doi.org/10.1029/2004GB002247, 2004.
44. Khider, D., Ahn, S., Lisiecki, L. E., Lawrence, C. E., and Kienast, M.: The Role of Uncertainty in Estimating Lead/Lag Relationships in Marine Sedimentary Archives: A Case Study From the Tropical Pacific, Paleoceanography, 32, 1275–1290, https://doi.org/10.1002/2016PA003057, 2017.
45. Klaas, M., Briers, M., de Freitas, N., Doucet, A., Maskell, S., and Lang, D.: Fast particle smoothing: if I had a million particles, in: Proceedings of the 23rd international conference on Machine learning - ICML '06, the 23rd international conference, Pittsburgh, Pennsylvania, 481–488, https://doi.org/10.1145/1143844.1143905, 2006.
46. Knaack, J.-J. and Sarnthein, M.: Stable isotopes of foraminifera of ODP Hole 108-658C, https://doi.org/10.1594/PANGAEA.227736, 2005.
47. Labeyrie, L., Waelbroeck, C., Cortijo, E., Michel, E., and Duplessy, J.-C.: Changes in deep water hydrology during the Last Deglaciation, Comptes Rendus Geoscience, 337, 919–927, https://doi.org/10.1016/j.crte.2005.05.010, 2005.
48. Langrené, N. and Warin, X.: Fast and Stable Multivariate Kernel Density Estimation by Fast Sum Updating, Journal of Computational and Graphical Statistics, 28, 596–608, https://doi.org/10.1080/10618600.2018.1549052, 2019a.
49. Langrené, N. and Warin, X.: Fast and Stable Multivariate Kernel Density Estimation by Fast Sum Updating, Journal of Computational and Graphical Statistics, 28, 596–608, https://doi.org/10.1080/10618600.2018.1549052, 2019b.
50. Lee, T. and Lawrence, C. E.: Heteroscedastic Gaussian Process Regression on the Alkenone over Sea Surface Temperatures, https://doi.org/10.5065/y82j-f154, 2019.
51. Lin, L., Khider, D., Lisiecki, L. E., and Lawrence, C. E.: Probabilistic sequence alignment of stratigraphic records, Paleoceanography, 29, 976–989, https://doi.org/10.1002/2014PA002713, 2014.
52. Lisiecki, L. E. and Lisiecki, P. A.: Application of dynamic programming to the correlation of paleoclimate records: DYNAMIC PROGRAMMING SIGNAL CORRELATION, Paleoceanography, 17, 1-1-1–12, https://doi.org/10.1029/2001PA000733, 2002.
53. Lisiecki, L. E. and Raymo, M. E.: A Pliocene-Pleistocene stack of 57 globally distributed benthic δ18O records, Paleoceanography, 20, https://doi.org/10.1029/2004PA001071, 2005.
54. Lisiecki, L. E. and Raymo, M. E.: Diachronous benthic δ18O responses during late Pleistocene terminations, Paleoceanography, 24, https://doi.org/10.1029/2009PA001732, 2009.
55. Lisiecki, L. E. and Stern, J. V.: Regional and global benthic δ^{18}O stacks for the last glacial cycle: Last Glacial Cycle Benthic δ^{18}O, Paleoceanography, 31, 1368–1394, https://doi.org/10.1002/2016PA003002, 2016.
56. Lougheed, B. C. and Obrochta, S. P.: MatCal: Open Source Bayesian ^{14}C Age Calibration in Matlab, JORS, 4, 42, https://doi.org/10.5334/jors.130, 2016.
57. Lougheed, B. C. and Obrochta, S. P.: A Rapid, Deterministic Age-Depth Modeling Routine for Geological Sequences With Inherent Depth Uncertainty, Paleoceanography and Paleoclimatology, 34, 122–133, https://doi.org/10.1029/2018PA003457, 2019.
58. Lund, D. C., Tessin, A. C., Hoffman, J. L., and Schmittner, A.: Southwest Atlantic water mass evolution during the last deglaciation, Paleoceanography, 30, 477–494, https://doi.org/10.1002/2014PA002657, 2015.
59. Marchitto, T. M., Curry, W. B., Lynch-Stieglitz, J., Bryan, S. P., Cobb, K. M., and Lund, D. C.: Improved oxygen isotope temperature calibrations for cosmopolitan benthic foraminifera, Geochimica et Cosmochimica Acta, 130, 1–11, https://doi.org/10.1016/j.gca.2013.12.034, 2014.
60. Martino, L., Read, J., and Luengo, D.: Independent Doubly Adaptive Rejection Metropolis Sampling Within Gibbs Sampling, IEEE Transactions on Signal Processing, 63, 3123–3138, https://doi.org/10.1109/TSP.2015.2420537, 2015a.

61. Martino, L., Read, J., and Luengo, D.: Independent Doubly Adaptive Rejection Metropolis Sampling Within Gibbs Sampling, IEEE Transactions on Signal Processing, 63, 3123–3138, https://doi.org/10.1109/TSP.2015.2420537, 2015b.
62. Metropolis, N., Rosenbluth, A. W., and Rosenbluth, M. N.: Equation of State Calculations by Fast Computing Machines, 7, n.d.
63. Murphy, K. P.: Machine learning: a probabilistic perspective, MIT Press, Cambridge, MA, 1067 pp., 2012.
64. Muschitiello, F., O'Regan, M., Martens, J., West, G., Gustafsson, Ö., and Jakobsson, M.: A new 30 000-year chronology for rapidly deposited sediments on the Lomonosov Ridge using bulk radiocarbon dating and probabilistic stratigraphic alignment, Geochronology, 2, 81–91, https://doi.org/10.5194/gchron-2-81-2020, 2020.
65. Oppo, D. W., Gebbie, G., Huang, K.-F., Curry, W. B., Marchitto, T. M., and Pietro, K. R.: Data Constraints on Glacial Atlantic Water Mass Geometry and Properties, Paleoceanography and Paleoclimatology, 33, 1013–1034, https://doi.org/10.1029/2018PA003408, 2018.
66. Pailler, D. and Bard, E.: High frequency palaeoceanographic changes during the past 140 000 yr recorded by the organic matter in sediments of the Iberian Margin, Palaeogeography, Palaeoclimatology, Palaeoecology, 181, 431–452, https://doi.org/10.1016/S0031-0182(01)00444-8, 2002.
67. Parnell, A. C., Haslett, J., Allen, J. R. M., Buck, C. E., and Huntley, B.: A flexible approach to assessing synchroneity of past events using Bayesian reconstructions of sedimentation history, Quaternary Science Reviews, 27, 1872–1885, https://doi.org/10.1016/j.quascirev.2008.07.009, 2008.
68. Peters, G.: Markov Chain Monte Carlo: stochastic simulation for Bayesian inference (2nd edn). Dani Gamerman and Hedibert F. Lopes, Chapman & Hall/CRC, Boca Raton, FL, 2006. No. of pages: xvii +323. Price: $69.95. ISBN10: 1-58488-587-4, ISBN13: 978-1-58488-587-0, Statistics in Medicine, 27, 3213–3214, https://doi.org/10.1002/sim.3240, 2008.
69. Pisias, N. G. and Shackleton, N. J.: Modelling the global climate response to orbital forcing and atmospheric carbon dioxide changes, Nature, 310, 757–759, https://doi.org/10.1038/310757a0, 1984.
70. Pöppelmeier, F., Blaser, P., Gutjahr, M., Jaccard, S. L., Frank, M., Max, L., and Lippold, J.: Northern-sourced water dominated the Atlantic Ocean during the Last Glacial Maximum, Geology, 48, 826–829, https://doi.org/10.1130/G47628.1, 2020.
71. Portilho-Ramos, R. C., Chiessi, C. M., Zhang, Y., Mulitza, S., Kucera, M., Siccha, M., Prange, M., and Paul, A.: Coupling of equatorial Atlantic surface stratification to glacial shifts in the tropical rainbelt, Sci Rep, 7, 1561, https://doi.org/10.1038/s41598-017-01629-z, 2017.
72. Quinonero-Candela, J., Ramussen, C. E., and Williams, C. K. I.: Approximation Methods for Gaussian Process Regression, 24, n.d.
73. Rabiner, L. R.: A tutorial on hidden Markov models and selected applications in speech recognition, Proceedings of the IEEE, 77, 257–286, https://doi.org/10.1109/5.18626, 1989.
74. Ramsey, C. B.: Deposition models for chronological records, Quaternary Science Reviews, 27, 42–60, https://doi.org/10.1016/j.quascirev.2007.01.019, 2008.
75. Ramsey, C. B. and Lee, S.: Recent and Planned Developments of the Program OxCal, Radiocarbon, 55, 720–730, https://doi.org/10.1017/S0033822200057878, 2013.
76. Reimer, P. J. and Reimer, R. W.: A Marine Reservoir Correction Database and On-Line Interface, Radiocarbon, 43, 461–463, https://doi.org/10.1017/S0033822200038339, 2001a.
77. Reimer, P. J. and Reimer, R. W.: A Marine Reservoir Correction Database and On-Line Interface, Radiocarbon, 43, 461–463, https://doi.org/10.1017/S0033822200038339, 2001b.
78. Reimer, P. J., Bard, E., Bayliss, A., Beck, J. W., Blackwell, P. G., Ramsey, C. B., Buck, C. E., Cheng, H., Edwards, R. L., Friedrich, M., Grootes, P. M., Guilderson, T. P., Haflidason, H., Hajdas, I., Hatté, C., Heaton, T. J., Hoffmann, D. L., Hogg, A. G., Hughen, K. A., Kaiser, K. F., Kromer, B., Manning, S. W., Niu, M., Reimer, R. W., Richards, D. A., Scott, E. M., Southon, J. R., Staff, R. A., Turney, C. S. M., and Plicht, J. van der: IntCal13 and Marine13 Radiocarbon Age Calibration Curves 0–50,000 Years cal BP, Radiocarbon, 55, 1869–1887, https://doi.org/10.2458/azu_js_rc.55.16947, 2013.
79. Reimer, P. J., Austin, W. E. N., Bard, E., Bayliss, A., Blackwell, P. G., Bronk Ramsey, C., Butzin, M., Cheng, H., Edwards, R. L., Friedrich, M., Grootes, P. M., Guilderson, T. P., Hajdas, I., Heaton, T. J., Hogg, A. G., Hughen, K. A., Kromer, B., Manning, S. W., Muscheler, R., Palmer, J. G., Pearson, C., van der Plicht, J., Reimer, R. W., Richards, D. A., Scott, E. M., Southon, J. R., Turney, C. S. M., Wacker, L., Adolphi, F., Büntgen, U., Capano, M., Fahrni, S. M., Fogtmann-Schulz, A., Friedrich, R.,

Köhler, P., Kudsk, S., Miyake, F., Olsen, J., Reinig, F., Sakamoto, M., Sookdeo, A., and Talamo, S.: The IntCal20 Northern Hemisphere Radiocarbon Age Calibration Curve (0–55 cal kBP), Radiocarbon, 62, 725–757, https://doi.org/10.1017/RDC.2020.41, 2020.
80. Sarnthein, M., Winn, K., Jung, S. J. A., Duplessy, J.-C., Labeyrie, L., Erlenkeuser, H., and Ganssen, G.: Changes in East Atlantic Deepwater Circulation over the last 30,000 years: Eight time slice reconstructions, Paleoceanography, 9, 209–267, https://doi.org/10.1029/93PA03301, 1994.
81. Shackleton, N.: Oxygen Isotope Analyses and Pleistocene Temperatures Re-assessed, Nature, 215, 15–17, https://doi.org/10.1038/215015a0, 1967.
82. Shackleton, N. J., Hall, M. A., and Vincent, E.: Phase relationships between millennial-scale events 64,000–24,000 years ago, Paleoceanography, 15, 565–569, https://doi.org/10.1029/2000PA000513, 2000.
83. Shackleton, N. J., Fairbanks, R. G., Chiu, T., and Parrenin, F.: Absolute calibration of the Greenland time scale: implications for Antarctic time scales and for Δ14C, Quaternary Science Reviews, 23, 1513–1522, https://doi.org/10.1016/j.quascirev.2004.03.006, 2004.
84. Sikes, E. L., Allen, K. A., and Lund, D. C.: Enhanced δ13C and δ18O Differences Between the South Atlantic and South Pacific During the Last Glaciation: The Deep Gateway Hypothesis, Paleoceanography, 32, 1000–1017, https://doi.org/10.1002/2017PA003118, 2017.
85. Skinner, L. C. and Shackleton, N. J.: An Atlantic lead over Pacific deep-water change across Termination I: implications for the application of the marine isotope stage stratigraphy, Quaternary Science Reviews, 24, 571–580, https://doi.org/10.1016/j.quascirev.2004.11.008, 2005.
86. Skinner, L. C., Shackleton, N. J., and Elderfield, H.: Millennial-scale variability of deep-water temperature and δ18Odw indicating deep-water source variations in the Northeast Atlantic, 0–34 cal. ka BP, Geochemistry, Geophysics, Geosystems, 4, https://doi.org/10.1029/2003GC000585, 2003.
87. Skinner, L. C., Waelbroeck, C., Scrivner, A. E., and Fallon, S. J.: Radiocarbon evidence for alternating northern and southern sources of ventilation of the deep Atlantic carbon pool during the last deglaciation, Proceedings of the National Academy of Sciences, 111, 5480–5484, https://doi.org/10.1073/pnas.1400668111, 2014a.
88. Skinner, L. C., Waelbroeck, C., Scrivner, A. E., and Fallon, S. J.: Radiocarbon evidence for alternating northern and southern sources of ventilation of the deep Atlantic carbon pool during the last deglaciation, Proceedings of the National Academy of Sciences, 111, 5480–5484, https://doi.org/10.1073/pnas.1400668111, 2014b.
89. Skinner, L. C., Muschitiello, F., and Scrivner, A. E.: Marine Reservoir Age Variability Over the Last Deglaciation: Implications for Marine CarbonCycling and Prospects for Regional Radiocarbon Calibrations, Paleoceanography and Paleoclimatology, 34, 1807–1815, https://doi.org/10.1029/2019PA003667, 2019.
90. Skinner, L. C., Freeman, E., Hodell, D., Waelbroeck, C., Vazquez Riveiros, N., and Scrivner, A. E.: Atlantic Ocean Ventilation Changes Across the Last Deglaciation and Their Carbon Cycle Implications, Paleoceanography and Paleoclimatology, 36, e2020PA004074, https://doi.org/10.1029/2020PA004074, 2021.
91. Stern, J. V. and Lisiecki, L. E.: North Atlantic circulation and reservoir age changes over the past 41,000 years, Geophysical Research Letters, 40, 3693–3697, https://doi.org/10.1002/grl.50679, 2013.
92. Stern, J. V. and Lisiecki, L. E.: Termination 1 timing in radiocarbon-dated regional benthic δ18O stacks, Paleoceanography, 29, 1127–1142, https://doi.org/10.1002/2014PA002700, 2014.
93. Stuiver, M. and Reimer, P. J.: Extended ^{14}C Data Base and Revised CALIB 3.0 ^{14}C Age Calibration Program, Radiocarbon, 35, 215–230, https://doi.org/10.1017/S0033822200013904, 1993.
94. Titsias, M. K.: Variational Learning of Inducing Variables in Sparse Gaussian Processes, 8, n.d.
95. Tjallingii, R., Claussen, M., Stuut, J.-B. W., Fohlmeister, J., Jahn, A., Bickert, T., Lamy, F., and Röhl, U.: Coherent high- and low-latitude control of the northwest African hydrological balance, Nature Geosci, 1, 670–675, https://doi.org/10.1038/ngeo289, 2008.
96. Voigt, I., Cruz, A. P. S., Mulitza, S., Chiessi, C. M., Mackensen, A., Lippold, J., Antz, B., Zabel, M., Zhang, Y., Barbosa, C. F., and Tisserand, A. A.: Variability in mid-depth ventilation of the western Atlantic Ocean during the last deglaciation, Paleoceanography, 32, 948–965, https://doi.org/10.1002/2017PA003095, 2017.
97. Waelbroeck, C., Duplessy, J.-C., Michel, E., Labeyrie, L., Paillard, D., and Duprat, J.: The timing of the last deglaciation in North Atlantic climate records, Nature, 412, 724–727, https://doi.org/10.1038/35089060, 2001.

98. Waelbroeck, C., Skinner, L. C., Labeyrie, L., Duplessy, J.-C., Michel, E., Vazquez Riveiros, N., Gherardi, J.-M., and Dewilde, F.: The timing of deglacial circulation changes in the Atlantic, Paleoceanography, 26, https://doi.org/10.1029/2010PA002007, 2011.
99. Waelbroeck, C., Lougheed, B. C., Vazquez Riveiros, N., Missiaen, L., Pedro, J., Dokken, T., Hajdas, I., Wacker, L., Abbott, P., Dumoulin, J.-P., Thil, F., Eynaud, F., Rossignol, L., Fersi, W., Albuquerque, A. L., Arz, H., Austin, W. E. N., Came, R., Carlson, A. E., Collins, J. A., Dennielou, B., Desprat, S., Dickson, A., Elliot, M., Farmer, C., Giraudeau, J., Gottschalk, J., Henderiks, J., Hughen, K., Jung, S., Knutz, P., Lebreiro, S., Lund, D. C., Lynch-Stieglitz, J., Malaizé, B., Marchitto, T., Martínez-Méndez, G., Mollenhauer, G., Naughton, F., Nave, S., Nürnberg, D., Oppo, D., Peck, V., Peeters, F. J. C., Penaud, A., Portilho-Ramos, R. da C., Repschläger, J., Roberts, J., Rühlemann, C., Salgueiro, E., Sanchez Goni, M. F., Schönfeld, J., Scussolini, P., Skinner, L. C., Skonieczny, C., Thornalley, D., Toucanne, S., Rooij, D. V., Vidal, L., Voelker, A. H. L., Wary, M., Weldeab, S., and Ziegler, M.: Consistently dated Atlantic sediment cores over the last 40 thousand years, Sci Data, 6, 165, https://doi.org/10.1038/s41597-019-0173-8, 2019.

III. Quantifying Benthic $\delta^{18}O$ Lags Across Termination 1: A Probabilistic Approach Based on Radiocarbon and Benthic $\delta^{18}O$ Chronologies

Abstract

Temporal offsets ("lags") between benthic $\delta^{18}O$ ($\delta^{18}O_b$) signals in different locations are not only a source of age model uncertainty during $\delta^{18}O_b$ stratigraphic alignment but also provide an opportunity to improve reconstructions of deep ocean circulation change during Termination 1 (T1). While methods based on the visual identification of identical $\delta^{18}O_b$ features have previously been used to estimate lags, here we present a novel method to calculate $\delta^{18}O_b$ lags and their statistical uncertainties by subtracting a core's radiocarbon age model from an age model based on its $\delta^{18}O_b$ alignment to a target stack. This method produces lag estimates as a function of time with statistical uncertainties. As an example of the approach, we calculate lags for a depth transect of 12 cores in the Brazil Margin whose lags were described qualitatively in Lund et al. (2015). Our new methodology supports a previously described lag between lower intermediate (1802-2296 m) and deep (2500-2951 m) water; specifically, we find a statistically significant lag across this boundary throughout T1, with a maximum of 2.08 kyr (95% credible interval: 1.36 - 2.85) at 14 ka BP. We also identify statistically significant lags between upper intermediate (1105-1627 m) and lower intermediate cores that were not previously described. Furthermore, we demonstrate that the Brazil Margin $\delta^{18}O_b$ lags during T1 are inconsistent with a tracer transport model under modern circulation pathways (Gebbie, 2012) that fits an Atlantic-Pacific $\delta^{18}O_b$ lag.

1 Introduction

The oxygen isotope ratio of benthic foraminiferal calcite ($\delta^{18}O_b$) from ocean sediment cores is a proxy for changes in global ice volume, local water temperature, and the $\delta^{18}O$ of seawater ($\delta^{18}O_{sw}$). Although many studies have focused on timescales where $\delta^{18}O_b$ appears globally synchronous (Imbrie et al., 1984, Lisiecki & Raymo, 2005), several studies have observed temporal offsets ("lags") of up to 4 kyr between some $\delta^{18}O_b$ records during Termination 1 (T1; 19-11.7 ka BP, Skinner & Shackleton, 2005**;** Stern & Lisiecki, 2014). These lags, which are larger than modern day ventilation ages (Devries & Primeau, 2011; Gebbie & Huybers, 2012), suggest different ocean circulation patterns during the deglaciation and/or diachronous climate forcings across hemispheres. However, lag estimates from previous studies are temporally discrete, rely on the identification of $\delta^{18}O_b$ tie points, have a limited spatial coverage, and lack statistical uncertainty estimates (Labeyrie et al., 2005; Lund et al., 2015; Skinner & Shackleton 2005; Stern & Lisiecki 2014; Waelbroeck et al., 2011). In addition, because each study uses a different technique to calculate lags, direct comparison between studies is difficult.

Here we present a novel method to probabilistically estimate lags as a function of time with statistical uncertainties by calculating the difference between a core's radiocarbon age model and $\delta^{18}O_b$-aligned age model (constructed by stratigraphically aligning a $\delta^{18}O_b$ signal to a target stack). Planktonic radiocarbon age models provide estimates of the true age of the sediment with uncertainty, whereas $\delta^{18}O_b$-alignment constructs an age model under the assumption that the $\delta^{18}O_b$ signals of the input core and the alignment target changed synchronously. Both radiocarbon and $\delta^{18}O_b$ age models are constructed with the Bayesian

software package BIGMACS (Lee & Rand et al., CPD). Age model uncertainties are propagated throughout the lag calculation by computing the joint likelihood of Markov Chain Monte Carlo (MCMC) age model samples. Furthermore, because BIGMACS constructs $\delta^{18}O_b$ age models with a probabilistic and automated alignment algorithm, our method does not rely on the visual identification of $\delta^{18}O_b$ tie points.

As a test case for this technique, we calculate $\delta^{18}O_b$ lags for a transect of twelve cores from the Brazil Margin between depths of 440-3924 m and compare our results with previously described temporal offsets (Lund et al., 2015). We find a statistically significant lag between lower intermediate (1802-2296 m) and deep (2500-2951 m) cores throughout T1 with a maximum value of 2.08 kyr (95% credible interval: 1.36-2.85) at 14 ka BP. In addition, we find statistically significant lags between upper intermediate and lower intermediate cores, which were not previously identified. Finally, we compare the vertical transect of Brazil Margin $\delta^{18}O_b$ lags with synthetic lags from a tracer transport model under modern circulation pathways (Gebbie, 2012). We find that our calculated lags have more structure than was anticipated by a previous deglacial inversion that captured Atlantic-Pacific interbasin lags, indicating that our method provides additional information about the Atlantic circulation.

2 Background

2.1 Defining Benthic $\delta^{18}O$ Lags

The timing of changes in $\delta^{18}O_b$ values is not synchronous with termination events as defined by global ice volume because $\delta^{18}O_b$ values are also affected by changes in deep water temperature, $\delta^{18}O_{sw}$, overturning circulation rates that propagate surface signals to the ocean interior, and shifts in water mass boundaries that affect which surface signals reach a

particular core location (Riveiros et al., 2010; Cortese et al., 2007; Mashiotta et al., 1999; Shackleton, 2000). For example, deep water properties were likely diachronous during T1 due to bipolar seesaw events such as Heinrich Stadial 1 (HS1, 17.5 – 14.7 ka BP) and the Younger Drias (12.8 – 11.7 ka BP) which occurred coeval with decreases in circulation rates and shifts in water mass boundaries (Schmittner et al., 2003; Shakun et al., 2012; Toggweiler & Lea, 2010; Barker 2009; Barker et al., 2011; Barbante et al., 2006; Curry & Oppo, 2005; He et al., 2013).

Previous studies identify lags between core sites for a single point in time when identifiable features in their $\delta^{18}O_b$ signals, such as the T1 onset or midpoint, occur at different times. However, we can equivalently define lags by the extent to which $\delta^{18}O_b$-aligned age models are incorrect. For example, a $\delta^{18}O_b$ record with a true T1 onset age of 15 ka BP aligned to a $\delta^{18}O_b$ signal from a different core with a T1 onset age of 18 ka BP would result in an age error of 3 kyr and indicate a 3-kyr $\delta^{18}O_b$ lag between those core sites. Measuring the difference between $\delta^{18}O_b$-aligned ages and absolute age estimates (e.g., from radiocarbon) produces time-series of lags with probabilistic uncertainty estimates that do not depend on subjectively identified $\delta^{18}O_b$ tie points. This method is used to define $\delta^{18}O_b$ lags relative to a specified alignment target; however, in section 6.2 we show that the lag difference between two cores aligned to the same target is largely independent of the choice of alignment target.

2.2 Previous Lag Measurements

Multiple studies have identified lags between cores or stacks from different ocean basins. Skinner & Shackleton (2005) measured a lag between one core from the deep equatorial Pacific and one core from the deep North Atlantic by placing each core on an

independent radiocarbon age model (supplemented with SST alignments) and locating the mid-point of $\delta^{18}O_b$ change in each core based on 5-point smoothed signals. The T1 midpoint was estimated to occur 3.9 kyr earlier in the Atlantic core than the Pacific core. Another study (Labeyrie et al., 2005) measured lags in a compilation of seven radiocarbon-dated cores from the Atlantic, Pacific, and Indian Ocean basins by comparing the timing of peaks in $\delta^{18}O_b$ time derivatives. In that study, deep water $\delta^{18}O_b$ records in the Atlantic and Pacific were observed to lag intermediate-depth records in the Atlantic and Indian by 1-1.5 kyr during HS1 and the YD.

An alternative approach is to estimate average lags between regions using stacks. Stern & Lisiecki (2014) assumed synchronous change within specified regions and constructed seven stacks, combining the radiocarbon data from all cores in each region to construct regional age models. During T1, the average lag between the Deep Pacific stack and the Deep North Atlantic stack was 1 kyr, with a maximum value of 1.7 kyr during the T1 midpoint. Although Stern & Lisiecki (2014) observed a smaller deep Pacific $\delta^{18}O_b$ lag than Skinner & Shackleton (2005), they found a 4 kyr lag for the onset of T1 between the Intermediate South Atlantic and Deep Indian stacks.

Several studies have observed lags within the Atlantic basin during T1. A compilation of nine individual Atlantic cores on radiocarbon age models found that intermediate-depth cores recorded the T1 onset 0.5 kyr before a deep North Atlantic core and 1.5 kyr before a deep South Atlantic core (Waelbroeck et al., 2011). Additionally, this study observed that $\delta^{18}O_b$ from the deep North Atlantic core decreased by 0.6 ‰ from 17-15 ka BP while the deep South Atlantic record only decreased by 0.2 ‰. In Lund et al., 2015, a depth transect of twelve cores from the Brazil Margin suggested that benthic $\delta^{18}O_b$ in

intermediate cores (1802-2296 m) changed 2-3 kyr before deep cores (2500-2951 m) in that region. A regional stack for the Intermediate South Atlantic recorded the T1 onset 1 kyr before Intermediate North Atlantic, Deep North Atlantic, and Deep South Atlantic stacks (Stern & Lisiecki, 2014).

These studies use inconsistent criteria to produce lag estimates at different times during T1, making it difficult to synthesize the results. Furthermore, these methods do not account for statistical age model uncertainties. Here we present and evaluate a new method to probabilistically calculate time-series of $\delta^{18}O_b$ lags with statistical uncertainties. This method can facilitate the comparison of lags between different regions which may improve understanding of the mechanisms that generate these lags.

2.3 Potential Causes of Benthic $\delta^{18}O$ Lags

Three potential factors that contribute to lags between $\delta^{18}O_b$ signals are (1) increased water mass ventilation ages during the LGM and T1 (Rafter et al., 2022), (2) asynchronous changes in water mass properties at deep water formation sites (EPICA community members, 2006; Pedro et al., 2011; Gebbie, 2012), and (3) water mass boundary shifts across core sites (Curry & Oppo, 2005). Here we summarize evidence for the contribution of each of these mechanisms to $\delta^{18}O_b$ lags during the LGM and T1.

The transit time of a $\delta^{18}O$-depleted meltwater signal from the surface ocean to a deep core site depends on circulation rates. Ventilation ages derived from benthic radiocarbon measurements suggest some sites may have been bathed by older water masses during the LGM, potentially contributing to $\delta^{18}O_b$ lags. The estimated 4 kyr lags between the Atlantic and Pacific Ocean (Skinner & Shackleton 2005) and the Atlantic and Indian Ocean (Stern & Lisiecki 2014) are likely affected by deep water ventilation ages of 2-5 kyr during the LGM

and T1 in the Pacific and Indian Oceans (Shackleton et al., 1988; Adkins & Boyle, 1997; Sikes et al., 2000; Marchitto et al., 2007; Bryan et al., 2010; Burke & Robinson, 2012; Sikes et al., 2016). Large ventilation ages have also been recorded during HS1 at the Iberian Margin (Skinner & Shackleton 2004), in the Atlantic sector of the Southern Ocean (Barker et al., 2010; Skinner et al., 2010), at the Brazil Margin (Mangini et al., 2010), and in the western subtropical Atlantic (Keigwin & Schlegel, 2002; Keigwin, 2004). Rafter et al., (2022) averaged a global compilation of ventilation ages along density surfaces and found that bottom waters (defined as waters below the 1028 kg m^{-3} isopycnal) had an average ventilation age that was 1050 years older in the LGM than in the pre-industrial. While Rafter et al., (2022) argues for a slowdown in overturning circulation, there is disagreement in the extent to which ventilation ages reflect past oceanographic changes. For example, a different study that compiled 1361 deep-sea radiocarbon measurements demonstrates that 87% of the data can be fit under modern circulation pathways and rates when age uncertainties are included (Zhao et al., 2018). Similarly, Broecker et al. (2004) found similar-to-modern ventilation ages during the LGM in the Western Equatorial Pacific below 2 km.

Secondly, the millennial-scale bipolar seesaw may have caused asynchronous changes in deep water mass properties that could have contributed to benthic $\delta^{18}O$ lags during T1. For example, a tracer transport model using modern-day circulation patterns proposed that the 4-kyr lag between the Pacific and the Atlantic (Skinner & Shackleton, 2004) could be explained by a late isotope maximum in local $\delta^{18}O_{sw}$ and temperature around Antarctica (Gebbie, 2012). Proxies recorded in ice cores such as $\delta^{18}O$, $\delta^{15}N$, and δD indicate that both the magnitude and timing of warming were different in the Northern and Southern Hemispheres (EPICA Community Members, 2006; Lemieux-Dudon et al., 2010; Pedro et

al., 2011; Buizert et al., 2014; WAIS Divide project Members, 2015). While climate events in the Arctic are characterized by large and abrupt temperature changes, Antarctic events are better defined by slow shifts of smaller magnitude (Blunier & Brook, 2001). These bipolar seesaw responses recorded near deep water formation sites were likely transported to the deep ocean as supported by observations in surface proxies of ocean sediment cores (Barker et al., 2009; Skinner et al., 2010; Skinner et al., 2014).

Lastly, if two deep water masses have different properties, then a water-mass boundary shift across a core site can affect the core's $\delta^{18}O$ signal. Millennial-scale events during T1 occurred coeval with transient water mass geometry and circulation changes. Northern hemisphere cold events (e.g., HS1 and the YD) are characterized by a weakening of the Atlantic Meridional Overturning Circulation (AMOC), shoaling of NADW, and vertical and latitudinal expansion of AABW, as indicated by measurements of $^{231}Pa/Th$ (McManus et al., 2004), Cd/Ca (Marchitto & Broecker, 2006; Makou et al., 2010), and $\delta^{13}C$ (Curry & Oppo, 2005). During the LGM, the core of NADW may have shoaled above 2 km (referred to as Glacial North Atlantic Intermediate Water) while AABW occupied depths as shallow as 2.5 km at the Brazil Margin (Boyle & Keigwin, 1987; Duplessy et al., 1988; Curry & Oppo, 2005; Marchitto & Broecker, 2006). Changes in the northern extent of Antarctic Intermediate Water (AAIW) during HS1 and the YD are uncertain, with some studies suggesting northward expansion (Pahnke et al., 2008; Rickaby & Elderfield, 2005; Thornalley et al., 2011) and others suggesting southward contraction (Came et al., 2008; Huang et al., 2014; Xie et al., 2012). As water mass boundaries shift across core sites, these sites have the potential to experience asynchronous changes in $\delta^{18}O_b$ due to differences in the temperature or $\delta^{18}O_{sw}$ between the water masses.

Today, Antarctic Bottom Water (AABW) has a lower salinity and potential temperature than North Atlantic Deep Water (NADW), which yields very similar $\delta^{18}O_b$ values throughout the deep Atlantic. However, the total $\delta^{18}O_b$ change from the LGM to the Holocene in the North Atlantic was 1.9 - 2.0 ‰ while the change in the South Atlantic was 1.6 - 1.7 ‰ (Adkins et al., 2002). Therefore, NADW and AABW likely produced different $\delta^{18}O_b$ values during the LGM and T1 (Friedrich & Timmermann, 2012; Lynch-Stieglitz et al., 2007; Oppo et al., 2015), and a shift in the NADW-AABW boundary could produce a $\delta^{18}O_b$ signal at sites within the shift's vicinity.

3 Data

3.1 Setting

The Brazil Margin provides a good test case for evaluating our lag calculation method. Past water mass geometries have been reconstructed with high spatial resolution on the margin (Curry & Oppo 2005; Lund et al., 2015; Makou et al., 2010; Oppo et al., 2015; Tessin & Lund, 2013), and cores with $\delta^{18}O_b$ and planktonic radiocarbon data span depths from 440 m to 3924 m. We can also infer similar reservoir ages for the ^{14}C measurements at each core site because of the close spatial proximity of the core locations. In addition, we can evaluate the extent to which our lag results reproduce previous interpretations (Lund et al., 2015) and whether previously identified lags are statistically significant. Because modern day ventilation ages of all cores in the depth transect are thought to differ by less than approximately 500 years (Devries & Primeau, 2011; Gebbie & Huybers 2012), any lags of a larger magnitude would be indicative of changes in circulation rates, water mass boundary shifts, and/or diachronous changes in water mass properties.

We use the twelve cores (Table 1) from the Brazil Margin depth transect analyzed by Lund et al. (2015). According to modern day water mass geometries (Figure 1a), one core samples South Atlantic Mode Water (440 m), two cores sample AAIW (1105-1268 m), seven cores sample NADW (1627-3589 m), and one samples AABW (3924 m). However, during the LGM, the water masses bathing some of the core sites were likely different. Five different LGM water mass reconstructions have been constructed that are consistent with available $\delta^{18}O_b$ and benthic $\delta^{13}C$ data, which produce different depth estimates for the boundary between AABW and NADW at the Brazil Margin (Gebbie, 2014; Gebbie et al., 2015; Oppo et al., 2018). The reconstruction that differs most from the present day is the alternative reconstruction from Gebbie (2014) which limits Southern Ocean $\delta^{13}C$ values to a minimum of -0.2‰ in accordance with a Mackensen effect correction (Figure 1b). Under this reconstruction, as many as seven cores (2082-3924 m) were bathed by AABW during the LGM, two by NADW (1627-1802 m), and two by AAIW (1105-1268 m).

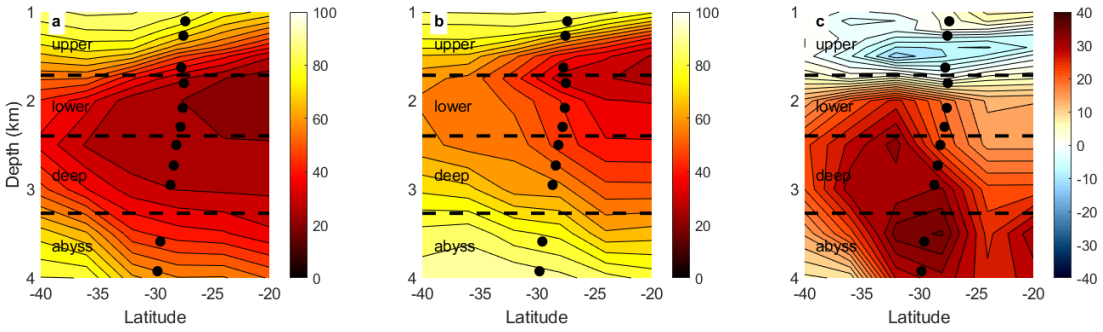

Figure 1: Possible water mass changes on the Brazil Margin. Percent of Southern Component Water (%SCW) for (a) modern day (Gebbie & Huybers, 2010) and (b) the alternative LGM simulation of Gebbie, 2014. (c) The glacial-modern difference, where positive values indicate more %SCW during the LGM than the modern. Black dots mark the 12 core locations from Lund et al. (2015). Dashed lines indicate the following depth sections: upper intermediate (1105 – 1714 m), lower intermediate (1714 – 2398 m), deep (2398 – 3270 m), and abyss (3270 – 3924 m).

Core	Lat °S	Lon °W	Depth m
14GGC[1]	26.68	46.5	441
90GGC[1]	27.35	46.63	1105
36GGC[2,4]	27.52	46.47	1268
17JPC[1,2]	27.7	46.48	1627
78GGC[2]	27.48	46.33	1802
33GGC[1,2]	27.57	46.18	2082
42JPC[3]	27.77	46.03	2296
30GGC[1,2]	28.13	46.07	2500
63GGC[1]	28.36	45.40	2732
20JPC[1]	28.64	45.54	2951
125GGC[3]	29.53	45.08	3589
22GGC[1,3]	29.78	45.58	3924

Table 1: Latitude, longitude, and depth for the twelve Brazil Margin cores. Superscripts indicate the following citations: [1]Lund et al., (2015), [2]Tessin & Lund (2013), [3]Hoffman & Lund (2012), [4]Sortor & Lund, (2011).

3.2 Brazil Margin Radiocarbon and Benthic $\delta^{18}O$

Benthic $\delta^{18}O$ for the Brazil margin cores are measured on *Cibicidoides wuellerstorfi, Cibicidoides spp.,* and *Planulina., spp.* with the average sample spacing ranging from 0.85 – 8.46 cm per measurement. Radiocarbon ages for the Brazil Margin cores were measured on the planktonic species *Globigerinoides ruber* and *Globigerinoides sacculifer* with 8-29 measurements per core. In order to assess whether our lag calculation method reproduces the temporal offsets previously observed, we reject the same radiocarbon outliers and reversals as prior studies. Ten of the twelve Brazil Margin cores contain reversals in their planktonic radiocarbon dates which were rejected by the original authors (Hoffman & Lund, 2012; Lund et al., 2015; Sortor & Lund 2011; Tessin & Lund 2013). In addition, two ages with overlapping uncertainties were averaged in 14GGC (Lund et al., 2015), and an age of 14.23 ka BP at 41 cm in 30GGC was rejected due to the large sedimentation rate it implied (Tessin & Lund, 2013).

Age reversals in these cores have been attributed to the effects of bioturbation based on stable isotope and radiocarbon analyses of benthic foraminifera (Sortor & Lund, 2011), low planktonic $\delta^{18}O$ and high $CaCO_3$ measurements (Lund et al., 2015), and low $\delta^{18}O_b$ values (Tessin & Lund, 2013). Bioturbation could potentially account for the observed age reversals across depth ranges of approximately 60 cm. Possible alternative causes of extensive age reversals are turbidite deposits or radiocarbon contamination.

4 Methods

4.1 Age Model Construction

All age models (Figures S1, S4 and S9) and stacks (Figures 2b, 4 and S8) are constructed using the Bayesian software package BIGMACS which can estimate multiproxy age models and $\delta^{18}O$ stacks from radiocarbon data, benthic $\delta^{18}O$ stratigraphic alignment, and any other age information that exists in the sediment (tephra layers, tie points, etc.). In this study, we use BIGMACS to construct two types of age models: ones based on radiocarbon data (which reflect the true age of the sediment) and ones based on $\delta^{18}O$ alignment (which reflect the age of the sediment if $\delta^{18}O$ changed synchronously). All age models are composed of 1000 MCMC samples drawn in proportion to their probabilities.

Radiocarbon age models are constructed using only the ^{14}C data from each core (with outliers removed as described above). Ages are calibrated using the Marine20 curve (Heaton et al., 2020), a reservoir age offset (ΔR) of zero, and a reservoir age standard deviation of 200 years. All Brazil Margin cores should have similar reservoir ages due to their close proximity.

Stratigraphically aligned $\delta^{18}O$ age models are constructed by probabilistically aligning each core's $\delta^{18}O$ to a multiproxy stack of Deep Northeast Atlantic (DNEA) $\delta^{18}O_b$ records from Lee & Rand et al. (CPD), which was also generated by BIGMACS. The DNEA stack (Figure 2b) is composed of six high resolution cores with both $\delta^{18}O$ and radiocarbon ages. The stack provides an excellent alignment target due to the high resolution radiocarbon records and good signal-to-noise ratios of $\delta^{18}O_b$ data from individual cores. During alignment, BIGMACS learns core-specific $\delta^{18}O_b$ shift and scale parameters that adjust for different depths, different species of foraminifera, and different magnitudes of $\delta^{18}O_b$ change

across T1 in each core. While reservoir age differences between the Brazil Margin and the locations of cores in the DNEA stack will affect the estimated lags, all Brazil Margin cores should be affected equally by these reservoir age assumptions. Therefore, any differences between calculated lags for Brazil Margin cores should be independent of the potential reservoir age offsets (see Section 6.2).

Because less $\delta^{18}O_b$ data is available to constrain each alignment at its start and end, we include an additional age constraint using the first and last age returned from the radiocarbon age model (green squares in Figure S2). These ages are modeled as Gaussian distributions with means equal to the mean of the respective radiocarbon age models and standard deviations derived from the radiocarbon age model's uncertainty. The effect of applying these age constraints is to produce similar $\delta^{18}O_b$-aligned and ^{14}C-dated age estimates at the start and end of each alignment (Figure S1) and, consequently, smaller (or more conservative) lag estimates. The start and end ages used are all outside of the time period over which lags are analyzed in this study (10-18 ka BP). The oldest start age used is 6.3 ka BP in core 22GGC, and the youngest end age is 18.7 ka BP in core 33GGC.

4.2 Lag Calculation

Lags and their uncertainties are calculated by subtracting all possible pairs of the 1000 sampled $\delta^{18}O_b$ alignments and the 1000 sampled radiocarbon age models. This results in one million lag samples drawn from the joint likelihood of the two age model types. Because we consider radiocarbon age samples to be drawn from the core's "true" age model, each lag sample is placed on its respective radiocarbon age model sample.

All $\delta^{18}O_b$ lags are measured relative to the target DNEA stack. A positive lag implies that a portion of the $\delta^{18}O_b$ signal (probabilistically identified by the alignment process)

occurred later in the Brazil Margin core than the corresponding $\delta^{18}O_b$ signal in the DNEA stack, while a negative lag (or a lead) implies a $\delta^{18}O_b$ feature occurred in the Brazil Margin core before the DNEA stack. Figure 2 illustrates the steps of the lag calculation process for an example core from the Brazil Margin (22GGC). Note that the inclusion of start and end radiocarbon age estimates (in green) during $\delta^{18}O_b$ alignment encourages agreement between the two age models at the LGM and Holocene. Thus, statistically significant lags are only generated during T1 if distinctive $\delta^{18}O_b$ features are present to robustly constrain (i.e., with small uncertainties) the alignment of the core to the stack.

Next, we define the lag difference between pairs of Brazil Margin cores as equal to the difference between their lags relative to the same alignment target. We expect this lag difference to be largely independent of the choice of alignment target, as supported by the results of sensitivity tests described in Section 6.2.

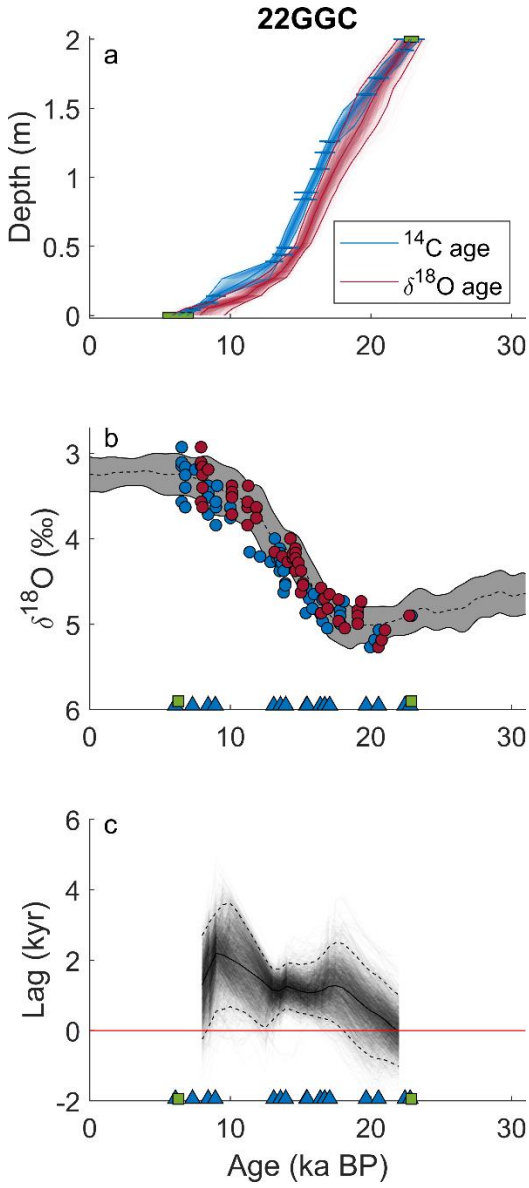

Figure 2: Illustration of the lag calculation method for core 22GGC. (a) The radiocarbon (blue) and benthic δ^{18}O-aligned (red) age models produced by BIGMACS. Shading indicates age model sample density. Blue horizontal lines are calibrated radiocarbon ages used for the radiocarbon age model, and green horizontal lines show the age estimates used to constrain the beginning and end of the $\delta^{18}O_b$ alignments. The 95% CI width and median age for each age model are shown with solid lines. (b) The $\delta^{18}O_b$ values (after applying core-specific shift and scale estimates) plotted on the radiocarbon age model (blue) and the $\delta^{18}O_b$ age model (red). Grey shading shows the DNEA target stack. Blue triangles and green squares show the median-calibrated radiocarbon ages and additional ages respectively. (c) The lag is calculated by subtracting $\delta^{18}O_b$ age samples from the ^{14}C age samples (i.e., the horizontal difference between the two age models in (a)). Solid and dotted lines denote the median lag and 95% credible intervals respectively.

5 Results

5.1 Age Model and Lag Results

Radiocarbon and $\delta^{18}O_b$ age models for the twelve cores from the Brazil Margin are plotted in Figure S1. The average 95% credible interval width for each core's radiocarbon age model range from 0.71 kyr to 1.46 kyr, with a mean of 1.06 kyr across all cores. The 95% credible interval width for the $\delta^{18}O_b$ age models is typically larger, with core averages of 1.17 kyr to 2.04 kyr and an overall mean of 1.6 kyr.

Lags between each core's $\delta^{18}O_b$ signal and the target stack are calculated between 10-18 ka BP (Figure S3). The largest median lag relative to the target stack occurs 10 ka BP in core 125GGC with a magnitude of 4.1 kyr. The largest median lead (i.e., negative lag) relative to the stack is -1.2 kyr in core 36GGC at 12 ka BP. The 95% credible interval width of lags averaged over T1 (10-18 ka BP) vary from 1.43 kyr to 2.32 kyr across cores, with a mean of 1.95 kyr. Leads and lags relative to the target stack are deemed statistically significant when the zero line falls outside of the 95% credible limits. Significant lags are observed in 10 of the 12 cores (Figure S3).

5.2 Lag Difference Calculations Compared to Lund et al., (2015)

Differences in the $\delta^{18}O_b$ signals of water masses at the Brazil Margin were previously defined based on lateral contour shifts in the Hovmöller diagram (Figure 3 right, reproduced from Lund et al., 2015). The contours in the diagram display the $\delta^{18}O_b$ departures (with a 2-kyr smoothing) from mean LGM values (defined from 19-23 ka BP) for each core and were used by Lund et al. (2015) to identify two "$\delta^{18}O_b$ delineated" water mass boundaries. The first boundary identified by Lund et al. (2015) is a 2-3 kyr contour shift

between 2000-2500 m water depth that persists throughout T1. The second shift is located between 2900-3500 m during HS1. To compare our lag results with the Hovmöller diagram, we calculate lags at 2-kyr intervals from 18-10 ka BP and plot the lags from each core at their respective core depths to create lag transects (Figure 3, left). Visually the lag transects match the pattern of $\delta^{18}O_b$ contours in time-depth space on the Hovmöller diagram. Salient features, such as the early arrival of light $\delta^{18}O_b$ at lower intermediate depths (1802-2296 m) and the preservation of heavier $\delta^{18}O_b$ in deep water (2500-2951 m), are easily visible at 16 ka BP and 14 ka BP.

To better quantify depth-dependent lags at the Brazil Margin as initially described Lund et al. (2015), we identify four depth groupings defined by shifts in the -0.2 ‰ contour in the Hovmöller diagram (Figure 3). Specifically, the depth intervals we define are the upper intermediate (three cores between 1105-1627 m), lower intermediate (three cores between 1802-2296 m), deep (three cores between 2500-2951 m), and abyss (two cores between 3589-3924 m). Similar core groups are loosely defined in Lund et al. (2015) based on benthic $\delta^{13}C$ and $\delta^{18}O_b$ data. However, the previous study included 17JPC at 1627 m in the lower intermediate group based on its benthic $\delta^{13}C$, whereas we place this core in the upper intermediate group.

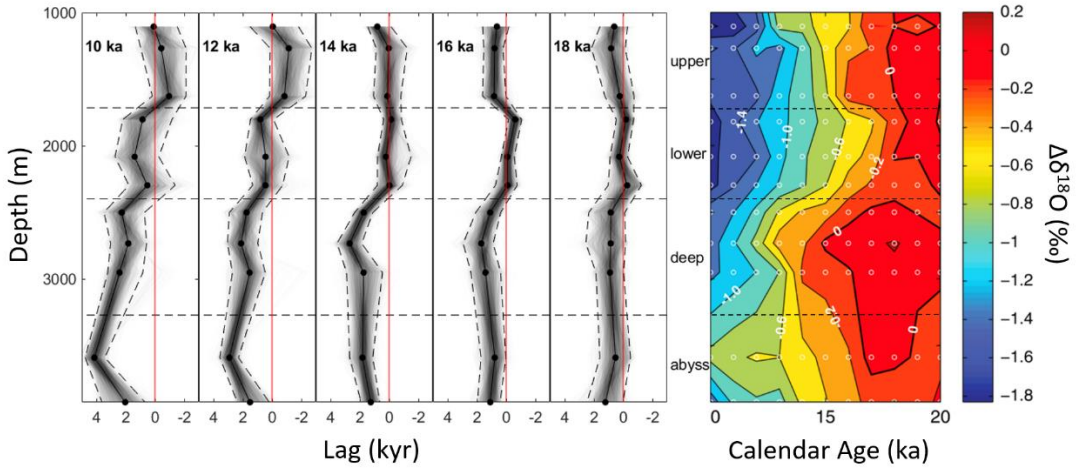

Figure 3: (Left) Lag versus core depth for 12 Brazil Margin cores, sampled every 2 kyr from 10-18 ka BP. Lags are defined relative to the DNEA stack of (Lee and Rand et al., in CPD). (Right) The Hovmöller diagram modified from Lund et al., (2015). Contours represent the $\delta^{18}O_b$ departure (after a 2-kyr smoothing) from the mean LGM value in each core. Dotted lines are added to mark the upper intermediate, lower intermediate, deep, and abyss depth ranges.

To measure lag differences between the depth intervals, we first construct lag stacks by averaging the lag samples from individual cores within each group. Median values and 95% credible intervals of each lag stack are defined by the distribution of the one million lag samples averaged (stacked) over the two or three individual cores within each depth range. The differences between lag stacks are considered independent of the choice of alignment target (see Section 6.2) and reflect the different timing of $\delta^{18}O_b$ change between neighboring depth intervals. The lag stacks, and the lag stack differences (calculated via pairwise sample subtraction) are displayed in Figure 4 for each depth interval. In addition, we estimate the average $\delta^{18}O_b$ signal for each depth interval by constructing multiproxy stacks (Figure 4, panels a, d, f) in BIGMACS (Lee & Rand et al., in CPD).

Table 2 presents the lag differences between neighboring depth intervals. The lag differences between the lower intermediate and deep stacks agree well with the 2-3 kyr offset identified in Lund et al., (2015). The lower intermediate group demonstrates a

statistically significant lead over the deep group, with values from -2.08 kyr (95% CI: -2.85 to -1.36 kyr) at 14 ka BP to -0.97 kyr (95% CI: -1.82 to -0.15 kyr) at 18 ka BP. The magnitude of the lag difference decreases towards the end of the termination, in agreement with the apparent straightening of the $\delta^{18}O_b$ contours in the Hovmöller diagram during the Holocene.

We also find statistically significant lag differences between the upper and lower intermediate depth intervals. The lower intermediate $\delta^{18}O_b$ signal leads the upper intermediate during the first half of T1 with a maximum value of 1.02 kyr (95% CI: 0.46-1.59) at 16 ka BP. During the second half of the termination, the upper intermediate leads the lower intermediate with a maximum value of 1.31 kyr (95% CI: 2.53-0.05); this lag reversal is displayed as a negative "upper minus lower" lag difference in Figure 4c. The lags between these depths were not visually identified by Lund et al. (2015), perhaps because they are smaller on average, change sign across the termination, or the because the different core groupings we use here. However, our method uses more statistical information to increase the power of detection.

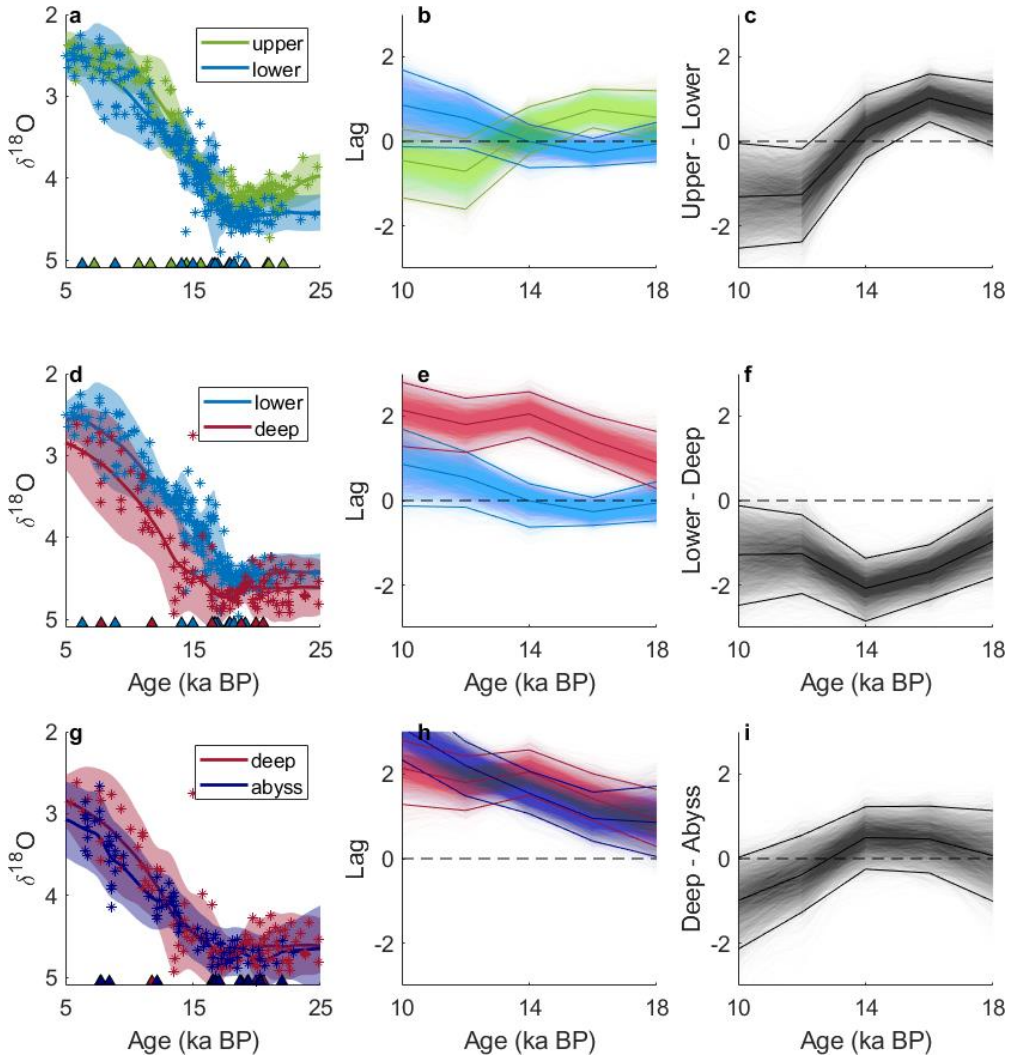

Figure 4: Average lag differences between upper and lower intermediate (a-c), lower intermediate and deep (d-f), and deep and abyss (g-i) depth sections. Panels (a), (d), and (g) compare multiproxy $\delta^{18}O_b$ stacks. Triangles represent radiocarbon ages. Panles (b), (e), and (h) plot the lag stack for each depth section. (c), (f), and (i) show the difference between the lag stacks.

Time	Upper – Lower	Lower – Deep	Deep – Abyss
10	**-1.31** [-2.53, -0.05]	**-1.28** [-2.48, -0.12]	-0.99 [-2.14, 0.03]
12	**-1.26** [-2.38, -0.18]	**-1.25** [-2.2, -0.34]	-0.38 [-1.27, 0.55]
14	0.31 [-0.4, 1.08]	**-2.08** [-2.85, -1.36]	0.5 [-0.25, 1.23]
16	**1.02** [.46, 1.59]	**-1.69** [-2.35, -1.04]	0.46 [-0.34, 1.24]
18	0.63 [-0.12, 1.39]	**-0.97** [-1.82, -0.15]	0.07 [-1.01, 1.13]

Table 2: The difference between lag stacks at 2 kyr increments from 18-10 ka BP between the upper and lower (column 1), the lower and deep (column 2), and the deep and abyss (column 3) depth sections. Lag difference 95% credible intervals for each time step are displayed in square brackets. Statistically significant lags are indicated with bold (i.e., when the credible interval does not span zero).

We do not find a statistically significant difference between the deep and abyssal depths, whereas Lund et al. (2015) identified a distinct $\delta^{18}O_b$-delineated boundary between the two during HS1. This discrepancy can be attributed to differences in the method we used to create age models for two cores within the deep group (30GGC and 20JPC). The previously published age models for these cores (Tessin & Lund, 2013; Lund et al., 2015) were extrapolated beyond the last radiocarbon date by maintaining a constant sedimentation rate. However, because our $\delta^{18}O_b$ age models are constrained by the first and last depths of the radiocarbon age models, the lags for 30GGC and 20JPC are constrained to be small at the start and end of the alignment. For 20JPC, we used an end age of 20.4 kyr at a depth of 1.74 m, whereas the age model for Lund et al., (2015) ends at 25.29 ka BP at a depth of 1.995 m. Likewise, we use an end age of 25.77 ka BP at 0.85 m for 30GGC while the age model from Lund et al., (2015) ends at 0.97 m with an age of 29.104 ka BP. Figure S4 shows revised $\delta^{18}O_b$ age models for 30GGC and 20JPC that use the end ages from Lund et al., (2015). Using alternate age models produced this way, we can reconstruct a marginally significant lag difference of 0.96 kyr (95% CI: 0.08 to 1.89) between the deep and abyss depths at 16 ka BP (Figure 5) that matches the interpretation of Lund et al., (2015).

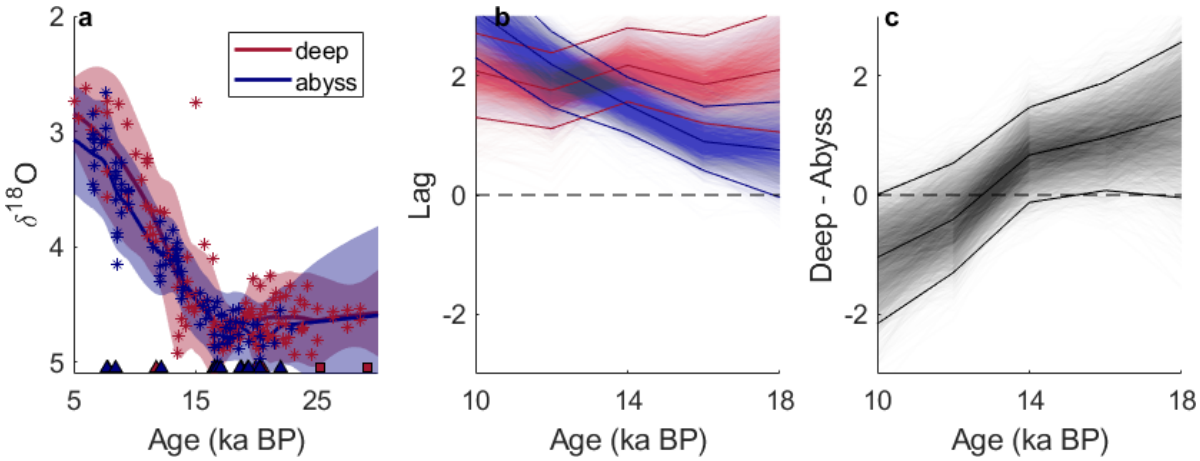

Figure 5: (a) Multiproxy stacks, (b) lag stacks, and (c) lag difference between the deep and the abyss depth sections using the alternate age models shown in Figure S4, which are more similar to those used by Lund et al. (2015). Red squares in (a) show the additional ages from Lund et al., (2015).

6 Discussion

6.1 Implications for Circulation Changes

A statistically significant relative lag between two cores indicates differences in the timing of $\delta^{18}O_b$ change at those sites. Lags larger than differences in modern ventilation ages could be indicative of different circulation rates during the LGM and T1, diachronous changes in water mass properties, shifts in water mass boundaries, or a combination of these factors. For example, a shift in water mass boundaries across a core site may also be accompanied by a change in ventilation age.

6.1.1 Deep Water Ventilation Ages

Ventilation age compilations (calculated from benthic-planktonic radiocarbon age differences) have provided evidence supporting mid-depth "age bulges" in the Atlantic, Pacific and Southern Oceans during the LGM (Marchitto et al., 2007; Burke & Robinson,

2012; Burke et al., 2015; Freeman et al., 2016; Skinner et al., 2017). The magnitude and depth of this poorly ventilated water mass is location-dependent (e.g., 3000 m at the Iberian Margin (Freeman et al., 2016), 4000 m in the Southern Ocean (Burke & Robinson 2012; Burke & Robinson 2015), and 2000 m in the North Pacific (Marchitto et al., 2007)) and is less pronounced in the Atlantic (Skinner et al., 2017). A glacial mid-depth age bulge at the Brazil Margin centered at 3000 m might contribute to the lag structure we measure during T1. This would further support the LGM circulation mode presented in Ferrari et al., (2014) in which isolated deep water is sandwiched between more ventilated intermediate and abyssal waters. Basin-wide lag calculations may help constrain the depth of the boundary between the upper and lower overturning circulation cells where older water is expected.

6.1.2 Diachronous Surface Signals

Diachronous surface signals between hemispheres may contribute to Brazil Margin lags. Gebbie (2012) demonstrates that the 4 kyr lag observed between the Iberian Margin and the equatorial Pacific (Skinner & Shackleton, 2005) can be reproduced under present day circulation pathways and rates, by assuming a delayed isotope maximum of local $\delta^{18}O_{sw}$ and temperature around Antarctica. In this scenario, the Atlantic-Pacific lag is caused by destructive interference between Northern and Southern Hemisphere signals.

To evaluate whether the transient tracer transport model presented in Gebbie (2012) reproduces the Brazil Margin lags observed here, we extract the modeled $\delta^{18}O_b$ signals from the Brazil Margin core locations. Modeled signals are translated to a synthetic depth scale by dividing model age (in years) by ten thousand, which creates a depth scale for each core between zero and three meters (figure S5). The modeled $\delta^{18}O_b$ signals are then aligned to the DNEA stack (Figure S6) and lags are calculated by taking the difference between the

aligned age and the modeled age (Figure S7). The modeled lags differ significantly from the observations. The synthetic lag transect (Figure 6) demonstrates that the lag differences between the lower intermediate and deep water do not manifest in the tracer transport simulation. Instead, the synthetic $\delta^{18}O_b$ signals in cores bathed by NADW lead cores more influenced by SCW (colored contours in Figure 1a).

The disagreement between modeled and observed lags demonstrates that the combination of circulation pathways/rates and surface boundary conditions in the transient run do not successfully reproduce lags at the Brazil Margin. These results favor a circulation regime during the LGM that is closer to the alternative reconstruction from Gebbie (2014). In the future, a basin-wide Atlantic lag compilation could be analyzed in conjunction with estimates of sea surface conditions in regions of deep water formation (e.g., Shakun et al. 2012) to find a range of T1 simulations of Atlantic circulation that successfully reproduce the observed lags (within statistical uncertainty estimates). Comparing different model scenarios should clarify whether the observed Atlantic lags can be reproduced with changes in only circulation rates, only water mass geometry, only diachronous surface forcings, or if a combination of these factors is necessary.

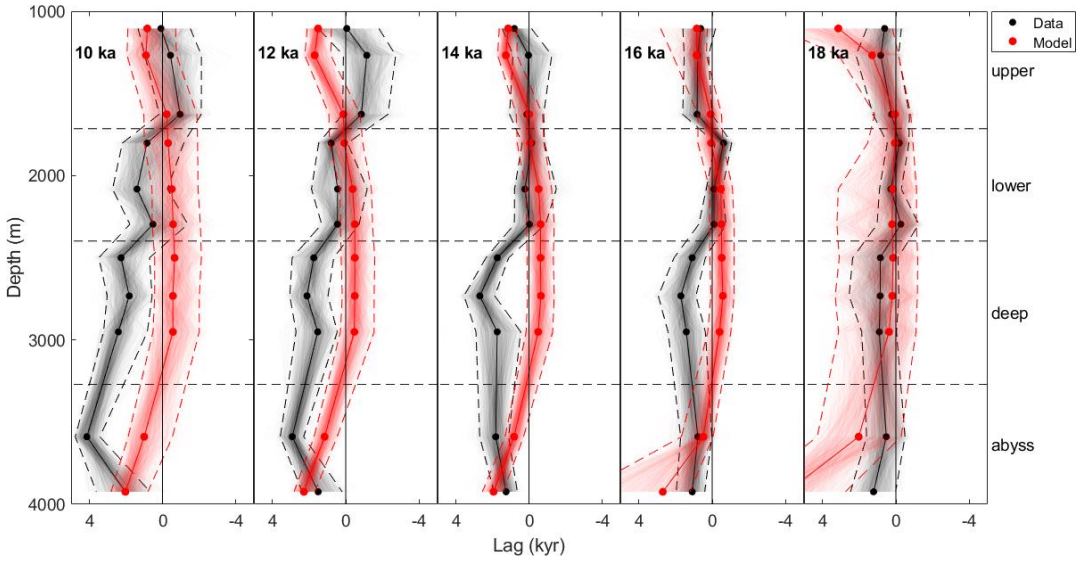

Figure 6: Comparison between modeled (red) and observed (black) lags relative to the DNEA stack. The modeled lags are calculated with an ocean circulation inverse model under current day circulation pathways and a delayed southern hemisphere LGM (Gebbie, 2012). Statistically significant differences between the observed and modeled lags indicate that the transient model does not successfully reproduce the observed Brazil Margin lags.

6.2 Sensitivity to the Alignment Target

Here we evaluate the effects our choice of alignment target have on the lag results. We perform a sensitivity test by replacing the DNEA stack with the Intermediate Tropical West Atlantic (ITWA) stack (Lee & Rand et al., in CPD) as the alignment target. The ITWA stack has a larger standard deviation and an earlier timing of $\delta^{18}O_b$ change during T1 which affects our lag calculations. Specifically, the larger standard deviation of the ITWA stack (which averages 0.25 ‰ from 10-20 ka BP, compared to 0.14 ‰ for the DNEA stack) effectively loosens constraints on the $\delta^{18}O_b$ alignment. This results in $\delta^{18}O_b$-aligned age models with 95% credible intervals that are on average 608 years wider than the alignments to the DNEA stack (again between 20 and 10 ka BP). This larger alignment uncertainty propagates throughout the lag calculation and ultimately results in lag differences with

larger uncertainties (Figure 7). The upper-lower and the lower-deep differences still show statistically significant lags, but the deep-abyss lag difference no longer shows any statistical significance, regardless of which end ages are used (i.e., from the radiocarbon age models or the ones from Lund et al. (2015)).

The earlier timing of $\delta^{18}O_b$ change in the ITWA stack effectively increases many of the core-specific lags (Figure S11) because they are measured relative to the alignment target. Multiple cores (e.g., 36GGC, 78GGC, 17JPC, 30GGC, and 22GGC) experience larger lags at the beginning of the termination. However, the lag differences between depths show similar trends and magnitudes as those derived from DNEA alignments (Figure 7) because we are taking the difference between core lags measured relative to the same target.

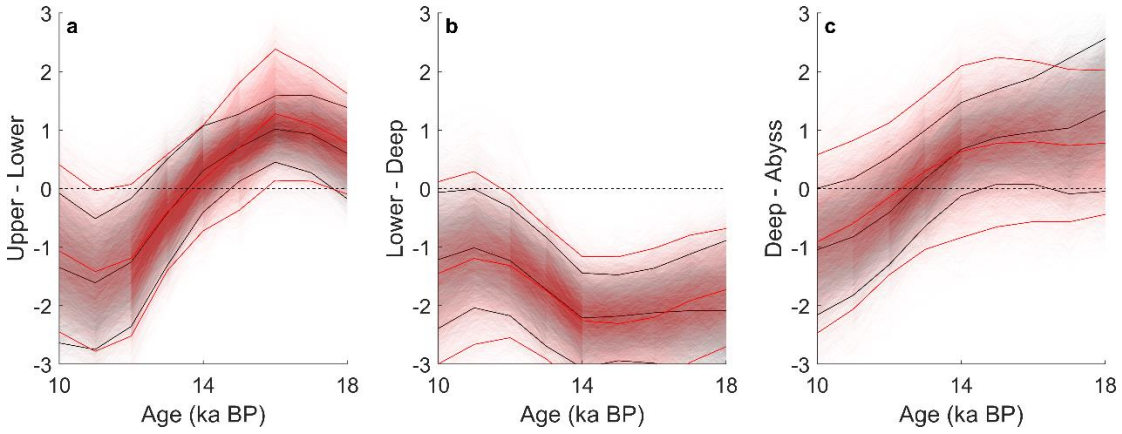

Figure 7: Comparison of the lag differences between depth intervals from the default run (black) calculated using the DNEA stack as the alignment target and from the sensitivity test (red) using the ITWA stack as the alignment target.

7 Conclusions

We present a novel method to quantify the magnitudes and uncertainties of temporal offsets (lags) in $\delta^{18}O$ signals between cores. By subtracting a core's radiocarbon age model from one based on $\delta^{18}O$ alignment, we calculate time-series of $\delta^{18}O$ lags relative to a target stack. Age models are constructed with the BIGMACS software package (Lee & Rand et al.,

in CPD) that draws MCMC age model samples in proportion to their probabilities. Lags are calculated relative to the DNEA stack from Lee & Rand et al. (in CPD), but we focus interpretation on lag differences between cores, which we show are largely independent of the $\delta^{18}O_b$ alignment target. Lag uncertainties are derived from radiocarbon and $\delta^{18}O_b$ alignment age uncertainties and allow for identification of statistically significant lags.

We use a transect of Brazil Margin data as a test case for our lag calculation method and compare our results with the qualitative lag descriptions of Lund et al. (2015). Specifically, we find a statistically significant difference between lower intermediate and deep cores across T1 with deep cores lagging by maximum value of 2.08 kyr (95% CI: 1.36-2.85 kyr) at 14 ka BP, similar to the description from Lund et al. (2015). We additionally find smaller statistically significant lags between the upper and lower intermediate depths that were not described by Lund et al. (2015). Identification of a statistically significant lag between deep and abyssal cores at 16 ka BP is found to be dependent upon the constraints applied to the start and end ages of two core's $\delta^{18}O_b$ alignments.

Unlike previous studies, the lag calculation methods presented here provide quantitative measurements of $\delta^{18}O_b$ lags and their uncertainties as a function of time. Our evaluation suggests that estimates of lag difference are largely insensitive to the choice of $\delta^{18}O_b$ alignment target. However, results are sensitive to additional age constraints used for the $\delta^{18}O_b$ age models near the time interval over which lags are measured. With consistent lag measurement techniques, $\delta^{18}O_b$ lag estimates at multiple locations throughout the Atlantic may help constrain reconstructions of deglacial deep ocean circulation changes. Here we find that a transect of Brazil Margin $\delta^{18}O_b$ lags is not consistent with the proposed $\delta^{18}O_b$ signals from a constant circulation model across T1 that was inferred from diachronous

$\delta^{18}O_b$ signals from only two core locations (Gebbie, 2012). The magnitude of lags at the Brazil Margin indicate that both a deglacial slowdown in the rate of circulation as well as changes in water mass boundaries are likely to have occurred during this time period.

Supplement

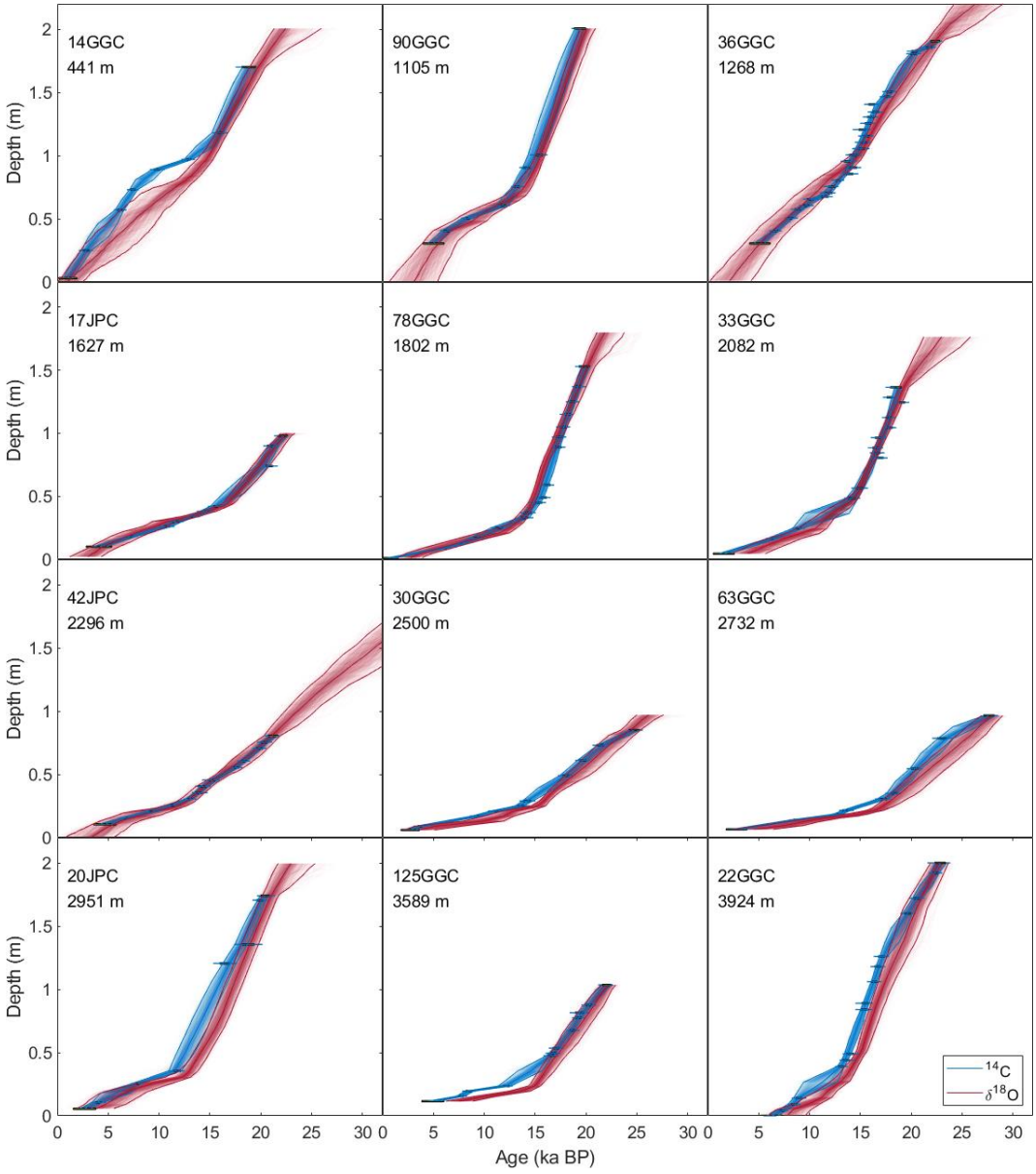

Figure S1: Default radiocarbon (blue) and $\delta^{18}O_b$ (red) age models for the Brazil Margin cores

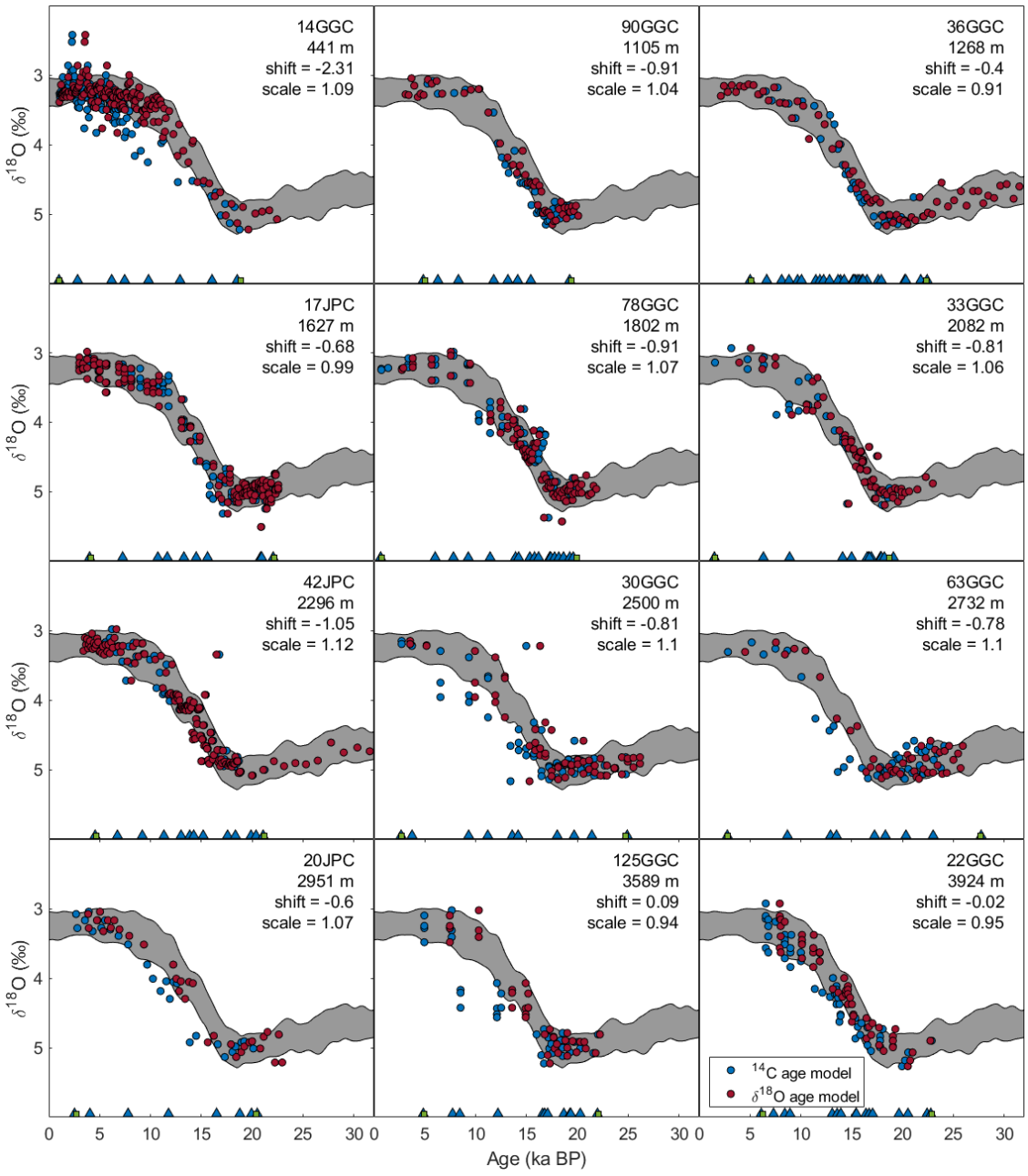

Figure S2: Benthic δ18Ob plotted on the radiocarbon (blue) and δ18Ob -aligned (red) age models. During alignment, BIGMACS applies an average δ18Ob shift and scale factor to each core's δ18Ob values that accounts for site-specific differences between the individual Brazil Margin core and the alignment target. The shift and scale factors correct for average temperature and δ18Osw differences between water masses and potential vital effect offsets between benthic species.

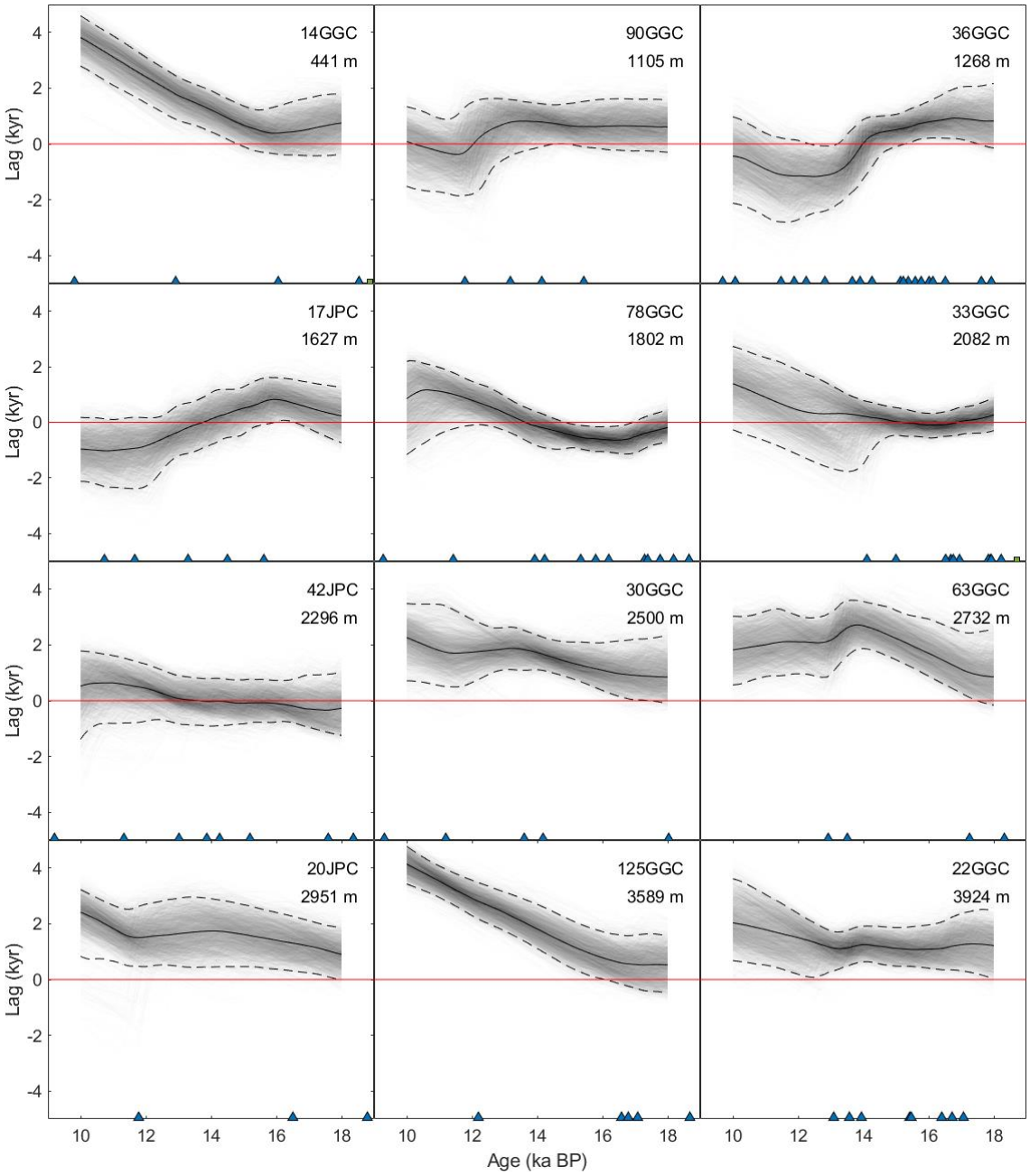

Figure S3: Benthic $\delta^{18}O_b$ lags relative to the DNEA stack (Lee & Rand et al., in review) for the Brazil Margin cores.

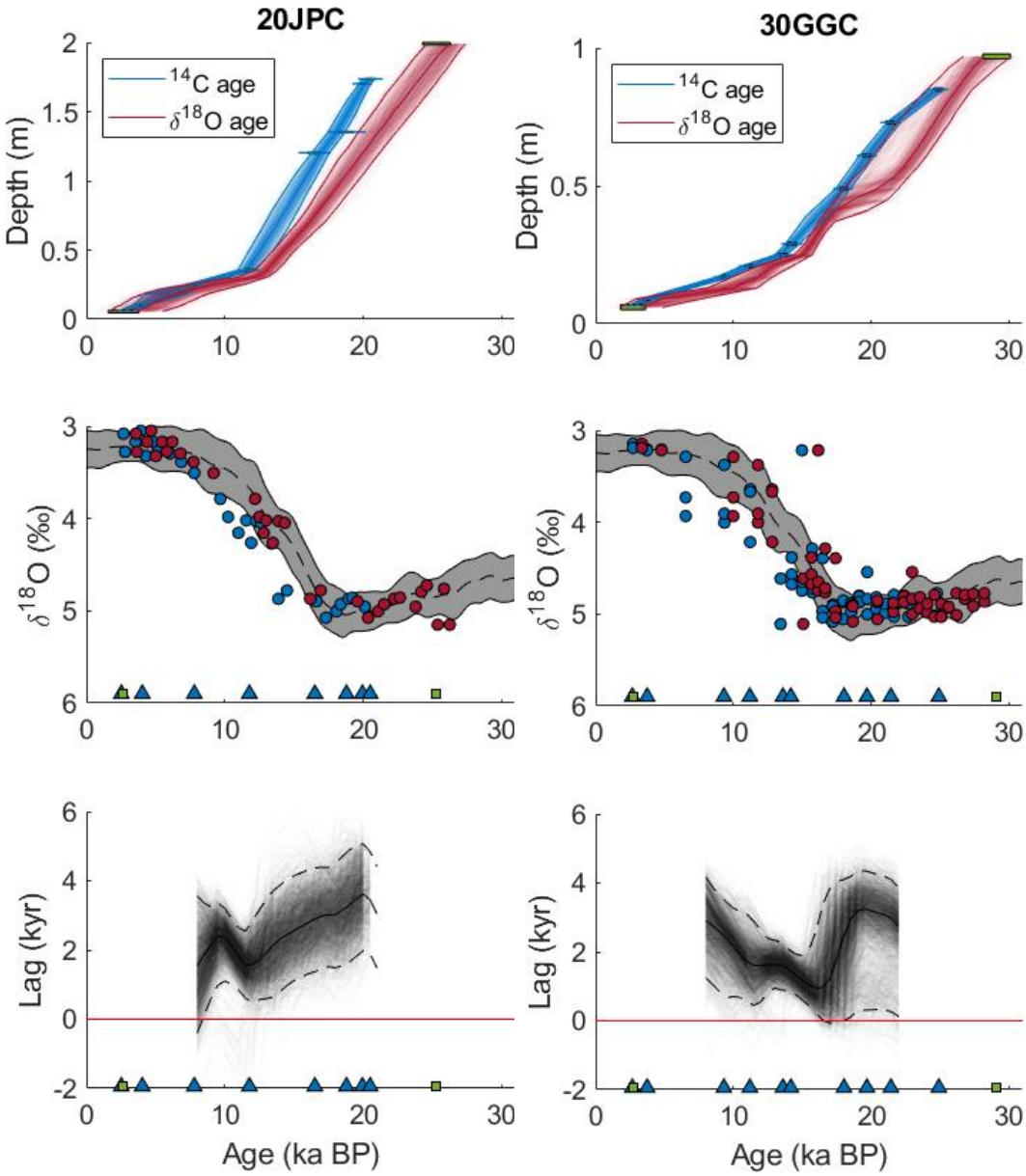

Figure S4: Revised $\delta^{18}O_b$ age models for 20JPC (left) and 30GGC (right) using an additional age suggestion from previously published age models (Lund et al., 2015). The added age suggestion creates larger lags during the LGM and Heinrich Stadial 1.

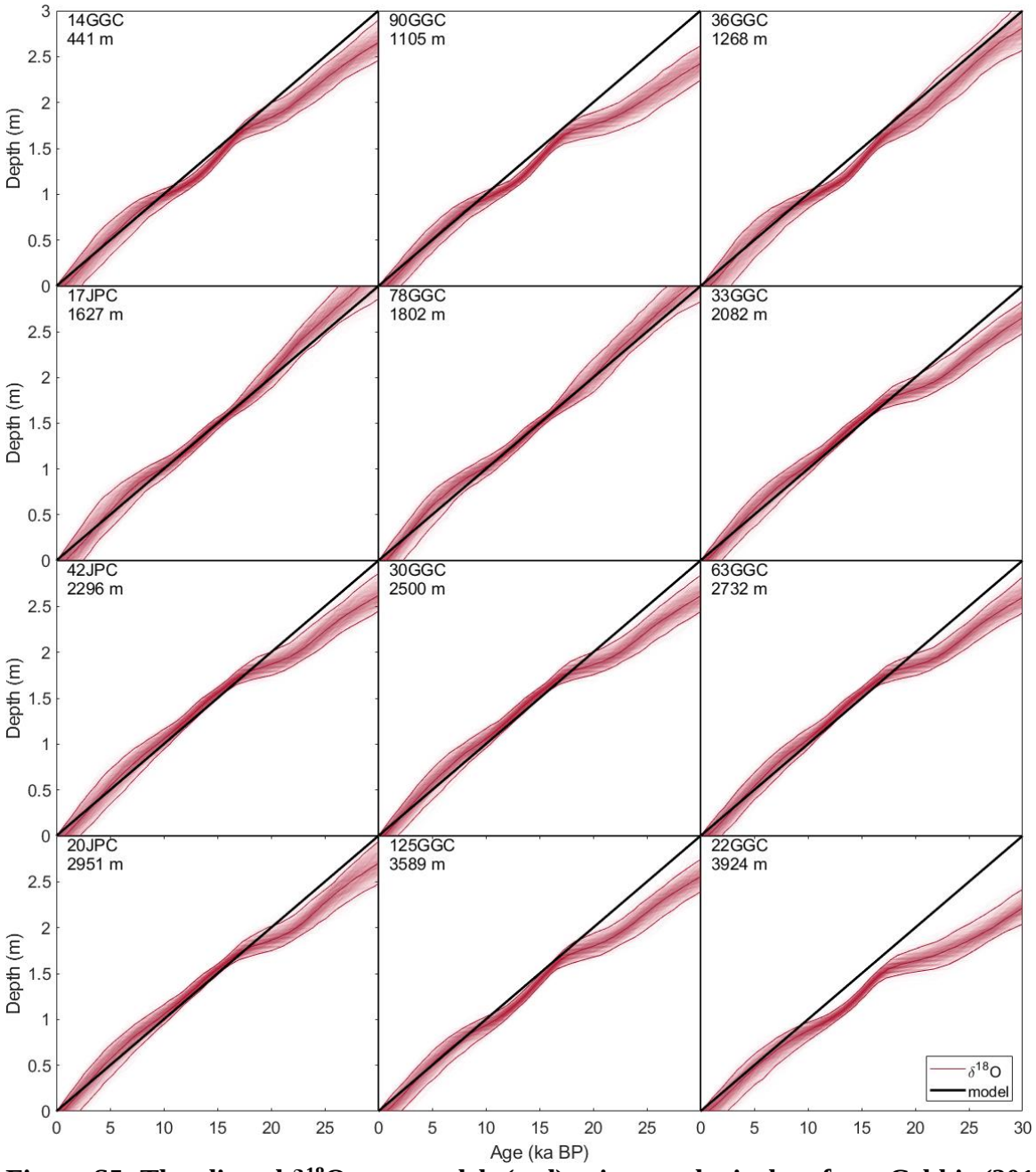

Figure S5: The aligned $\delta^{18}O_b$ age models (red) using synthetic data from Gebbie (2012) compared to the model age (solid black line).

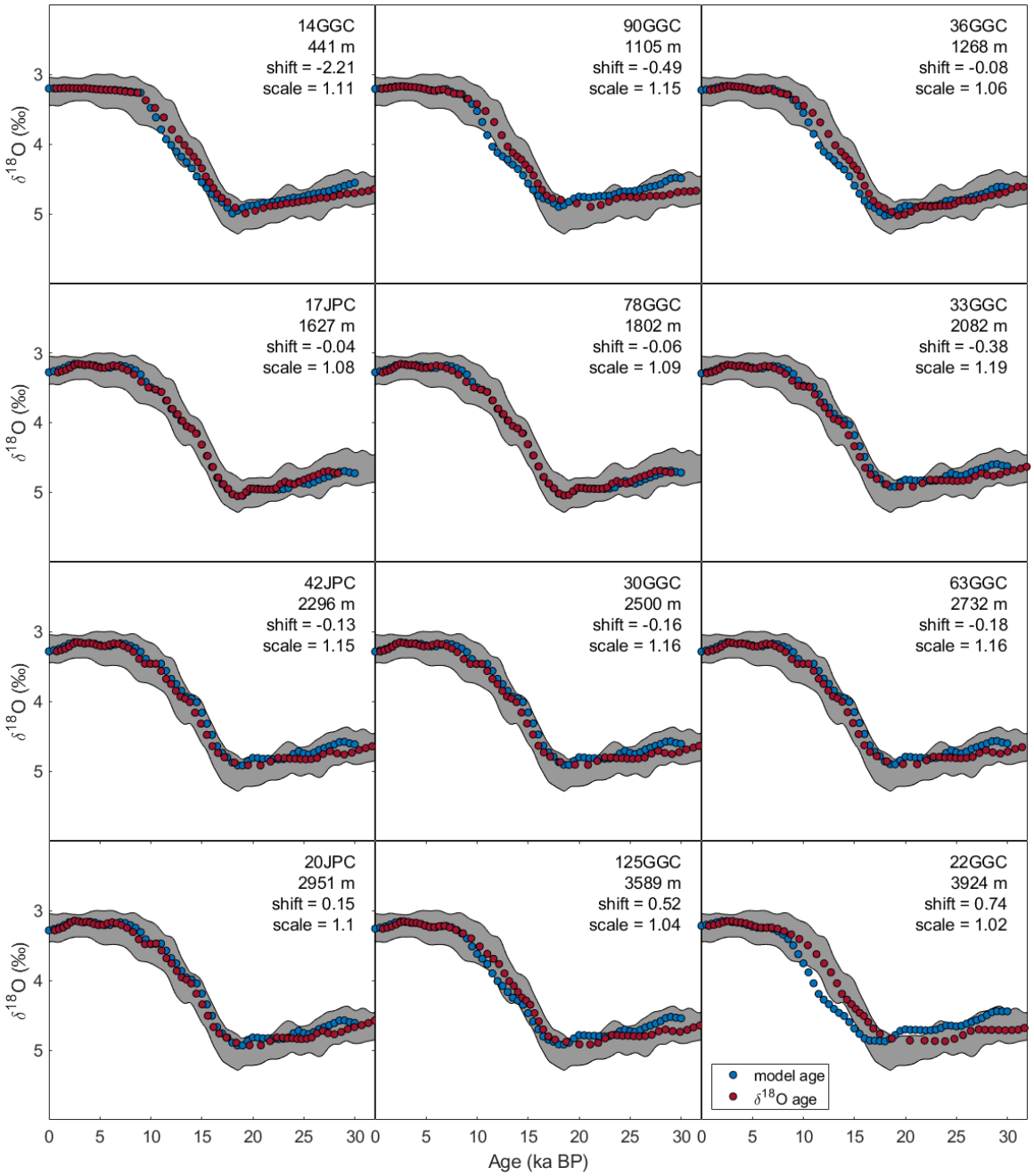

Figure S6: Synthetic $\delta^{18}O_b$ data from Gebbie (2012) plotted on the model age (blue) and $\delta^{18}O_b$ aligned age models (red).

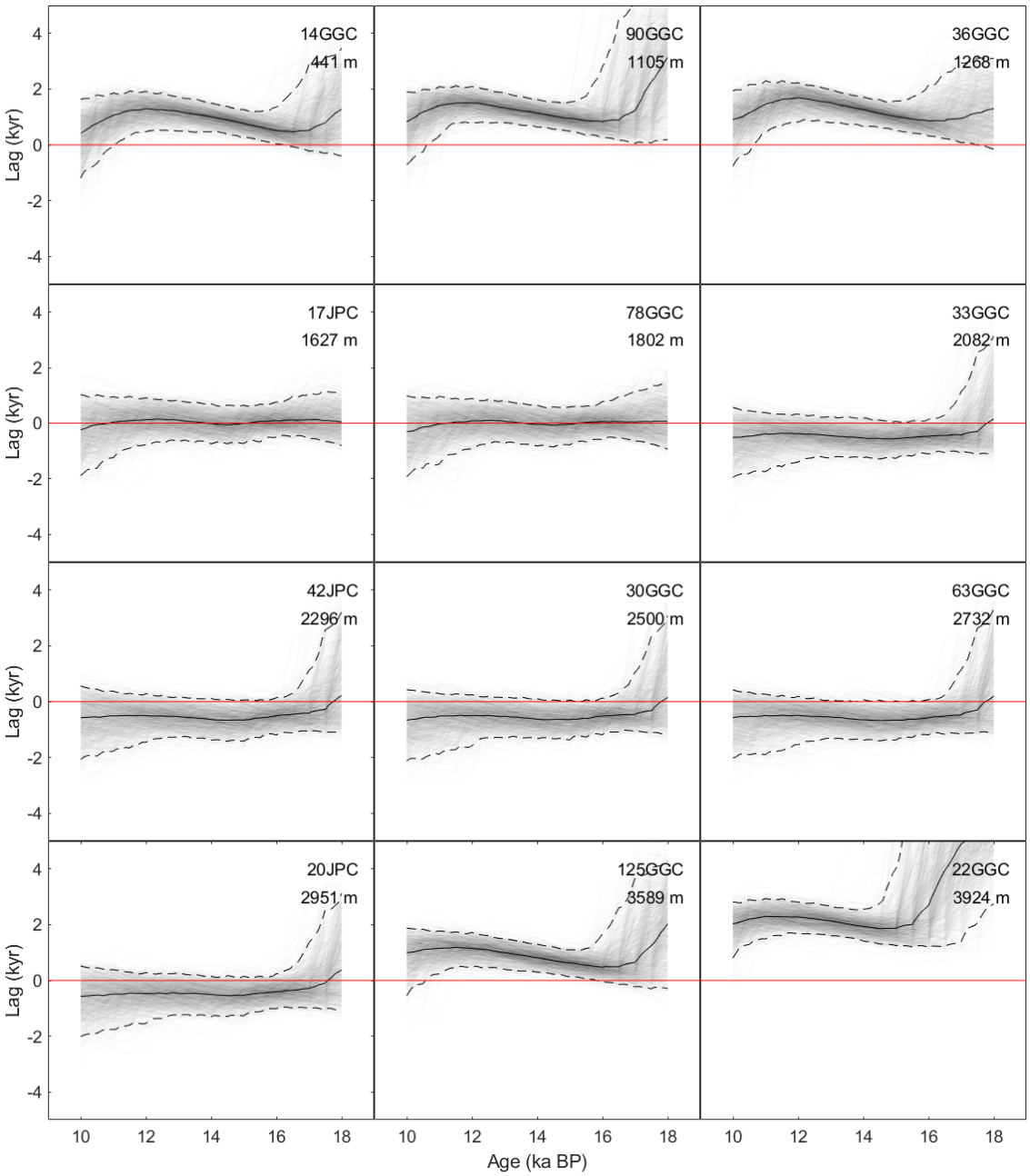

Figure S7: Lags calculated from the synthetic $\delta^{18}O_b$ data from Gebbie (2012).

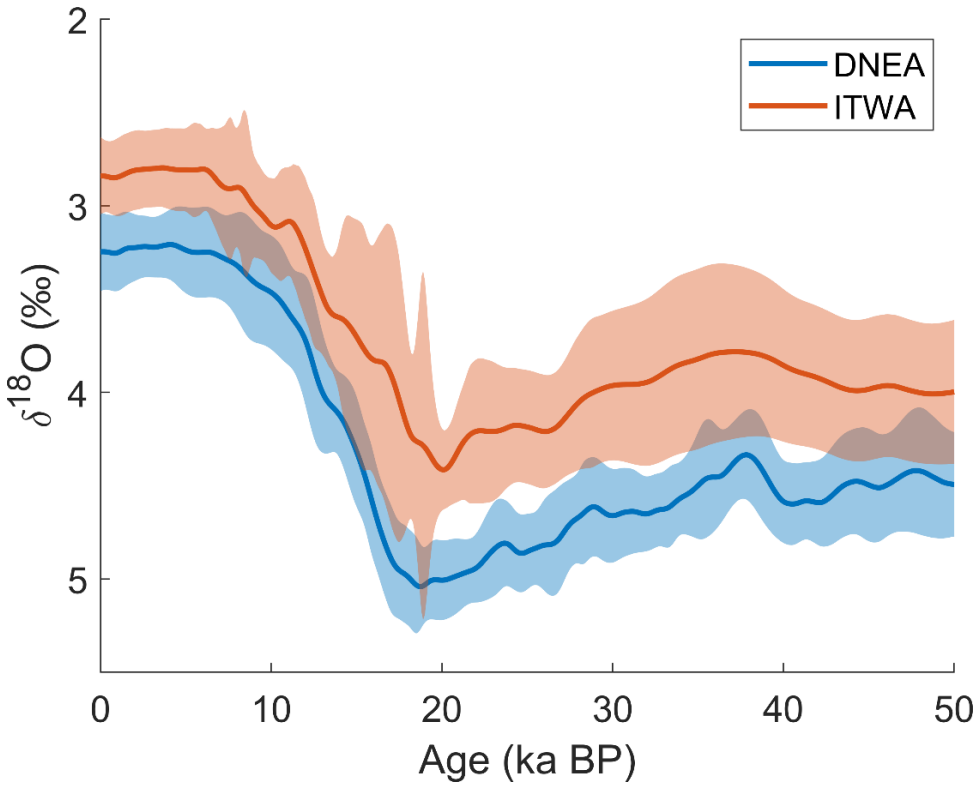

Figure S8: Comparison of the DNEA stack (blue) with the ITWA stack (red) from Lee & Rand et al., (in review). Between 20 and 10 ka BP, the ITWA stack has the larger standard deviation of 0.251 ‰ compared to the smaller DNEA standard deviation of 0.139 ‰. In addition, the ITWA stack records a T1 signal before the DNEA stack. Both of these factors will affect the core-specific lags which are relative to the target stack. The $\delta^{18}O_b$ -aligned age models

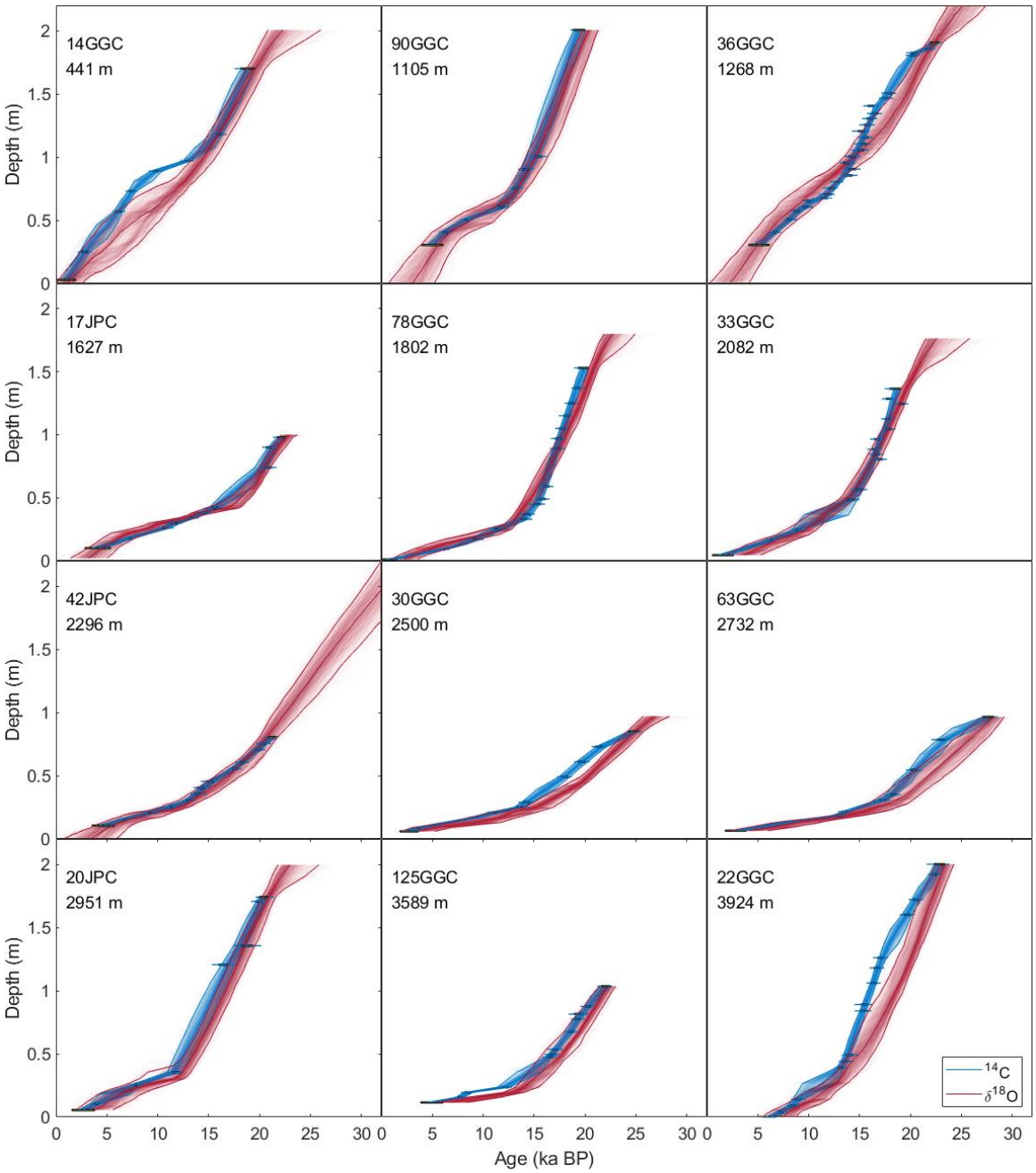

Figure S9: Default Radiocarbon age models (blue) and $\delta^{18}O_b$ (red) age models aligned to the ITWA stack.

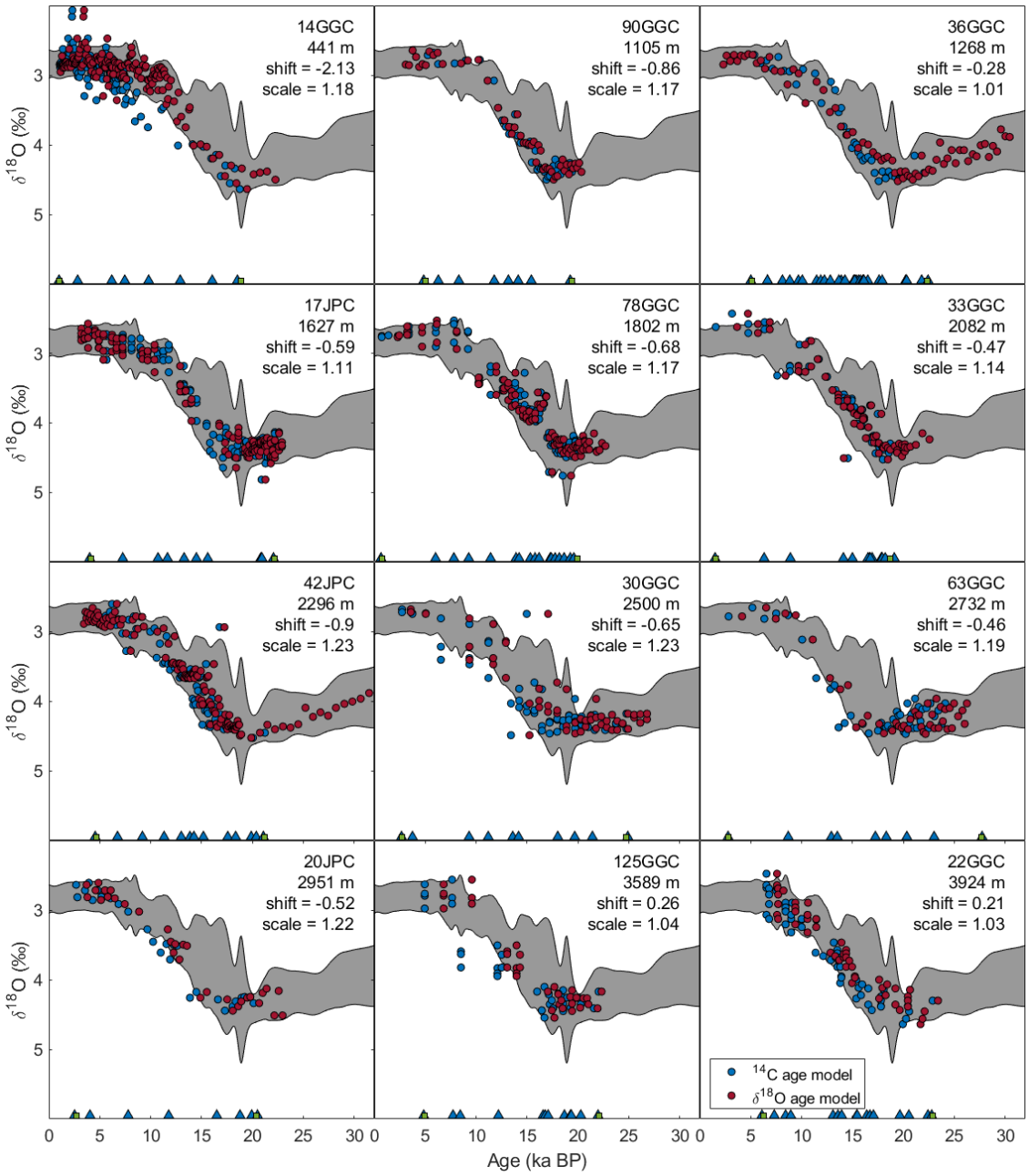

Figure S10: Benthic $\delta^{18}O_b$ plotted on the default radiocarbon age models (blue) and $\delta^{18}O_b$ age models aligned to the ITWA stack (red).

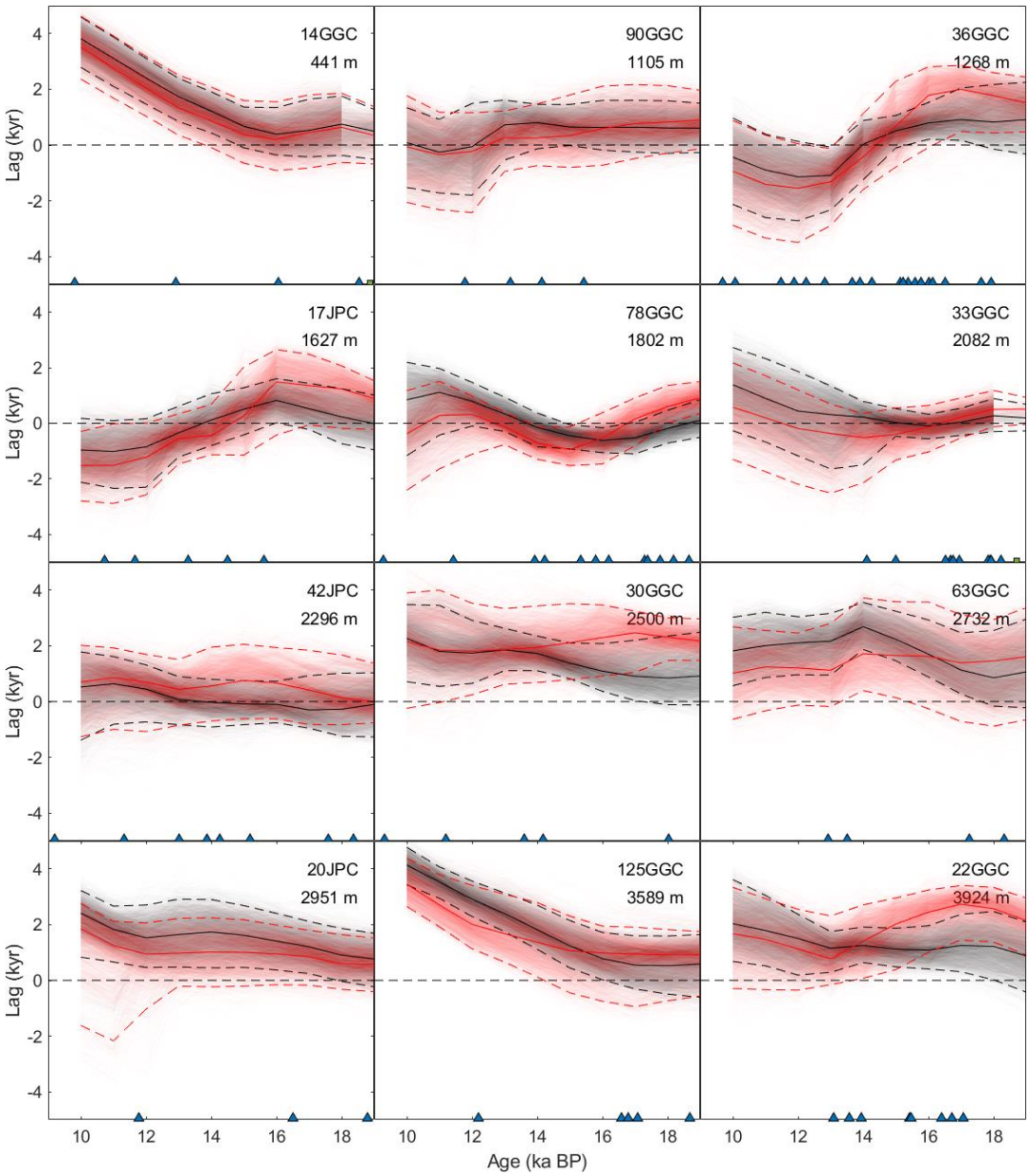

Figure S11: Lags resulting from the ITWA target stack (red) compared to the default lags using the DNEA target stack (black).

References

1. Adkins, J. F. and Boyle, E. A.: Changing atmospheric Δ14C and the record of deep water paleoventilation ages, Paleoceanography, 12, 337–344, https://doi.org/10.1029/97PA00379, 1997.
2. Barbante, C., Barnola, J.-M., Becagli, S., Beer, J., Bigler, M., Boutron, C., Blunier, T., Castellano, E., Cattani, O., Chappellaz, J., Dahl-Jensen, D., Debret, M., Delmonte, B., Dick, D., Falourd, S., Faria, S., Federer, U., Fischer, H., Freitag, J., Frenzel, A., Fritzsche, D., Fundel, F., Gabrielli, P., Gaspari, V., Gersonde, R., Graf, W., Grigoriev, D., Hamann, I., Hansson, M., Hoffmann, G., Hutterli, M. A., Huybrechts, P., Isaksson, E., Johnsen, S., Jouzel, J., Kaczmarska, M., Karlin, T., Kaufmann, P., Kipfstuhl, S., Kohno, M., Lambert, F., Lambrecht, A., Lambrecht, A., Landais, A., Lawer, G., Leuenberger, M., Littot, G., Loulergue, L., Lüthi, D., Maggi, V., Marino, F., Masson-Delmotte, V., Meyer, H., Miller, H., Mulvaney, R., Narcisi, B., Oerlemans, J., Oerter, H., Parrenin, F., Petit, J.-R., Raisbeck, G., Raynaud, D., Röthlisberger, R., Ruth, U., Rybak, O., Severi, M., Schmitt, J., Schwander, J., Siegenthaler, U., Siggaard-Andersen, M.-L., Spahni, R., Steffensen, J. P., Stenni, B., Stocker, T. F., Tison, J.-L., Traversi, R., Udisti, R., Valero-Delgado, F., van den Broeke, M. R., van de Wal, R. S. W., Wagenbach, D., Wegner, A., Weiler, K., Wilhelms, F., Winther, J.-G., Wolff, E., and EPICA Community Members: One-to-one coupling of glacial climate variability in Greenland and Antarctica, Nature, 444, 195–198, https://doi.org/10.1038/nature05301, 2006.
3. Barker, S., Diz, P., Vautravers, M. J., Pike, J., Knorr, G., Hall, I. R., and Broecker, W. S.: Interhemispheric Atlantic seesaw response during the last deglaciation, Nature, 457, 1097–1102, https://doi.org/10.1038/nature07770, 2009.
4. Barker, S., Knorr, G., Vautravers, M. J., Diz, P., and Skinner, L. C.: Extreme deepening of the Atlantic overturning circulation during deglaciation, Nature Geosci, 3, 567–571, https://doi.org/10.1038/ngeo921, 2010.
5. Barker, S., Knorr, G., Edwards, R. L., Parrenin, F., Putnam, A. E., Skinner, L. C., Wolff, E., and Ziegler, M.: 800,000 Years of Abrupt Climate Variability, Science, 334, 347–351, https://doi.org/10.1126/science.1203580, 2011.
6. Blunier, T. and Brook, E. J.: Timing of Millennial-Scale Climate Change in Antarctica and Greenland During the Last Glacial Period, Science, 291, 109–112, https://doi.org/10.1126/science.291.5501.109, 2001.
7. Boyle, E. A. and Keigwin, L.: North Atlantic thermohaline circulation during the past 20,000 years linked to high-latitude surface temperature, Nature, 330, 35–40, https://doi.org/10.1038/330035a0, 1987.
8. Broecker, W., Barker, S., Clark, E., Hajdas, I., Bonani, G., and Stott, L.: Ventilation of the Glacial Deep Pacific Ocean, Science, 306, 1169–1172, https://doi.org/10.1126/science.1102293, 2004.
9. Bryan, S. P., Marchitto, T. M., and Lehman, S. J.: The release of 14C-depleted carbon from the deep ocean during the last deglaciation: Evidence from the Arabian Sea, Earth and Planetary Science Letters, 298, 244–254, https://doi.org/10.1016/j.epsl.2010.08.025, 2010.
10. Buizert, C., Gkinis, V., Severinghaus, J. P., He, F., Lecavalier, B. S., Kindler, P., Leuenberger, M., Carlson, A. E., Vinther, B., Masson-Delmotte, V., White, J. W. C., Liu, Z., Otto-Bliesner, B., and Brook, E. J.: Greenland temperature response to climate forcing during the last deglaciation, Science, 345, 1177–1180, https://doi.org/10.1126/science.1254961, 2014.
11. Burke, A. and Robinson, L. F.: The Southern Ocean's Role in Carbon Exchange During the Last Deglaciation, Science, 335, 557–561, https://doi.org/10.1126/science.1208163, 2012.
12. Burke, A., Stewart, A. L., Adkins, J. F., Ferrari, R., Jansen, M. F., and Thompson, A. F.: The glacial mid-depth radiocarbon bulge and its implications for the overturning circulation, Paleoceanography, 30, 1021–1039, https://doi.org/10.1002/2015PA002778, 2015.
13. Came, R. E., Oppo, D. W., Curry, W. B., and Lynch-Stieglitz, J.: Deglacial variability in the surface return flow of the Atlantic meridional overturning circulation, Paleoceanography, 23, https://doi.org/10.1029/2007PA001450, 2008.

14. Cortese, G., Abelmann, A., and Gersonde, R.: The last five glacial-interglacial transitions: A high-resolution 450,000-year record from the subantarctic Atlantic, Paleoceanography, 22, https://doi.org/10.1029/2007PA001457, 2007.
15. Curry, W. B. and Oppo, D. W.: Glacial water mass geometry and the distribution of δ13C of ΣCO2 in the western Atlantic Ocean, Paleoceanography, 20, https://doi.org/10.1029/2004PA001021, 2005.
16. DeVries, T. and Primeau, F.: Dynamically and Observationally Constrained Estimates of Water-Mass Distributions and Ages in the Global Ocean, Journal of Physical Oceanography, 41, 2381–2401, https://doi.org/10.1175/JPO-D-10-05011.1, 2011.
17. Duplessy, J. C., Shackleton, N. J., Fairbanks, R. G., Labeyrie, L., Oppo, D., and Kallel, N.: Deepwater source variations during the last climatic cycle and their impact on the global deepwater circulation, Paleoceanography, 3, 343–360, https://doi.org/10.1029/PA003i003p00343, 1988.
18. Ferrari, R., Jansen, M. F., Adkins, J. F., Burke, A., Stewart, A. L., and Thompson, A. F.: Antarctic sea ice control on ocean circulation in present and glacial climates, Proceedings of the National Academy of Sciences, 111, 8753–8758, https://doi.org/10.1073/pnas.1323922111, 2014.
19. Freeman, E., Skinner, L. C., Waelbroeck, C., and Hodell, D.: Radiocarbon evidence for enhanced respired carbon storage in the Atlantic at the Last Glacial Maximum, Nat Commun, 7, 11998, https://doi.org/10.1038/ncomms11998, 2016.
20. Friedrich, T., Timmermann, A., Abe-Ouchi, A., Bates, N. R., Chikamoto, M. O., Church, M. J., Dore, J. E., Gledhill, D. K., González-Dávila, M., Heinemann, M., Ilyina, T., Jungclaus, J. H., McLeod, E., Mouchet, A., and Santana-Casiano, J. M.: Detecting regional anthropogenic trends in ocean acidification against natural variability, Nature Clim Change, 2, 167–171, https://doi.org/10.1038/nclimate1372, 2012.
21. Gebbie, G.: Tracer transport timescales and the observed Atlantic-Pacific lag in the timing of the Last Termination, Paleoceanography, 27, https://doi.org/10.1029/2011PA002273, 2012.
22. Gebbie, G.: How much did Glacial North Atlantic Water shoal?, Paleoceanography, 29, 190–209, https://doi.org/10.1002/2013PA002557, 2014.
23. Gebbie, G. and Huybers, P.: The Mean Age of Ocean Waters Inferred from Radiocarbon Observations: Sensitivity to Surface Sources and Accounting for Mixing Histories, Journal of Physical Oceanography, 42, 291–305, https://doi.org/10.1175/JPO-D-11-043.1, 2012.
24. Gebbie, G., Peterson, C. D., Lisiecki, L. E., and Spero, H. J.: Global-mean marine δ13C and its uncertainty in a glacial state estimate, Quaternary Science Reviews, 125, 144–159, https://doi.org/10.1016/j.quascirev.2015.08.010, 2015.
25. He, F., Shakun, J. D., Clark, P. U., Carlson, A. E., Liu, Z., Otto-Bliesner, B. L., and Kutzbach, J. E.: Northern Hemisphere forcing of Southern Hemisphere climate during the last deglaciation, Nature, 494, 81–85, https://doi.org/10.1038/nature11822, 2013.
26. Heaton, T. J., Köhler, P., Butzin, M., Bard, E., Reimer, R. W., Austin, W. E. N., Bronk Ramsey, C., Grootes, P. M., Hughen, K. A., Kromer, B., Reimer, P. J., Adkins, J., Burke, A., Cook, M. S., Olsen, J., and Skinner, L. C.: Marine20—The Marine Radiocarbon Age Calibration Curve (0–55,000 cal BP), Radiocarbon, 62, 779–820, https://doi.org/10.1017/RDC.2020.68, 2020.
27. Hoffman, J. L. and Lund, D. C.: Refining the stable isotope budget for Antarctic Bottom Water: New foraminiferal data from the abyssal southwest Atlantic, Paleoceanography, 27, https://doi.org/10.1029/2011PA002216, 2012.
28. Huang, K.-F., Oppo, D. W., and Curry, W. B.: Decreased influence of Antarctic intermediate water in the tropical Atlantic during North Atlantic cold events, Earth and Planetary Science Letters, 389, 200–208, https://doi.org/10.1016/j.epsl.2013.12.037, 2014.
29. Keigwin, L. D.: Radiocarbon and stable isotope constraints on Last Glacial Maximum and Younger Dryas ventilation in the western North Atlantic, Paleoceanography, 19, https://doi.org/10.1029/2004PA001029, 2004.
30. Keigwin, L. D. and Schlegel, M. A.: Ocean ventilation and sedimentation since the glacial maximum at 3 km in the western North Atlantic, Geochemistry, Geophysics, Geosystems, 3, 1–14, https://doi.org/10.1029/2001GC000283, 2002.

31. Labeyrie, L., Waelbroeck, C., Cortijo, E., Michel, E., and Duplessy, J.-C.: Changes in deep water hydrology during the Last Deglaciation, Comptes Rendus Geoscience, 337, 919–927, https://doi.org/10.1016/j.crte.2005.05.010, 2005.
32. Lee, T., Rand, D., Lisiecki, L. E., Gebbie, G., and Lawrence, C. E.: Bayesian age models and stacks: Combining age inferences from radiocarbon and benthic δ^{18}O stratigraphic alignment, EGUsphere, 1–29, https://doi.org/10.5194/egusphere-2022-734, 2022.
33. Lemieux-Dudon, B., Blayo, E., Petit, J.-R., Waelbroeck, C., Svensson, A., Ritz, C., Barnola, J.-M., Narcisi, B. M., and Parrenin, F.: Consistent dating for Antarctic and Greenland ice cores, Quaternary Science Reviews, 29, 8–20, https://doi.org/10.1016/j.quascirev.2009.11.010, 2010.
34. Lisiecki, L. E. and Raymo, M. E.: A Pliocene-Pleistocene stack of 57 globally distributed benthic δ18O records, Paleoceanography, 20, https://doi.org/10.1029/2004PA001071, 2005.
35. Lund, D. C., Tessin, A. C., Hoffman, J. L., and Schmittner, A.: Southwest Atlantic water mass evolution during the last deglaciation, Paleoceanography, 30, 477–494, https://doi.org/10.1002/2014PA002657, 2015.
36. Lynch-Stieglitz, J., Adkins, J. F., Curry, W. B., Dokken, T., Hall, I. R., Herguera, J. C., Hirschi, J. J.-M., Ivanova, E. V., Kissel, C., Marchal, O., Marchitto, T. M., McCave, I. N., McManus, J. F., Mulitza, S., Ninnemann, U., Peeters, F., Yu, E.-F., and Zahn, R.: Atlantic Meridional Overturning Circulation During the Last Glacial Maximum, Science, 316, 66–69, https://doi.org/10.1126/science.1137127, 2007.
37. Makou, M. C., Eglinton, T. I., Oppo, D. W., and Hughen, K. A.: Postglacial changes in El Niño and La Niña behavior, Geology, 38, 43–46, https://doi.org/10.1130/G30366.1, 2010.
38. Mangini, A., Godoy, J. M., Godoy, M. L., Kowsmann, R., Santos, G. M., Ruckelshausen, M., Schroeder-Ritzrau, A., and Wacker, L.: Deep sea corals off Brazil verify a poorly ventilated Southern Pacific Ocean during H2, H1 and the Younger Dryas, Earth and Planetary Science Letters, 293, 269–276, https://doi.org/10.1016/j.epsl.2010.02.041, 2010.
39. Marchitto, T. M. and Broecker, W. S.: Deep water mass geometry in the glacial Atlantic Ocean: A review of constraints from the paleonutrient proxy Cd/Ca, Geochemistry, Geophysics, Geosystems, 7, https://doi.org/10.1029/2006GC001323, 2006.
40. Marchitto, T. M., Lehman, S. J., Ortiz, J. D., Flückiger, J., and van Geen, A.: Marine Radiocarbon Evidence for the Mechanism of Deglacial Atmospheric CO2 Rise, Science, 316, 1456–1459, https://doi.org/10.1126/science.1138679, 2007.
41. Mashiotta, T. A., Lea, D. W., and Spero, H. J.: Glacial–interglacial changes in Subantarctic sea surface temperature and δ18O-water using foraminiferal Mg, Earth and Planetary Science Letters, 170, 417–432, https://doi.org/10.1016/S0012-821X(99)00116-8, 1999.
42. McManus, J. F., Francois, R., Gherardi, J.-M., Keigwin, L. D., and Brown-Leger, S.: Collapse and rapid resumption of Atlantic meridional circulation linked to deglacial climate changes, Nature, 428, 834–837, https://doi.org/10.1038/nature02494, 2004.
43. Members, W. D. P.: Precise interpolar phasing of abrupt climate change during the last ice age., Nature, 520, 661–665, https://doi.org/10.1038/nature14401, 2015.
44. Oppo, D. W., Curry, W. B., and McManus, J. F.: What do benthic δ13C and δ18O data tell us about Atlantic circulation during Heinrich Stadial 1?, Paleoceanography, 30, 353–368, https://doi.org/10.1002/2014PA002667, 2015.
45. Oppo, D. W., Gebbie, G., Huang, K.-F., Curry, W. B., Marchitto, T. M., and Pietro, K. R.: Data Constraints on Glacial Atlantic Water Mass Geometry and Properties, Paleoceanography and Paleoclimatology, 33, 1013–1034, https://doi.org/10.1029/2018PA003408, 2018.
46. Pahnke, K., Goldstein, S. L., and Hemming, S. R.: Abrupt changes in Antarctic Intermediate Water circulation over the past 25,000 years, Nature Geosci, 1, 870–874, https://doi.org/10.1038/ngeo360, 2008.
47. Pedro, J. B., van Ommen, T. D., Rasmussen, S. O., Morgan, V. I., Chappellaz, J., Moy, A. D., Masson-Delmotte, V., and Delmotte, M.: The last deglaciation: timing the bipolar seesaw, Clim. Past, 7, 671–683, https://doi.org/10.5194/cp-7-671-2011, 2011.

48. Pedro, J. B., Jochum, M., Buizert, C., He, F., Barker, S., and Rasmussen, S. O.: Beyond the bipolar seesaw: Toward a process understanding of interhemispheric coupling, Quaternary Science Reviews, 192, 27–46, https://doi.org/10.1016/j.quascirev.2018.05.005, 2018.
49. Rafter, P. A., Gray, W. R., Hines, S. K. V., Burke, A., Costa, K. M., Gottschalk, J., Hain, M. P., Rae, J. W. B., Southon, J. R., Walczak, M. H., Yu, J., Adkins, J. F., and DeVries, T.: Global reorganization of deep-sea circulation and carbon storage after the last ice age, Science Advances, 8, eabq5434, https://doi.org/10.1126/sciadv.abq5434, 2022.
50. Rickaby, R. E. M. and Elderfield, H.: Evidence from the high-latitude North Atlantic for variations in Antarctic Intermediate water flow during the last deglaciation, Geochemistry, Geophysics, Geosystems, 6, https://doi.org/10.1029/2004GC000858, 2005.
51. Schmittner, A., Saenko, O. A., and Weaver, A. J.: Coupling of the hemispheres in observations and simulations of glacial climate change, Quaternary Science Reviews, 22, 659–671, https://doi.org/10.1016/S0277-3791(02)00184-1, 2003.
52. Shackleton, N. J., Duplessy, J.-C., Arnold, M., Maurice, P., Hall, M. A., and Cartlidge, J.: Radiocarbon age of last glacial Pacific deep water, Nature, 335, 708–711, https://doi.org/10.1038/335708a0, 1988.
53. Shackleton, N. J., Hall, M. A., and Vincent, E.: Phase relationships between millennial-scale events 64,000–24,000 years ago, Paleoceanography, 15, 565–569, https://doi.org/10.1029/2000PA000513, 2000.
54. Shakun, J. D., Clark, P. U., He, F., Marcott, S. A., Mix, A. C., Liu, Z., Otto-Bliesner, B., Schmittner, A., and Bard, E.: Global warming preceded by increasing carbon dioxide concentrations during the last deglaciation, Nature, 484, 49–54, https://doi.org/10.1038/nature10915, 2012.
55. Sikes, E. L., Samson, C. R., Guilderson, T. P., and Howard, W. R.: Old radiocarbon ages in the southwest Pacific Ocean during the last glacial period and deglaciation, Nature, 405, 555–559, https://doi.org/10.1038/35014581, 2000.
56. Skinner, L. C. and Shackleton, N. J.: Rapid transient changes in northeast Atlantic deep water ventilation age across Termination I, Paleoceanography, 19, https://doi.org/10.1029/2003PA000983, 2004.
57. Skinner, L. C. and Shackleton, N. J.: An Atlantic lead over Pacific deep-water change across Termination I: implications for the application of the marine isotope stage stratigraphy, Quaternary Science Reviews, 24, 571–580, https://doi.org/10.1016/j.quascirev.2004.11.008, 2005.
58. Skinner, L. C., Fallon, S., Waelbroeck, C., Michel, E., and Barker, S.: Ventilation of the Deep Southern Ocean and Deglacial CO2 Rise, Science, 328, 1147–1151, https://doi.org/10.1126/science.1183627, 2010.
59. Skinner, L. C., Waelbroeck, C., Scrivner, A. E., and Fallon, S. J.: Radiocarbon evidence for alternating northern and southern sources of ventilation of the deep Atlantic carbon pool during the last deglaciation, Proceedings of the National Academy of Sciences, 111, 5480–5484, https://doi.org/10.1073/pnas.1400668111, 2014.
60. Skinner, L. C., Primeau, F., Freeman, E., de la Fuente, M., Goodwin, P. A., Gottschalk, J., Huang, E., McCave, I. N., Noble, T. L., and Scrivner, A. E.: Radiocarbon constraints on the glacial ocean circulation and its impact on atmospheric CO2, Nat Commun, 8, 16010, https://doi.org/10.1038/ncomms16010, 2017.
61. Sortor, R. N. and Lund, D. C.: No evidence for a deglacial intermediate water Δ14C anomaly in the SW Atlantic, Earth and Planetary Science Letters, 310, 65–72, https://doi.org/10.1016/j.epsl.2011.07.017, 2011.
62. Stern, J. V. and Lisiecki, L. E.: Termination 1 timing in radiocarbon-dated regional benthic δ18O stacks, Paleoceanography, 29, 1127–1142, https://doi.org/10.1002/2014PA002700, 2014.
63. Tessin, A. C. and Lund, D. C.: Isotopically depleted carbon in the mid-depth South Atlantic during the last deglaciation, Paleoceanography, 28, 296–306, https://doi.org/10.1002/palo.20026, 2013.
64. Thornalley, D. J. R., Barker, S., Broecker, W. S., Elderfield, H., and McCave, I. N.: The Deglacial Evolution of North Atlantic Deep Convection, Science, 331, 202–205, https://doi.org/10.1126/science.1196812, 2011.
65. Toggweiler, J. R. and Lea, D. W.: Temperature differences between the hemispheres and ice age climate variability, Paleoceanography, 25, https://doi.org/10.1029/2009PA001758, 2010.

66. Vázquez Riveiros, N., Waelbroeck, C., Skinner, L., Roche, D. M., Duplessy, J.-C., and Michel, E.: Response of South Atlantic deep waters to deglacial warming during Terminations V and I, Earth and Planetary Science Letters, 298, 323–333, https://doi.org/10.1016/j.epsl.2010.08.003, 2010.
67. Waelbroeck, C., Skinner, L. C., Labeyrie, L., Duplessy, J.-C., Michel, E., Vazquez Riveiros, N., Gherardi, J.-M., and Dewilde, F.: The timing of deglacial circulation changes in the Atlantic, Paleoceanography, 26, https://doi.org/10.1029/2010PA002007, 2011.
68. Xie, R. C., Marcantonio, F., and Schmidt, M. W.: Deglacial variability of Antarctic Intermediate Water penetration into the North Atlantic from authigenic neodymium isotope ratios, Paleoceanography, 27, https://doi.org/10.1029/2012PA002337, 2012.
69. Zhao, N., Marchal, O., Keigwin, L., Amrhein, D., and Gebbie, G.: A Synthesis of Deglacial Deep-Sea Radiocarbon Records and Their (In)Consistency With Modern Ocean Ventilation, Paleoceanography and Paleoclimatology, 33, 128–151, https://doi.org/10.1002/2017PA003174, 2018

IV. Benthic $\delta^{18}O$ Lags in the Atlantic During Termination 1

Abstract

Recent studies have identified lags between Atlantic benthic $\delta^{18}O$ records during Termination 1 (T1). These lags can introduce age errors during stratigraphic alignment but also offer an opportunity to improve ocean circulation reconstructions. However, lags and their uncertainties have yet to be mapped on a basin-wide scale. We present continuous lag time series with time-dependent uncertainties for 33 Atlantic cores between latitudes of 38^{o} N and 30^{o} S. A lag is defined by the difference between a core's radiocarbon age model and an age model based on synchronous $\delta^{18}O$ change (i.e., $\delta^{18}O$ stratigraphic alignment to the same stack; Rand et al., in review). Statistically significant negative lags (i.e., leads) with magnitudes reaching 2.07 [95% CI: 0.70 – 2.77] kyr are observed in the tropical West Atlantic at intermediate depths in the first half of Termination 1. In contrast, West Atlantic lags below 2500 m are positive and increase in the second half of the termination, reaching a magnitude of 3.45 [95% CI: 2.63 – 4.08] kyr. Statistically significant lags are less common in the East Atlantic. I find a statistically significant correlation ($r = -0.86$, $p = 10^{-4}$) between lags and the % change in SCW from the Last Glacial Maximum (LGM) to the modern. In addition to water mass geometry changes, leads in the intermediate West Atlantic may have also been caused by sub-surface warming associated with a cessation of the Atlantic Meridional Overturning Circulation (AMOC) or brine rejection due by sea ice formation. Furthermore, lags in the deep West Atlantic may be caused by a mid-depth age maximum. Using an idealized deglacial d18O signal and an ocean circulation inverse model, I empirically derive a lag equation to solve for a plausible combination of the factors that may

have caused the lags. I find that lags can be fit within their uncertainties 16 ka BP by enforcing a 2-kyr Southern Hemisphere surface lag, a 3 factor decrease in SCW circulation rates, and a 2 km shoaling of NADW.

1 Introduction

If lags can be consistently mapped on a basin wide scale, they may provide new evidence to constrain the physical phenomena that cause them (e.g., Waelbroeck et al., 2011). However, observations from previous studies are temporally discrete, have poor spatial coverage, and lack uncertainty estimates (Labeyrie et al., 2005; Skinner & Shackleton, 2005; Waelbroeck et al., 2011; Stern & Lisiecki, 2014; Lund et al., 2015). In addition, because each study uses a different lag calculation method, direct comparison between studies is difficult.

Here I present lags for a compilation of 33 Atlantic cores between latitudes of 38^{o} North and 30^{o} South and depths spanning 767 to 5010 m. Lags are calculated following the methods of Chapter 2 in which age models are constructed using the Bayesian software package BIGMACS (Lee & Rand et al., accepted). Time series of lags and their uncertainties are calculated by subtracting radiocarbon age model samples from $\delta^{18}O$ age model samples. Lags are relative to the Deep North East Atlantic (DNEA) stack (Lee & Rand et al., accepted) and are deemed statistically significant when the zero line falls outside of the lag's 95% credible interval. Here I analyze lags between 12 and 18 ka BP.

I find statistically significant leads in six cores primarily located at intermediate depths in the low-latitude West Atlantic reaching magnitudes of 2.07 [95% CI: 0.70 – 2.77] kyr. Statistically significant lags are calculated in nine cores from the deep and abyssal Brazil Margin and the abyssal North Atlantic with a maximum value equal to 3.45 [95% CI:

2.63 – 4.08] kyr. Furthermore, leads are observed to reach maximum values between 18-16 ka BP while lags have a larger magnitude 14-12 ka BP.

Lags can be caused by water mass geometry changes, asynchronous surface forcings, and/or changes in circulation rates. For example, brine rejection (Waelbroeck et al., 2011) or sub-surface warming (Marcott et al., 2011) may cause the observed leads in the intermediate West Atlantic during Heinrich Stadial 1 (HS1) while a longer surface-to-deep transit may be responsible for lags in the deep Brazil Margin and abyssal North Atlantic. Furthermore, if Northern Component Water (NCW) and Southern Component Water (SCW) had different $\delta^{18}O_{sw}$ values, a change in the local water mass geometry would also translate to the benthic $\delta^{18}O$ record. I present one method to solve for a combination of these factors capable of fitting lags within their 95% credible intervals. I find that lags can be reproduced with a 2-kyr Southern Hemisphere surface lag, a 3 factor decrease in SCW circulation rates, and a 2 km shoaling of NADW.

2 Background

Different circulation regimes during the LGM and T1 may be responsible for producing previously observed $\delta^{18}O_b$ lags in Atlantic cores (Waelbroeck et al., 2011, Layberie et al., 2005; Stern & Lisiecki 2014). Specifically, three potential contributing factors are (1) water mass boundary shifts, (2) circulation rate changes, and (3) asynchronous hemispheric surface forcings.

While modern seawater measurements of salinity, dissolved nutrients, and oxygen indicate North Atlantic Deep Water (NADW) flows south at depths centered between 2.5 – 3 km, proxy data indicates that NADW may have shoaled above 2 km during the LGM to form Glacial North Atlantic Intermediate Water (GNAIW). Measurements of benthic $\delta^{13}C$

(Boyle & Keigwin 1987; Duplessy et al., 1988; Curry & Oppo, 2005), Cd/Ca (Marchitto & Broecker, 2006; Makou et al., 2010), ε_{ND} (Howe et al., 2016 and references therein), and deep water ^{14}C ventilation ages (Skinner et al., 2014; Freeman et al., 2016; Skinner et al., 2017) indicate that AABW may have replaced NADW in the deep North Atlantic. However, the extent to which the interface between NADW and AABW shoaled is unclear, with some data inversions indicating the boundary may have been at a similar depth as today (Gebbie, 2014; Oppo et al., 2018). In addition, a recent compilation of ε_{ND} data found no evidence of AABW in the North Atlantic after accounting for changing end-member values (Pöppelmeier et al., 2020), and an inversion of benthic radiocarbon ages found a modern circulation state can fit the LGM radiocarbon distribution within uncertainty estimates (Zhao et al., 2018).

Lags may also have been caused by circulation rate changes during T1. Benthic-planktonic radiocarbon age differences and U/Th dates from corals suggest a poorly ventilated Southern Ocean and a mid-depth age maximum in the Atlantic during the LGM (Skinner et al., 2010; Mangini et al., 2010; Skinner 2017; Freeman et al., 2016). Furthermore, $^{231}Pa/^{230}Th$ ratios indicate a decrease in circulation rates in the North Atlantic during the LGM (Marchal et al., 2000; Hall et al., 2006), Heinrich Stadial 1 (HS1) and the Younger Dryas (YD, McManus et al., 2004; Gherardi et al., 2005; Bradtmiller et al., 2018). However, there is disagreement on the magnitude of the circulation slow down, with some studies suggesting a 50% reduction (Marchal et al., 2000) and others indicating a complete cessation during HS1 (McManus et al., 2004). Furthermore, the proxy's capability to accurately reconstruct circulation rates is uncertain due to a fractionation factor that is dependent on the particulate chemical composition during scavenging (Walter et al., 1997;

Yu et al., 2001; Chase et al., 2002; Geibert & Usbeck 2004). In addition, an inversion of $^{231}Pa/^{230}Th$ data found that modern circulation rates are capable of fitting the data when plausible uncertainties from age models and scavenging are accounted for (Burke et al., 2011).

Asynchronous changes in water mass properties caused by different hemispheric surface forcings may also contribute to $\delta^{18}O_b$ lags. Ice core proxies such as $\delta^{18}O_{ice}$, $\delta^{15}N$ and δD indicate that both the magnitude and timing of warming were different in the Northern and Southern Hemispheres (EPICA Community Members, 2006; Lemieux-Dudon et al., 2010; Pedro et al., 2011; Buizert et al., 2014; WAIS Divide project Members, 2015). This may have caused different water mass property changes for northern and southern sourced water. For example, in an Antarctic $\delta^{18}O$ ice core composite record significant warming begins 18.98 ka BP and continues until the Antarctic Climate Reversal 14.6 ka BP (ACR, Pedro et al., 2011). In Greenland, glacial conditions continue through HS1 until the onset of the Bølling at 14.64 ka BP (NGRIP members, 2004; Kindler et al., 2014).

3 Methods

3.1 Data Description

I initially compiled 50 Atlantic cores between latitudes of 40° North and 40° South that contained both benthic foraminiferal $\delta^{18}O$ and planktonic radiocarbon ages. Cores were rejected from the compilation if the of number of radiocarbon ages or $\delta^{18}O$ data points between 12 and 18 ka BP was less than 2 and 11 respectively, or if either record did not span the full time period. Additionally, one core (KNR159-5-14GGC) was rejected due to a shallow water depth of 440 m (see Table 2 for a list of rejected cores). Of the initial 50 cores that I compiled, 33 are included in the analysis spanning latitudes of 38° North to 30° South

and seafloor depths of 767 – 5010 m. The average number of radiocarbon ages per core between 12-18 ka BP is 6. (Six cores each have only two ages, and GeoB1711-4 has 24 ages.) The average number of $\delta^{18}O$ data points over the same time window is 46 (with a minimum of 11 in cores KNR197-10-17GGC and PC-CAM61 and a maximum 174 in core KNR197-3-9GGC). In total this study includes 206 radiocarbon ages and 1528 benthic $\delta^{18}O$ data points between 12 and 18 ka BP.

During analysis I separate cores into East and West Atlantic transects defined by -25 degree East longitude. In total, 10 cores are sampled from the East Atlantic (six of which are included in the DNEA stack) and 23 cores are from the West Atlantic.

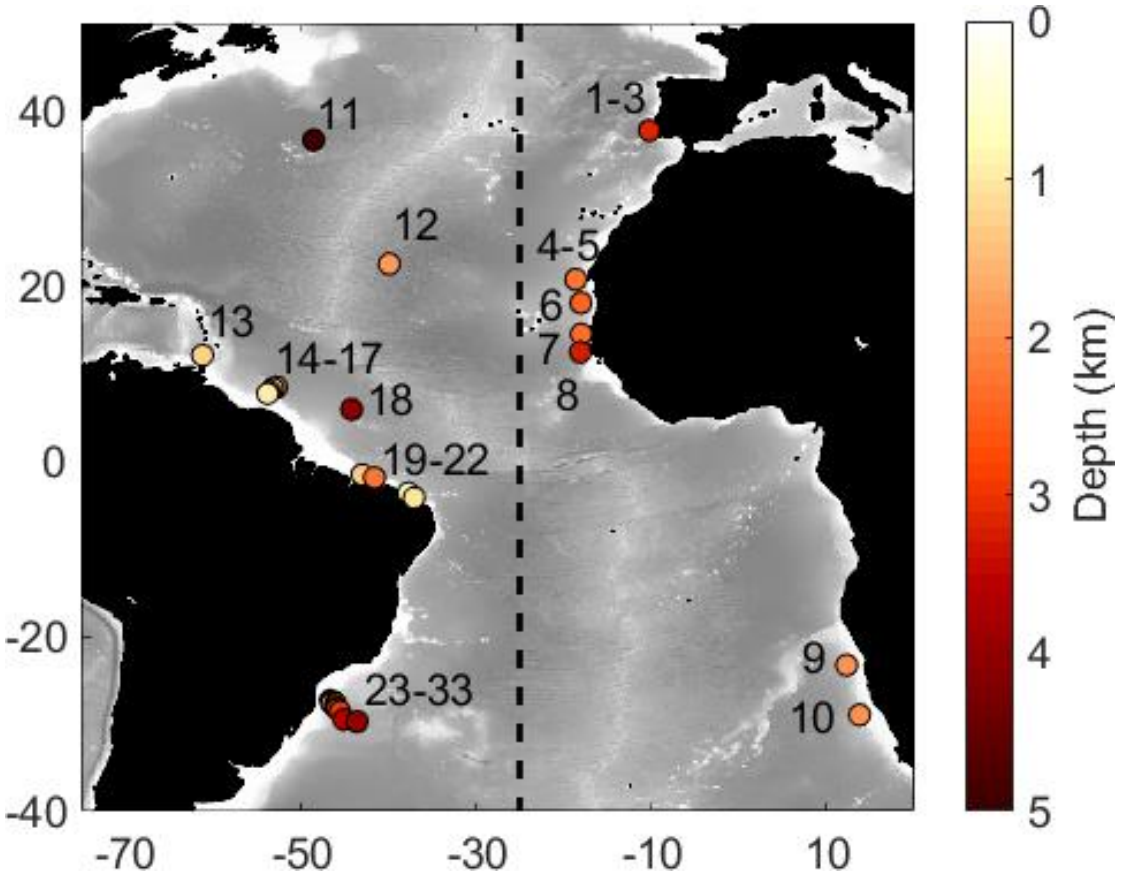

Figure 1: Atlantic core locations. Dotted line at -25 degrees East represents the separation between East and West cores. Numbers refer to the core numbers in Table 1 and Figures 2 and 3.

Core	Lat	Lon	Depth	Reference
East Atlantic				
1: MD95-2042	37.8	-10.17	3146	Bard et al., 2004; Hoogakker al., 2015; Shackleton et al., 2000; Shackleton et al., 2004
2: MD99-2334	37.8	-10.17	3166	Waelbroeck et al., 2019; Skinner & Shackleton, 2004;
3: SU81-18	37.77	-10.18	3135	Vogelsang et al., 2001; Waelbroeck et al., 2001
4: GeoB7920-2	20.75	-18.58	2278	Collins et al., 2011; Tjallingii et al., 2008
5: ODP658C	20.75	-18.58	2273	deMenocal et al., 2000; Knaack & Sarnthein, 2005
6: GIK13289-2	18.07	-18.01	2485	Sarnthein et al., 1994;
7: GeoB9508-5	14.5	-17.95	2384	Mulitza et al., 2008;
8: GeoB9526-5	12.44	-18.06	3223	Waelbroeck et al., 2019; Zarriess & Mackensen, 2011; Zarriess et al., 2011
9: GeoB1711-4	-23.32	12.38	1967	Little et al., 1997; Vidal et al., 1999; Shi et al., 2001; Waelbroeck et al., 2011; Balmer et al., 2016;
10: GeoB1720-2	-29	13.84	1997	Dickson et al., 2009
West Atlantic				
11: KNR197-10-17GGC	36.67	-48.54	5010	Keigwin & Swift,2017;
12: PC-CAM61	22.52	-39.9	1890	Umling et al., 2019
13: M35003-4	12.09	-61.24	1299	Hüls & Zahn 2000;
14: KNR197-3-36GGC	8.42	-52.79	2422	Oppo et al., 2018
15: KNR197-3-53GGC	8.23	-53.23	1272	Oppo et al., 2018
16: KNR197-3-9GGC	7.93	-53.58	1100	Oppo et al., 2018
17: KNR197-3-46CDH	7.7	-53.79	947	Oppo et al., 2018
18: EW9209-1JPC	5.91	-44.2	4056	Curry et al., 1996; Curry et al., 1999
19: GeoB16206-1	-1.58	-43.02	1367	Portilho-Ramos et al., 2017; Voigt et al., 2017; Mulitza et al., 2017
20: GeoB16206-2	-1.91	-41.59	2247	Portilho-Ramos et al., 2017; Voigt et al., 2017; Mulitza et al., 2017
21: GeoB3104-1	-3.67	-37.72	767	Arz et al., 1998; Arz et al., 1999
22: GS07-150-17-1GC-A	-4.21	-37.07	1000	Voigt et al., 2017; Waelbroeck et al., 2019;
23: KNR159-5-90GGC	-27.35	-46.63	1105	Lund et al., 2015
24: KNR159-5-78GGC	-27.48	-46.33	1802	Tessin & Lund, 2013
25: KNR159-5-36GGC	-27.52	-46.47	1268	Sortor & Lund, 2011; Lund et al., 2015
26: KNR159-5-33GGC	-27.57	-46.18	2082	Tessin & Lund, 2013; Lund et al., 2015
27: KNR159-5-17JPC	-27.7	-46.48	1627	Tessin & Lund, 2013; Lund et al., 2015
28: KNR159-5-42JPC	-27.77	-46.03	2296	Hoffman & Lund, 2012

29: KNR159-5-30GGC	-28.13	-46.07	2500	Tessin & Lund, 2013; Lund et al., 2015
30:KNR159-5-63GGC	-28.36	-45.84	2732	Lund et al., 2015
31:KNR159-5-20JPC	-28.64	-45.54	2951	Lund et al., 2015
32: KNR159-5-125GGC	-29.53	-45.08	3589	Hoffman & Lund, 2012
33: KNR159-5-22GGC	-29.78	-43.58	3924	Hoffman & Lund, 2012; Lund et al., 2015;

Table 1: Core locations and data citations. Rows 1 – 11 are cores from the East Atlantic and 12 – 34 are cores from the West Atlantic (defined by the -25 degree East longitude displayed in Figure 1). Core numbers are consistent for Figures 1, 2, and 4.

3.2 Age Model Construction and Lag Calculation

The age model construction and lag calculation method is the same that outlined in chapter 2. I use the Bayesian software package BIGMACS (Lee & Rand et al., accepted) to construct ^{14}C-only and $\delta^{18}O$-only age models. Radiocarbon ages are calibrated with the Marine20 calibration curve (Heaton et al., 2020), a reservoir age offset (ΔR) equal to zero, and a reservoir age standard deviation equal to 200 years. Benthic $\delta^{18}O$-only age models are constructed by aligning records to the DNEA stack (Lee & Rand et al., accepted). Additional ages are added to the $\delta^{18}O$-only age models at the depth locations of the first and last radiocarbon ages to assist the alignments. These ages are modeled as Gaussian distributions with medians equal to the median of the respective radiocarbon age model and standard deviations equal to the 68% half width. Because the additional ages are derived from the radiocarbon age models, they serve to encourage a lag equal to zero. No additional age falls within the 12-18 ka BP time period. The oldest start age is equal to 9.16 ka BP in core GIK13289-2, and the youngest end age is equal to 18.73 ka BP in core KNR159-5-17JPC.

Lags are calculated by subtracting radiocarbon age model samples from $\delta^{18}O$ age model samples. The age model for each lag is determined by its respective radiocarbon age model sample. A positive lag indicates a later timing of $\delta^{18}O$ change in that core compared

to the DNEA stack, while a negative lag (or lead) implies an earlier timing of $\delta^{18}O$ change. Age models and lags are calculated every 1 kyr between 5 and 25 ka BP to the extent permitted by ^{14}C and $\delta^{18}O$ data coverage. However, because $\delta^{18}O$ alignments (and therefore lags) are less reliable during time periods where $\delta^{18}O$ signals are relatively flat (e.g., the Holocene and the LGM), we restrict analysis of lags to a time window of 12-18 ka BP.

4 Results

4.1 Age Model and Lag Results

Age models and lag time series are displayed for the 33 Atlantic cores in Figure 2. The average widths of the 95% credible intervals for the ^{14}C-only and $\delta^{18}O$-only age models are 1.20 kyr and 1.79 kyr, respectively. The uncertainty from both age models is incorporated into the lag results, giving an average 95% credible width of 2.43 kyr for lag estimates between 12 - 18 kyr BP. The median value of all calculated lags is equal to 0.20 kyr with a standard deviation of 1.01 kyr, indicating that the DNEA stack approximates the average timing of T1 benthic $\delta^{18}O$ change for the Atlantic cores in this compilation. The largest lag between 12 and 18 ka BP is equal to 3.45 [95% CI: 2.63 – 4.08] kyr at 12 ka BP in core EW9209-1JPC in the deep North Atlantic and the largest lead is equal to 2.07 [95% CI: 0.70 – 2.77] kyr at 15 ka BP in core KNR197-3-46CDH in intermediate waters at the Demerara Rise. Figures 3 and 4 display the spatial distribution of lags for the East and West Atlantic. The East Atlantic contains only one statistically significant lag in core ODP658C equal to 1.15 [95% CI: 0.06 – 2.28] kyr at 16 ka BP.

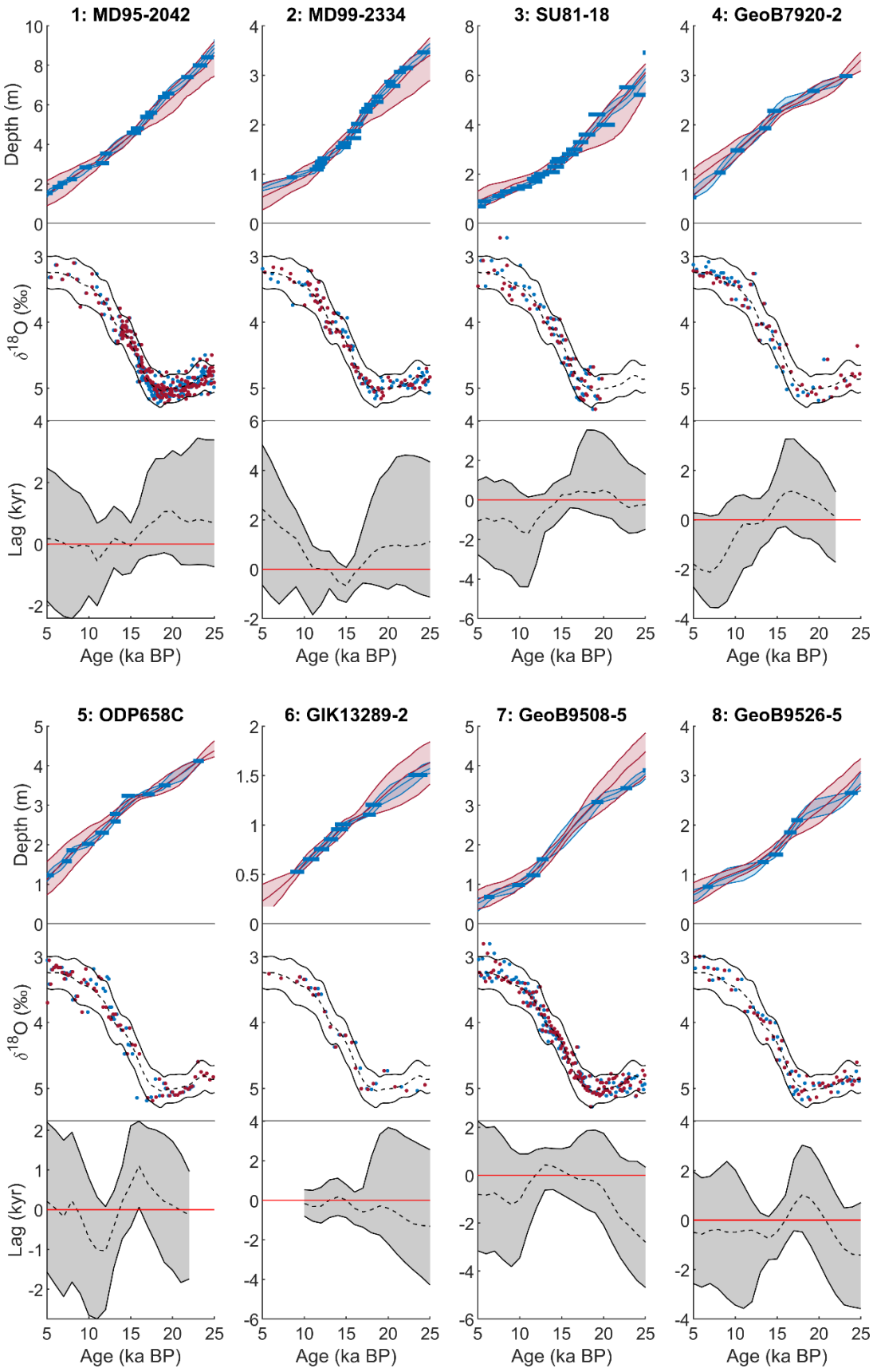
1: MD95-2042
2: MD99-2334
3: SU81-18
4: GeoB7920-2
5: ODP658C
6: GIK13289-2
7: GeoB9508-5
8: GeoB9526-5
Depth (m)
δ18O (‰)
Lag (kyr)
Age (ka BP)

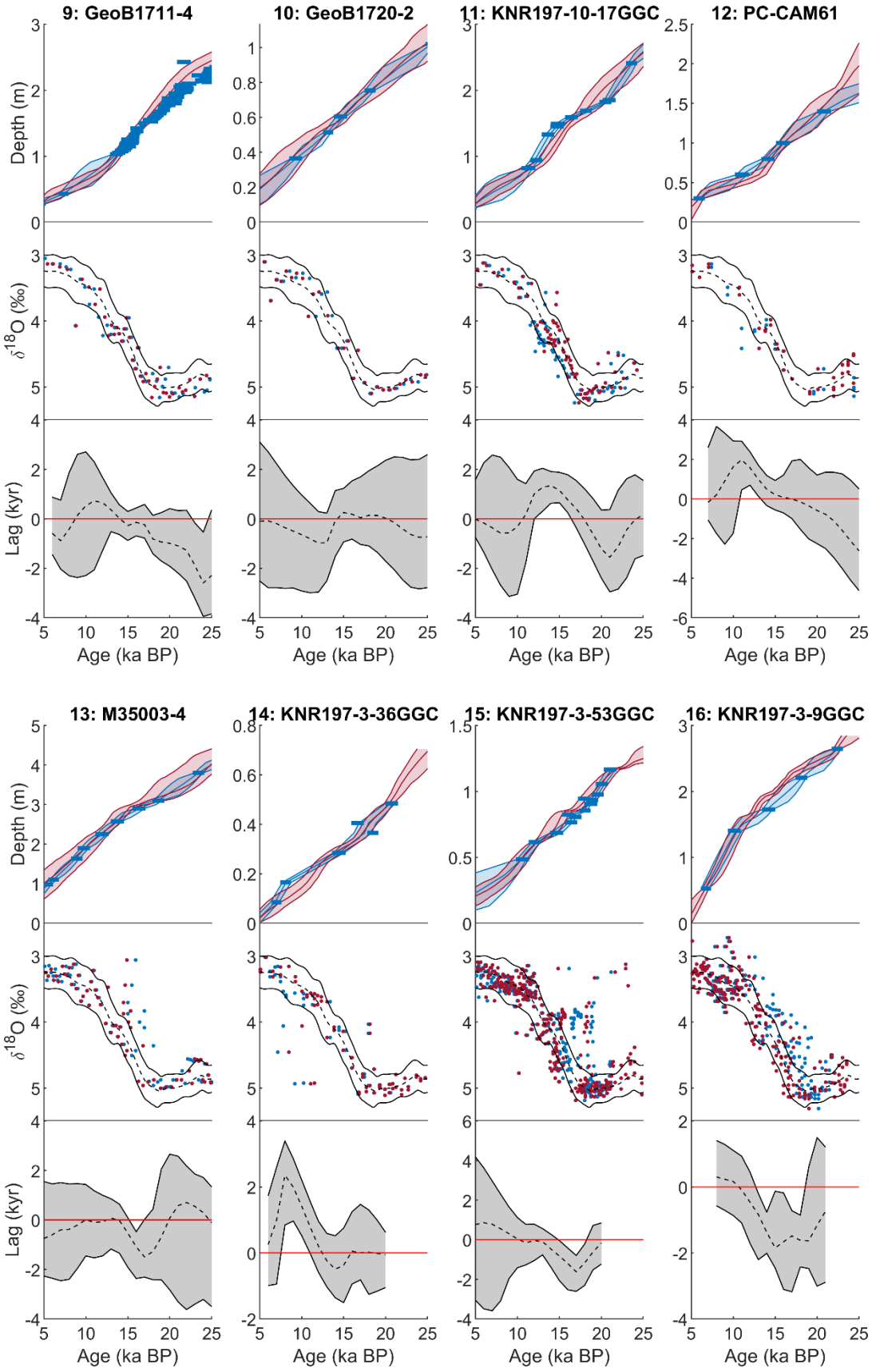
9: GeoB1711-4
10: GeoB1720-2
11: KNR197-10-17GGC
12: PC-CAM61
13: M35003-4
14: KNR197-3-36GGC
15: KNR197-3-53GGC
16: KNR197-3-9GGC
Depth (m)
δ18O (‰)
Lag (kyr)
Age (ka BP)

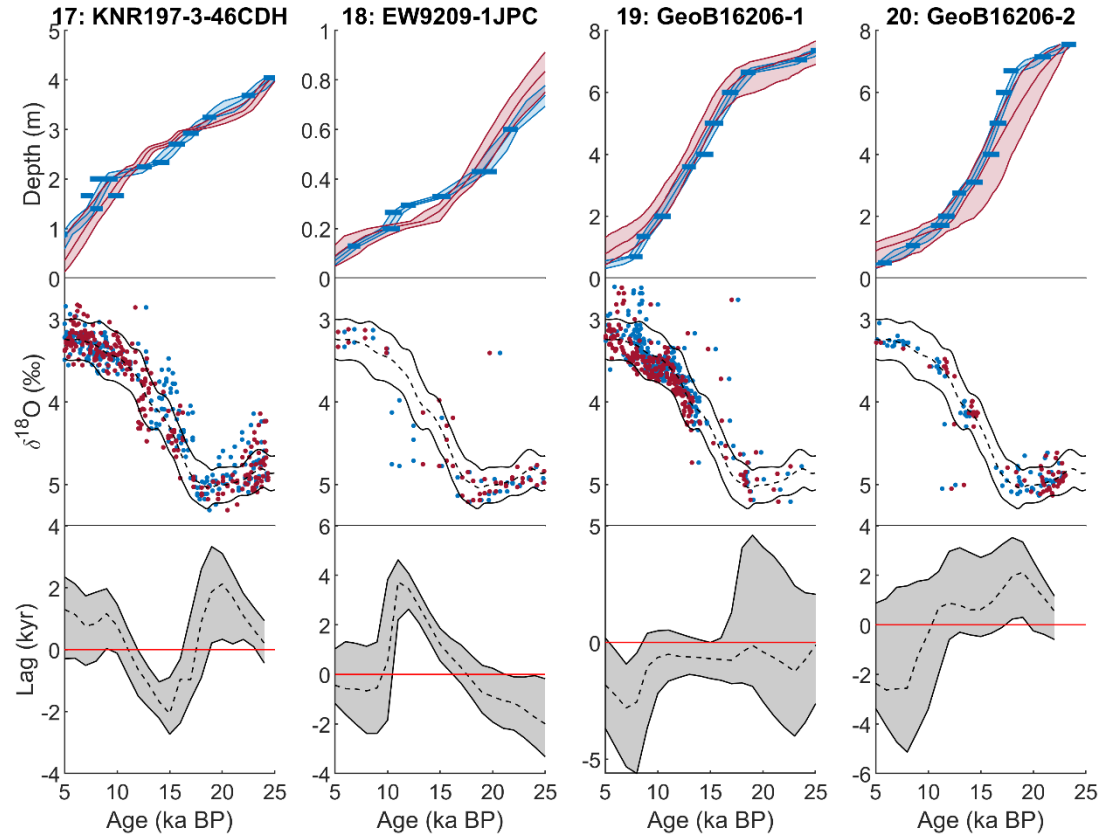
17: KNR197-3-46CDH
18: EW9209-1JPC
19: GeoB16206-1
20: GeoB16206-2
Depth (m)
δ18O (‰)
Lag (kyr)
Age (ka BP)

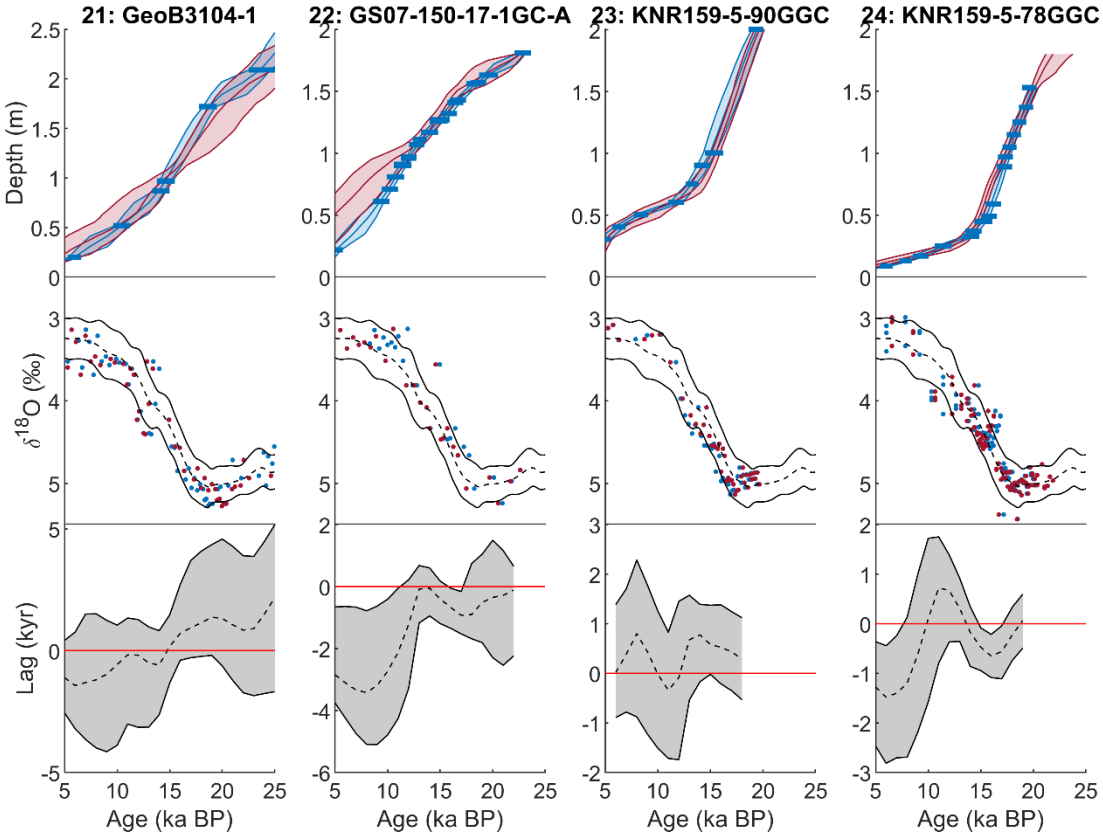
21: GeoB3104-1
22: GS07-150-17-1GC-A
23: KNR159-5-90GGC
24: KNR159-5-78GGC
Depth (m)
δ18O (‰)
Lag (kyr)
Age (ka BP)

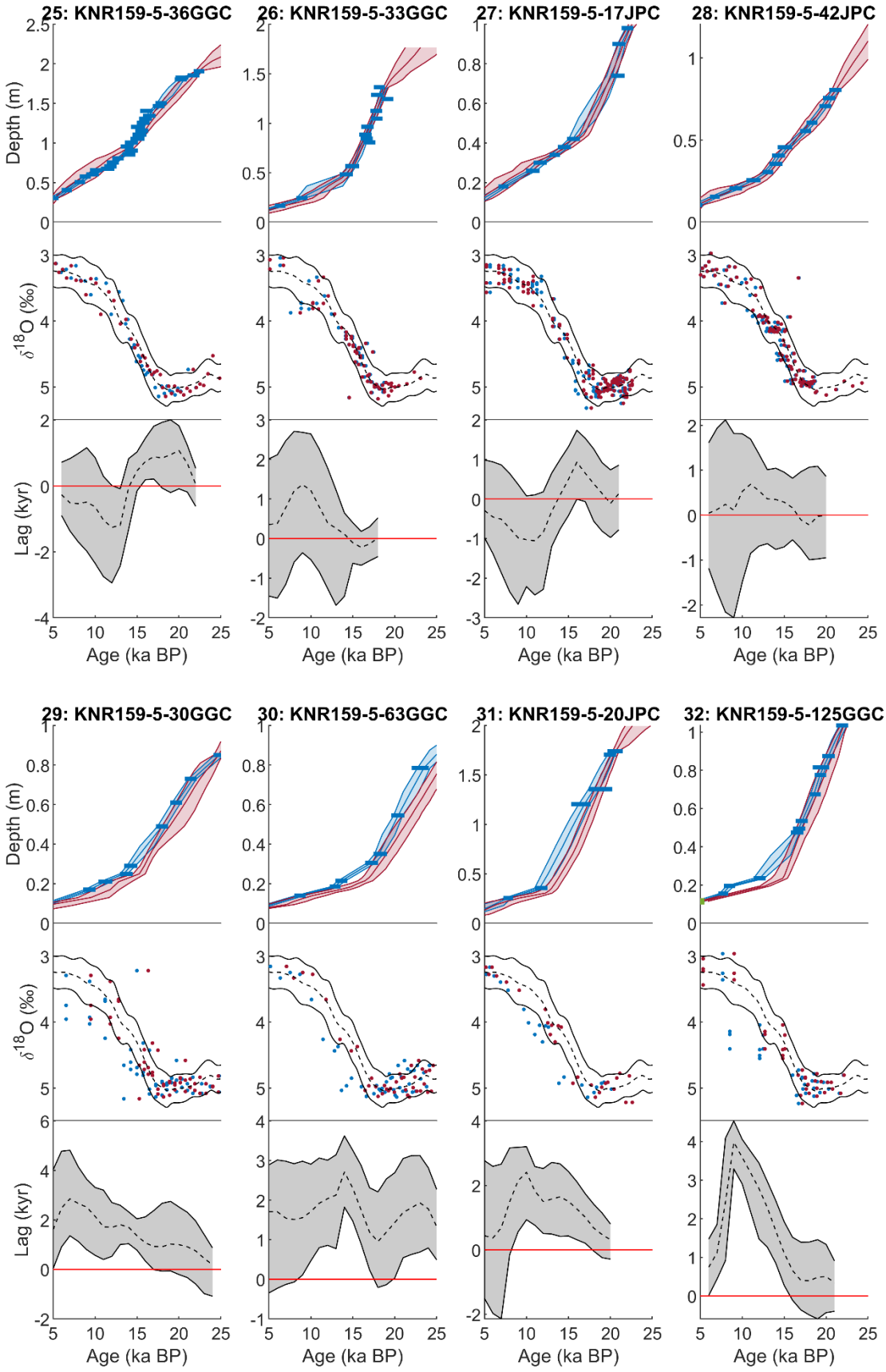
25: KNR159-5-36GGC
26: KNR159-5-33GGC
27: KNR159-5-17JPC
28: KNR159-5-42JPC
29: KNR159-5-30GGC
30: KNR159-5-63GGC
31: KNR159-5-20JPC
32: KNR159-5-125GGC
Depth (m)
δ18O (‰)
Lag (kyr)
Age (ka BP)

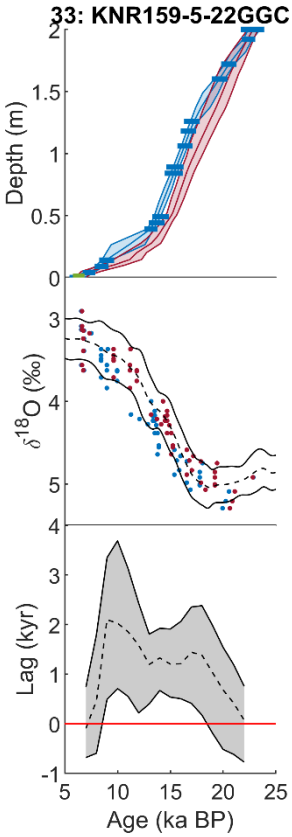

Figure 2: Age model and lag results for the 34 Atlantic cores included in this study. (Top) Age vs. Depth plot comparing the C14-only (blue) and $\delta^{18}O$-only (red) age models. Solid vertical lines represent upper and lower 95% credible intervals and median values and the thick blue horizontal lines represent radiocarbon ages. (Middle) The shifted and scaled $\delta^{18}O$ data on the C14-only age model (blue) and the $\delta^{18}O$ -only age model (red) plotted against the DNEA stack (solid and dotted black lines represent the upper and lower 2-sigma and median values respectively). (Bottom) The lag time-series for each core calculated by subtracting C14-only from $\delta^{18}O$-only samples.

In total 9 cores from the West Atlantic result in statistically significant (positive) lags relative to the DNEA stack during T1. These are primarily deep cores from below 2.5 km, with five from the deep and abyssal Brazil Margin, one near the equator at a depth of 4056 m (EW9209-1JPC), one from the deep North Atlantic (at 36.67° North at a depth of 5010 m), one from 22.52° North at a depth of 1890 m, and the last at 1.91° South at a depth of 2247 m. Each core has a maximum statistically significant lag in the latter half of the

termination (between 14 and 12 ka BP) except for core GeoB16206-2 which has a maximum lag at 18 ka BP (Figure 5).

Statistically significant leads (negative lags) relative to the DNEA stack are observed in 6 West Atlantic cores shallower than 2 km. One core is from the Bahamas, 3 cores are from the Demerara rise, one core is sampled off the North coast of Brazil, and one core is from the lower intermediate depth group of the Brazil Margin, as described in Chapter 2. The maximum statistically significant lead for each core occurs before 15 ka BP. Core GS07-150-17-1GC-A, which has a maximum lead at 12 ka BP, also has a locally maximum lead that is statistically significant at approximately 18 ka BP (Figure 6).

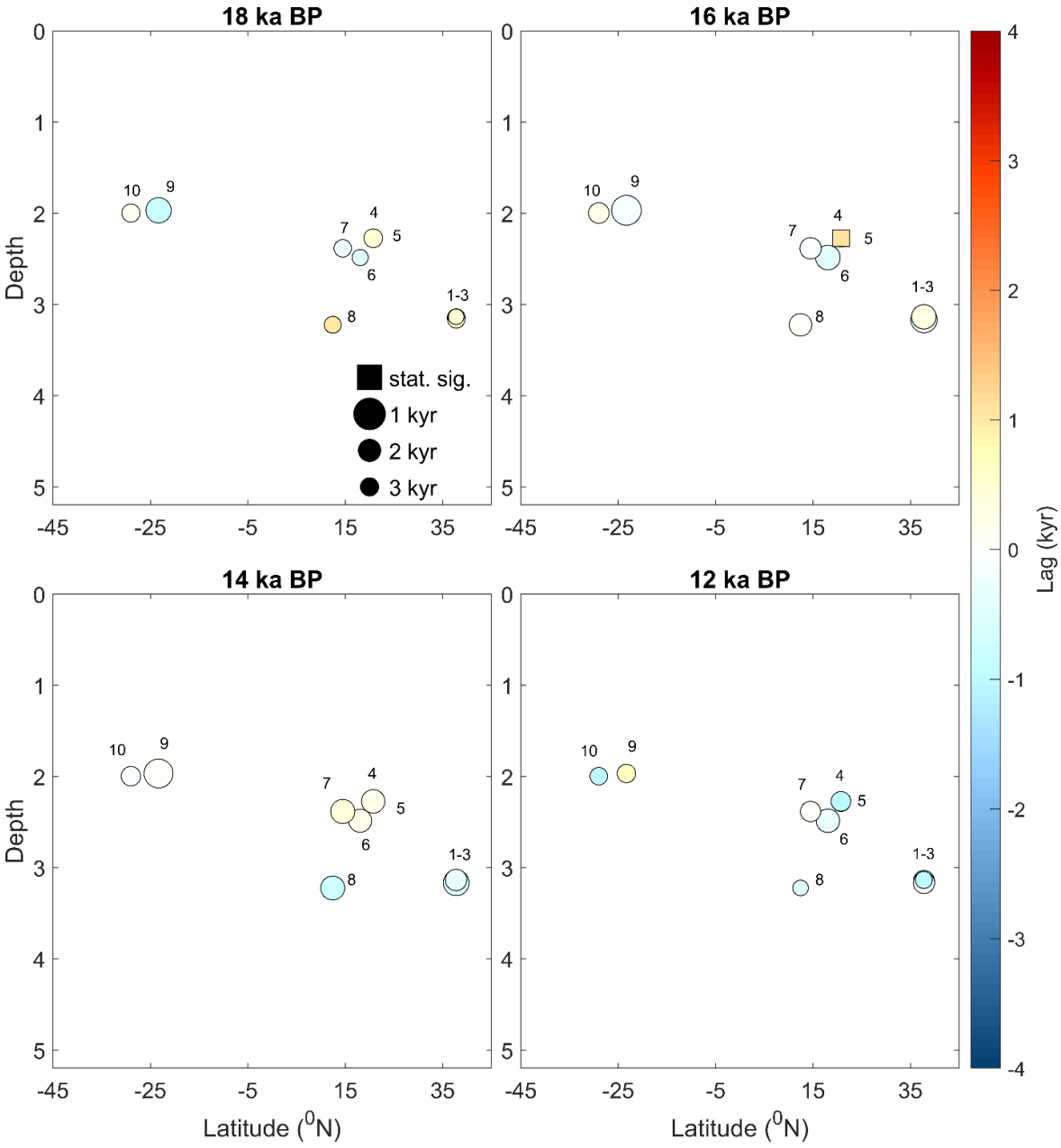

Figure 3: East Atlantic Lags plotted from 12 to 18 ka BP. Size of the symbol is inversely proportional to the 95% credible interval width, colors correspond to the magnitude of the lag, and squares denote lags that are statistically significant.

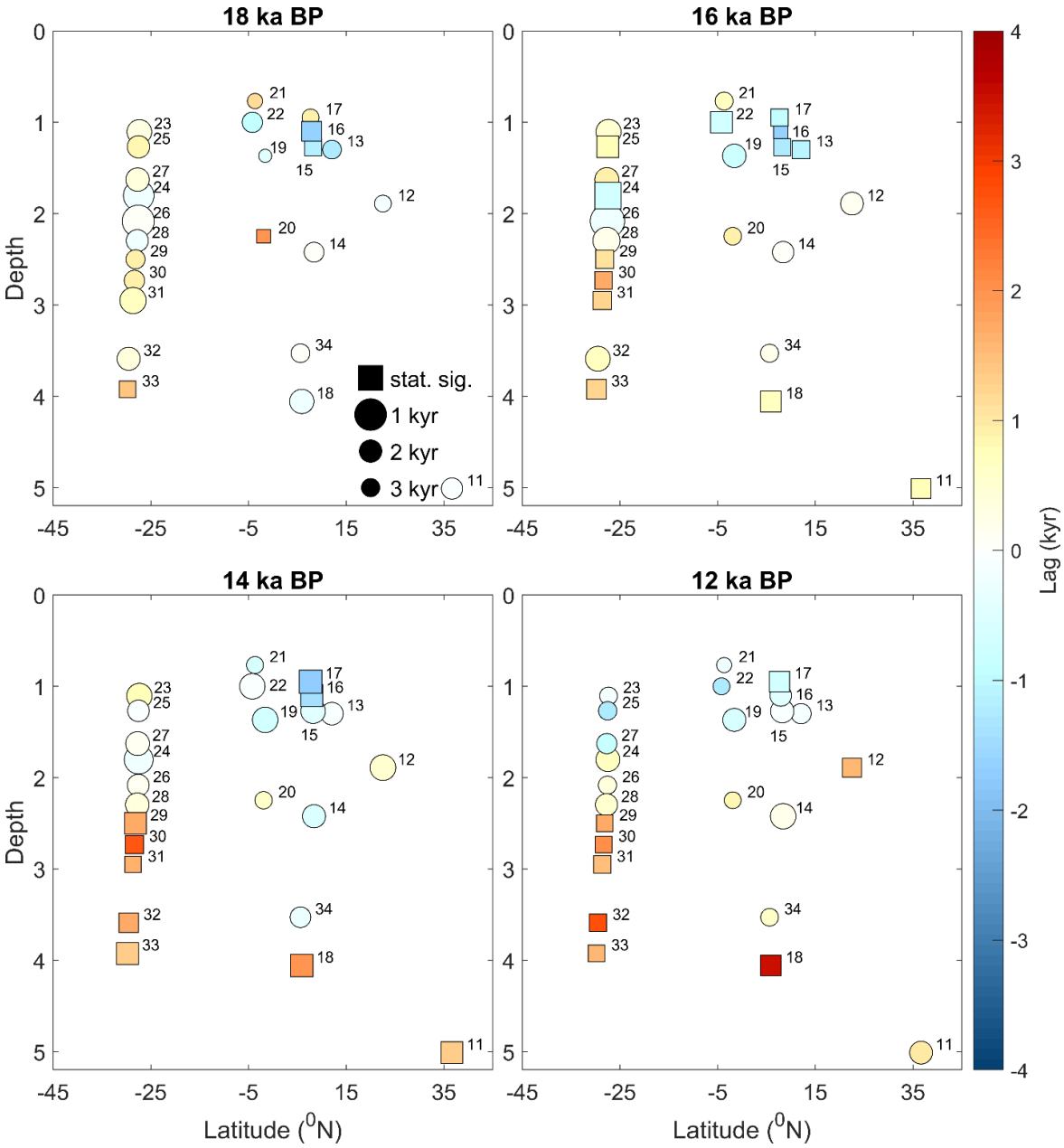

Figure 4: West Atlantic Lags plotted from 12 to 18 ka BP

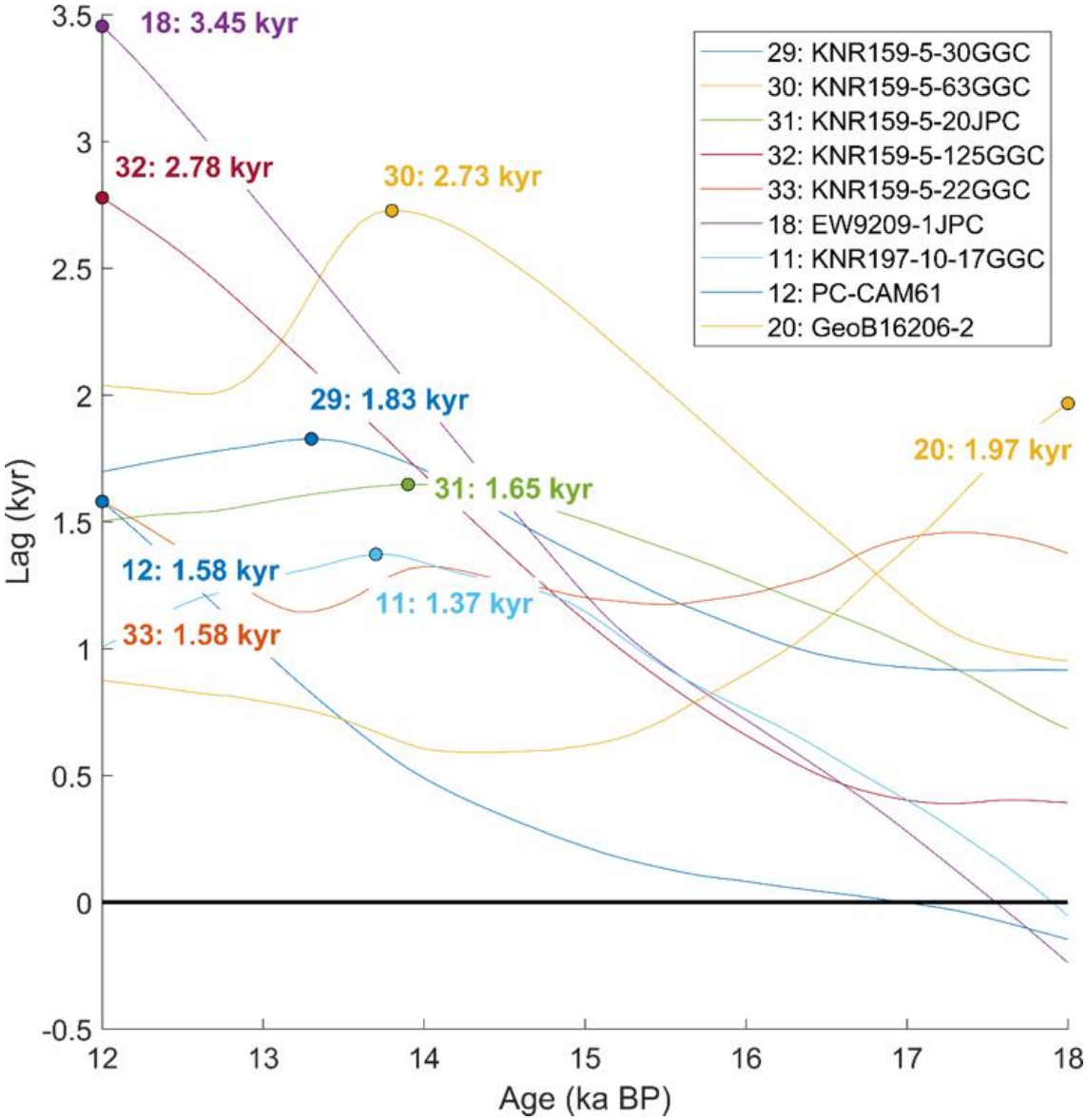

Figure 5: The median lags for all cores that have statistically significant lags between 10 and 18 ka BP. The maximum lag for every core except one (GeoB16206-2) is 14 ka BP or later. In addition, each maximum lag potted here is statistically significant.

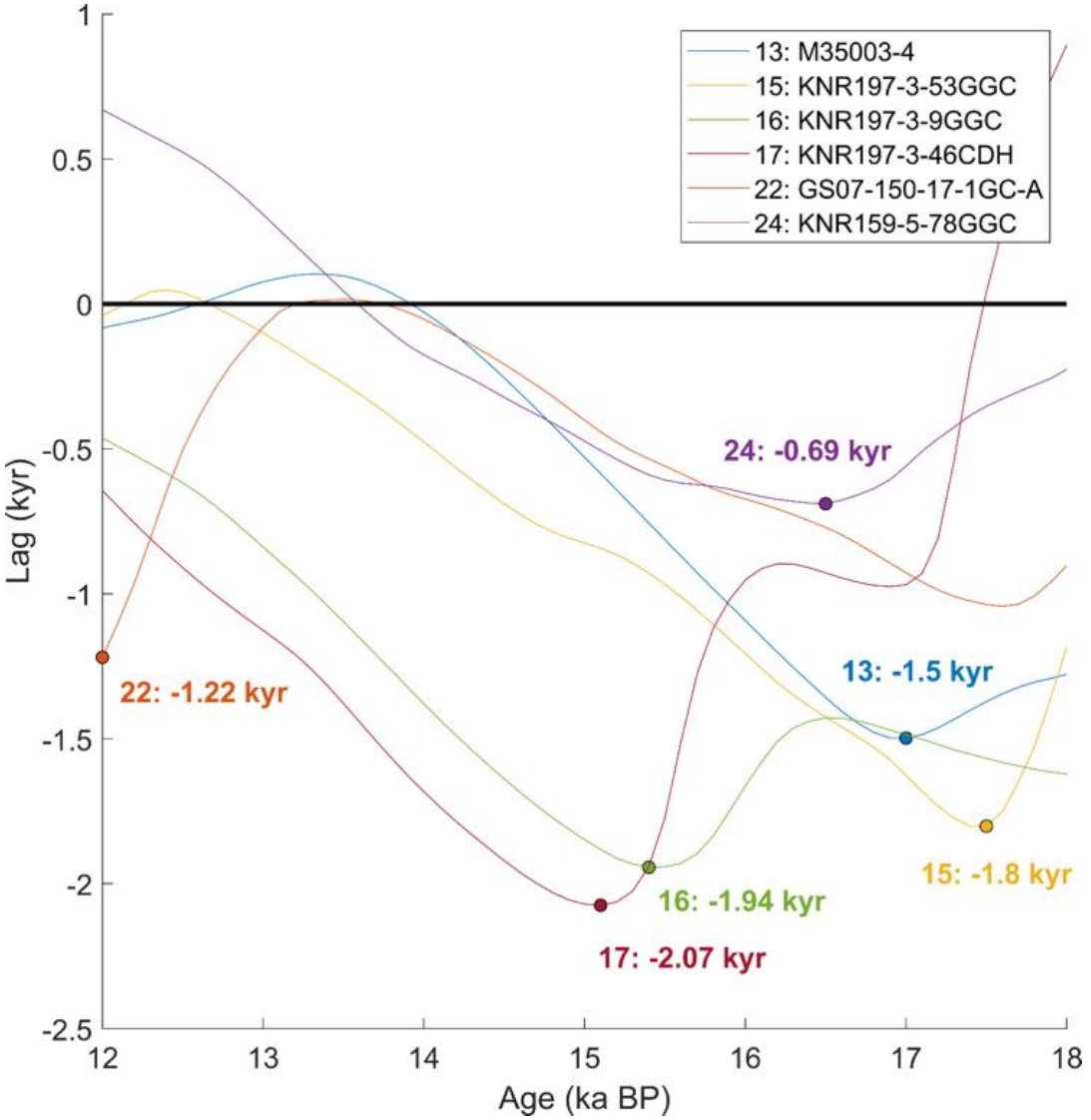

Figure 6: The median lags for all cores that have statistically significant leads (or negative lags). The maximum lead for every core is before 15 ka BP except for GS07-150-17-1GC-A. All maximum leads are statistically significant. Furthermore, core GS07-150-17-1GC-A has a statistically significant lead between 17 and 18 ka BP of 1.04 ka BP.

5 Discussion

5.1 Correspondence Between Leads and Lags and the Spatial Distribution of SCW

Here I investigate the connection between water mass geometries during the modern and LGM and the magnitudes of statistically significant leads and lags. I query local Southern Component Water percentages (%SCW) for each core using two reconstructions: an LGM reconstruction (Oppo et al., 2018) and a modern reconstruction (Gebbie & Huybers, 2010). In addition, I calculate the difference in %SCW (ΔSCW) between these two reconstructions at each core site. Specifically, ΔSCW is equal to the %SCW of the modern reconstruction minus the %SCW of the glacial reconstruction. In this sense, cores with a positive/negative difference gained/lost %SCW during T1. Figure 7 displays the cores with statistically significant leads and lags and the water mass reconstructions for the LGM, the modern, and the difference between them.

The correlations between maximum lags/leads and %SCW for the LGM and modern are equal to 0.38 and -0.34, respectively, with large p-values of 0.16 and 0.21, indicating that we cannot reject the null-hypothesis. However, there is a significant negative correlation ($r = -0.86$, $p = 10^{-4}$) between the maximum lags/leads and ΔSCW (Figure 8). Cores with statistically significant lags have a negative ΔSCW values (more SCW during the LGM than the modern) while cores with statistically significant leads have a positive ΔSCW difference (more SCW during the modern than the LGM). There are two obvious outliers in this correlation: core 12 (PC-CAM61) which has a statistically significant lag but a negative ΔSCW, and core 11 (KNR197-10-17GGC). However, the benthic $\delta^{18}O$ record for the former (PC-CAM61) has the lowest resolution of the 33 cores during Termination 1, and, furthermore, the lag is caused by only two $\delta^{18}O$ data points. Figure 9 displays the results if

these two data points are removed, and the lag is no longer statistically significant. If this core is removed the strength of the ΔSCW correlation increases ($r = -0.90$, $p = 10^{-5}$). This strong correlation suggests that water mass geometry changes played a role in generating statistically significant benthic $\delta^{18}O$ leads and lags.

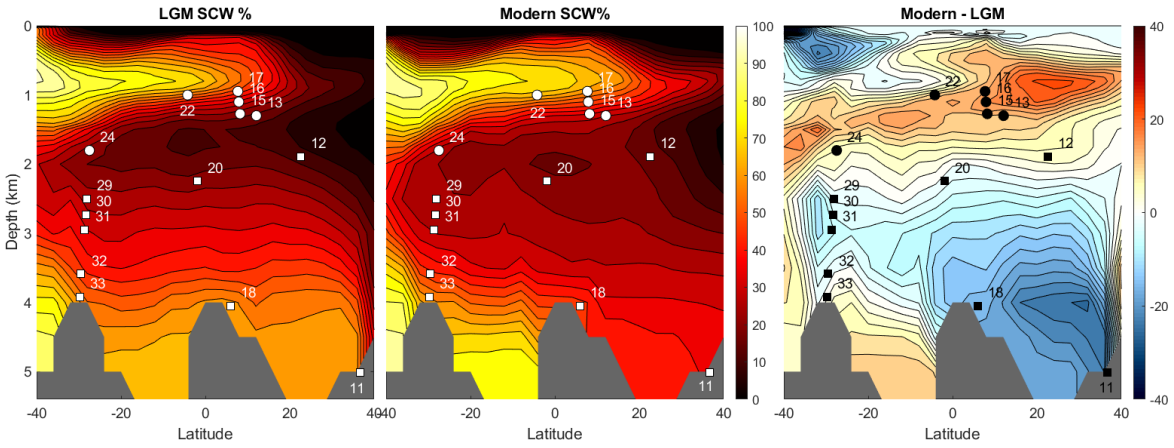

Figure 7: Reconstructions of LGM (Gebbie, 2018) and Modern (Gebbie, 2010) Southern Component Water percentages and the difference between them. Squares denote cores widths statistically significant lags while circles are cores with statistically significant leads.

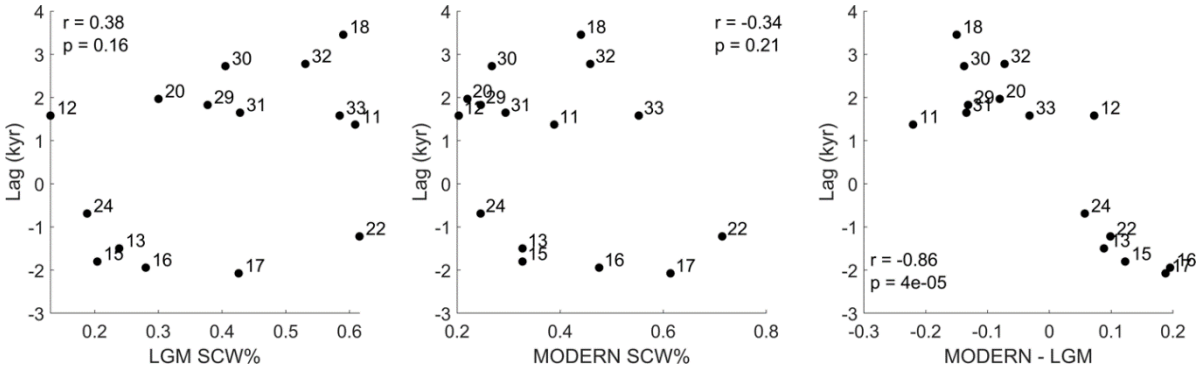

Figure 8: The correlations (or lack there of) between lags and LGM %SCW (Left, Oppo et al., 2018), modern %SCW (middle, Gebbie & Huybers, 2010), and the %SCW difference between the two reconstructions (Right).

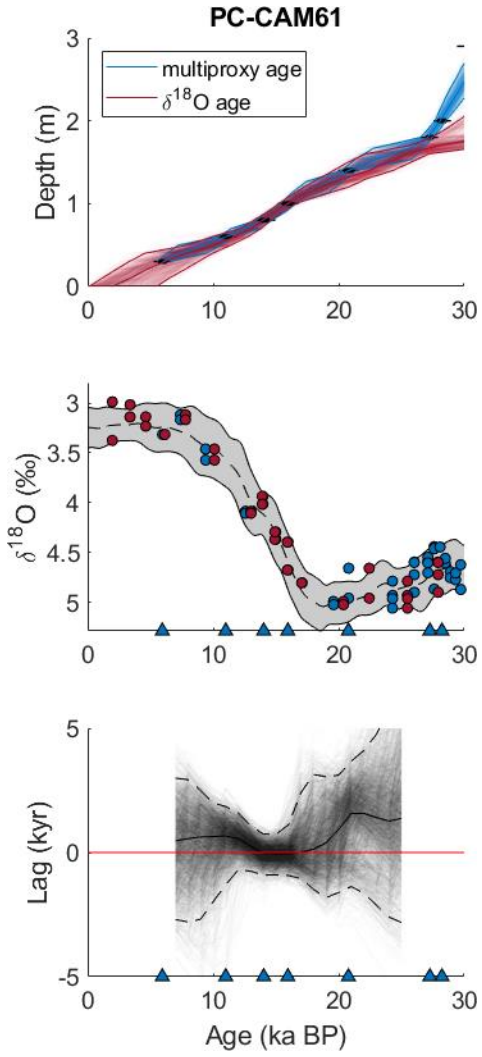

Figure 9: The lag results for core PC-CAM61 after removing two outlying $\delta^{18}O$ data points during Termination 1. The lag is no longer statistically significant.

It should also be noted that four of the statistically significant lags are still increasing at 12 ka BP (Figure 6). Figures 10 and 11 show the leads and lags extended to 5 and 25 ka BP. Six of the eight statistically significant lags and two of the six leads reach their maximum values after 12 ka BP. Using the extended calculations, I observe trends between %SCW for the modern and LGM if lags and leads are considered separately (Figure 12). Specifically, both maximum lags and leads tend to increase with %SCW. The correlation with leads and %SCW is statistically significant, with r-values equal to -0.94 and -0.87 and

p-values equal to 0.005 and 0.02 for the LGM and modern reconstructions respectively. The correlation between lags and %SCW is still not statistically significant due to two outliers (11: KNR197-10-17GGC and 33: KNR159-5-22GGC). However, lags calculated in the Holocene may be skewed by both additional ages used during $\delta^{18}O$-alignments as well as the flat $\delta^{18}O$ signal of the target stack. For example, many of the lags in Figure 10 quickly approach zero after their maximum values. This is due to additional ages included during $\delta^{18}O$ age model construction encouraging a lag equal to zero.

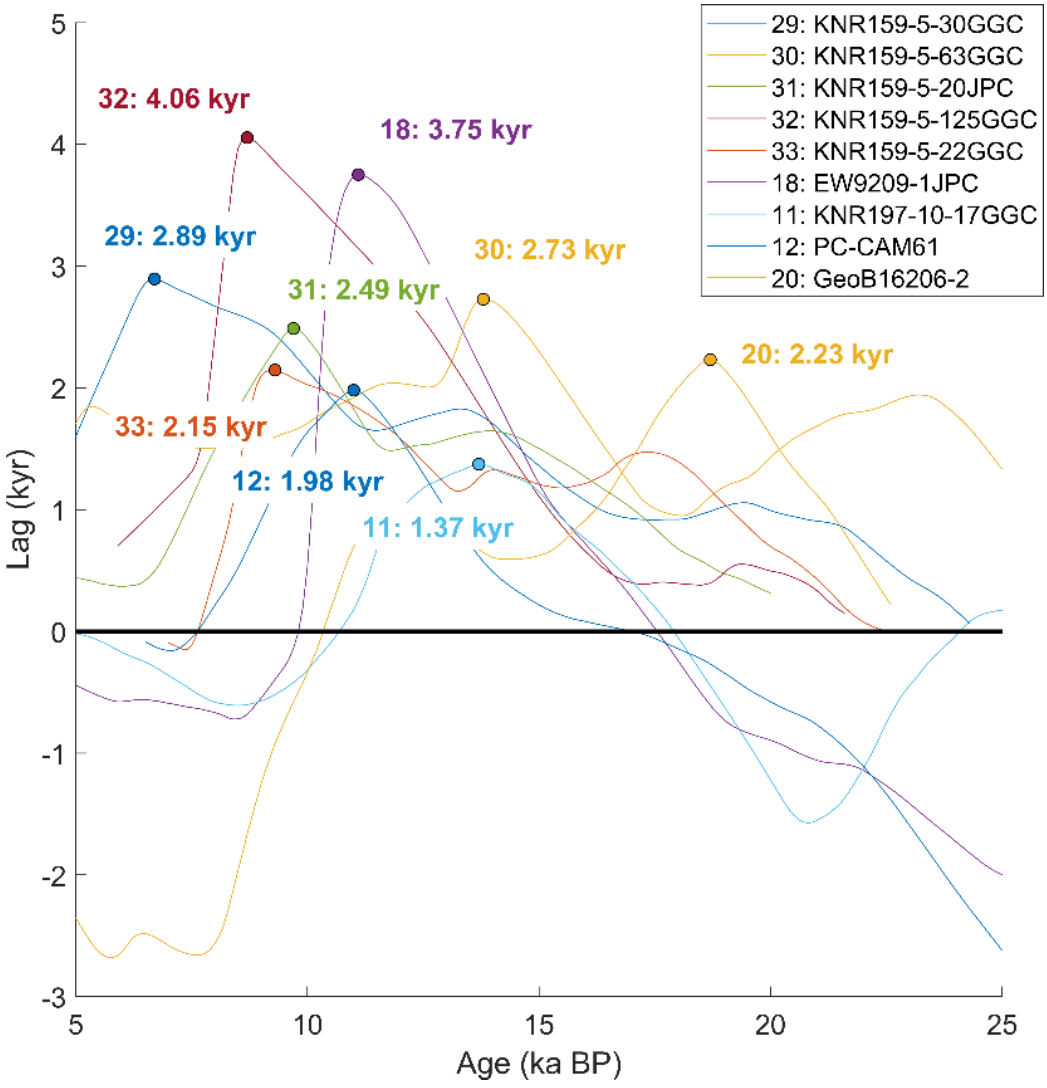

Figure 10: Statistically significant lags calculated from 5 to 25 ka BP

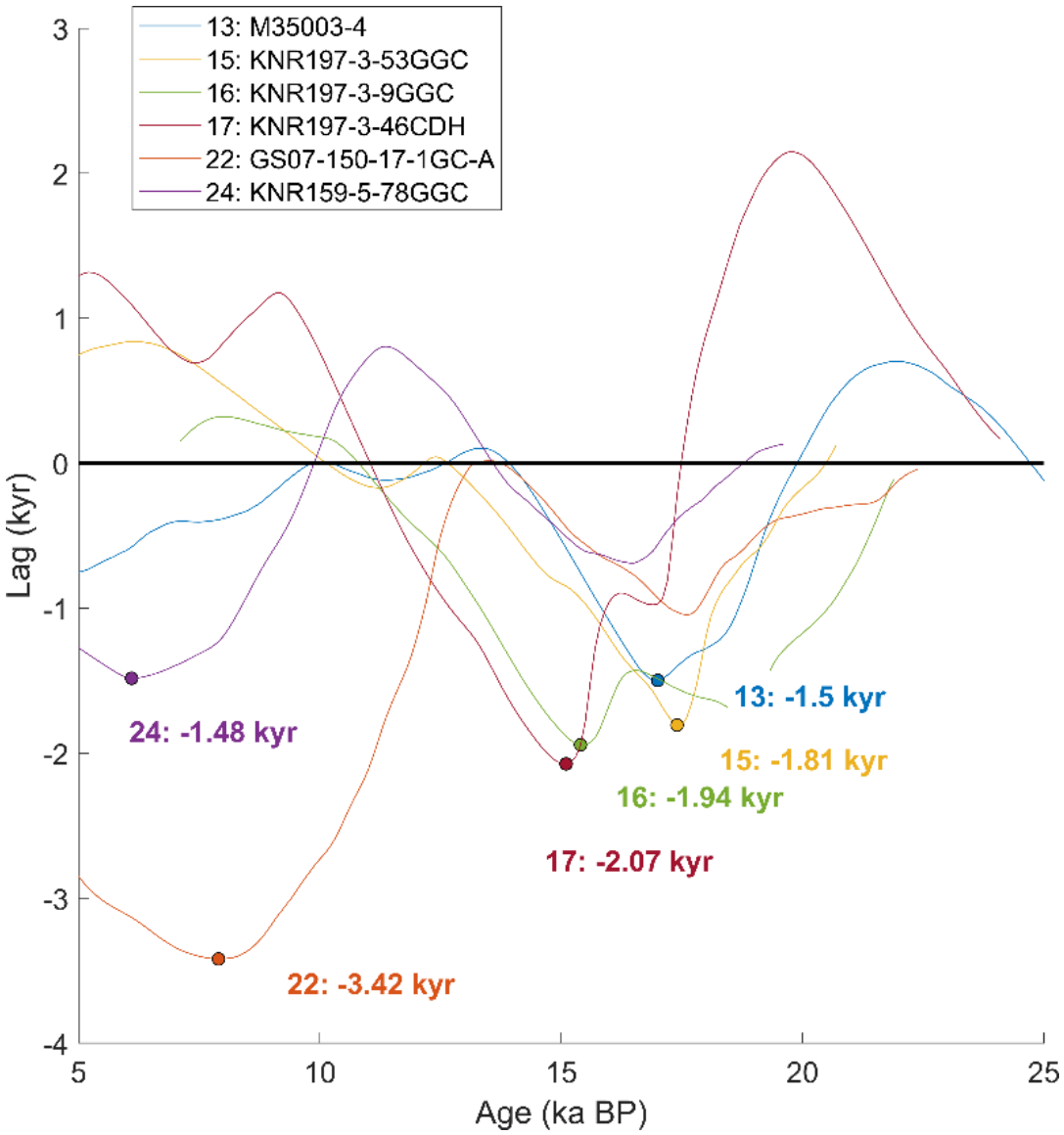

Figure 11: Statistically significant leads calculated from 5 to 25 ka BP.

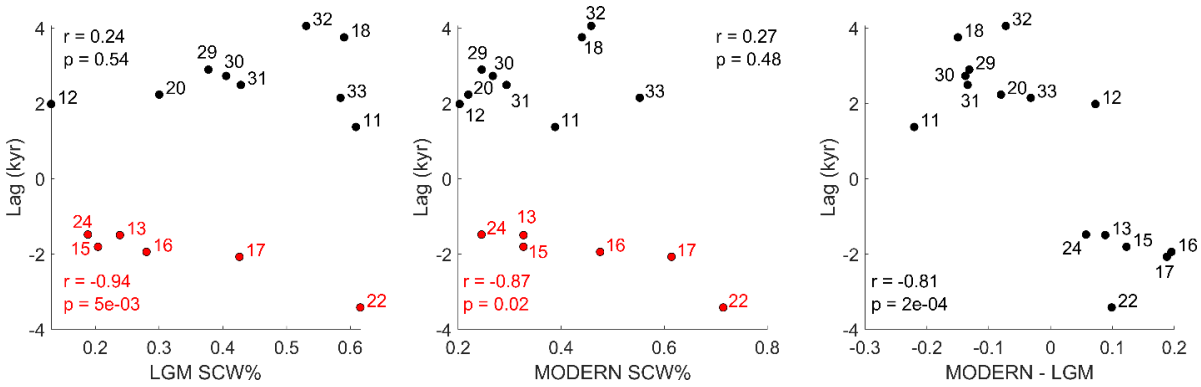

Figure 12: Correlations calculated separately between leads and lags with LGM %SCW (Left), modern %SCW (Middle), and the difference (Right). The leads (red) show statistically significant correlations with LGM and modern %SCW while the lags (black) do not. The correlation between ΔSCW is still significant with the correlation calculation including leads and lags together.

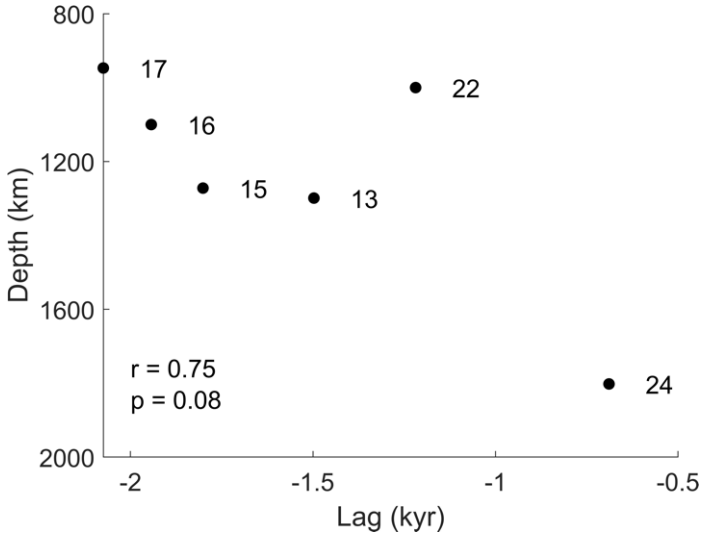

Figure 13: Correlation between leads and core-depth.

Other factors may have also caused or contributed to the leads in the intermediate West Atlantic and the lags in the deep Brazil Margin and abyssal North Atlantic. Previous studies have observed rapid decreases in $\delta^{18}O$ during Heinrich Stadial 1 (HS1) in cores from the deep sub-polar North Atlantic (Lund et al., 2015; Oppo et al., 2015), the Nordic Seas (Dokken & Jansen, 1999), and the intermediate West Atlantic (Waelbroeck et al., 2011; Marcott et al., 2011). While some studies have attributed the early decreases to brine

rejection caused by sea ice formation which effectively injects low-$\delta^{18}O$ meltwater to intermediate depths (Waelbroeck et al., 2011; Dokken & Jansen, 1999), others have favored sub-surface warming triggered by an AMOC slowdown (Liu et al., 2009; Marcott et al., 2011). Figure 13 displays the correlation ($r = 0.75$) between core-depth and the leads in the intermediate West Atlantic (with shallow core-depths associated with larger leads), which potentially supports these explanations. However, this correlation falls slightly short of the 95% confidence level ($p = 0.08$) due to a smaller number of data points and an outlier core (22: GS07-150-17-1GC-A).

The 2-3 kyr lags at the deep Brazil Margin, previously discussed in chapter 2, have been attributed to the mid-depth age maximum during the LGM which is caused by the upper return flow of the AABW convection cell (Ferrari et al., 2014). This age maximum is supported by radiocarbon ventilation ages (Burke & Robinson, 2012; Burke & Robinson, 2015; Freeman et al., 2016; Skinner et al., 2017 Rafter et al., 2022) which reach 2.5 kyr in the South Atlantic during HS1. This hypothesis may explain the

Lack of correlation between positive lags and %SCW. The largest lags at the Brazil Margin are observed for cores from a depth range of 2500-2951 m (Lund et al., 2015; Rand et al., in review) which were bathed in the upper southward flowing arm of the AABW convection cell. This arm would have lower %SCW than the bottom arm flowing North but more %SCW than NADW flowing South. However, the previously observed ventilation ages rapidly decreased during the latter half of T1, suggesting a shift to a modern circulation regime when the lags presented here reach their maximum values. This potentially suggests that an additional mechanism is required to cause the lags (e.g., a water mass boundary change).

Ultimately, statistically significant benthic $\delta^{18}O$ leads and lags likely result a combination of water mass geometry changes (e.g., LGM minus Holocene %SCW), circulation rates (e.g., the mid-depth ventilation age maximum), and surface forcings (sub-surface warming/brine rejection in the intermediate West Atlantic). The next section describes an inversion model that may help solve for non-unique combinations of these factors capable of fitting the measured Atlantic lags.

5.2 Glacial Circulation Changes

Here I investigate the combined effects of potential deglacial changes in water mass geometries, circulation rates, and asynchronous hemispheric surface signals that fit the observed lags within their uncertainty estimates. An ocean circulation model was used to develop a lag equation that depends on local NCW vs. SCW percentages, local water mass transit times, and a southern hemisphere surface lag. This equation can be used to calculate non-unique combinations of these variables that fit within the uncertainty of my lag results.

The lag equation is derived by modeling surface water $\delta^{18}O$ values as an idealized ramp function across T1 with a constant delay between the northern and southern hemispheres. Boundary Green functions derived from modern circulation pathways (Gebbie, 2012) propagate the surface $\delta^{18}O$ signal to interior core sites. The benthic $\delta^{18}O$ lag, τ_i, at a core location *i* is calculated relative to the Northern Hemisphere surface signal using the equation

$$\tau_i = m_i^N a_i^N + m_i^S (a_i^S + \tau_{sfc}) \quad \textbf{(1)}$$

where m_i^N and m_i^S are the northern and southern water mass percentages, a_i^N and a_i^S are the northern and southern water mass ages, and τ_{sfc} is the southern hemisphere surface lag. To compare the modeled lags with our measured lags (which are relative to the target stack) the above equation is adjusted to include the average lag of the target stack (τ_{stack}) relative to the Northern Hemisphere surface signal

$$\lambda_i = m_i^N a_i^N + m_i^S \left(a_i^S + \tau_{sfc}\right) - \tau_{stack}.$$

(2)

By minimizing the square residual between our observed lags and equation (2), we can solve for combinations of water mass percentages, circulation rates, and a southern hemisphere surface lag. However, this problem is non-unique and solutions could range between limiting cases. For example, if water mass ages for NCW and SCW are set to be equal at each core site i ($a_i^N = a_i^S = a_i$), equation (2) simplifies to

$$\lambda_i = a_i + \left(m_i^S * \tau_{sfc}\right) - \tau_{stack}$$

(3)

after setting $m_i^N + m_i^S = 1$. In this case, the spatial distribution of lags would be fit entirely by the propagation of a southern hemisphere surface lag and the precent SCW at each core site. In the opposing limiting case, in which there is no southern hemisphere surface lag ($\tau_{sfc} = 0$), equation (2) becomes

$$\lambda_i = m_i^N a_i^N + m_i^S a_i^S - \tau_{stack}$$

(4)

and relies solely on the difference in circulation rates between NCW and SCW and the local water mass percentages. Finally, if the Atlantic was filled only by a single water mass ($m_i^N = 0, m_i^S = 1$), equation (2) simplifies to

$$\lambda_i = \left(a_i^S + \tau_{sfc}\right) - \tau_{stack} \quad \textbf{(5)}$$

and lags would be reproduced by the transit times for SCW and a southern hemisphere surface lag.

However, I find one plausible solution in which Atlantic lags at 16 ka BP can be fit by shoaling NADW, slowing circulation rates, and applying a southern hemisphere lag to the Northern Hemisphere. Specifically, the core of NADW is shoaled above 2 km, SCW ages are increased by a factor of 3, and a 2-kyr surface lag is applied to the southern hemisphere (Figure 9).

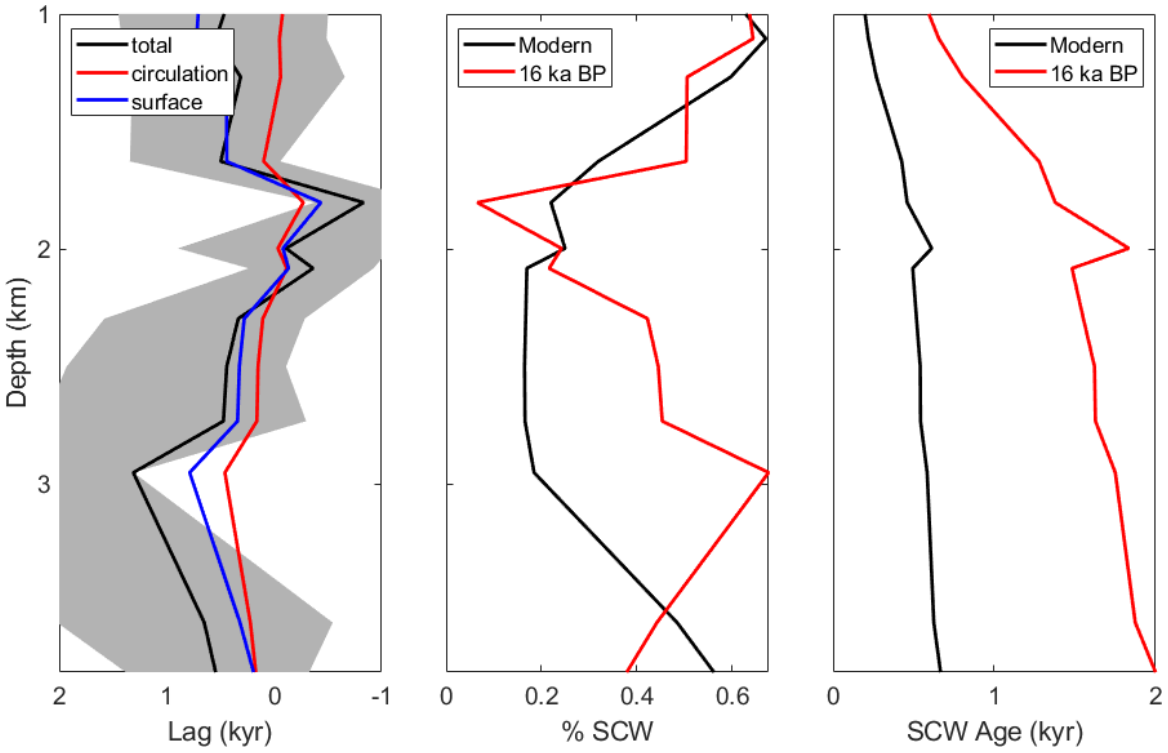

Figure 14: (Left) Modeled lags at the Brazil Margin (black line) fit within the uncertainties of the calculated lags (grey shaded region). Red and blue lines show modeled lags that result from the circulation rate slow down and the southern hemisphere surface lag respectively. (Middle) The modern SCW percentage at the Brazil Margin (black line) vs. the modeled SCW percentage 16 ka BP (red line). To fit the calculated lags, the core of NADW was shoaled above 2 km (represented by low SCW percentage). (Right) Modern SCW age at the Brazil Margin (black line) vs. the modeled SCW age 16 ka BP. The modeled age is three times greater than the modern age.

While equation (2) was empirically derived to be consistent with an idealized deglaciation, one limitation of this method is its lack of time-dependence. Here I find that leads primarily occur in the former half of Termination 1 while lags occur in the latter half (and potentially into the Holocene). This method could be improved if structured as a transient simulation, thereby capturing the temporal evolution of leads and lags and incorporating time-dependence on the factors that cause them. Furthermore, the deglaciation is not an idealized ramp function, but rather is superimposed with millennial scale climate

events and hemispheric oscillations (i.e., the bipolar seesaw). The climate signals propagating from the northern and southern hemispheres are not only asynchronous, but also have different magnitudes and trends. Future work should incorporate a more realistic deglacial signal and fit the observed, time-dependent lags.

5.3 Implications of Benthic $\delta^{18}O$-Aligned Age Models

This study emphasizes the importance of selecting appropriate alignment targets based on geographic locations and water mass histories (Lee & Rand et al., accepted). Poor selection of an alignment target may result in age errors as large as 3 kyr, even if the two cores aligned are both in the Atlantic. Importantly, the alignment uncertainty returned by BIGMACS and reported here does not include uncertainty associated with potentially diachronous $\delta^{18}O$ signals. This additional uncertainty should always be considered when constructing $\delta^{18}O$ age models. Thus, direct age constraints (e.g., radiocarbon, tephra layers, etc.) are recommended when studying millennial scale climate events.

Previous studies have constructed regional Atlantic benthic $\delta^{18}O$ stacks for use as alignment targets (Stern & Lisiecki, 2014; Lisiecki & Stern 2016; Lee & Rand et al., accepted). Stern & Lisiecki (2014) and Lisiecki & Stern (2016) divided the Atlantic into four broad regions: the Intermediate North Atlantic, the deep North Atlantic, the intermediate South Atlantic, and the deep South Atlantic. North and south regions have latitudes ranging from 0-65^{o} N and 0-35^{o} S respectively, while intermediate and deep regions have depths ranging from 1000 – 2000 m and 2000 – 5000 m, respectively. Waelbroeck et al (2011) suggested that early d18O change in the North Atlantic occurred above depths of 2200 m. My results generally agree with these depth boundaries. Specifically, I find that the depth separating intermediate and deep regions is approximately 2500 m in the South West

Atlantic and 2200 m in the North West Atlantic. This range is defined by the shallowest statistically significant lags: core KNR159-5-30GGC is located at the Brazil Margin with a depth of 2500 m and GeoB16206-2 which is located off the north coast of Brazil with a depth of 2247 m. Limited data from the East Atlantic do not reveal any latitudinal or depth boundaries in the deglacial timing of d18O change between 2000-3200 m water depth.

Lee & Rand et al., (accepted) present two stacks which offer regional alignment targets during T1: the DNEA stack (used here) and the Intermediate Tropical West Atlantic (ITWA) stack. The DNEA stack is composed of six cores from the East Atlantic with depths ranging from 2273 m to 3227 m while the ITWA stack is composed of 4 cores with depths ranging from 1100 – 1367 m. Due to the lack of statistically significant lags in the East Atlantic, the DNEA stack appears to be a valid alignment target for all analyzed East Atlantic cores (especially from the North East Atlantic), while the ITWA stack captures the leads observed at intermediate depths from the low latitude West Atlantic. Three of the four cores in the ITWA stack show statistically significant leads while one core is just insignificant (GeoB16206-1).

6 Conclusion

Lags are calculated for 33 Atlantic cores between latitudes of 38^{o} North to 30^{o} South and depths between 767 and 5010 m. I find statistically significant leads in the first half of T1 in the intermediate West Atlantic with magnitudes up to 2.07 [95% CI: 0.70 – 2.77] kyr and statistically significant lags in the deep/abyssal Brazil Margin and abyssal North Atlantic in the latter half of Termination 1 with magnitudes reaching 3.45 [95% CI: 2.63 – 4.08] kyr. Leads may have been caused by sub-surface warming associated with an AMOC slow-down (Marcott et al., 2011) or/and brine rejection due to sea ice formation

(Waelbroeck et al., 2011) while lags were likely affected by a mid-depth age maximum (Ferrari et al., 2014). However, I also find a statistically significant correlation of the %SCW difference between LGM (Oppo et al., 2018) and Modern (Gebbie & Huybers, 2010) reconstructions and lag magnitude. Finally, I present a method to solve for non-unique combinations of water mass geometries, circulation rates, and asynchronous surface forcings capable of fitting the calculated lags. I find that lags can be fit within their 95% credible intervals by a 2 km shoaling of NADW, a three factor decrease in SCW circulation, and a 2 kyr Southern Hemisphere surface lag.

Cores	**Lat**	**Lon**	**Depth**	**Reference**	**Reason**
EW9209-2JPC	5.64	-44.47	3528	Curry et al., 1996; Curry et al., 1999	Radiocarbon Resolution
EW9209-3JPC	5.31	-44.26	3288	Curry et al., 1996; Curry et al., 1999	Radiocarbon Resolution
GeoB16203-1	-2.03	-41.72	1591	Voigt et al., 2017	Short
GeoB16205-4	-1.35	-43.1	1955	Voig et al., 2017	Short
GeoB16224-1	6.66	-52.08	2510	Zhang et al., 2015; Voigt et al., 2017	Short
GeoB3202-1	-21.62	-39.98	1090	Behling et al., 2002; Arz et al., 1999;	Radiocarbon and $\delta^{18}O$ Resolution
GEOFAR KF13	37.58	-31.84	2690	Richter et al., 1998	$\delta^{18}O$ Resolution
KNR159-5-105JPC	-27.35	-46.63	1108	Umling et al., 2019	Short
KNR159-5-14GGC	-26.68	-46.5	441	Lund et al., 2015	Shallow
KNR197-3-47CDH	7.84	-53.66	671	Oppo et al., 2018	Short
KNR197-3-60	8.44	-52.97	2642	Oppo et al., 2018	Radiocarbon and $\delta^{18}O$ Resolution
KNR31-GPC5	33.69	-57.63	4583	Waelbroeck et al., 2011; Keigwin & Boyle 2011	Short
MD02-2575	29	-87.12	847	Nürnberg et al., 2008	Radiocarbon Resolution

MD99-2339	35.89	-7.53	1177	Voelker et al., 2006;	Radiocarbon Resolution
POS200-10-6-2	37.82	-9.5	1086	Abrantes et al., 2001	Short
RC16-84	-26.7	-43.33	2438	Oppo & Horowitz, 2000;	$\delta^{18}O$ Resolution
V24-253	-26.95	-44.67	2069	Oppo & Horowitz, 2000;	$\delta^{18}O$ Resolution

Table 2: Cores that were excluded from the compilation. Reasons for exclusion are listed in the final column.

References

1. Abrantes, F., 2001. Paleoceanographic Conditions along the Portuguese Margin during the Last 30 ka: A Multiple Proxy Study. Comunicações do Instituto Geológico e Mineiro 88, 161–184.
2. Andersen, K.K., Azuma, N., Barnola, J.-M., Bigler, M., Biscaye, P., Caillon, N., Chappellaz, J., Clausen, H.B., Dahl-Jensen, D., Fischer, H., Flückiger, J., Fritzsche, D., Fujii, Y., Goto-Azuma, K., Grønvold, K., Gundestrup, N.S., Hansson, M., Huber, C., Hvidberg, C.S., Johnsen, S.J., Jonsell, U., Jouzel, J., Kipfstuhl, S., Landais, A., Leuenberger, M., Lorrain, R., Masson-Delmotte, V., Miller, H., Motoyama, H., Narita, H., Popp, T., Rasmussen, S.O., Raynaud, D., Rothlisberger, R., Ruth, U., Samyn, D., Schwander, J., Shoji, H., Siggard-Andersen, M.-L., Steffensen, J.P., Stocker, T., Sveinbjörnsdóttir, A.E., Svensson, A., Takata, M., Tison, J.-L., Thorsteinsson, Th., Watanabe, O., Wilhelms, F., White, J.W.C., North Greenland Ice Core Project members, 2004. High-resolution record of Northern Hemisphere climate extending into the last interglacial period. Nature 431, 147–151. https://doi.org/10.1038/nature02805
3. Arz, H.W., Pätzold, J., Wefer, G., 1999. The deglacial history of the western tropical Atlantic as inferred from high resolution stable isotope records off northeastern Brazil. Earth and Planetary Science Letters 167, 105–117. https://doi.org/10.1016/S0012-821X(99)00025-4
4. Arz, H.W., Pätzold, J., Wefer, G., 1998. Correlated Millennial-Scale Changes in Surface Hydrography and Terrigenous Sediment Yield Inferred from Last-Glacial Marine Deposits off Northeastern Brazil. Quaternary Research 50, 157–166. https://doi.org/10.1006/qres.1998.1992
5. Atlantic Circulation and Ice Sheet Influences on Upper South Atlantic Temperatures During the Last Deglaciation - Umling - 2019 - Paleoceanography and Paleoclimatology - Wiley Online Library [WWW Document], n.d. URL https://agupubs.onlinelibrary.wiley.com/doi/full/10.1029/2019PA003558 (accessed 8.27.23).
6. Balmer, S., Sarnthein, M., Mudelsee, M., Grootes, P.M., 2016. Refined modeling and 14C plateau tuning reveal consistent patterns of glacial and deglacial 14C reservoir ages of surface waters in low-latitude Atlantic. Paleoceanography 31, 1030–1040. https://doi.org/10.1002/2016PA002953
7. Barbante, C., Barnola, J.-M., Becagli, S., Beer, J., Bigler, M., Boutron, C., Blunier, T., Castellano, E., Cattani, O., Chappellaz, J., Dahl-Jensen, D., Debret, M., Delmonte, B., Dick, D., Falourd, S., Faria, S., Federer, U., Fischer, H., Freitag, J., Frenzel, A., Fritzsche, D., Fundel, F., Gabrielli, P., Gaspari, V., Gersonde, R., Graf, W., Grigoriev, D., Hamann, I., Hansson, M., Hoffmann, G., Hutterli, M.A., Huybrechts, P., Isaksson, E., Johnsen, S., Jouzel, J., Kaczmarska, M., Karlin, T., Kaufmann, P., Kipfstuhl, S., Kohno, M., Lambert, F., Lambrecht, Anja, Lambrecht, Astrid, Landais, A., Lawer, G., Leuenberger, M., Littot, G., Loulergue, L., Lüthi, D., Maggi, V., Marino, F., Masson-Delmotte, V., Meyer, H., Miller, H., Mulvaney, R., Narcisi, B., Oerlemans, J., Oerter, H., Parrenin, F., Petit, J.-R., Raisbeck, G., Raynaud, D., Röthlisberger, R., Ruth, U., Rybak, O., Severi, M., Schmitt, J., Schwander, J., Siegenthaler, U., Siggaard-Andersen, M.-L., Spahni, R., Steffensen, J.P., Stenni, B., Stocker, T.F., Tison, J.-L., Traversi, R., Udisti, R., Valero-Delgado, F., van den Broeke, M.R., van de Wal, R.S.W., Wagenbach, D., Wegner, A., Weiler, K., Wilhelms, F., Winther, J.-G., Wolff, E., EPICA Community Members, 2006. One-to-one coupling of glacial climate variability in Greenland and Antarctica. Nature 444, 195–198. https://doi.org/10.1038/nature05301
8. Bard, E., Rostek, F., Ménot-Combes, G., 2004. Radiocarbon calibration beyond 20,000 14C yr B.P. by means of planktonic foraminifera of the Iberian Margin. Quaternary Research 61, 204–214. https://doi.org/10.1016/j.yqres.2003.11.006
9. Behling, H., 2002. South and southeast Brazilian grasslands during Late Quaternary times: a synthesis. Palaeogeography, Palaeoclimatology, Palaeoecology, Reconstruction and Modeling of grass-dominated ecosystems 177, 19–27. https://doi.org/10.1016/S0031-0182(01)00349-2
10. Boyle, E.A., Keigwin, L., 1987. North Atlantic thermohaline circulation during the past 20,000 years linked to high-latitude surface temperature. Nature 330, 35–40. https://doi.org/10.1038/330035a0
11. Bradtmiller, L.I., McManus, J.F., Robinson, L.F., 2014. 231Pa/230Th evidence for a weakened but persistent Atlantic meridional overturning circulation during Heinrich Stadial 1. Nat Commun 5, 5817. https://doi.org/10.1038/ncomms6817

12. Buizert, C., Gkinis, V., Severinghaus, J.P., He, F., Lecavalier, B.S., Kindler, P., Leuenberger, M., Carlson, A.E., Vinther, B., Masson-Delmotte, V., White, J.W.C., Liu, Z., Otto-Bliesner, B., Brook, E.J., 2014. Greenland temperature response to climate forcing during the last deglaciation. Science 345, 1177–1180. https://doi.org/10.1126/science.1254961
13. Burke, A., Marchal, O., Bradtmiller, L.I., McManus, J.F., François, R., 2011. Application of an inverse method to interpret 231Pa/230Th observations from marine sediments. Paleoceanography 26. https://doi.org/10.1029/2010PA002022
14. Burke, A., Robinson, L.F., 2012. The Southern Ocean's Role in Carbon Exchange During the Last Deglaciation. Science 335, 557–561. https://doi.org/10.1126/science.1208163
15. Burke, A., Stewart, A.L., Adkins, J.F., Ferrari, R., Jansen, M.F., Thompson, A.F., 2015. The glacial mid-depth radiocarbon bulge and its implications for the overturning circulation. Paleoceanography 30, 1021–1039. https://doi.org/10.1002/2015PA002778
16. Chase, Z., Anderson, R.F., Fleisher, M.Q., Kubik, P.W., 2002. The influence of particle composition and particle flux on scavenging of Th, Pa and Be in the ocean. Earth and Planetary Science Letters 204, 215–229. https://doi.org/10.1016/S0012-821X(02)00984-6
17. Collins, J.A., Schefuß, E., Heslop, D., Mulitza, S., Prange, M., Zabel, M., Tjallingii, R., Dokken, T.M., Huang, E., Mackensen, A., Schulz, M., Tian, J., Zarriess, M., Wefer, G., 2011. Interhemispheric symmetry of the tropical African rainbelt over the past 23,000 years. Nature Geosci 4, 42–45. https://doi.org/10.1038/ngeo1039
18. Curry, W.B., 1996. Late Quaternary Deep Circulation in the Western Equatorial Atlantic, in: Wefer, G., Berger, W.H., Siedler, G., Webb, D.J. (Eds.), The South Atlantic: Present and Past Circulation. Springer, Berlin, Heidelberg, pp. 577–598. https://doi.org/10.1007/978-3-642-80353-6_29
19. Curry, W.B., Oppo, D.W., 2005. Glacial water mass geometry and the distribution of δ13C of ΣCO2 in the western Atlantic Ocean. Paleoceanography 20. https://doi.org/10.1029/2004PA001021
20. deMenocal, P., Ortiz, J., Guilderson, T., Adkins, J., Sarnthein, M., Baker, L., Yarusinsky, M., 2000. Abrupt onset and termination of the African Humid Period:: rapid climate responses to gradual insolation forcing. Quaternary Science Reviews 19, 347–361. https://doi.org/10.1016/S0277-3791(99)00081-5
21. Dickson, A.J., Beer, C.J., Dempsey, C., Maslin, M.A., Bendle, J.A., McClymont, E.L., Pancost, R.D., 2009a. Oceanic forcing of the Marine Isotope Stage 11 interglacial. Nature Geosci 2, 428–433. https://doi.org/10.1038/ngeo527
22. Dickson, A.J., Beer, C.J., Dempsey, C., Maslin, M.A., Bendle, J.A., McClymont, E.L., Pancost, R.D., 2009b. Oceanic forcing of the Marine Isotope Stage 11 interglacial. Nature Geosci 2, 428–433. https://doi.org/10.1038/ngeo527
23. Dokken, T.M., Jansen, E., 1999. Rapid changes in the mechanism of ocean convection during the last glacial period. Nature 401, 458–461. https://doi.org/10.1038/46753
24. Duplessy, J.C., Shackleton, N.J., Fairbanks, R.G., Labeyrie, L., Oppo, D., Kallel, N., 1988. Deepwater source variations during the last climatic cycle and their impact on the global deepwater circulation. Paleoceanography 3, 343–360. https://doi.org/10.1029/PA003i003p00343
25. EGUsphere - Bayesian age models and stacks: Combining age inferences from radiocarbon and benthic δ18O stratigraphic alignment [WWW Document], n.d. URL https://egusphere.copernicus.org/preprints/2022/egusphere-2022-734/ (accessed 9.9.23).
26. Ferrari, R., Jansen, M.F., Adkins, J.F., Burke, A., Stewart, A.L., Thompson, A.F., 2014. Antarctic sea ice control on ocean circulation in present and glacial climates. Proceedings of the National Academy of Sciences 111, 8753–8758. https://doi.org/10.1073/pnas.1323922111
27. Freeman, E., Skinner, L.C., Waelbroeck, C., Hodell, D., 2016. Radiocarbon evidence for enhanced respired carbon storage in the Atlantic at the Last Glacial Maximum. Nat Commun 7, 11998. https://doi.org/10.1038/ncomms11998
28. Gebbie, G., 2014. How much did Glacial North Atlantic Water shoal? Paleoceanography 29, 190–209. https://doi.org/10.1002/2013PA002557
29. Gebbie, G., Huybers, P., 2010. Total Matrix Intercomparison: A Method for Determining the Geometry of Water-Mass Pathways. Journal of Physical Oceanography 40, 1710–1728. https://doi.org/10.1175/2010JPO4272.1
30. Geibert, W., Usbeck, R., 2004. Adsorption of thorium and protactinium onto different particle types: experimental findings 11Associate editor: S. Krishnaswami. Geochimica et Cosmochimica Acta 68, 1489–1501. https://doi.org/10.1016/j.gca.2003.10.011

31. Gherardi, J.-M., Labeyrie, L., McManus, J.F., Francois, R., Skinner, L.C., Cortijo, E., 2005. Evidence from the Northeastern Atlantic basin for variability in the rate of the meridional overturning circulation through the last deglaciation. Earth and Planetary Science Letters 240, 710–723. https://doi.org/10.1016/j.epsl.2005.09.061
32. Hall, I.R., Moran, S.B., Zahn, R., Knutz, P.C., Shen, C.-C., Edwards, R.L., 2006. Accelerated drawdown of meridional overturning in the late-glacial Atlantic triggered by transient pre-H event freshwater perturbation. Geophysical Research Letters 33. https://doi.org/10.1029/2006GL026239
33. Heaton, T.J., Köhler, P., Butzin, M., Bard, E., Reimer, R.W., Austin, W.E.N., Bronk Ramsey, C., Grootes, P.M., Hughen, K.A., Kromer, B., Reimer, P.J., Adkins, J., Burke, A., Cook, M.S., Olsen, J., Skinner, L.C., 2020. Marine20—The Marine Radiocarbon Age Calibration Curve (0–55,000 cal BP). Radiocarbon 62, 779–820. https://doi.org/10.1017/RDC.2020.68
34. Hoffman, J.L., Lund, D.C., 2012. Refining the stable isotope budget for Antarctic Bottom Water: New foraminiferal data from the abyssal southwest Atlantic. Paleoceanography 27. https://doi.org/10.1029/2011PA002216
35. Howe, J.N.W., Piotrowski, A.M., Rennie, V.C.F., 2016. Abyssal origin for the early Holocene pulse of unradiogenic neodymium isotopes in Atlantic seawater. Geology 44, 831–834. https://doi.org/10.1130/G38155.1
36. Hüls, M., Zahn, R., 2000. Millennial-scale sea surface temperature variability in the western tropical North Atlantic from planktonic foraminiferal census counts. Paleoceanography 15, 659–678. https://doi.org/10.1029/1999PA000462
37. Keigwin, L.D., 1999. Mechanisms of Global Climate Change at Millennial Time Scales. American Geophysical Union.
38. Keigwin, L.D., Swift, S.A., 2017. Carbon isotope evidence for a northern source of deep water in the glacial western North Atlantic. Proceedings of the National Academy of Sciences 114, 2831–2835. https://doi.org/10.1073/pnas.1614693114
39. Kindler, P., Guillevic, M., Baumgartner, M., Schwander, J., Landais, A., Leuenberger, M., 2014. Temperature reconstruction from 10 to 120 kyr b2k from the NGRIP ice core. Climate of the Past 10, 887–902. https://doi.org/10.5194/cp-10-887-2014
40. Knaack, J.-J., Sarnthein, M., 2005. Stable isotopes of foraminifera of ODP Hole 108-658C. https://doi.org/10.1594/PANGAEA.227736
41. Labeyrie, L., Waelbroeck, C., Cortijo, E., Michel, E., Duplessy, J.-C., 2005. Changes in deep water hydrology during the Last Deglaciation. Comptes Rendus Geoscience 337, 919–927. https://doi.org/10.1016/j.crte.2005.05.010
42. Lee, T., Rand, D., Lisiecki, L.E., Gebbie, G., Lawrence, C.E., 2022. Bayesian age models and stacks: Combining age inferences from radiocarbon and benthic δ^{18}O stratigraphic alignment. EGUsphere 1–29. https://doi.org/10.5194/egusphere-2022-734
43. Lemieux-Dudon, B., Blayo, E., Petit, J.-R., Waelbroeck, C., Svensson, A., Ritz, C., Barnola, J.-M., Narcisi, B.M., Parrenin, F., 2010. Consistent dating for Antarctic and Greenland ice cores. Quaternary Science Reviews 29, 8–20. https://doi.org/10.1016/j.quascirev.2009.11.010
44. Little, M.G., Schneider, R.R., Kroon, D., Price, B., Bickert, T., Wefer, G., 1997. Rapid palaeoceanographic changes in the Benguela Upwelling System for the last 160,000 years as indicated by abundances of planktonic foraminifera. Palaeogeography, Palaeoclimatology, Palaeoecology 130, 135–161. https://doi.org/10.1016/S0031-0182(96)00136-8
45. Liu, Z., Otto-Bliesner, B.L., He, F., Brady, E.C., Tomas, R., Clark, P.U., Carlson, A.E., Lynch-Stieglitz, J., Curry, W., Brook, E., Erickson, D., Jacob, R., Kutzbach, J., Cheng, J., 2009. Transient Simulation of Last Deglaciation with a New Mechanism for Bølling-Allerød Warming. Science 325, 310–314. https://doi.org/10.1126/science.1171041
46. Lund, D.C., Tessin, A.C., Hoffman, J.L., Schmittner, A., 2015. Southwest Atlantic water mass evolution during the last deglaciation. Paleoceanography 30, 477–494. https://doi.org/10.1002/2014PA002657
47. Makou, M.C., Eglinton, T.I., Oppo, D.W., Hughen, K.A., 2010. Postglacial changes in El Niño and La Niña behavior. Geology 38, 43–46. https://doi.org/10.1130/G30366.1
48. Mangini, A., Godoy, J.M., Godoy, M.L., Kowsmann, R., Santos, G.M., Ruckelshausen, M., Schroeder-Ritzrau, A., Wacker, L., 2010. Deep sea corals off Brazil verify a poorly ventilated Southern Pacific Ocean during H2, H1 and the Younger Dryas. Earth and Planetary Science Letters 293, 269–276. https://doi.org/10.1016/j.epsl.2010.02.041

49. Marchal, O., François, R., Stocker, T.F., Joos, F., 2000. Ocean thermohaline circulation and sedimentary 231Pa/230Th ratio. Paleoceanography 15, 625–641. https://doi.org/10.1029/2000PA000496
50. Marchitto, T.M., Broecker, W.S., 2006. Deep water mass geometry in the glacial Atlantic Ocean: A review of constraints from the paleonutrient proxy Cd/Ca. Geochemistry, Geophysics, Geosystems 7. https://doi.org/10.1029/2006GC001323
51. Marcott, S.A., Clark, P.U., Padman, L., Klinkhammer, G.P., Springer, S.R., Liu, Z., Otto-Bliesner, B.L., Carlson, A.E., Ungerer, A., Padman, J., He, F., Cheng, J., Schmittner, A., 2011. Ice-shelf collapse from subsurface warming as a trigger for Heinrich events. Proceedings of the National Academy of Sciences 108, 13415–13419. https://doi.org/10.1073/pnas.1104772108
52. Members, W.D.P., 2015. Precise interpolar phasing of abrupt climate change during the last ice age. Nature 520, 661–665. https://doi.org/10.1038/nature14401
53. Mulitza, S., Chiessi, C.M., Schefuß, E., Lippold, J., Wichmann, D., Antz, B., Mackensen, A., Paul, A., Prange, M., Rehfeld, K., Werner, M., Bickert, T., Frank, N., Kuhnert, H., Lynch-Stieglitz, J., Portilho-Ramos, R.C., Sawakuchi, A.O., Schulz, M., Schwenk, T., Tiedemann, R., Vahlenkamp, M., Zhang, Y., 2017. Synchronous and proportional deglacial changes in Atlantic meridional overturning and northeast Brazilian precipitation. Paleoceanography 32, 622–633. https://doi.org/10.1002/2017PA003084
54. Mulitza, S., Prange, M., Stuut, J.-B., Zabel, M., von Dobeneck, T., Itambi, A.C., Nizou, J., Schulz, M., Wefer, G., 2008. Sahel megadroughts triggered by glacial slowdowns of Atlantic meridional overturning. Paleoceanography 23. https://doi.org/10.1029/2008PA001637
55. Oppo, D.W., Curry, W.B., McManus, J.F., 2015. What do benthic δ13C and δ18O data tell us about Atlantic circulation during Heinrich Stadial 1? Paleoceanography 30, 353–368. https://doi.org/10.1002/2014PA002667
56. Oppo, D.W., Gebbie, G., Huang, K.-F., Curry, W.B., Marchitto, T.M., Pietro, K.R., 2018. Data Constraints on Glacial Atlantic Water Mass Geometry and Properties. Paleoceanography and Paleoclimatology 33, 1013–1034. https://doi.org/10.1029/2018PA003408
57. Oppo, D.W., Horowitz, M., 2000. Glacial deep water geometry: South Atlantic benthic foraminiferal Cd/Ca and δ13C evidence. Paleoceanography 15, 147–160. https://doi.org/10.1029/1999PA000436
58. Pedro, J.B., van Ommen, T.D., Rasmussen, S.O., Morgan, V.I., Chappellaz, J., Moy, A.D., Masson-Delmotte, V., Delmotte, M., 2011. The last deglaciation: timing the bipolar seesaw. Clim. Past 7, 671–683. https://doi.org/10.5194/cp-7-671-2011
59. Pöppelmeier, F., Blaser, P., Gutjahr, M., Jaccard, S.L., Frank, M., Max, L., Lippold, J., 2020. Northern-sourced water dominated the Atlantic Ocean during the Last Glacial Maximum. Geology 48, 826–829. https://doi.org/10.1130/G47628.1
60. Portilho-Ramos, R.C., Chiessi, C.M., Zhang, Y., Mulitza, S., Kucera, M., Siccha, M., Prange, M., Paul, A., 2017. Coupling of equatorial Atlantic surface stratification to glacial shifts in the tropical rainbelt. Sci Rep 7, 1561. https://doi.org/10.1038/s41598-017-01629-z
61. Rafter, P.A., Gray, W.R., Hines, S.K.V., Burke, A., Costa, K.M., Gottschalk, J., Hain, M.P., Rae, J.W.B., Southon, J.R., Walczak, M.H., Yu, J., Adkins, J.F., DeVries, T., 2022. Global reorganization of deep-sea circulation and carbon storage after the last ice age. Science Advances 8, eabq5434. https://doi.org/10.1126/sciadv.abq5434
62. Regional and global benthic δ18O stacks for the last glacial cycle - Lisiecki - 2016 - Paleoceanography - Wiley Online Library [WWW Document], n.d. URL https://agupubs.onlinelibrary.wiley.com/doi/full/10.1002/2016PA003002 (accessed 9.9.23).
63. Sarnthein, M., Winn, K., Jung, S.J.A., Duplessy, J.-C., Labeyrie, L., Erlenkeuser, H., Ganssen, G., 1994. Changes in East Atlantic Deepwater Circulation over the last 30,000 years: Eight time slice reconstructions. Paleoceanography 9, 209–267. https://doi.org/10.1029/93PA03301
64. Sedimentary fluxes at the Mid-Atlantic Ridge: sediment sources, accumulation rates, and geochemical characterisation. - OceanRep [WWW Document], n.d. URL https://oceanrep.geomar.de/id/eprint/30473/ (accessed 8.27.23).
65. Shackleton, N.J., Fairbanks, R.G., Chiu, T., Parrenin, F., 2004. Absolute calibration of the Greenland time scale: implications for Antarctic time scales and for Δ14C. Quaternary Science Reviews 23, 1513–1522. https://doi.org/10.1016/j.quascirev.2004.03.006
66. Shackleton, N.J., Hall, M.A., Vincent, E., 2000. Phase relationships between millennial-scale events 64,000–24,000 years ago. Paleoceanography 15, 565–569. https://doi.org/10.1029/2000PA000513

67. Shi, N., Schneider, R., Beug, H.-J., Dupont, L.M., 2001. Southeast trade wind variations during the last 135 kyr: evidence from pollen spectra in eastern South Atlantic sediments. Earth and Planetary Science Letters 187, 311–321. https://doi.org/10.1016/S0012-821X(01)00267-9
68. Skinner, L.C., Fallon, S., Waelbroeck, C., Michel, E., Barker, S., 2010. Ventilation of the Deep Southern Ocean and Deglacial CO2 Rise. Science 328, 1147–1151. https://doi.org/10.1126/science.1183627
69. Skinner, L.C., Primeau, F., Freeman, E., de la Fuente, M., Goodwin, P.A., Gottschalk, J., Huang, E., McCave, I.N., Noble, T.L., Scrivner, A.E., 2017. Radiocarbon constraints on the glacial ocean circulation and its impact on atmospheric CO2. Nat Commun 8, 16010. https://doi.org/10.1038/ncomms16010
70. Skinner, L.C., Shackleton, N.J., 2005. An Atlantic lead over Pacific deep-water change across Termination I: implications for the application of the marine isotope stage stratigraphy. Quaternary Science Reviews 24, 571–580. https://doi.org/10.1016/j.quascirev.2004.11.008
71. Skinner, L.C., Shackleton, N.J., 2004. Rapid transient changes in northeast Atlantic deep water ventilation age across Termination I. Paleoceanography 19. https://doi.org/10.1029/2003PA000983
72. Skinner, L.C., Waelbroeck, C., Scrivner, A.E., Fallon, S.J., 2014. Radiocarbon evidence for alternating northern and southern sources of ventilation of the deep Atlantic carbon pool during the last deglaciation. Proceedings of the National Academy of Sciences 111, 5480–5484. https://doi.org/10.1073/pnas.1400668111
73. Sortor, R.N., Lund, D.C., 2011. No evidence for a deglacial intermediate water Δ14C anomaly in the SW Atlantic. Earth and Planetary Science Letters 310, 65–72. https://doi.org/10.1016/j.epsl.2011.07.017
74. Stern, J.V., Lisiecki, L.E., 2014. Termination 1 timing in radiocarbon-dated regional benthic δ18O stacks. Paleoceanography 29, 1127–1142. https://doi.org/10.1002/2014PA002700
75. Tessin, A.C., Lund, D.C., 2013. Isotopically depleted carbon in the mid-depth South Atlantic during the last deglaciation. Paleoceanography 28, 296–306. https://doi.org/10.1002/palo.20026
76. Tjallingii, R., Claussen, M., Stuut, J.-B.W., Fohlmeister, J., Jahn, A., Bickert, T., Lamy, F., Röhl, U., 2008. Coherent high- and low-latitude control of the northwest African hydrological balance. Nature Geosci 1, 670–675. https://doi.org/10.1038/ngeo289
77. Umling, N.E., Oppo, D.W., Chen, P., Yu, J., Liu, Z., Yan, M., Gebbie, G., Lund, D.C., Pietro, K.R., Jin, Z.D., Huang, K.-F., Costa, K.B., Toledo, F. a. L., 2019. Atlantic Circulation and Ice Sheet Influences on Upper South Atlantic Temperatures During the Last Deglaciation. Paleoceanography and Paleoclimatology 34, 990–1005. https://doi.org/10.1029/2019PA003558
78. Vidal, L., Schneider, R.R., Marchal, O., Bickert, T., Stocker, T.F., Wefer, G., 1999. Link between the North and South Atlantic during the Heinrich events of the last glacial period. Climate Dynamics 15, 909–919. https://doi.org/10.1007/s003820050321
79. Voelker, A.H.L., Lebreiro, S.M., Schönfeld, J., Cacho, I., Erlenkeuser, H., Abrantes, F., 2006. Mediterranean outflow strengthening during northern hemisphere coolings: A salt source for the glacial Atlantic? Earth and Planetary Science Letters 245, 39–55. https://doi.org/10.1016/j.epsl.2006.03.014
80. Vogelsang, E., Sarnthein, M., Pflaumann, U., 2001. d18O Stratigraphy, chronology, and sea surface temperatures of Atlantic sediment records (GLAMAP-2000 Kiel), Berichte - Reports, Institut für Geowissenschaften. Kiel, Germany. https://doi.org/10.2312/reports-ifg.2001.13
81. Voigt, I., Cruz, A.P.S., Mulitza, S., Chiessi, C.M., Mackensen, A., Lippold, J., Antz, B., Zabel, M., Zhang, Y., Barbosa, C.F., Tisserand, A.A., 2017a. Variability in mid-depth ventilation of the western Atlantic Ocean during the last deglaciation. Paleoceanography 32, 948–965. https://doi.org/10.1002/2017PA003095
82. Voigt, I., Cruz, A.P.S., Mulitza, S., Chiessi, C.M., Mackensen, A., Lippold, J., Antz, B., Zabel, M., Zhang, Y., Barbosa, C.F., Tisserand, A.A., 2017b. Variability in mid-depth ventilation of the western Atlantic Ocean during the last deglaciation. Paleoceanography 32, 948–965. https://doi.org/10.1002/2017PA003095
83. Voigt, I., Cruz, A.P.S., Mulitza, S., Chiessi, C.M., Mackensen, A., Lippold, J., Antz, B., Zabel, M., Zhang, Y., Barbosa, C.F., Tisserand, A.A., 2017c. Variability in mid-depth ventilation of the western Atlantic Ocean during the last deglaciation. Paleoceanography 32, 948–965. https://doi.org/10.1002/2017PA003095

84. Waelbroeck, C., Duplessy, J.-C., Michel, E., Labeyrie, L., Paillard, D., Duprat, J., 2001. The timing of the last deglaciation in North Atlantic climate records. Nature 412, 724–727. https://doi.org/10.1038/35089060
85. Waelbroeck, C., Lougheed, B.C., Vazquez Riveiros, N., Missiaen, L., Pedro, J., Dokken, T., Hajdas, I., Wacker, L., Abbott, P., Dumoulin, J.-P., Thil, F., Eynaud, F., Rossignol, L., Fersi, W., Albuquerque, A.L., Arz, H., Austin, W.E.N., Came, R., Carlson, A.E., Collins, J.A., Dennielou, B., Desprat, S., Dickson, A., Elliot, M., Farmer, C., Giraudeau, J., Gottschalk, J., Henderiks, J., Hughen, K., Jung, S., Knutz, P., Lebreiro, S., Lund, D.C., Lynch-Stieglitz, J., Malaizé, B., Marchitto, T., Martínez-Méndez, G., Mollenhauer, G., Naughton, F., Nave, S., Nürnberg, D., Oppo, D., Peck, V., Peeters, F.J.C., Penaud, A., Portilho-Ramos, R. da C., Repschläger, J., Roberts, J., Rühlemann, C., Salgueiro, E., Sanchez Goni, M.F., Schönfeld, J., Scussolini, P., Skinner, L.C., Skonieczny, C., Thornalley, D., Toucanne, S., Rooij, D.V., Vidal, L., Voelker, A.H.L., Wary, M., Weldeab, S., Ziegler, M., 2019. Consistently dated Atlantic sediment cores over the last 40 thousand years. Sci Data 6, 165. https://doi.org/10.1038/s41597-019-0173-8
86. Waelbroeck, C., Skinner, L.C., Labeyrie, L., Duplessy, J.-C., Michel, E., Vazquez Riveiros, N., Gherardi, J.-M., Dewilde, F., 2011. The timing of deglacial circulation changes in the Atlantic. Paleoceanography 26. https://doi.org/10.1029/2010PA002007
87. Walter, H.J., Rutgers van der Loeff, M.M., Hoeltzen, H., 1997. Enhanced scavenging of 231Pa relative to 230Th in the South Atlantic south of the Polar Front: Implications for the use of the 231Pa/230Th ratio as a paleoproductivity proxy. Earth and Planetary Science Letters 149, 85–100. https://doi.org/10.1016/S0012-821X(97)00068-X
88. Yu, E.-F., Francois, R., Bacon, M.P., Fleer, A.P., 2001. Fluxes of 230Th and 231Pa to the deep sea: implications for the interpretation of excess 230Th and 231Pa/230Th profiles in sediments. Earth and Planetary Science Letters 191, 219–230. https://doi.org/10.1016/S0012-821X(01)00410-1
89. Zarriess, M., Johnstone, H., Prange, M., Steph, S., Groeneveld, J., Mulitza, S., Mackensen, A., 2011. Bipolar seesaw in the northeastern tropical Atlantic during Heinrich stadials. Geophysical Research Letters 38. https://doi.org/10.1029/2010GL046070
90. Zarriess, M., Mackensen, A., 2011. Testing the impact of seasonal phytodetritus deposition on δ13C of epibenthic foraminifer Cibicidoides wuellerstorfi: A 31,000 year high-resolution record from the northwest African continental slope. Paleoceanography 26. https://doi.org/10.1029/2010PA001944
91. Zhang, Y., Chiessi, C.M., Mulitza, S., Zabel, M., Trindade, R.I.F., Hollanda, M.H.B.M., Dantas, E.L., Govin, A., Tiedemann, R., Wefer, G., 2015. Origin of increased terrigenous supply to the NE South American continental margin during Heinrich Stadial 1 and the Younger Dryas. Earth and Planetary Science Letters 432, 493–500. https://doi.org/10.1016/j.epsl.2015.09.054
92. Zhao, N., Marchal, O., Keigwin, L., Amrhein, D., Gebbie, G., 2018. A Synthesis of Deglacial Deep-Sea Radiocarbon Records and Their (In)Consistency With Modern Ocean Ventilation. Paleoceanography and Paleoclimatology 33, 128–151. https://doi.org/10.1002/2017PA003174

V. Revisiting the Benthic $\delta^{18}O$ Lag Between the Iberian Margin and the Eastern Equatorial Pacific

Abstract

Benthic $\delta^{18}O$ records from ocean sediment cores are often assumed to change synchronously with global ice volume, however non-glacioeustatic factors can cause temporal offsets, or lags, between different regions. Previous studies have observed lags between the Atlantic and Pacific during Termination 1; one widely cited study measured a 3.9 kyr lag between two individual records from the Iberian Margin and Eastern Equatorial Pacific (Skinner & Shackleton, 2005). Here I calculate the average lag between the Eastern Equatorial Pacific and the Iberian Margin during Termination 1 by constructing a local stack for each region. Stacks increase the signal-to-noise ratios by averaging multiple signals and thus offer an improvement over comparing individual records. Stacks are constructed using the new Bayesian software package, BIGMACS (Lee and Rand et al., accepted), and each stack is composed of cores within a close spatial proximity that are evaluated to have similar water mass compositions. I calculate the lag between the two stacks using three different methods that produce time-dependent lags representative of the average offset between the two regions. I find that the Eastern Equatorial Pacific lags behind the Iberian Margin by mean values of 2.11 to 2.52 kyr with local maxima occurring between 14.2-11.4 ka BP. All three methods found statistically significant lags in this time range with 95% credible intervals of 0.08– 3.70 kyr. Accurate lag measurements can help estimate the potential for age errors during benthic $\delta^{18}O$ stratigraphic alignment and can also be used as constraints on deep water overturning rates and changes in seawater properties (e.g., Gebbie, 2012).

1 Introduction

Skinner & Shackleton (2005) identified a 3.9 kyr lag between benthic $\delta^{18}O$ signals sampled from the Eastern Equatorial Pacific and the Iberian Margin, which if substantiated has implications regarding the basinal manifestation of bipolar seesaw and circulation changes that occurred during Termination 1 (T1). However, the previous reconstruction relies on the relatively subjective choice of the termination midpoint, does not include statistical uncertainty, and was measured between only a pair of sediment cores rather than average signals representative of each region.

Here I calculate the regional lag between the Iberian Margin and the Eastern Equatorial Pacific by creating a 3-core Iberian Margin stack and a 5-core Eastern Equatorial Pacific stack. The lag between the two stacks is calculated using three different methods. The first follows the methodology of Chapter 2 in which lags are calculated by subtracting multiproxy age models from $\delta^{18}O$-only age models. The average lag is calculated by constructing a lag stack from the core-specific lags. The second method calculates an average lag by translating the Iberian Margin stack to a synthetic depth scale in order to align the stack's mean to the Eastern Equatorial Pacific stack. In this method the average lag is calculated by taking the difference between the aligned age model and the Iberian Margin stack's "true" age model. The third method calculates the lag directly from the two stacks using a Bayesian inversion. For the remainder of the chapter, I will refer to these methods as Method 1, Method 2 and Method 3.

I find that each method produces lags of similar magnitude during T1, with maximum mean values indicating that the Eastern Equatorial Pacific lagged the Iberian

Margin by 2.11 - 2.52 kyr (~ 1.5 kyr smaller than the lag calculated by Skinner & Shackleton, 2005) in the time range of 14.2-11.4 ka BP. In addition, all three methods produced lags that are statistically significant during T1 but not during the LGM and the Holocene.

2 Background

2.1 Overview of Skinner & Shackleton (2005)

Skinner & Shackleton (2005) estimated the lag between benthic $\delta^{18}O$ signals measured in a core from Iberian Margin (MD99-2334K) and a core from the Eastern Equatorial Pacific (TR1633-31B, Figure 1). Chronologies were constructed from planktonic radiocarbon ages calibrated with the Marine13 curve (Reimer et al., 2013) after subtracting a reservoir age of 580 years for TR163-31B and 400 years for MD99-2334K. In addition, the age model for MD99-2334K was supplemented with planktonic $\delta^{18}O$ tied to Greenland ice core $\delta^{18}O$ on the GISP2 age model. The lag between the two records was calculated by visually estimating the difference in time between the termination midpoint of the smoothed $\delta^{18}O$ signals. This method produced a single estimate that the Pacific core lagged the Iberian Margin core by 3.9 kyr between approximately 10 and 15 ka BP.

However, this method is potentially susceptible to local variability and noise in each $\delta^{18}O$ signal, sediment disturbances within each core, and subjectivity when identifying the termination midpoint. In addition, statistical uncertainty stemming from either core's chronology is not included in the measurement. Comparing the timing of $\delta^{18}O$ change in several nearby cores can provide context for the cause and implications of the observed lag and better estimate the size of the $\delta^{18}O$ lag between these two ocean regions.

2.2 Potential Cause of Lag

The 3.9 kyr lag observed by Skinner & Shackleton (2005) is larger than the difference between modern ventilation ages at the Iberian Margin (~300 years) and Eastern Equatorial Pacific (~1200 years, Devries & Primeau 2011), and therefore implies changes in water mass geometries, circulation rates, and/or asynchronous hemispheric surface signals during T1.

Today North Atlantic Deep Water (NADW) enters the Antarctic Circumpolar Current (ACC) at depths similar to the Drake Passage sill. The sea floor barrier maintains a zonal pressure gradient causing net southward geostrophic flow and allowing NADW to surface off the coast of Antarctica and form Antarctic Bottom Water (AABW) in the Ross and Wedell Seas (Talley, 2013). In the Pacific and Indian Oceans, AABW flows north and forms Pacific Deep Water (PDW) through diffusive heating. PDW then returns south at depths above NADW and contributes to Upper Circumpolar Deep Water (UCDW), Antarctic Intermediate Water (AAIW), and SubAntarctic Mode Water (SAMW). If NADW shoaled above the Drake Passage sill depth during the LGM (Curry & Oppo, 2005), the water mass may have been cut off from the Pacific Ocean (Sikes et al., 2017).

An increase in transit time of Antarctic surface signals to the deep Pacific could also be responsible for the $\delta^{18}O$ offset. A recent compilation of benthic ventilation ages observed a "flipped" glacial Pacific basin with oldest ventilation ages in the deep Pacific reaching 3 kyr (unlike the modern configuration in which the oldest Pacific waters are found at intermediate depths) and persisted throughout the early deglaciation (Rafter et al., 2022). However, ventilation ages in the deep Pacific rapidly decreased during Heinrich Stadial 1 (HS1) and were roughly similar to intermediate-depth values during the latter half of the termination. Benthic ventilation ages have also been measured in core MD99-2334K (used here in the

Iberian Margin stack) and were observed to oscillate with the bipolar seesaw during T1 (Skinner et al., 2014). Ventilation ages measured in this core increased to ~3 kyr during HS1 and ~2 kyr during the Younger Dryas (YD).

Asynchronous changes in water mass properties caused by different hemispheric surface forcings may also contribute to $\delta^{18}O_b$ lags. Ice core proxies such as $\delta^{18}O_{ice}$, $\delta^{15}N$ and δD indicate that both the magnitude and timing of warming were different in the Northern and Southern Hemispheres (EPICA Community Members, 2006; Lemieux-Dudon et al., 2010; Pedro et al., 2011; Buizert et al., 2014; WAIS Divide project Members, 2015). This may have caused different water mass property changes for northern and southern sourced water. For example, significant warming in an Antarctic $\delta^{18}O$ ice core composite record begins 18.98 ka BP and continues until the Antarctic Climate Reversal 14.6 ka BP (ACR, Pedro et al., 2011). In Greenland, glacial conditions continue through HS1 until the onset of the Bølling at 14.64 ka BP (NGRIP members, 2004; Kindler et al., 2014).

3 Methods

3.1 Data

The Iberian Margin and Eastern Equatorial Pacific stacks are composed of three and five cores, respectively. The cores within each region are geographically close and all cores are sampled from depths between 2830 and 3205 m (Figure 1, Table 1). Given the spatial proximity of cores within each region, I assume that their benthic $\delta^{18}O$ signals are recording the same water mass at each location such that they change synchronously and that the cores are appropriate to stack.

Each core contains both radiocarbon and benthic $\delta^{18}O$ data except for TR163-31P. Radiocarbon ages were calibrated with the Marine20 curve (Heaton et al., 2020), a reservoir

age offset (ΔR) of 0, and a reservoir age standard deviation of 200 years to account for changes in past reservoir ages. See section 5.1 for a discussion of reservoir ages and the effect they would have on our lag calculations. For cores which use different benthic species, the $\delta^{18}O$ values are corrected to the *Uvigerina* scale; however, this correction does not affect alignment results due to the learned shift and scale parameters BIGMACS applies during the alignment process.

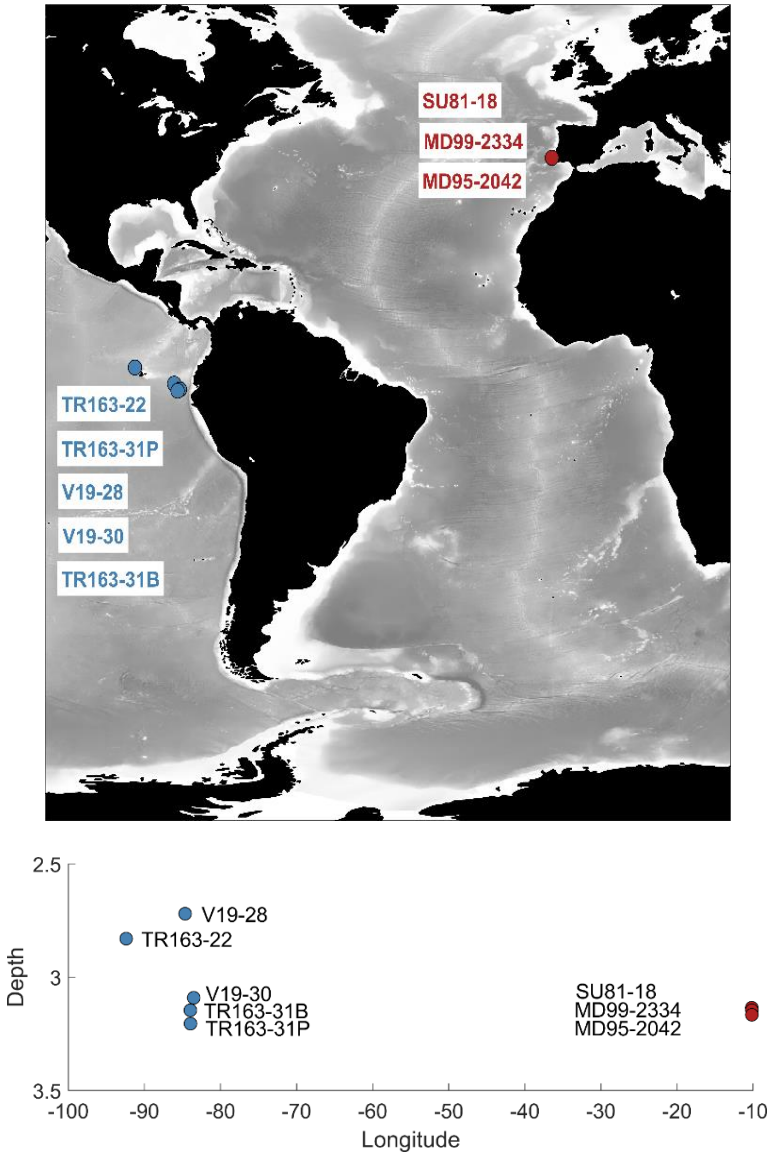

Figure 1: Locations of cores used in the Eastern Equatorial Pacific stack (blue) and the Iberian Margin stack (red).

Core	Lat	Lon	Depth	Citations
MD95-2042	37.8	-10.17	3146	Shackleton et al., 2004; Bard et al., 2017; Shackleton et al., 2000
MD99-2334K	37.8	-10.17	3166	Skinner et al., 2003; Skinner & Shackleton, 2004; Skinner & Shackleton 2005; Skinner et al., 2014; Skinner et al., 2021
SU81-18	37.8	-10.18	3135	Vogelsang et al., 2001; Waelbroeck et al., 2001
TR163-22	0.5	-92.4	2830	Lea et al., (2006)
TR163-31P	-3.58	-83.95	3205	Shackleton et al., (1988); Martin et al., (2002)
TR163-31B	-3.62	-83.97	3146	Shackleton et al., 1988; Skinner & Shackleton, 2005
V19-28	-2.37	-84.65	2720	Koutavas & Lynch-Stieglitz, (2003); Loubere & Richaud, (2007); CLIMAP project members, (1981)
V19-30	-3.38	-83.52	3091	Bond et al., (1997)

Table 1: Core locations and data citations.

3.2 Stacking and Age Model Construction

The 3-core Iberian Margin stack and 5-core Eastern Equatorial Pacific stack are both constructed with BIGMACS using default settings. During the stacking procedure, a multiproxy age model (an age model constrained by both radiocarbon and $\delta^{18}O$ stratigraphic alignment) is constructed for each core (see Chapter 1). Due to the radiocarbon age constraints as well as the reliability of the local alignment targets, I consider the multiproxy age models to reflect the "true" age of each core. Additionally, benthic $\delta^{18}O$-only age models are created for Method 1, in which $\delta^{18}O$-aligned ages are compared with the "true" multiproxy stack ages. Benthic $\delta^{18}O$-only age models are created for the three Iberian Margin cores by aligning them to the Pacific stack. These alignments are assisted by two additional ages at the first and last

depth of the radiocarbon ages of each core, following the methods from Chapter 2. All additional ages fall outside the lag calculation time interval (5-25 ka BP).

Lastly, a $\delta^{18}O$-only age model is created for the Iberian Margin stack aligned to the Eastern Equatorial Pacific stack. Before alignment, the Iberian Margin stack is translated to a depth scale by dividing the stack's age by 10; thus, each kiloyear of stack time is simulated as 0.1 m (10 cm) of core length. The $\delta^{18}O$ signal is constructed by sampling the stack's median value every half kyr (5 cm) between 5 and 25 ka BP, which creates a record composed of 41 points spanning a depth range of 0.5 and 2.5 m. Two additional ages (i.e., tie points) were used at 5 and 25 ka BP using the Iberian Margin stack's multiproxy age model.

3.3 Lag Calculation Method

I estimate lags using three different methods. The first follows the methods of Chapter 2, in which $\delta^{18}O$-only age models are constructed by aligning the individual Iberian Margin cores to the Eastern Equatorial Pacific stack. In the second method I translate the Iberian Margin stack to a synthetic depth scale and align it to the Eastern Equatorial Pacific stack. In the third method I calculate the lag directly from the stacks using a Bayesian inversion.

For the first method, lags and their uncertainties are calculated by subtracting all possible pairs of age model samples from each Iberian Margin core's $\delta^{18}O$ alignment to the Pacific stack and its multiproxy age models produced during Atlantic stack construction (resulting in 1 million lag samples). The multiproxy age models are considered to give the "true" age of the core and take the place of ^{14}C-only age models from Chapter 2. Each lag sample is placed on the associated multiproxy age. This results in one lag as a function of time that is composed of 1 million samples for each core (Figure 3). The lag average is calculated by averaging together pairs of lag samples in the same manner as Chapter 2 (Figure 4).

In the second method, the lag is calculated by subtracting the age samples generated by aligning the Iberian Margin to the Eastern Equatorial Pacific stack from the true age of the Iberian Margin stack. This results in a time-series composed of 1000 samples.

In the third method, the lag is calculated directly from the two stacks by finding the required time shift applied to the Iberian Margin stack to equate the two $\delta^{18}O$ signals. The stacks are drawn with a Gaussian process regression, thus every time-slice from the stack is modeled with a Gaussian distribution. Therefore, the difference between the stacks is also Gaussian. A Bayesian inversion is used to reverse the direction of inference and calculate the posterior probability of a lag given the likelihood that the two stacks are in fact equal.

Given the lag L_t at time t, the difference in $\delta^{18}O$ signals between the two stacks can be expressed by

$$Z_t = \frac{Y_{IM,t-L_t} - h}{s} - Y_{EEP,t}.$$

In the above equation, $Y_{EEP,t} \sim N(\mu_{EEP,t}, \sigma_{EEP,t})$ represents the $\delta^{18}O$ values from the Eastern Equatorial Pacific stack at time t and $Y_{IM,t-L_t} \sim N(\mu_{IM,t-L_t}, \sigma_{IM,t-L_t})$ represents the $\delta^{18}O$ values from the Iberian margin stack at time $t - L_t$. The variables h and s are the shift and scale parameters applied to the Iberian Margin stack to achieve a similar magnitude of $\delta^{18}O$ change across T1. I use the same shift and scale parameters of 0.13 and 1.01 that are learned by BIGMACS in Method 2 during the alignment process. The likelihood can then be given by the following normal distribution

$$p(Z_t = 0|L_t) = N\left(Z_t = 0 \middle| \frac{\mu_{IM,t-L_t} - h}{s} - \mu_{EEP,t},\ sqrt\left(\sigma^2{}_{EEP,t} + \frac{\sigma^2{}_{IM,t-L_t}}{s^2}\right)\right).$$

I perform a sensitivity tests for different possible priors using a Gaussian distribution with a mean of zero and standard deviations ranging from 0.5 to 4 kyr and a Uniform

distribution centered at zero with ranges from plus and minus 1 to 6 kyr. In addition, I also calculate the posterior distribution using a physically realistic prior modeled as a Gaussian distribution with mean 1 kyr and standard deviation 2 kyr. The mean reflects the modern difference in transit times between the Iberian Margin and the Eastern Equatorial Pacific while the 2-sigma encompasses the 3.9 kyr lag estimated by Skinner & Shackleton (2005).

Now we can use Baye's theorem to reverse the direction of inference and solve for the posterior distribution for a lag that results in Z_t equal to zero

$$p(L_t|Z_t = 0) \propto p(Z_t = 0|L_t) * p(L_t).$$

Because the likelihood and prior can be expressed exactly, we can solve for the posterior distribution of each time step analytically (i.e., Markov-Chain Monte Carlo sampling is not required).

4 Results

4.1 Stack Results

The Iberian Margin and Eastern Equatorial Pacific stacks are plotted in Figure 2. Between 5 and 25 ka BP, the Iberian Margin stack is composed of 323 benthic $\delta^{18}O$ data points and 115 radiocarbon ages. The Eastern Equatorial Pacific stack is composed of 311 $\delta^{18}O$ data points and 72 radiocarbon ages. For both probabilistic stacks, the stack $\delta^{18}O$ values have an average standard deviation of 0.14 per mil. The average 95% credible interval width for the multiproxy age models of the Iberian Margin cores is 1.12 kyr, and the average credible interval width for the Eastern Equatorial Pacific cores is 2.21 kyr. The larger age uncertainty in the Eastern Equatorial Pacific stack is likely due to fewer

radiocarbon ages and $\delta^{18}O$ data points. For example, TR163-31P lacks radiocarbon age constraints (Figure S6) and V19-28 has a low resolution $\delta^{18}O$ signal (Figure S7).

The lag between the two stacks can be observed as the more rapid change in the mean of the Iberian Margin stack (Figure 2). Furthermore, the mean signal of each stack eventually falls outside the 2-sigma credible interval of the other stack during the termination. Millennial scale variations in the slope of the Iberian Margin stack likely reflect the climatic events that occurred during T1 (HS1, the Bølling Allerød, and the YD). These rapid and transient changes are contrasted with the more gradual and smooth signal in the Eastern Equatorial Pacific. The most positive $\delta^{18}O$ values (reflecting the approximate timing of the LGM in each stack) are different; the Iberian Margin reaches values of 5.13‰ at 18.7 ka BP while the most positive Eastern Equatorial Pacific value is 4.91‰ at 20.8 ka BP. Both stacks converge to similar Holocene values of ~3.30‰ by 4 ka BP.

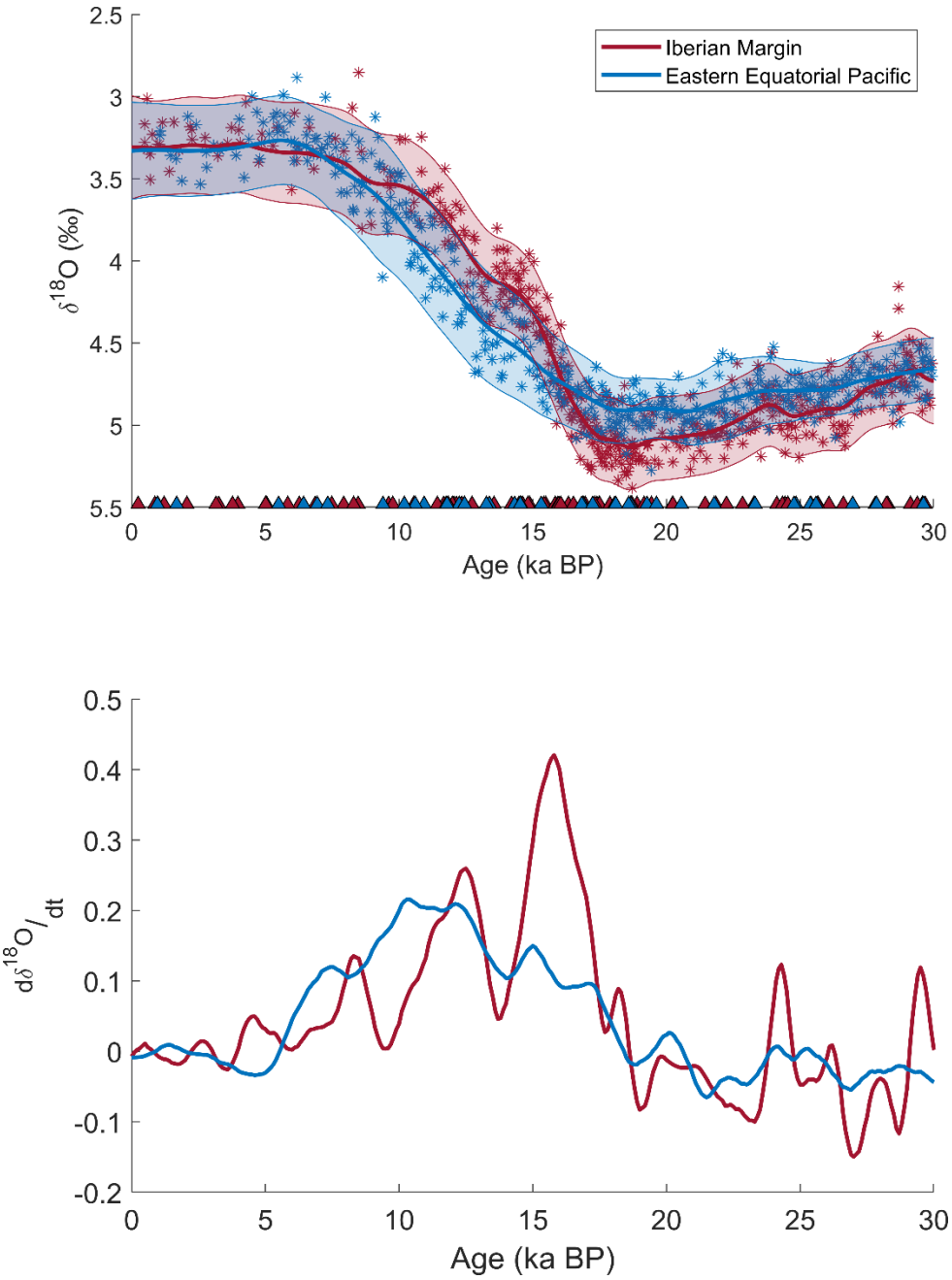

Figure 2: (Top) Comparison between the Iberian Margin stack (red) and the Eastern Equatorial Pacific stack (blue) with the shaded regions covering the upper and lower 2-sigma intervals. Triangles represent median radiocarbon ages constraining their respective stacks and stars are the individual $\delta^{18}O$ measurements that have been shifted and scaled during stack construction. (Bottom) The time derivative of the median values for the Iberian Margin (red) and Eastern Equatorial Pacific (blue) stacks. The difference in the derivatives emphasizes the different signals contained in each stack. While the Iberian Margin stack is characterized by rapid climate swings characteristic of the arctic, the Eastern Equatorial Pacific stack is more consistent and reminiscent of the Antarctic.

4.2 Lag Results

Three different methods are used to estimate lags between the Eastern Equatorial Pacific and the Iberian Margin between 5 and 25 ka BP at a temporal resolution of 0.1 kyr (Figures 3-8). The mean lag and 95% credible interval for each method is listed in Table 2.

The core-specific lags for Method 1 (Figure 3) show similar results for all Iberian Margin cores: statistically insignificant lags during the LGM and the Holocene and a lead of the Iberian Margin during the termination. Specifically, cores MD95-2042 and MD99-2334K both show maximum Pacific lags of 2.45 and 2.44 kyr at 14.8 and 14.7 ka BP, respectively. Core SU81-18 has a later maximum lag of 3.11 kyr at 11.3 ka BP. The average lag for Method 1 (Figure 4) shows two dips; the first has a maximum value of 2.31 (95% CI: 2.95 – 1.66) kyr at 14 ka BP and the second has a maximum value of 2.44 (95% CI: 1.62 – 3.34) kyr at 11.40 ka BP. The 95% credible interval of the lag estimate has an average width of 1.68 kyr between 10 and 18 ka BP.

The lag resulting from Method 2 (Figure 5) has a maximum lag equal to 2.52 (95% CI: 1.58 – 3.32) kyr at 14.2 ka BP. This lag does not show any sign of millennial scale variability and has a larger uncertainty with an average 95% credible interval width of 2.21 kyr from 10-18 ka BP.

The sensitivity tests for Method 3 reveal that between roughly 10 and 13 ka BP, the mean lags and 95% credible intervals produced with Gaussian and Uniform distributions converge to the same values if the prior's standard deviation is sufficiently large (Figure 6). Specifically, I choose to analyze the lag's sensitivity to the prior distribution at 12.3 ka BP when the lag for all priors appears to have the smallest statistical uncertainty. During this time, the lag results become insensitive to the choice of prior once the standard deviation for

the Gaussian distribution is greater than or equal to 2.5 and the range of the Uniform distribution is from [-4 4].

Figure 7 compares the results between the physically realistic prior (a Gaussian distribution with mean and standard deviation equal to 1 and 2 kyr) and the non-informative Uniform prior distribution with a range of [-4 4] kyr. The two posterior distributions are very similar and both show two periods of statistical significance. Results from the uniform prior show statistically significant lags of 2.30 (95% CI: 0.24 – 3.79) kyr at 12.4 ka BP and 1.8 (95% CI: 0.02 – 3.73) kyr at 14.5 ka BP. The statistically significant lags using the physically realistic Gaussian prior have maximum values of 2.11 (95% CI: 0.08 – 3.70) kyr at 12.9 ka BP and 1.91 (95% CI: 0.02 – 3.77) kyr at 14 ka BP. Due to the similarity of the two posteriors, for the remainder of the paper I will focus on the results using the physically realistic prior. However, outside of the termination the posterior becomes sensitive to the choice of prior distribution.

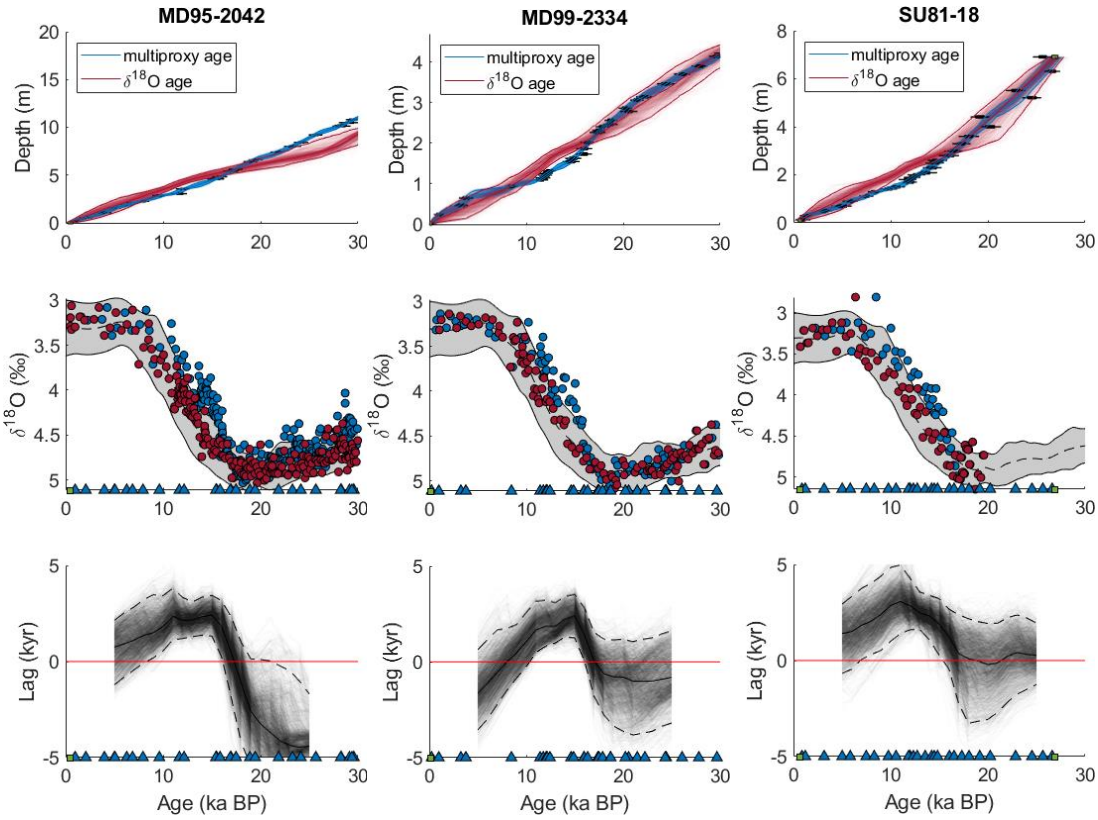

Figure 3: Core specific results for Method 1. (Top Row) Multiproxy (blue) vs. $\delta^{18}O$ -only (red) age models for Iberian Margin cores. Calibrated radiocarbon ages are displayed as black horizontal lines. (Middle Row) Benthic $\delta^{18}O$ record on the multiproxy age models (blue) and $\delta^{18}O$-only age models (red) aligned to the Eastern Equatorial Pacific stack (gray). Blue triangles and green squares represent the median radiocarbon ages and additional ages. (Bottom Row) The core-specific lags, including the median (solid black line), 95% credible intervals (dotted black lines), and the zero line (red).

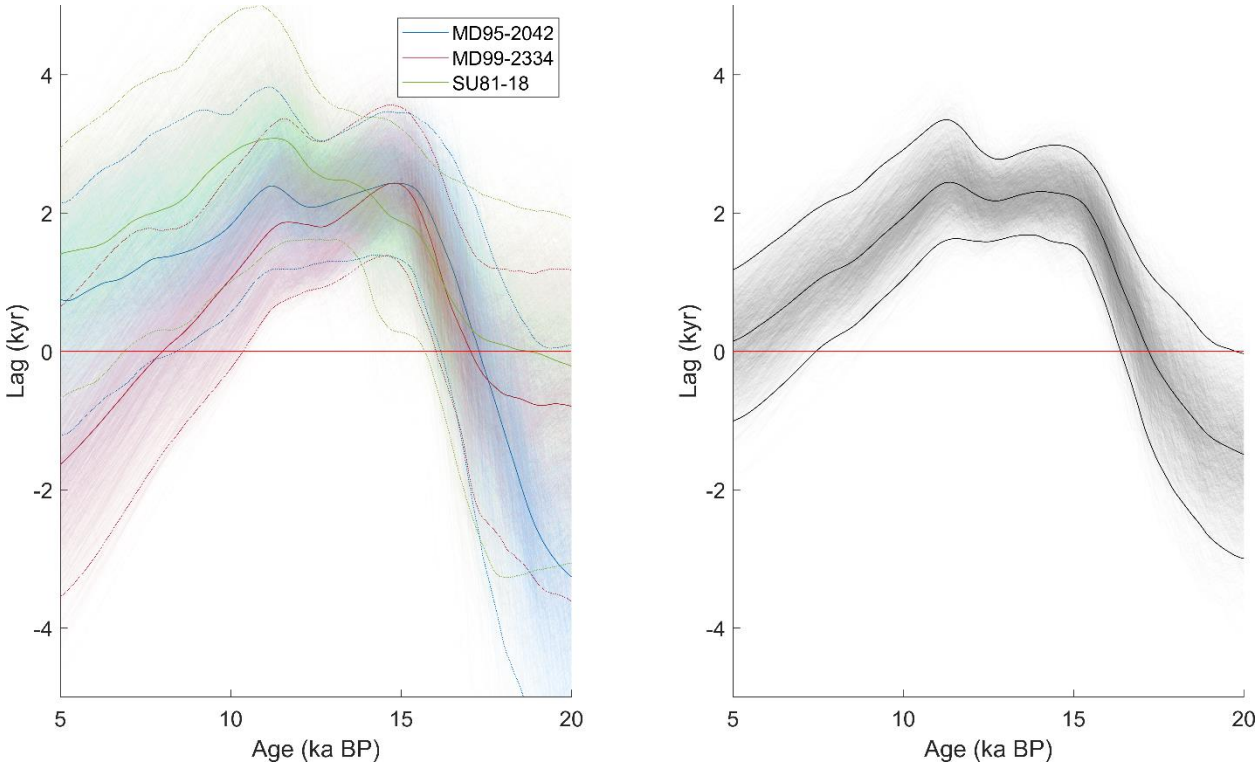

Figure 4: (Left) Core-specific lags produced by Method 1. (Right) Regional lag calculated by averaging core-specific lags.

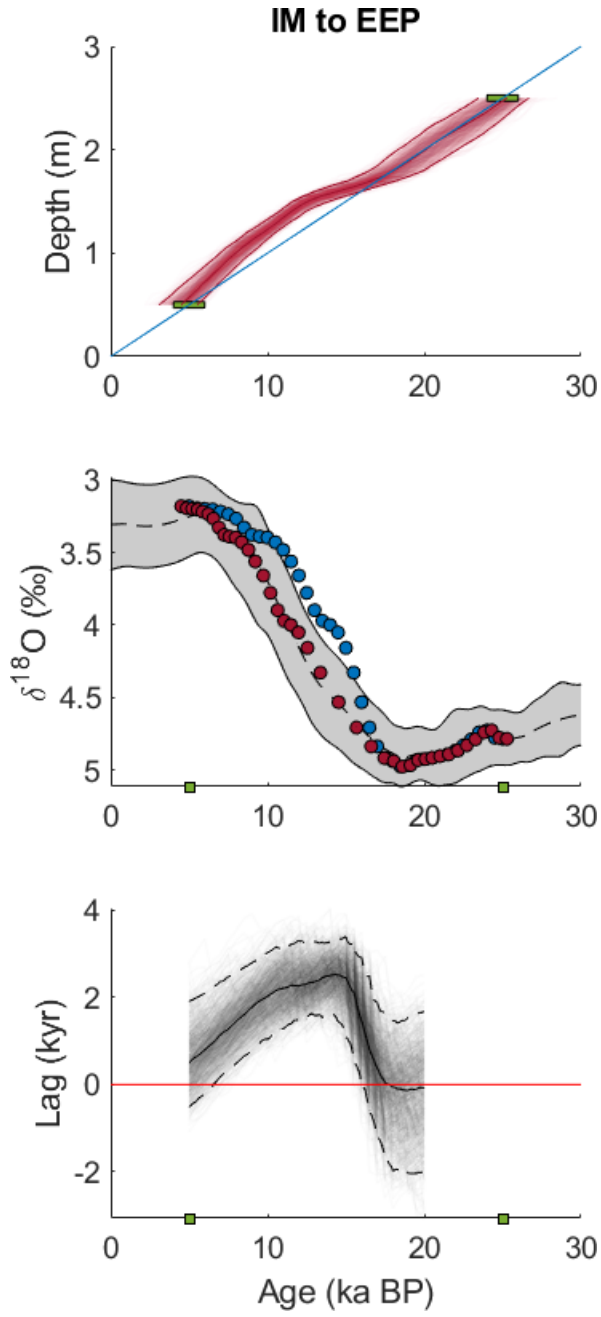

Figure 5: Age model for the Iberian Margin stack translated to a pseudo-depth scale and aligned to the Eastern Equatorial Pacific Stack (Method 2). (Top) The δ^{18}O-only age model (red), additional ages (green rectangles), and the "true" multiproxy age from the Iberian Marin stack (blue line). (Middle) The Iberian Margin stack on the original age model (blue) and aligned to the Eastern Equatorial Pacific stack (red). (Bottom) The median lag (solid black line) and 95% credible interval (dotted black lines) produced by Method 2.

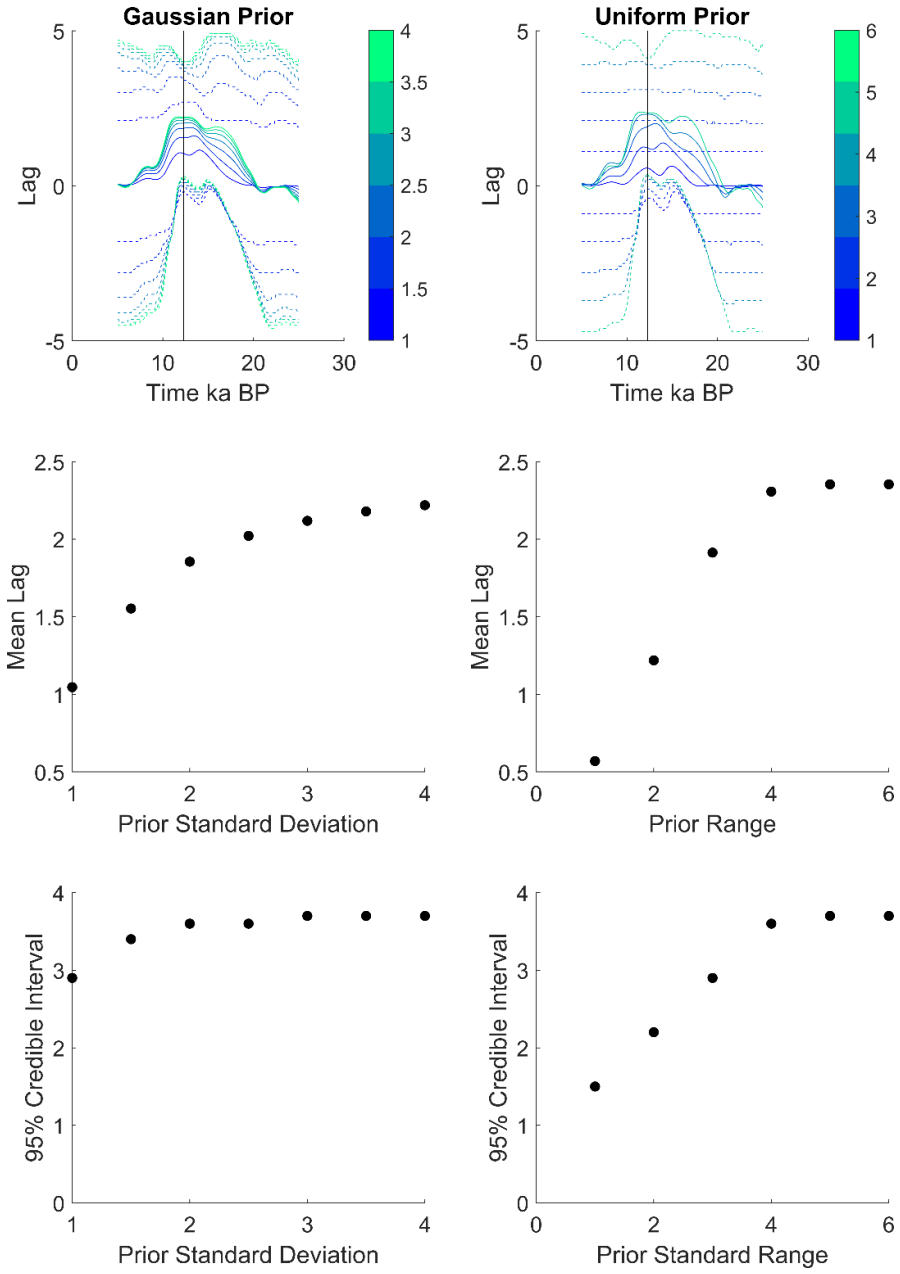

Figure 6: The sensitivity of Method 3 to the choice of prior distribution. (Top Row) Lags produced using a Gaussian prior with standard deviations ranging from 1 to 4 kyr (left) and a Uniform distribution with ranges from [-1 1] to [-6 6] kyr (right). The color denotes the standard deviation and range of the priors and the black vertical line is drawn at 12.3 ka BP, a time period that is particularly well constrained for all runs. Solid colored lines reflect the mean lag under the corresponding prior and dotted lines are the 95% credible intervals. (Middle Row) The mean lag at 12.3 ka BP for the different prior distributions. Results begin to converge when the Gaussian prior is greater than or equal to 2.5 ka BP and the Uniform range is greater than or equal to [-4 4] kyr. (Bottom Row) The 95% credible interval for the Gaussian and Uniform Priors at 12.3 ka BP.

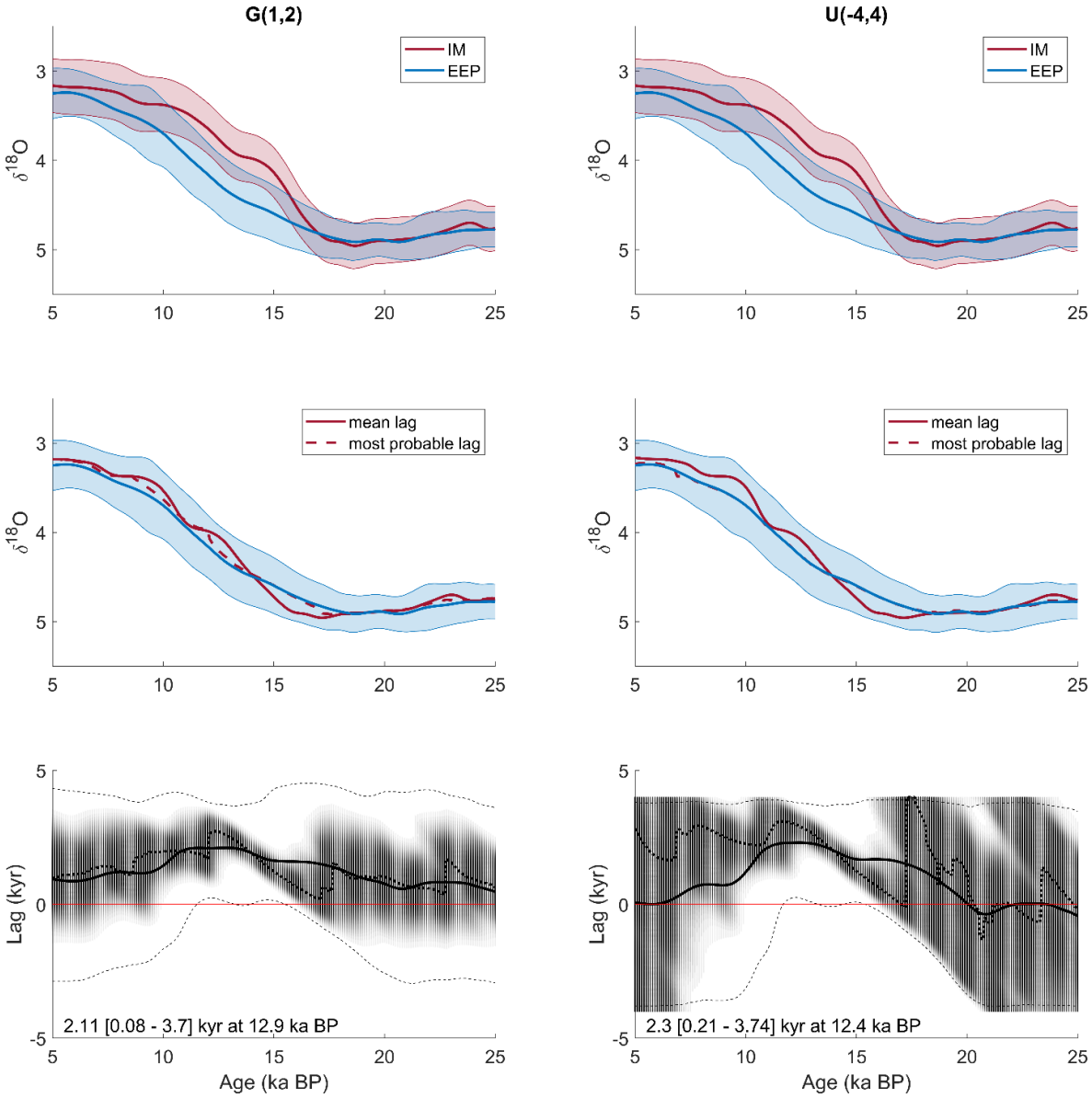

Figure 7: The lags produced by Method 3 using a physically realistic Gaussian distribution with mean and standard deviation of 1 and 2 kyr (left), and a uniform prior distribution with a range of [-4 4] kyr (right). (Top) The Eastern Equatorial Pacific stack with the shifted and scaled Iberian Margin stack. (Middle) The Eastern Equatorial Pacific stack plotted with the Iberian Margin stack with the mean lag (solid red) and the most probable lag (dotted red). (Bottom) The posterior lag distributions with the upper and lower 95% credible intervals (dotted black lines), the mean lag (solid black line), and the most probable lag (bold dotted line). Shading indicates posterior probability, with darker shading revealing areas of higher probability. Text indicates the magnitude, timing, and 95% credible intervals of the maximum lag.

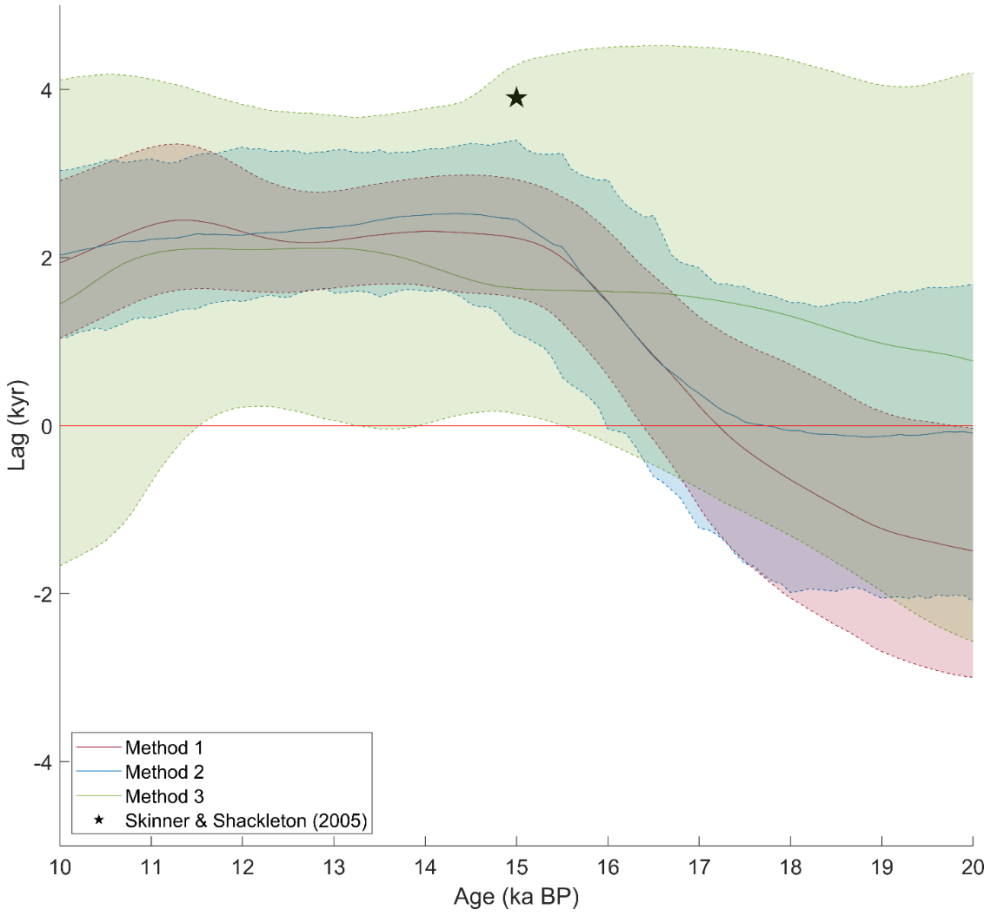

Figure 8: Comparison of lags produced by each method with the zero line (red) and the 3.9 kyr lag estimated by Skinner & Shackleton (2005) (black star).

Age	Method 1	Method 2	Method 3
6	0.43 [-0.067, 1.5]	0.8 [-0.22, 2.10]	0.86 [-2.85, 4.22]
8	**1.16 [0.23 2.16]**	**1.45 [0.48, 2.57]**	1.21 [-2.35, 3.99]
10	**1.93 [1.06, 2.86]**	**2.03 [1.04, 3.03]**	1.45 [-1.67, 4.11]
12	**2.31 [1.62, 3.08]**	**2.26 [1.48, 3.31]**	**2.09 [0.22, 3.82]**
14	**2.31 [1.66, 2.95]**	**2.51 [1.60, 3.29]**	**1.91 [0.02, 3.77]**
16	**1.47 [0.58, 2.30]**	1.47 [-0.04, 2.93]	1.60 [-0.21, 4.50]
18	0.63 [-2.04, 0.72]	-0.06 [-1.99, 1.46]	1.30 [-1.31, 4.35]

Table 2: Median, upper 95%, and lower 95% credible limits for the lags calculated by each method. Bold indicates values that are statistically significant.

5 Discussion

5.1 Potential Causes

Using three methods, I estimate that the maximum lag between the Eastern Equatorial Pacific and the Iberian Margin is between 2.11 and 2.52 kyr between roughly 11.4 and 14.2 ka BP (approximately 1.5 kyr smaller than the 3.9 kyr lag estimated by Skinner & Shackleton, 2005). Furthermore, Methods 1 and 3 have indications of millennial scale variations at roughly 14 and 12 ka BP. Interpretation of the original lag concluded that the benthic $\delta^{18}O$ offset was caused by delayed Antarctic warming and a series of coupled deep water $\delta^{18}O_{sw}$ and temperature changes in the North Atlantic (Skinner & Shackleton 2005; Gebbie 2012). However, northern and southern hemisphere temperature stacks have since revealed that the southern hemisphere likely warmed before the northern hemisphere (albeit at a slower rate, Shakun et al., 2012), and the 2.5 kyr lag calculated here could also be reproduced by changes in ocean circulation during T1 and/or a larger reservoir age at the Iberian Margin.

Today, water bathing the core sites in the Eastern Equatorial Pacific is approximately 1 kyr older than the water mass located at the deep Iberian Margin. Thus a lag of 2.5 kyr could be accomplished under a modern circulation regime solely by a reservoir age that is 1.5 kyr larger at the Iberian Margin than at the Eastern Equatorial Pacific. Skinner et al. (2019) constructed regional reservoir age splines for the high latitude Northeast Atlantic, the Iberian Margin, and the Southern Ocean. Mean values for the Iberian Margin spline range from approximately 400 and 1000 years during T1 (Figure 8). For the Eastern Equatorial Pacific, results vary across different studies. Two studies measured reservoir ages by

comparing planktonic radiocarbon ages with chronostratigraphic tie points and found reservoir ages up to 1.5 and 2 kyr (de la Fuente et al., 2015; Umling & Thunell, 2017). However, a different study was able to avoid stratigraphic alignment by comparing planktonic ages with ages measured in wood fragments (Zhao & Keigwin, 2018) and found reservoir ages that are similar to today (Zhao & Keigwin, 2018; Figure 8). From these studies (Skinner et al., 2019; de la Fuente 2015; Umling & Thunell, 2017; Zhao & Keigwin, 2018) it does not appear that the reservoir age at the Iberian Margin was more than 1.5 kyr greater than the Eastern Equatorial Pacific, implying that additional or different factors are needed to produce the lag calculated here.

It is difficult to corroborate how changing deep water ventilation ages may have contributed to the 2.1-2.5 kyr lag observed in the latter half of T1. If responsible for the lag, ventilation ages in the deep Eastern Equatorial Pacific would have to be up to 2.5 kyr larger than at the Iberian Margin during the Bølling Allerød (BA) and YD. However, by this time ventilation ages in these two sites were approximately equal, reaching values between 1.5 and 2 kyr (Skinner et al., 2014; Umling et al., 2017; de la Fuente et al., 2015; Zhao & Keigwin, 2018; Rafter et al., 2022).

Thus, the lag is most likely caused by contributions from different factors, including asynchronous surface forcings and water-mass geometry changes. Evidence from ice core records sampled from Greenland and Antarctica support opposing millennial scale trends in the Northern and Southern hemispheres (EPICA Community Members, 2006; Lemieux-Dudon et al., 2010; Pedro et al., 2011; Buizert et al., 2014; WAIS Divide Project Members 2015) which would have been translated to the deep ocean core sites via Northern Sourced (for the Iberian Margin) and Southern Sourced (for the Eastern Equatorial Pacific) water

masses. Furthermore, these differences would have been accentuated if Northern Sourced water was cut off from the Pacific (Sikes et al., 2017). Although early Antarctic warming could contribute to a $\delta^{18}O$ lead in SCW and the deep Pacific, meltwater input to the North Atlantic and subsequent brine rejection during HS1 would generate a large, early change in the seawater $\delta^{18}O$ of NADW (Waelbroeck et al., 2011). However, the presence of NADW at the Iberian Margin may have also been decreased during HS1. The oscillating ventilation ages measured in MD99-2334K are accompanied by deep water temperature changes and low $\delta^{18}O_{sw}$ values (Skinner et al., 2003; Skinner et al., 2007), implying that the increased ventilation ages likely reflect a change in water mass (i.e., shoaling of NADW) rather than an increased transit time of NADW to the deep Iberian Margin.

The millennial scale trends in the Iberian Margin stack and the results of Methods 1 and 3 may reflect the transient climate events during T1. However, it is challenging to disentangle the roles that the different factors discussed above may have played and the lag between the two regions is likely caused by a combination of these factors.

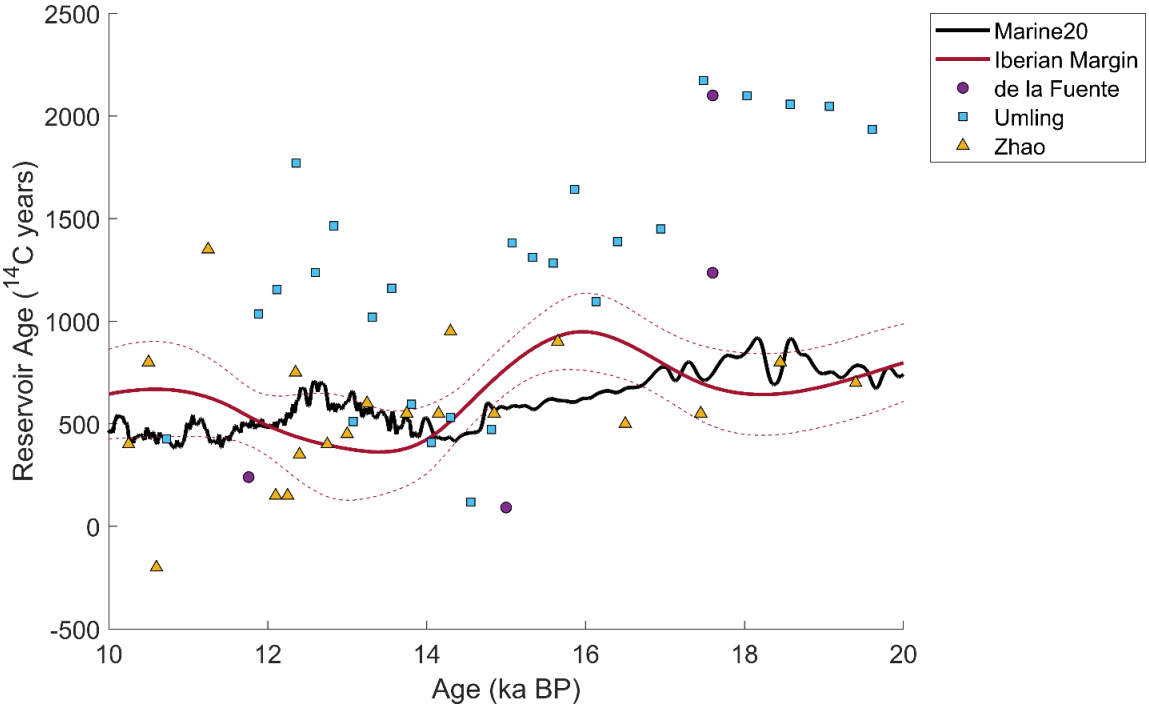

Figure 9: Comparisons of surface reservoir ages at the Iberian Margin (Skinner et al., 2019), Eastern Equatorial Pacific (de la Fuente et al., 2015; Umling et al., 2017; Zhao & Keigwin, 2018), and an idealized global average used in the Marine20 curve (Heaton et al., 2020).

5.2 Sensitivities

The lags presented here have sensitivities that require further examination. For example, all lags are sensitive to the time-dependent standard deviation of the Eastern Equatorial Pacific stack (and thus the choice of Pacific cores included in the stack). In chapter 2 I demonstrate that an increase in the target stack's standard deviation ultimately increases the statistical uncertainty of the resulting lag. Furthermore, the additional ages used when constructing the δ^{18}O-only age models can potentially skew the lag results. In Chapter 2 I found that the lags for two cores were sensitive to the choice of these additional ages.

A potentially problematic feature of Method 2 is its disregard of the standard deviation of the Iberian Margin stack. The standard deviation could potentially be included by adding noise to the sampled $\delta^{18}O$ signal that is modeled as normal distribution with mean and standard deviation equal to that of the Iberian Margin stack. Furthermore, Method 2 required the implementation of a synthetic sedimentation rate, and it is possible that the choice of sedimentation rate affects the resulting alignment.

Finally, the statistical uncertainty for Method 3 is large due to a lack of autocorrelation in the lag samples. Applying a prior on the lag's autocorrelation and drawing Markov Chain Monte Carlo samples via the Hamiltonian Monte Carlo algorithm offers a potential improvement to this method. This would likely decrease the statistical uncertainty and judging by the locations of high probability in Figure 7, would potentially result in a larger lag towards the end of T1. Furthermore, Method 3 is sensitive to the shift and scale parameters, which were selected to match those from Method 2. These parameters from Method 2 are in turn potentially sensitive to the start and end ages chosen to truncate the Iberian Margin stack before alignment. Only a small change in shift and scale parameters is estimated when the Iberian Margin stack is truncated at 0 and 30 ka BP rather than 5 and 25 ka BP (Figure 9). The former results in a shift of -0.02 and scale of 1.03 which is very similar to the latter parameters of 0.13 and 1.01. Although the resulting lag estimates using these new shift and scale parameters are very similar to the default, the lags are no longer statistically significant at the 95% confidence level during T1.

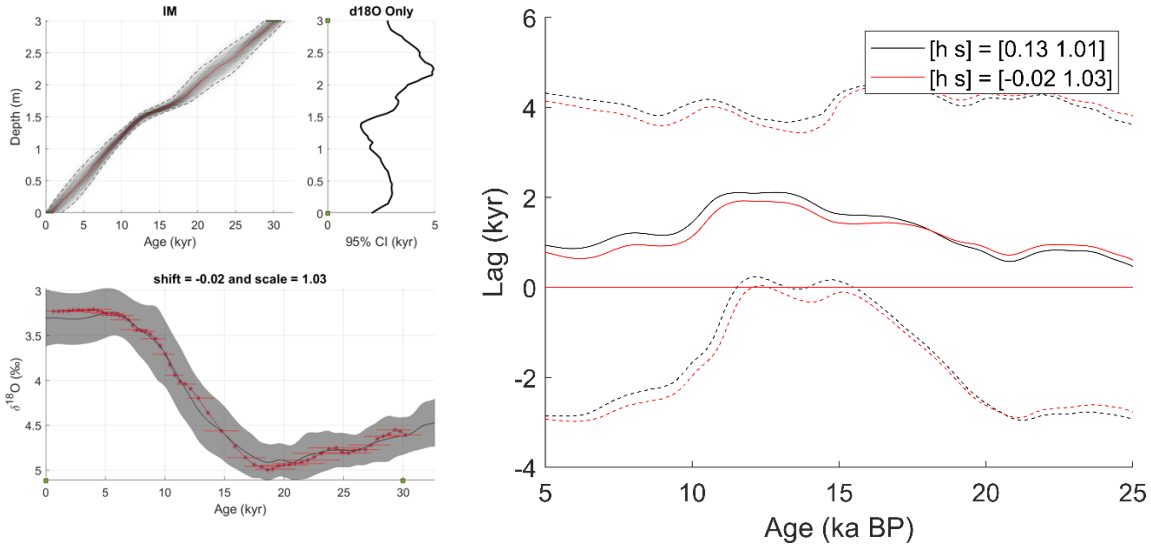

Figure 10: (Left) Results from BIGMACS of aligning the median Iberian Margin signal truncated at 30 ka BP to the Eastern Equatorial Pacific stack. Truncating the Iberian Margin stack at 30 ka BP instead 5 and 25 ka BP results in only a small shift and scale difference of -0.02 and 1.03 opposed to 0.13 and 1.01. (Right) Comparison of the lag posterior produced by Method 3 using the default shift and scale parameters (black) and the shift and scale parameters of -0.02 and 10.3.

6 Conclusion

I revisit the 3.9 kyr lag estimated between the Atlantic and Pacific during T1 (Skinner & Shackleton, 2005) by constructing regional stacks for the Iberian Margin and Eastern Equatorial Pacific. I calculate the lag between the stacks using three different techniques and find that the results from each method agree well, producing maximum lags of 2.44 (95% CI: 1.62 – 3.34) kyr, 2.52 (95% CI: 1.58 – 3.31) kyr, and 2.11 (95% CI: 0.08 – 3.70) kyr at 11.4, 14.2, and 12.9 ka BP. These results imply that the lag between the Eastern Equatorial Pacific and the Iberian Margin is potentially 1.5 kyr smaller than initially estimated by Skinner & Shackleton (2005), and reaches a maximum in the latter half of the termination. The lag is likely caused by a combination of factors, including asynchronous hemispheric surface signals, water mass geometry changes, a longer surface to deep transit

time in the Eastern Equatorial Pacific, and/or a larger surface reservoir age at the Iberian Margin.

7 Supplemental Figures

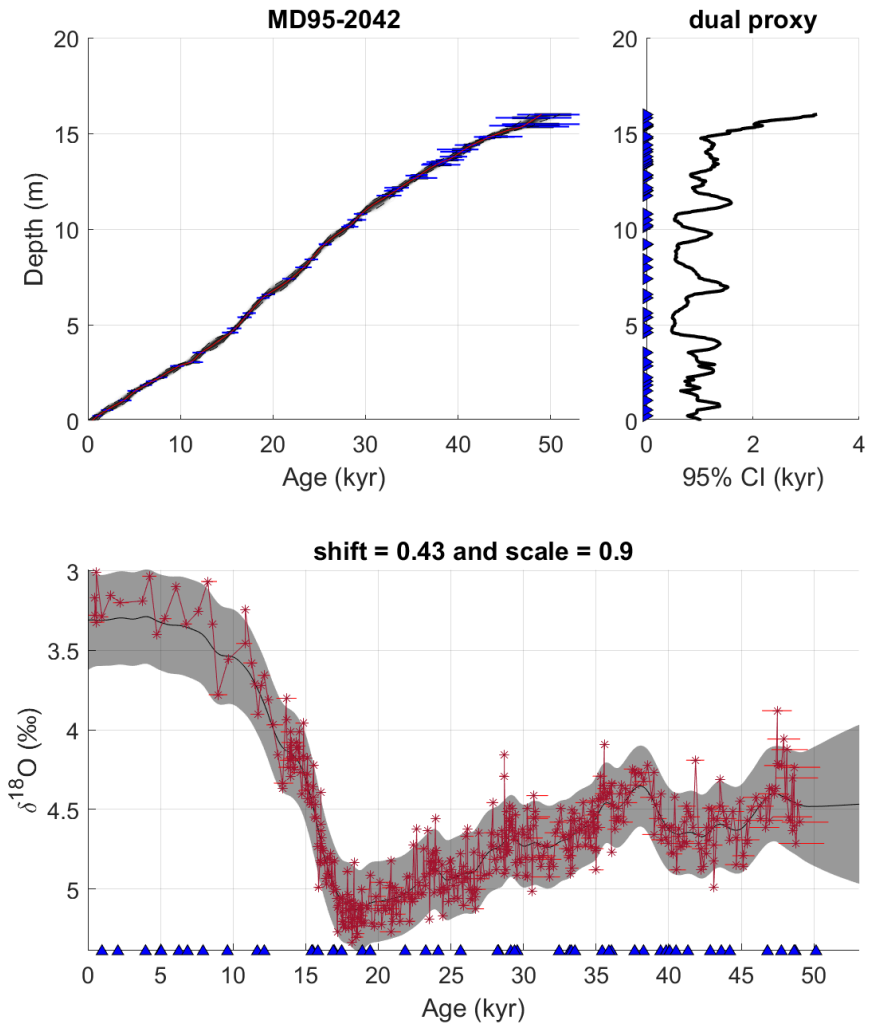

Figure S1: Age mode summary for core MD95-2042.

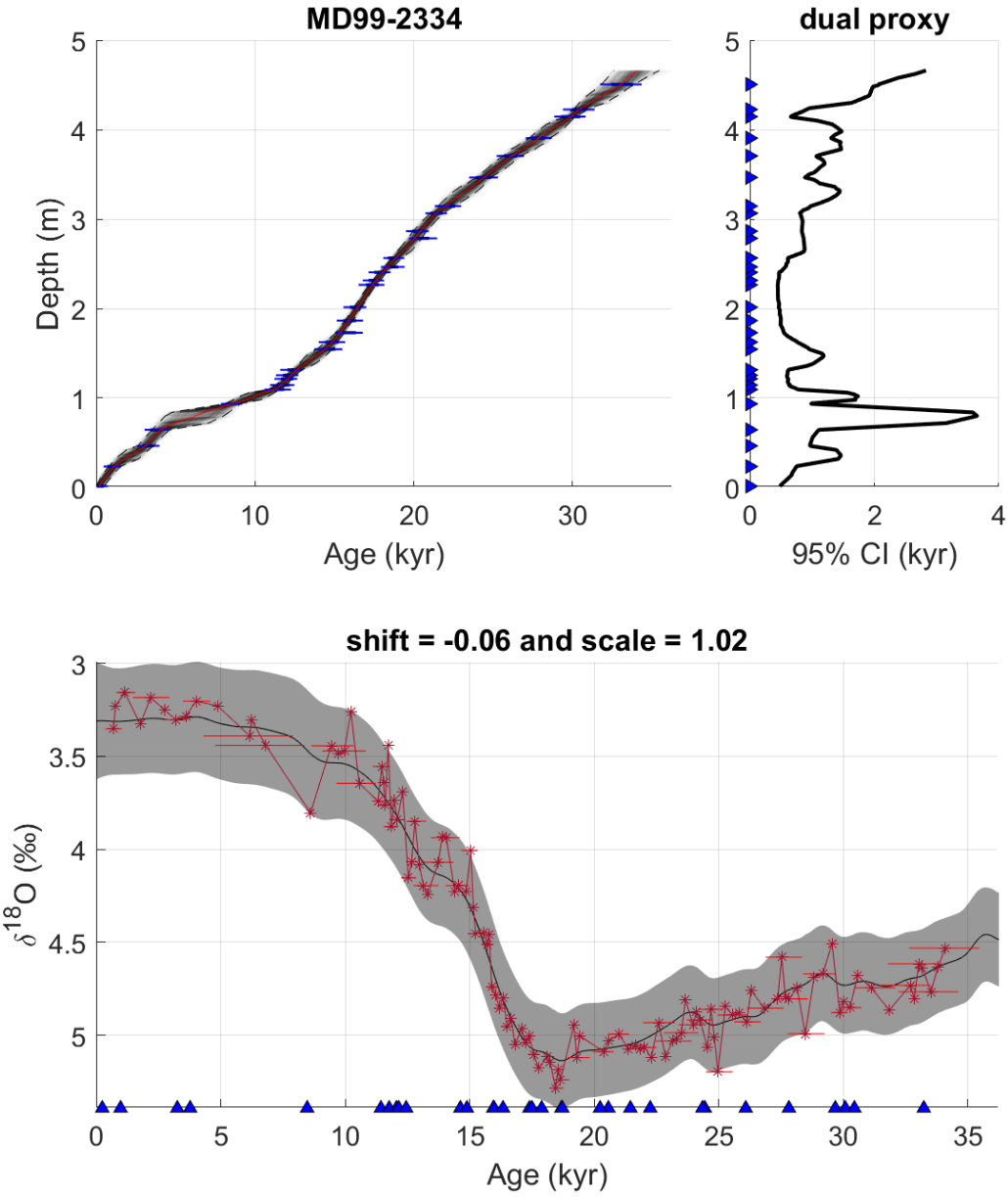

Figure S2: Age mode summary for core MD99-2334K.

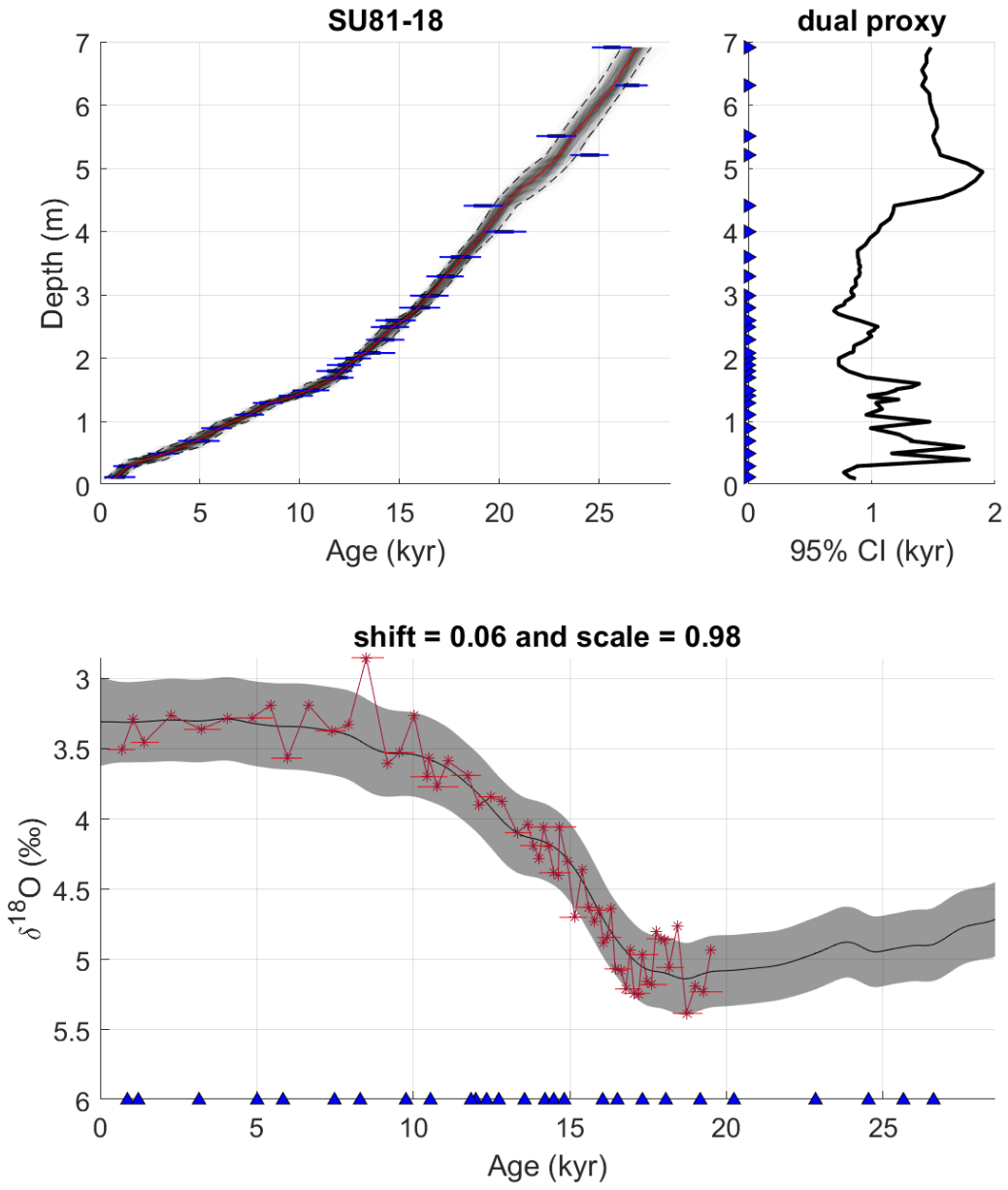

Figure S3: Age mode summary for core SU81-18.

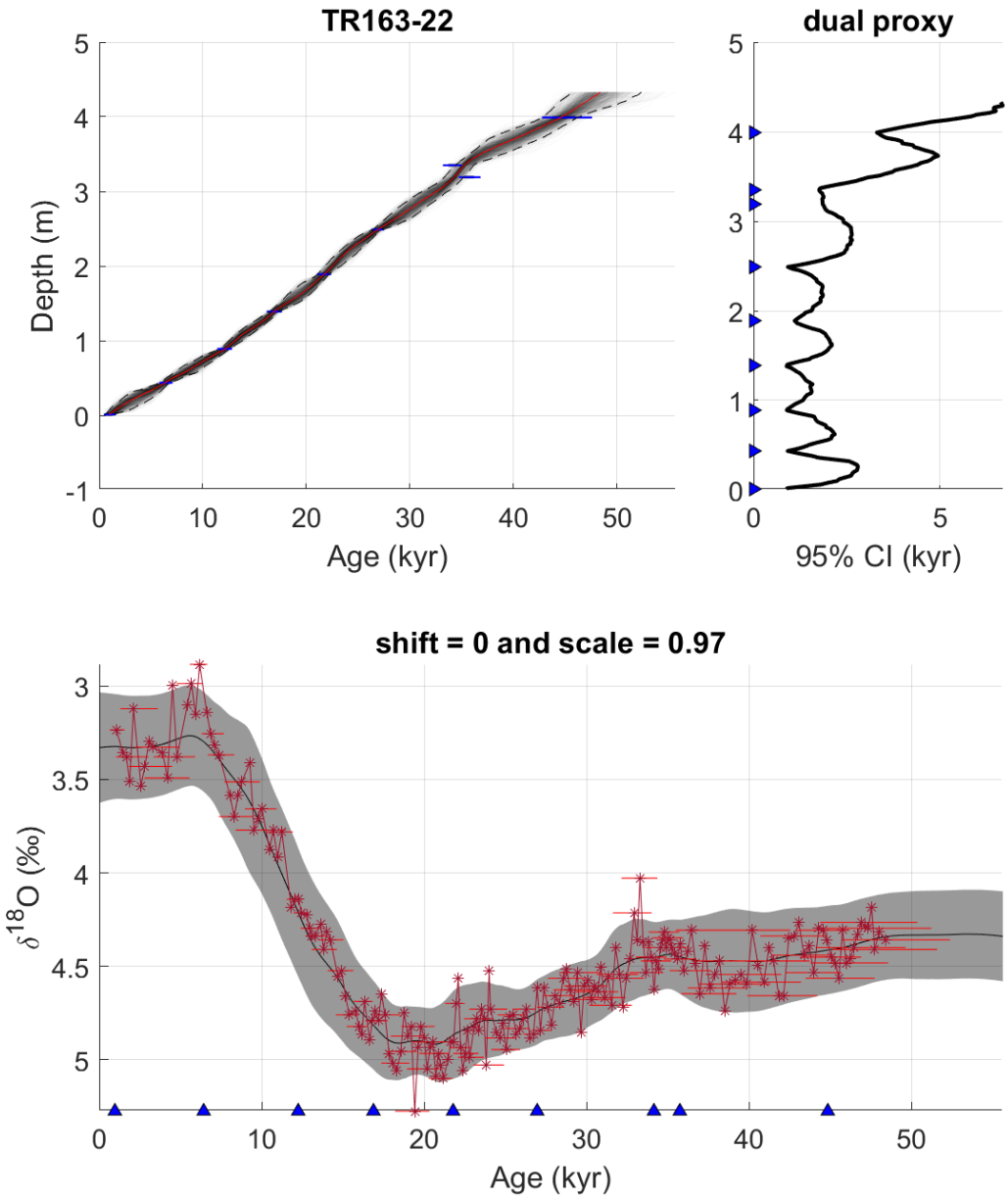

Figure S4: Age mode summary for core TR163-22.

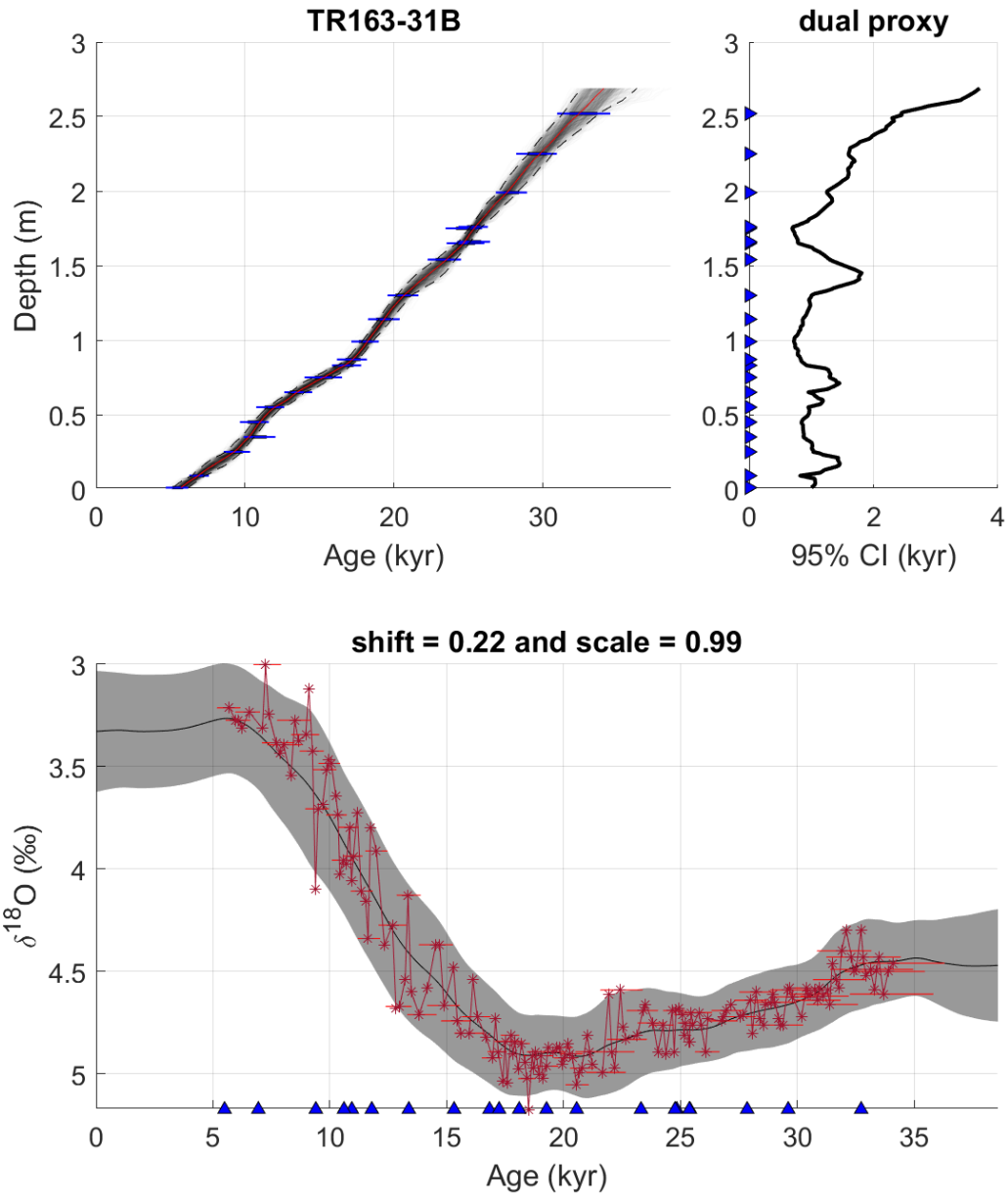

Figure S5: Age mode summary for core TR163-31B.

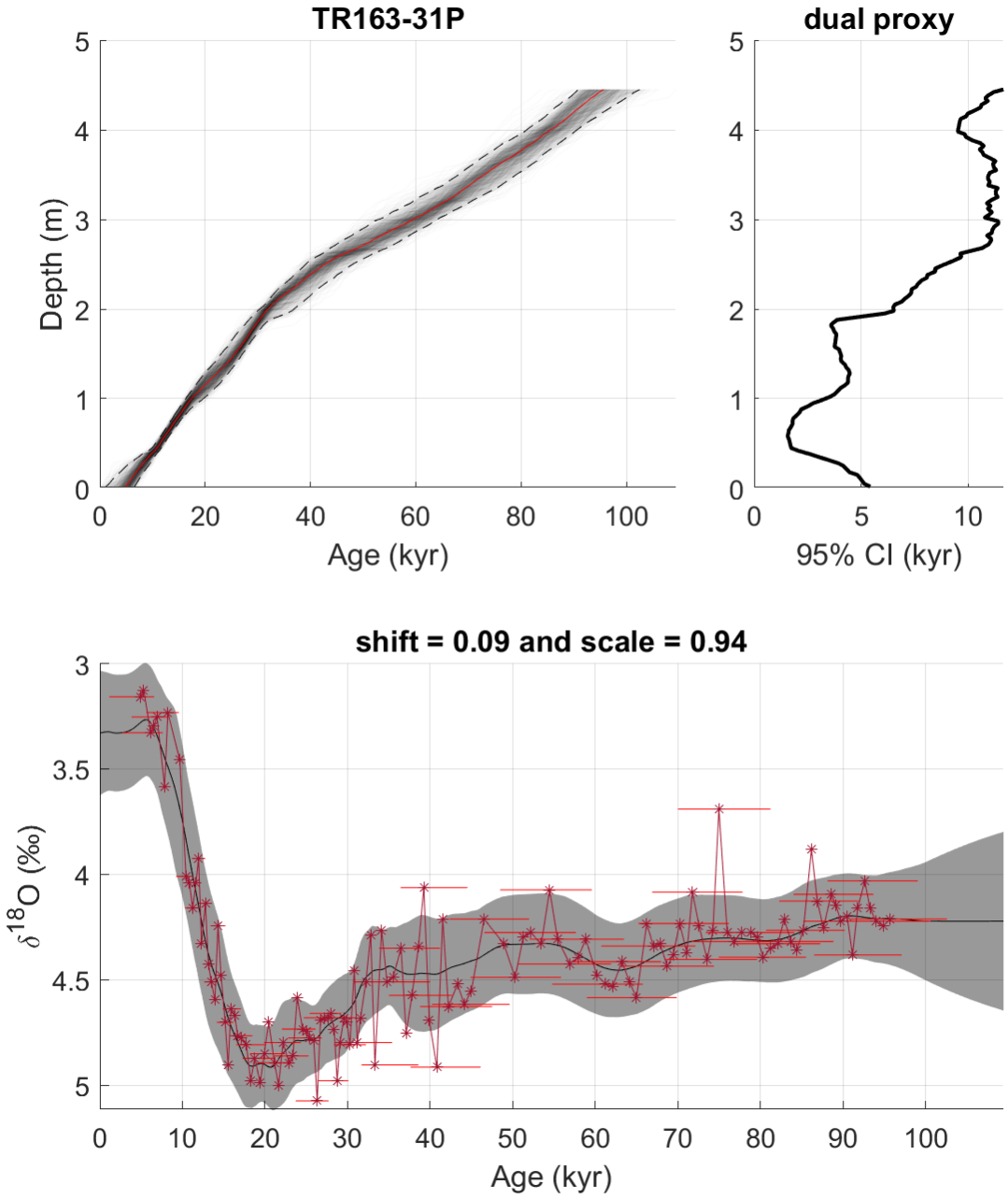

Figure S6: Age mode summary for core TR163-31P.

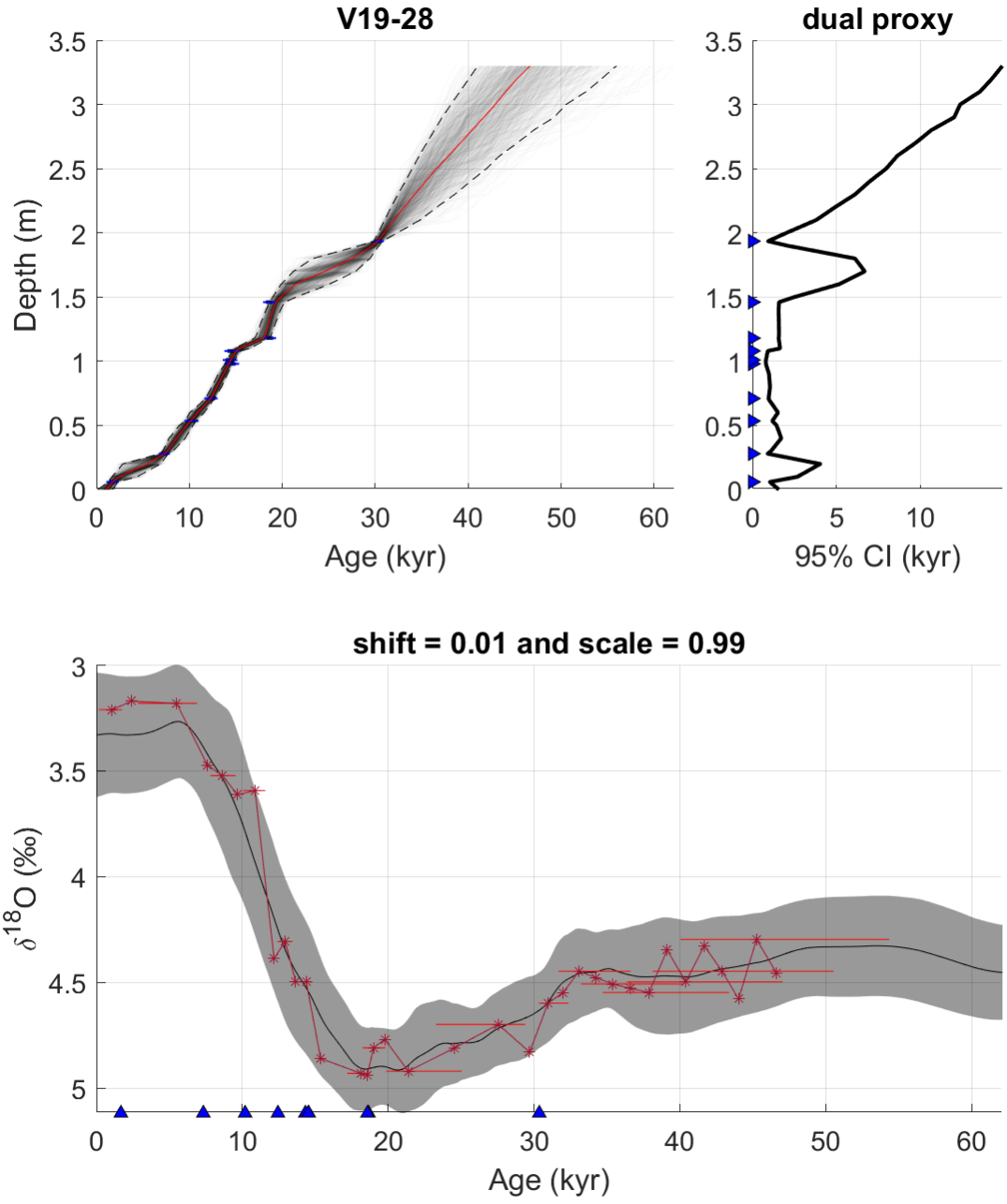

Figure S7: Age mode summary for core V19-28.

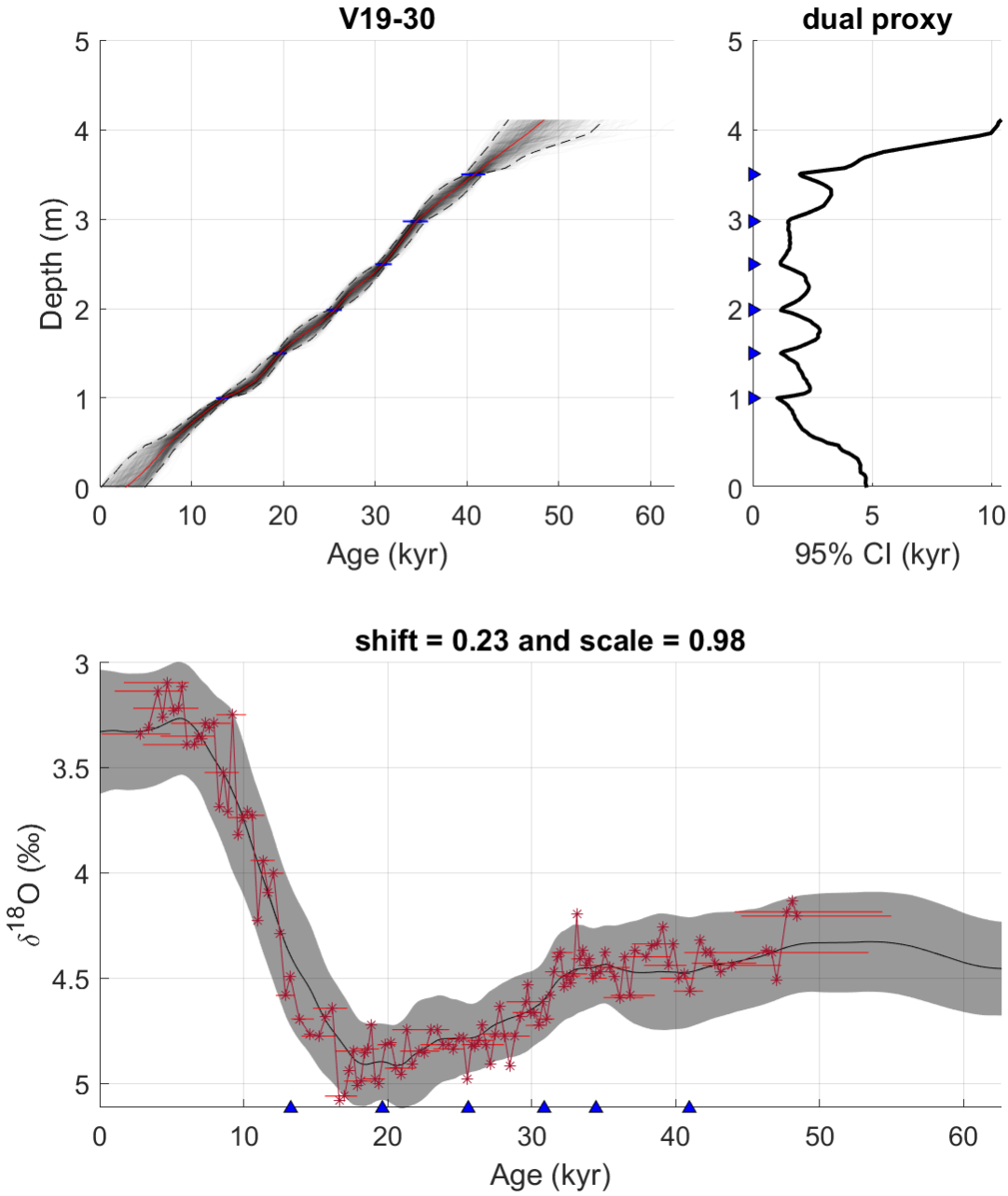

Figure S8: Age mode summary for core V19-30.

8 References

1. Andersen, K.K., Azuma, N., Barnola, J.-M., Bigler, M., Biscaye, P., Caillon, N., Chappellaz, J., Clausen, H.B., Dahl-Jensen, D., Fischer, H., Flückiger, J., Fritzsche, D., Fujii, Y., Goto-Azuma, K., Grønvold, K., Gundestrup, N.S., Hansson, M., Huber, C., Hvidberg, C.S., Johnsen, S.J., Jonsell, U., Jouzel, J., Kipfstuhl, S., Landais, A., Leuenberger, M., Lorrain, R., Masson-Delmotte, V., Miller, H., Motoyama, H., Narita, H., Popp, T., Rasmussen, S.O., Raynaud, D., Rothlisberger, R., Ruth, U., Samyn, D., Schwander, J., Shoji, H., Siggard-Andersen, M.-L., Steffensen, J.P., Stocker, T., Sveinbjörnsdóttir, A.E., Svensson, A., Takata, M., Tison, J.-L., Thorsteinsson, Th., Watanabe, O., Wilhelms, F., White, J.W.C., North Greenland Ice Core Project members, 2004. High-resolution record of Northern Hemisphere climate extending into the last interglacial period. Nature 431, 147–151. https://doi.org/10.1038/nature02805
2. Barbante, C., Barnola, J.-M., Becagli, S., Beer, J., Bigler, M., Boutron, C., Blunier, T., Castellano, E., Cattani, O., Chappellaz, J., Dahl-Jensen, D., Debret, M., Delmonte, B., Dick, D., Falourd, S., Faria, S., Federer, U., Fischer, H., Freitag, J., Frenzel, A., Fritzsche, D., Fundel, F., Gabrielli, P., Gaspari, V., Gersonde, R., Graf, W., Grigoriev, D., Hamann, I., Hansson, M., Hoffmann, G., Hutterli, M.A., Huybrechts, P., Isaksson, E., Johnsen, S., Jouzel, J., Kaczmarska, M., Karlin, T., Kaufmann, P., Kipfstuhl, S., Kohno, M., Lambert, F., Lambrecht, Anja, Lambrecht, Astrid, Landais, A., Lawer, G., Leuenberger, M., Littot, G., Loulergue, L., Lüthi, D., Maggi, V., Marino, F., Masson-Delmotte, V., Meyer, H., Miller, H., Mulvaney, R., Narcisi, B., Oerlemans, J., Oerter, H., Parrenin, F., Petit, J.-R., Raisbeck, G., Raynaud, D., Röthlisberger, R., Ruth, U., Rybak, O., Severi, M., Schmitt, J., Schwander, J., Siegenthaler, U., Siggaard-Andersen, M.-L., Spahni, R., Steffensen, J.P., Stenni, B., Stocker, T.F., Tison, J.-L., Traversi, R., Udisti, R., Valero-Delgado, F., van den Broeke, M.R., van de Wal, R.S.W., Wagenbach, D., Wegner, A., Weiler, K., Wilhelms, F., Winther, J.-G., Wolff, E., EPICA Community Members, 2006. One-to-one coupling of glacial climate variability in Greenland and Antarctica. Nature 444, 195–198. https://doi.org/10.1038/nature05301
3. Bond, G., Showers, W., Cheseby, M., Lotti, R., Almasi, P., deMenocal, P., Priore, P., Cullen, H., Hajdas, I., Bonani, G., 1997. A Pervasive Millennial-Scale Cycle in North Atlantic Holocene and Glacial Climates. Science 278, 1257–1266. https://doi.org/10.1126/science.278.5341.1257
4. Buizert, C., Gkinis, V., Severinghaus, J.P., He, F., Lecavalier, B.S., Kindler, P., Leuenberger, M., Carlson, A.E., Vinther, B., Masson-Delmotte, V., White, J.W.C., Liu, Z., Otto-Bliesner, B., Brook, E.J., 2014. Greenland temperature response to climate forcing during the last deglaciation. Science 345, 1177–1180. https://doi.org/10.1126/science.1254961
5. Curry, W.B., Oppo, D.W., 2005. Glacial water mass geometry and the distribution of δ13C of ΣCO2 in the western Atlantic Ocean. Paleoceanography 20. https://doi.org/10.1029/2004PA001021
6. de la Fuente, M., Skinner, L., Calvo, E., Pelejero, C., Cacho, I., 2015. Increased reservoir ages and poorly ventilated deep waters inferred in the glacial Eastern Equatorial Pacific. Nat Commun 6, 7420. https://doi.org/10.1038/ncomms8420
7. DeVries, T., Primeau, F., 2011. Dynamically and Observationally Constrained Estimates of Water-Mass Distributions and Ages in the Global Ocean. Journal of Physical Oceanography 41, 2381–2401. https://doi.org/10.1175/JPO-D-10-05011.1
8. Gebbie, G., 2012. Tracer transport timescales and the observed Atlantic-Pacific lag in the timing of the Last Termination. Paleoceanography 27. https://doi.org/10.1029/2011PA002273
9. Kindler, P., Guillevic, M., Baumgartner, M., Schwander, J., Landais, A., Leuenberger, M., 2014. Temperature reconstruction from 10 to 120 kyr b2k from the NGRIP ice core. Climate of the Past 10, 887–902. https://doi.org/10.5194/cp-10-887-2014
10. Koutavas, A., Lynch-Stieglitz, J., 2003. Glacial-interglacial dynamics of the eastern equatorial Pacific cold tongue-Intertropical Convergence Zone system reconstructed from oxygen isotope records. Paleoceanography 18. https://doi.org/10.1029/2003PA000894
11. Lea, D.W., Pak, D.K., Belanger, C.L., Spero, H.J., Hall, M.A., Shackleton, N.J., 2006. Paleoclimate history of Galápagos surface waters over the last 135,000yr. Quaternary Science Reviews 25, 1152–1167. https://doi.org/10.1016/j.quascirev.2005.11.010
12. Lee, T., Rand, D., Lisiecki, L.E., Gebbie, G., Lawrence, C.E., 2022. Bayesian age models and stacks: Combining age inferences from radiocarbon and benthic δ^{18}O stratigraphic alignment. EGUsphere 1–29. https://doi.org/10.5194/egusphere-2022-734

13. Lemieux-Dudon, B., Blayo, E., Petit, J.-R., Waelbroeck, C., Svensson, A., Ritz, C., Barnola, J.-M., Narcisi, B.M., Parrenin, F., 2010. Consistent dating for Antarctic and Greenland ice cores. Quaternary Science Reviews 29, 8–20. https://doi.org/10.1016/j.quascirev.2009.11.010
14. Loubere, P., Richaud, M., 2007. Some reconciliation of glacial-interglacial calcite flux reconstructions for the eastern equatorial Pacific. Geochemistry, Geophysics, Geosystems 8. https://doi.org/10.1029/2006GC001367
15. Martin, P.A., Lea, D.W., Rosenthal, Y., Shackleton, N.J., Sarnthein, M., Papenfuss, T., 2002. Quaternary deep sea temperature histories derived from benthic foraminiferal Mg/Ca. Earth and Planetary Science Letters 198, 193–209. https://doi.org/10.1016/S0012-821X(02)00472-7
16. Members, W.D.P., 2015. Precise interpolar phasing of abrupt climate change during the last ice age. Nature 520, 661–665. https://doi.org/10.1038/nature14401
17. Pedro, J.B., van Ommen, T.D., Rasmussen, S.O., Morgan, V.I., Chappellaz, J., Moy, A.D., Masson-Delmotte, V., Delmotte, M., 2011. The last deglaciation: timing the bipolar seesaw. Clim. Past 7, 671–683. https://doi.org/10.5194/cp-7-671-2011
18. Rafter, P.A., Gray, W.R., Hines, S.K.V., Burke, A., Costa, K.M., Gottschalk, J., Hain, M.P., Rae, J.W.B., Southon, J.R., Walczak, M.H., Yu, J., Adkins, J.F., DeVries, T., 2022. Global reorganization of deep-sea circulation and carbon storage after the last ice age. Science Advances 8, eabq5434. https://doi.org/10.1126/sciadv.abq5434
19. Reimer, P.J., Bard, E., Bayliss, A., Beck, J.W., Blackwell, P.G., Ramsey, C.B., Buck, C.E., Cheng, H., Edwards, R.L., Friedrich, M., Grootes, P.M., Guilderson, T.P., Haflidason, H., Hajdas, I., Hatté, C., Heaton, T.J., Hoffmann, D.L., Hogg, A.G., Hughen, K.A., Kaiser, K.F., Kromer, B., Manning, S.W., Niu, M., Reimer, R.W., Richards, D.A., Scott, E.M., Southon, J.R., Staff, R.A., Turney, C.S.M., Plicht, J. van der, 2013. IntCal13 and Marine13 Radiocarbon Age Calibration Curves 0–50,000 Years cal BP. Radiocarbon 55, 1869–1887. https://doi.org/10.2458/azu_js_rc.55.16947
20. Shackleton, N.J., Duplessy, J.-C., Arnold, M., Maurice, P., Hall, M.A., Cartlidge, J., 1988. Radiocarbon age of last glacial Pacific deep water. Nature 335, 708–711. https://doi.org/10.1038/335708a0
21. Shackleton, N.J., Fairbanks, R.G., Chiu, T., Parrenin, F., 2004. Absolute calibration of the Greenland time scale: implications for Antarctic time scales and for Δ14C. Quaternary Science Reviews 23, 1513–1522. https://doi.org/10.1016/j.quascirev.2004.03.006
22. Shakun, J.D., Clark, P.U., He, F., Marcott, S.A., Mix, A.C., Liu, Z., Otto-Bliesner, B., Schmittner, A., Bard, E., 2012. Global warming preceded by increasing carbon dioxide concentrations during the last deglaciation. Nature 484, 49–54. https://doi.org/10.1038/nature10915
23. Sikes, E.L., Allen, K.A., Lund, D.C., 2017a. Enhanced δ13C and δ18O Differences Between the South Atlantic and South Pacific During the Last Glaciation: The Deep Gateway Hypothesis. Paleoceanography 32, 1000–1017. https://doi.org/10.1002/2017PA003118
24. Sikes, E.L., Allen, K.A., Lund, D.C., 2017b. Enhanced δ13C and δ18O Differences Between the South Atlantic and South Pacific During the Last Glaciation: The Deep Gateway Hypothesis. Paleoceanography 32, 1000–1017. https://doi.org/10.1002/2017PA003118
25. Skinner, L.C., Freeman, E., Hodell, D., Waelbroeck, C., Vazquez Riveiros, N., Scrivner, A.E., 2021. Atlantic Ocean Ventilation Changes Across the Last Deglaciation and Their Carbon Cycle Implications. Paleoceanography and Paleoclimatology 36, e2020PA004074. https://doi.org/10.1029/2020PA004074
26. Skinner, L.C., Muschitiello, F., Scrivner, A.E., 2019. Marine Reservoir Age Variability Over the Last Deglaciation: Implications for Marine CarbonCycling and Prospects for Regional Radiocarbon Calibrations. Paleoceanography and Paleoclimatology 34, 1807–1815. https://doi.org/10.1029/2019PA003667
27. Skinner, L.C., Shackleton, N.J., 2005. An Atlantic lead over Pacific deep-water change across Termination I: implications for the application of the marine isotope stage stratigraphy. Quaternary Science Reviews 24, 571–580. https://doi.org/10.1016/j.quascirev.2004.11.008
28. Skinner, L.C., Shackleton, N.J., 2004. Rapid transient changes in northeast Atlantic deep water ventilation age across Termination I. Paleoceanography 19. https://doi.org/10.1029/2003PA000983
29. Skinner, L.C., Shackleton, N.J., Elderfield, H., 2003. Millennial-scale variability of deep-water temperature and δ18Odw indicating deep-water source variations in the Northeast Atlantic, 0–34 cal. ka BP. Geochemistry, Geophysics, Geosystems 4. https://doi.org/10.1029/2003GC000585

30. Skinner, L.C., Waelbroeck, C., Scrivner, A.E., Fallon, S.J., 2014. Radiocarbon evidence for alternating northern and southern sources of ventilation of the deep Atlantic carbon pool during the last deglaciation. Proceedings of the National Academy of Sciences 111, 5480–5484. https://doi.org/10.1073/pnas.1400668111
31. Talley, L.D., 2013. Closure of the Global Overturning Circulation Through the Indian, Pacific, and Southern Oceans: Schematics and Transports. Oceanography 26, 80–97.
32. The 100,000-Year Ice-Age Cycle Identified and Found to Lag Temperature, Carbon Dioxide, and Orbital Eccentricity | Science [WWW Document], n.d. URL https://www.science.org/doi/full/10.1126/science.289.5486.1897 (accessed 8.20.23).
33. Umling, N.E., Thunell, R.C., 2017. Synchronous deglacial thermocline and deep-water ventilation in the eastern equatorial Pacific. Nat Commun 8, 14203. https://doi.org/10.1038/ncomms14203
34. Vogelsang, E., Sarnthein, M., Pflaumann, U., 2001. d18O Stratigraphy, chronology, and sea surface temperatures of Atlantic sediment records (GLAMAP-2000 Kiel), Berichte - Reports, Institut für Geowissenschaften. Kiel, Germany. https://doi.org/10.2312/reports-ifg.2001.13
35. Waelbroeck, C., Duplessy, J.-C., Michel, E., Labeyrie, L., Paillard, D., Duprat, J., 2001. The timing of the last deglaciation in North Atlantic climate records. Nature 412, 724–727. https://doi.org/10.1038/35089060
36. Waelbroeck, C., Skinner, L.C., Labeyrie, L., Duplessy, J.-C., Michel, E., Vazquez Riveiros, N., Gherardi, J.-M., Dewilde, F., 2011. The timing of deglacial circulation changes in the Atlantic. Paleoceanography 26. https://doi.org/10.1029/2010PA002007
37. Zhao, N., Keigwin, L.D., 2018. An atmospheric chronology for the glacial-deglacial Eastern Equatorial Pacific. Nat Commun 9, 3077. https://doi.org/10.1038/s41467-018-05574-x

VI. Conclusion

This thesis has presented novel methods to enhance the precision and accuracy of ocean sediment core age models, to construct continuous and regional benthic $\delta^{18}O$ stacks, and to calculate time-dependent benthic $\delta^{18}O$ lags complete with statistical uncertainties.

Chapter II outlined the new Bayesian software package, BIGMACS, to construct ocean sediment core age models using direct age constraints such as radiocarbon data as well as the probabilistic stratigraphic alignment of benthic $\delta^{18}O$ signals. BIGMACS is also capable of constructing regional and continuous benthic $\delta^{18}O$ stacks from a smaller number of sediment cores.

Chapter III introduced a new method for calculating time-dependent benthic $\delta^{18}O$ lags by subtracting radiocarbon age models from $\delta^{18}O$-aligned age models. Furthermore, through the subtraction of Markov Chain Monte Carlo Samples, the statistical uncertainty from each age model is incorporated into the lag results. This method was validated against previous observations of benthic $\delta^{18}O$ offsets at the Brazil Margin.

Chapter IV applied the methods of Chapter III to calculate lags for a compilation of 33 Atlantic sediment cores which revealed three distinct regions defined by the timing of $\delta^{18}O$ change during Termination 1. Statistically significant leads were observed in the intermediate West Atlantic, statistically significant lags were found in the deep South West Atlantic and the abyssal North West Atlantic, and the East Atlantic was found to have a similar timing of $\delta^{18}O$ change to the DNEA target stack.

Finally, Chapter V revisited the lag between the Iberian Margin and the Eastern Equatorial Pacific and, using three different techniques, concluded that it is 1.5 kyr smaller than originally estimated.

In conclusion, the combined contributions of a new statistical software package and a map of benthic $\delta^{18}O$ lags offer two improvements to future ocean sediment core age models. First, researchers can now statistically incorporate direct age information, such as radiocarbon data, with benthic $\delta^{18}O$ stratigraphic alignment, effectively improving both the accuracy and the precision of the final age model. Second, the Atlantic map of benthic $\delta^{18}O$ lags will aid investigators when selecting or constructing target stacks for benthic $\delta^{18}O$ alignment. Furthermore, this map will provide investigators with estimates of the uncertainties sourced from diachronous benthic $\delta^{18}O$ signals.

Additionally, benthic $\delta^{18}O$ lags have improved our understanding of the effects that asynchronous hemispheric surface signals, surface to deep transit times, and shifts water mass geometries have on climate signals recorded in the deep ocean. I have attributed the leads measured in the intermediate West Atlantic to subsurface warming during Heinrich Stadial 1. I have also ascribed the lags in the deep South West Atlantic and abyssal North West Atlantic to a mid-depth age maximum formed by the upper southward flowing arm of the glacial Antarctic Bottom Water convection cell. Furthermore, I find a statistically significant correlation between the percent change in Southern Component Water and the magnitude of leads and lags, emphasizing the importance of water mass geometry changes. Finally, using an ocean circulation inverse model paired with an idealized deglacial ramp function, I derive an equation to fit benthic $\delta^{18}O$ lags as the sum of a southern hemisphere surface lag, surface to deep transit times, and Southern Component Water percentages.